



## Doctoral Thesis

# **Body-mounted antennas the effect of the human body on the RF transmission of small body-mounted biotelemetry- and portable radio antennas in the frequency range 10-1000 MHz and safety considerations**

**Author(s):**

Neukomm, Peter A.

**Publication Date:**

1979

**Permanent Link:**

<https://doi.org/10.3929/ethz-a-000161229> →

**Rights / License:**

[In Copyright - Non-Commercial Use Permitted](#) →

This page was generated automatically upon download from the [ETH Zurich Research Collection](#). For more information please consult the [Terms of use](#).

Diss. ETH No. 6413

# **Body-Mounted Antennas**

**The Effect of the Human Body on the RF Transmission of Small  
Body-Mounted Biotelemetry- and Portable Radio Antennas in the  
Frequency Range 10-1000 MHz and Safety Considerations**

*A Dissertation submitted to the*

**SWISS FEDERAL INSTITUTE OF TECHNOLOGY ZURICH**  
for the degree of  
**Doctor of Technical Sciences**

presented by

**PETER A. NEUKOMM**  
Dipl. El. Ing. ETH  
born July 28, 1943  
Citizen of Hallau, Schaffhausen

Accepted on the Recommendation of  
Prof. H. Baggenstos, referee  
Prof. Dr. E. Baumann, co-referee

Juris Druck + Verlag Zurich  
1979

ISBN 3 260 04682 8

## PREFACE

This work is an attempt to present a survey on the problems dealing with body-mounted antennas. The effect of the human body on the radiation patterns has been investigated by theoretical models and experiments. A polarization transformation effect has been discovered which leads to a new class of antennas for the resonance frequency range of man. The safety aspects have been investigated by studying the available literature on biological effects of radio- and microwaves.

The author wishes to thank all who have contributed to this work. Valuable scientific support came especially from :

- Prof. H.Baggenstos in electromagnetic theory (ETH, Inst. Electronics)
- Prof. R.F.Harrington in computer programs and theory (Syracuse Univ.)
- Dr. R.M.Bevensee in near-field analysis and computer programs (Lawrence Livermore Laboratory)
- Prof. O.P.Gandhi in resonance absorption (University of Utah)
- Prof. A.W.Guy in phantom techniques (University of Seattle)
- Dr. Z.R.Glaser and Dr. D.L.Conover in safety aspects (NIOOSH)

The experiments could be only performed by the technical assistance of:

- R.Graner and M.Knaute in antenna measurements (Division of Military aerodromes)
- W.Kerle in RF-instrumentation (PTT Switzerland)

I extend my thanks to the directors of the Laboratory of Biomechanics, ETH Zürich:

- Dr. B.M.Nigg and the late, much admired, Prof. J.Wartenweiler (ETH) for the general support of this work as a side branch of biomechanics.

Finally I appreciated the valuable comments and suggestions by

- Dr. J.Denoth (ETH, Laboratory of Biomechanics)
- Mrs. P.Fritz (Zürich)
- Prof. E.Baumann (ETH, Institute of Applied Physics)
- Prof. D.Kaufmann (University of Florida, visiting professor ETH)

and the drawing of the figures by Michael Fritz

P.A. Neukomm



to Vreni

## CONTENTS

page

### PREFACE

1. INTRODUCTION	9
2. PROJECT	13
3. SYMBOLS AND DEFINITIONS	15
4. SAFETY ASPECTS OF RADIO- AND MICROWAVES	23
4.1. Introduction and Historical Background	23
4.2. Electric and Magnetic Properties of Biological Materials	27
4.3. Absorption of Electromagnetic Energy in Biological Material	29
4.4. Observed Biological Effects of RF and MW	34
4.5. High Frequency Fields from Electrically Small Antennas near a Body	38
4.6. Current Trends in International Safety Standards Development	44
4.7. Recommendations for Safety Limits for Body-Mounted Antennas	46
5. ANALYSIS OF THE ANTENNA-BODY SYSTEM	49
5.1. Description of the Antenna-Body Problem	49
5.1.1. Definition of the Basic Goals in Antenna-Body Modelling	49
5.1.2. Parameter description of the General Antenna-Body System	49
5.2. Parameter Evaluation and Modelling of the Antenna-Body System	53
5.2.1. Transformation of the Problem with the Reciprocity Theorem	53
5.2.2. Antenna Length and Field Homogeneity	55
5.2.3. Relation of Body-Dimensions to Wavelengths	59
5.2.4. Influence of the Human Body's Material on the Scattered Field	61
5.3. General Considerations on Antenna Measurements	63
5.3.1. Antenna Measurements in Proximity to the Ground	63
5.3.2. Reflections from the Ground and Wave Polarization	64
5.3.3. Field Homogeneity along the Body Axis at Vertical Polarization	68
5.4. Antenna-Body Models for Computation and Experiment	71
5.4.1. Body Models	71
5.4.2. Antenna-Body Models for Computation	73
5.4.3. Antenna-Body Models for Experiment	73

6. FUNDAMENTAL THEORY FOR THE COMPUTATION OF SCATTERING FROM CONDUCTING BODIES	75
6.1. Purpose of the Theory	75
6.2. Penetration Depth of the EM Field in Conducting Bodies	75
6.3. Charge- and Current Densities at the Surface of a Conducting Body	77
6.3.1. Boundary-Value Problem	77
6.3.2. The Effect of the Surface Current Density $\vec{J}$	80
6.3.3. The Effect of the Surface Charge Density $\sigma_{su}$	81
6.3.4. The Field Outside of the Conducting Medium	81
6.3.5. Determination of the Current Density $\vec{J}$ and the Charge Density $\sigma$	82
6.4. Scattering from Bodies of Revolution with the Method of Moments	84
6.4.1. Generalized Network Parameters for Bodies of Revolution	84
6.4.2. Impedance Matrices	88
6.4.2.1. Evaluation of the Impedances	88
6.4.2.2. Limitations of the Numerical Computations of the Impedances	91
6.4.3. Measurement Matrices	91
6.4.4. General Plane-Wave Scattering	94
6.4.5. Near-Field Computation	94
6.4.5.1. Method of Solution	94
6.4.5.2. Limitations of the Near-Field Computations	98
6.5. Scattering from Long Circular Cylinders: An Analytical Approach	99
6.5.1. Purpose of the Analytical Approach	99
6.5.2. Method of Solution	99
6.5.3. Limitations of the Analytical Near-Field Computation	101
7. TWO-DIMENSIONAL COMPUTATION OF SCATTERING FROM AN INFINITE CIRCULAR CYLINDER	103
7.1. Computational Model and Goals	103
7.2. Computer Program PANA: Near-Field Pattern Computation of the Infinite Cylinder IZYL	103
7.2.1. Computational Formulas and Parameters	103
7.2.2. Program Description PANA	104
7.2.3. Program Limitations and Accuracy	107
7.3. Computed Results of the Two-Dimensional Model IZYL	108
7.3.1. Azimuthal and Directive Radiation Patterns of Antenna-IZYL Model	108
7.3.2. Minimum Gain depending on Frequency and Cylinder Radius	112
8. MEASURING METHOD	113
8.1. Purpose of the Experiment	113
8.2. Description of the Antenna-Body Test Set-Up	113

8.3. Antennas and Feeding	117
8.3.1. Body-Mounted Antenna A <sub>1</sub>	117
8.3.2. RF-Chokes	118
8.3.3. Remote Antenna A <sub>2</sub>	119
8.4. Measuring Equipment	119
8.4.1. Revolving Stage for Antenna-Body Rotation	119
8.4.2. Trackway for Antenna-Body Translation	121
8.4.3. Field Measuring Equipment	122
8.5. Antenna Set-Up Testing and Experimental Procedure	123
9. COMPARISON OF EXPERIMENTAL DATA WITH THEORETICAL DATA	127
9.1. Investigated Parameters	127
9.1.1. Effect of Frequency and Body Material	127
9.1.2. Effect of Antenna-Body Distance and Body Material	129
9.1.3. Effect of the Azimuthal Angle	133
9.1.4. Effect of the Body Material	134
9.1.5. Verification of the Reciprocity Theorem	135
9.2. Discussion of the Limitations of Experiment and Computation	135
10. THREE-DIMENSIONAL COMPUTATION OF SCATTERING FROM FINITE BODIES OF REVOLUTION	137
10.1. Computational Models and Goals	137
10.2. Computer Programs for Near-Field Computations	137
10.2.1. General Overview	137
10.2.2. Parameter Description	138
10.2.3. Program Description HARRA	141
10.2.4. Program Description PANB	142
10.2.5. Program Description PANC	148
10.3. Investigation of Program Limitations and Computational Accuracy	152
10.3.1. Program Limitations	152
10.3.2. Computational Time Limitations	153
10.3.3. Storage Capacity Limitations	154
10.3.4. Investigation of Computational Accuracy	154
10.3.4.1. Minimum Mode Number KK	154
10.3.4.2. Difference between the two Azimuthal Field Components	156
10.3.4.3. Difference between Results at Different Test Segment Lengths	157
10.3.5. Field Homogeneity around a Near Field Point	158
10.3.5.1. Significance of the Field Homogeneity and Computational Data	158
10.3.5.2. Computational Data for Antenna Design	161
10.4. Results from Three-Dimensional Computations on Antenna-Body Models	163
10.4.1. Overview of Investigated Parameters and Explanations	164
10.4.2. Effect of the Frequency on Vertical and Radial Field	163
10.4.3. Effect of the Antenna-Body Distance	
10.4.4. Effect of the Azimuthal Angle	167
10.4.5. Effect of the Irradiation Angle	168
10.4.6. Effect of the Relative Antenna Height	169
10.4.7. Effect of the Frequency on Azimuthal Radiation Pattern	170

10.4.8. Effect of the Frequency on Directive Radiation Pattern	174
10.4.9. Effect of Different Body Shapes on the Fields in the Shadow Zone	178
10.4.10. Effect of Different Body Shapes on Azimuthal Patterns	182
11. EXTENDED MEASURING METHOD FOR FIELD COMPONENTS SEPARATIONS	187
11.1. Purpose of the Extended Experiments	187
11.2. Antenna Manipulator	188
11.3. Electrically Small Dipole Antennas with Built-In Oscillator	189
11.4. Test Program and some Experimental Results Obtained with AO 1 to AO 4	192
12. COMPARISON OF IMPROVED EXPERIMENTAL DATA WITH THREE-DIMENSIONAL COMPUTATIONAL DATA	195
12.1. Investigated Parameters	195
12.1.1. Effect of the Frequency on the Field Components at FZYL and MET	195
12.1.2. Effect of Antenna Height and Proximity to the Ground	197
12.1.3. Effect of the Antenna-Body Distance	200
12.1.4. Effect of the Frequency on the Field Components at a Human Body	202
12.1.5. Azimuthal Radiation Patterns of MET, SUB, FZYL and MANMOD 1 & 2	203
12.2. Discussion of the Limitations of Experiment and Computation	208
13. CONCLUSIONS AND PERSPECTIVES	211
13.1. Important Investigated Parameters of the Antenna-Body System	211
13.1.1. Overview of the Investigated Antenna-Body System	211
13.1.2. The Effect of the Frequency on the Field Distribution	212
13.1.3. The Effect of the Antenna-Body Distance	213
13.1.4. The Dominant Rule of the Radial E-Field Component	214
13.2. Interesting Additional Features of the Antenna-Body System	217
13.2.1. The Broad-Band Characteristics of the Human Body	217
13.2.2. Body-Mounted Antenna Arrays	219
13.3. Proposals for Efficient, Body-Mounted Antennas	220
13.3.1. Vertical Polarized Antennas	220
13.3.2. Radial Polarized Antennas	220
13.4. The Optimal Frequency Range for Body-Mounted Antennas	223
13.4.1. Conclusions from the Obtained Data	223
13.4.2. Future Frequencies for Biotelemetry	224
14. SUMMARIES	
14.1. Summary	225
14.2. Zusammenfassung	227
15. REFERENCES	229
16. APPENDIX	235

## 1. INTRODUCTION

Biotelemetry is concerned with the obtaining and transmission of measuring data from a free-moving subject. Among other transmission methods such as infrared and ultrasonic it is utilized for all modulated radiowaves in the frequency range 10 to 1000 MHz.

In radio telemetry one distinguishes between tracking (radio bearing and identification of subjects) and real measuring data transmission. In contrast to voice communication systems a non-interrupted data flow is required from a moving subject, because the redundancy of the signals is small and the test situation happens only once in many cases.

Multichannel telemetry equipment for the continuous recording of physiological, chemical, biomechanical and other data are primarily applied on human subjects in patient monitoring, exercise physiology and sport research. The encumbrance for the subject due to weight and volume of the equipment and the feedback of the apparatus on the measuring data should be as little as possible. With today's technology it is possible to produce miniature transducers and transmitters. Missing are, however, small, body-mounted antennas with good omnidirectional properties.

A small, trunk-mounted, or even a non-visible, efficient antenna on the subject would open new fields of application not only for biotelemetry. Many applications of mobile voice communication for security personnel, police agents, etc., require a camouflaged antenna (GOUBAU and SCHWERING [32], KING [48]). Experience demonstrates however, that the transmission loss of small, body-mounted antennas amounts up to about 20-30 dB. This means that less than one percent of the RF energy can be utilized for transmission in unfavorable conditions. An enhancement of the power of the transmitter output for the improvement of transmission performance cannot be recommended for two reasons: In modern equipment the battery determines the final weight and volume of the transmitter, and RF-power in excess of 100 mW may exceed the safety limits for uncontrolled RF exposure (DDR-Standard [18], NEUKOMM [64]).

In the last few years various experimentalists attempted to quantify the influence of the human body on the radiation pattern of body-mounted antennas. Azimuthal radiation pattern measurements with horizontal polarized antennas were performed in the frequency range 6 to 280 MHz (BUCHANAN, MOORE and RICHTER [12]). Investigations with vertical polarized  $\lambda/2$  dipoles

demonstrated a dominant, but not explicable influence of the antenna-body distance at 450 and 900 MHz (KING and WONG [49]). The fitting of relatively large antennas to the body was investigated in the frequency range 33 to 170 MHz by means of the VSWR, and a main resonance of the human body was postulated to occur at 60-80 MHz (KRUPKA [53]). As a result from these works one may conclude, that the human body acts as a director, reflector or absorber at frequencies above 30 MHz. In spite of considerable effort no systematic relationship was found between body geometry, antenna-body-distance, frequency and radiation pattern.

A first attempt to compute the radiation pattern of an antenna-body system came out in 1977 (NYQUIST, CHEN and GURU [66]). The model consisted of a short dipole antenna with assumed sinusoidal current distribution, parallel to a rectangular cylinder subdivided in dielectrical volume elements. By means of tensor Green's functions various results at 50 MHz were computed, such as power depositions in the body, impedance change of the antenna and also the azimuthal radiation pattern for some antenna locations.

Up to now a general theory about the radiation characteristics of an antenna-body system is missing. The reasons for that gap are mainly:

- An antenna is a complicated radiation source. The fields around an antenna can be roughly categorized in near zone ( $r < \lambda/2\pi$ ), far zone ( $r > \lambda$ ) and transition zone. Within the near zone a strong reactive near field exists which is partially converted within the transition zone into an effective, real, radiating field. The final far field in the far zone is clearly described by the antenna parameter, as long as the near zone is not disturbed. But exactly this happens in the practical application of body-mounted antennas. Any antenna, especially an electrically small antenna, will be detuned by the body proximity. In spite of VSWR measurements one knows little about the radiated power and its radiation characteristics. If the antenna is combined with a fix transmitter (e.g., walkie-talkie) it is difficult to define a radiation reference level. If the antenna is remotely fed, surface waves on the feeding coaxial cables may radiate more than the antenna itself. Reflections from the ground effect a further, but estimable influence. In general, it is quite difficult to construct an antenna test set-up for antenna-body distances ( $d_{at}$ ) below 0.2 m and signal levels below - 15 dB (0 dB = antenna in free space) with a measuring error of less than 3 dB. Therefore, system-

atic effects could not be detected by experiments in the past.

- Most experiments have been performed at some fixed frequencies and with some fixed antenna-body distances where the future use of the transmitter was planned. A systematic relationship can be recognized only if these parameters are changed in little steps over a large range.
- The human body exhibits a complicated, variable shape. The dielectric inherent properties of the individual body organs vary around 1:10. In addition they are strongly dependent on the frequency, with a distinct change at about 100 MHz (JOHNSON and GUY [45]).
- The frequency range of interest covers the resonance region of the human body. The largest circumference of a body (human body : measured from head to feet) is roughly equal to the wavelength of the first resonant frequency. In fact this is demonstrated by absorption computation and thermographic investigations, where the maximum absorption occurs at about 65 MHz, if a human body model is irradiated by a plane wave (GANDHI, HAGMANN and D'ANDREA [24], CHEN and GURU [14]).

From the literature neither analytical resolvable models nor approximative methods are available which explain the radiation characteristics of actual body-mounted antennas in the entire frequency range. The method of NYQUIST, CHEN and GURU [66] could lead to a systematic explanation, if the model could be improved by parameter variation. However, an extension of that method exceeds the limited storage capacity and the computation time limits of our ETH computer. Thus, other models and computation methods have to be found in order to understand the systematic correlations in a antenna-body system and in order to develop new, efficient antenna configurations.



Leer - Vide - Empty

## 2. PROJECT

The fundamentals have to be prepared for the development of efficient, electrically small, body-mounted antennas with omnidirectional radiation patterns in the horizontal plane.

An antenna-body model has to be created which allows the computation of the systematic relation among frequency, body geometry, relative position of the antenna to the body and transmission loss. The model should be applicable for the entire frequency range from 10 to 1000 MHz.

A measuring method has to be developed which allows radiation pattern recording of body-mounted antennas in the entire frequency range from 10 to 1000 MHz. The measuring error should be less than 3 dB.

An investigation about the possible risks of body-mounted antennas has to be performed. The safety standard of some countries would prohibit the use of transmitters with sufficient power in combination with electrically small antennas. The international findings on biological effects of radio- and microwaves are controversial and the safety standards vary greatly from country to country. Biological effects may have an influence on the accuracy of biotelemetrical data and could lead to health hazards. The investigation should conclude in recommendations for reliable and safe use of transmitting devices with body-mounted antennas.

Leer - Vide - Empty

### 3. SYMBOLS AND DEFINITIONS

SYMBOL	NAME AND DEFINITION	UNIT
$a$	radius	m
$a_s$	radius of the radiansphere (4.5.) , $\lambda/2\pi$	m
$\vec{a}$	spherical radius vector (5.2.1.)	
ARP	azimuthal radiation pattern (7.2.1.)	
$A_1$	body-mounted antenna (5.1.2.) , usually electrically small ( $h < \lambda/4$ )	
$A_2$	remote antenna (5.1.2., 8.3.3.) , large broadband antenna	
$\vec{A}$	magnetic vector potential (6.3.2.)	Vs/m
$\vec{A}^{scat}$	scattered magnetic vector potential (6.3.2.)	Vs/m
B	bandwidth , $2\Delta f_{450}$ or frequency range between - 3dB, (4.5.,16.1.)	MHz
BK	wave propagation constant k in computer programs (10.2.2.)	1/m
BMR	basal metabolic rate (4.1.), metabolic power dissipation	W/kg
$\vec{B}$	magnetic induction $\mu_r \mu_0 \vec{H}$	Vs/m <sup>2</sup>
c	velocity of light in vacuum, $2.9979 \cdot 10^8$ m/s	m/s
$\overrightarrow{curl}$	curl vector function, $\overrightarrow{curl} \vec{E} = \vec{\nabla} \times \vec{E}$	
C	capacitance, 1 Farad = 1 Coulomb/Volt	As/V
C	central nervous system (4.4.)	
CW	continuous wave	
$C_{max}$	maximum circumference of the body in wavelengths	1
d	transmission distance ( $d \gg \lambda$ ) (5.1.2., 8.2.)	m
div	divergence vector function, $div \vec{E} = \vec{\nabla} \cdot \vec{E}$	
$d_{at}$	antenna-body distance , distance from $A_1$ to body surface (5.1.2)	m
$d_g$	thickness of the reflecting layer (5.3.2.)	m
dB	decibel, relative measure for power or field strength (5.1.2.) power: $10 \log (P/P_0)$ , field: $20 \log (E/E_0)$	1
D	refracted wave (5.3.2.)	
DRP	directive radiation pattern (7.2.1.)	
$D_c$	diameter of the infinite cylinder IZYL (5.4.1., 6.5.2.)	m
$D_h$	diameter of the helical antenna (4.5., 16.1.1.)	m
$D_B$	mean diameter of the trunk of a TS or test body (10.4.9.)	m
DTEST	1/4 of the test segment length in program PANB (6.4.5.1.,10.2.2.)	m

SYMBOL	NAME AND DEFINITION	UNIT
e	constant, $e = 2.718$	
EEG	electroencephalogram	
EM	electromagnetic (-wave)	
$E_0$	reference electric field strength for 0 dB, received field strength at optimal antenna polarization in quasi-free-space condition (5.2.1.)	V/m
$E_h$	horizontal component ( $\phi$ -component) of an E-field near a body (5.2.1.)	V/m
$E_n$	perpendicular (normal) component of an E-field to a surface (6.3.)	V/m
$E_r$	radial component of an E-field with respect to body axis (5.2.1.)	V/m
$E_t$	tangential component of an E-field with respect to a surface (6.3.)	V/m
$E_v$	vertical component of an E-field near a body ( $  $ body axis) (5.2.1.)	V/m
$E_z^{inc}$	incident electric field strength in z-direction	V/m
$E_z^{ind}$	induced electric field strength in z-direction	V/m
$E_z^{scat}$	scattered electric field strength in z-direction	V/m
$E_z^{tot}$	total electric field strength in z-direction	V/m
$\underline{E}$	electric field intensity, complex vector	V/m
$\vec{E}_{inc}$	general incident electric field	V/m
$\vec{E}_{ref}$	general reflected electric field	V/m
$\vec{E}(a)$	electric field at the relative position $\vec{a}$ to the body (5.2.1.)	V/m
$\vec{E}_\theta$	$\theta$ - ('vertical') polarized incident E-field (6.4.3.)	V/m
$\vec{E}_\phi$	$\phi$ - ('horizontal') polarized incident E-field (6.4.3.)	V/m
f	frequency in MHz, $f = \omega/2\pi$	1/s
$f_{res}$	resonant frequency (usually in MHz)	MHz
$f_{lim1}$	lower frequency limit due to Fresnel condition (5.3.1.)	MHz
$f_{lim2}$	lower frequency limit due to Rayleigh criterion (5.3.2.)	MHz
$f_{lim3}$	upper frequency limit due to plane wave condition (5.3.3.)	MHz
$f_{lim4}$	lower frequency limit due to far-field condition (5.3.3.)	MHz
$f_{lim5}$	maximum computational frequency in program HARRA (10.3.1.)	MHz
F	frequency in MHz in all computer programs	MHz
FFHD	flat folded helical dipole (16.1.2.)	
FHD	flat helical dipole (16.1.2.)	
FSL	free-space level = $E_0 = 0$ dB (5.1.2.)	dB

SYMBOL	NAME AND DEFINITION	UNIT
FZYL	finite cylinder, computational body model (5.4.1.)	
$g_n$	Green's function (6.4.2.1.)	
$\vec{\text{grad}}$	gradient vector operator, $\vec{\text{grad}} \phi = \vec{\nabla} \phi$	
$G_2$	gain of the remote antenna $A_2$ (5.3.2.)	1
GA	ground plane antenna (16.1.2.)	
$G_n$	evaluated Green's function (6.4.2.1.)	
Gain <sub>B</sub>	transmission gain, gain of antenna $A_1$ when body-mounted with respect to the quasi-free-space performance (5.1.2.)	dB
h	hour	h
h	physical length of an electrically small (monopole) antenna (4.5.)	m
$h_1$	height of $A_1$ above ground (5.1.2.)	m
$h_2$	height of $A_2$ above ground (5.1.2.)	m
$h_{\text{eff}}$	effective height of an antenna (for $U_{\text{ind}}$ computation)	
$h_B$	relative height of the center of $A_1$ with respect to the feet of the test body, z-coordinate of $A_1$ in computation (5.1.2., 10.2.5.)	m
HDR	heat development rate, usually relative value (4.3.)	1
$H_n$	perpendicular (normal) component of a H-field to a surface (6.3.)	A/m
$H_t$	tangential component of an H-field with respect to a surface (5.3.)	A/m
$H_x^{\text{inc}}$	incident magnetic field strength in x-direction	A/m
$H_x^{\text{scat}}$	scattered magnetic field strength in x-direction	A/m
$H_x^{\text{tot}}$	total magnetic field strength in x-direction	A/m
$\vec{H}$	magnetic field intensity, complex vector	A/m
$\vec{H}_{\text{inc}}$	general incident magnetic field	A/m
$\vec{H}_{\text{ref}}$	general reflected magnetic field	A/m
$H_n^{(2)}(kr)$	Hankel function, second kind, order n (6.5.2.)	
I	current	A
j	square root of -1, imaginary number	1
$\vec{j}$	electric current density in a volume element (6.3.4.)	A/m <sup>2</sup>
$J_t$	tangential electric current density (6.3.1.)	A/m
$J_n(kr)$	Bessel function, order n (6.5.2.)	
$\vec{J}$	electric current density on a surface (6.3.1.)	A/m
$k_m$	amount of the wave propagation factor in a medium	1/m

SYMBOL	NAME AND DEFINITION	UNIT
$\vec{k}$	wave propagation factor $2\pi/\lambda$ in free space	1/m
KK	number of regarded modes $n$ in computer program PANB	1
L	inductance, 1 Henry = 1 Vs/A	Vs/A
LPD	logarithmic periodic antenna (remote antenna $A_2$ ) (8.3.3.)	
$L_B$	length of the TS or test body (10.4.9.)	m
Loss <sub>B</sub>	transmission loss caused by the body, ( $= - \text{Gain}_B$ ) (5.1.2.)	dB
L(J)	integro-differential operator (6.4.1.)	
$m$	refraction index, $m = k_m/k$ (5.3.2.)	1
M	number of division of the interval 0 to $\pi$ in computer programs	1
MANMOD	conducting human body model, sagittal or lateral view (5.4.1.)	
MET	metallic cylinder (for experiments) (5.4.1.)	
MHz	megahertz, $10^6$ Hz	1/s
MW	microwave, frequencies above 300 MHz	
$n$	mode number (in expansion functions) (6.4., 6.5., 10.3.1.)	1
N	number of tangential units along the contour curve of a body of revolution (6.4.)	1
NN	number of modes to be computed in program HARRA	1
NP	number of body contour points, $(NP-1)/2 = N$ , program HARRA and PANB	1
NPHI	number of division of the interval 0 to $\pi$ in program HARRA and PANB	1
NNPHI	number of computed azimuthal field points in program PANB and PANC	1
NTEST	number of test segments in program PANB (10.2.4.)	1
$N_h$	number of turns of a helical monopole antenna (16.1.)	1
$P_1$	polarization of antenna $A_1$ , orientation of the main polarization axis in the space, vertical, radial or horizontal (5.1.2., 10.2.5.)	
$P_2$	polarization of antenna $A_2$ , vertical or horizontal (5.1.2.)	
P	real power in watt	VA
PHA	phantom cylinder (for experiments) (5.4.1.)	
$P_{abs}$	absorbed power in a lossy medium, watt (4.3.)	VA
$P_{in}$	input power at a transmitting antenna, watt (5.3.2.)	VA
$P_{loss}$	dissipated power in a transmitting antenna, watt (4.5.)	VA
$P_{rad}$	radiated power from a transmitting antenna, watt (4.5.)	VA
$P_{reac}$	reactive power near a transmitting antenna (4.5.)	VA

SYMBOL	NAME AND DEFINITION	UNIT
$P_{\text{real}}$	real power (rad+loss) from and in a transmitting antenna (4.5.)	VA
$P_{\text{scat}}$	total scattered power from an object (5.2.3.)	VA
$\vec{P}$	power density, Poynting vector $\vec{P} = \vec{E} \times \vec{H}$ , usually in mW/cm <sup>2</sup> (4.5.)	VA/m <sup>2</sup>
$\vec{P}_{\text{real}}$	real power density, computed from $P_{\text{rad}}$ only, mW/cm <sup>2</sup> (4.5.)	VA/m <sup>2</sup>
$\vec{P}_{\text{reac}}$	reactive power density, $ \vec{P}_{\text{real}}  \cdot Q$ , mVA/cm <sup>2</sup> (4.5.)	VA/m <sup>2</sup>
Q	Q-factor, ratio $f_{\text{res}}/B$ or stored energy/radiated+losses energy in an RLC network (4.5.)	1
r	radius or distance	m
$\vec{r}$	radius vector from origin of coordinate system (6.3.2.)	m
$\vec{r}'$	radius vector of a source point from origin of coordinate system	m
R	amount of the distance between source and observation point, $ \vec{R}  =  \vec{r} - \vec{r}' $ (6.3.2., 6.4.)	m
R	resistance, Ohm	V/A
RACS	relative absorption cross section (4.3.)	1
RCS	radar cross section, usually related to shadow area (5.2.3.)	m <sup>2</sup>
RF	radio frequencies, frequencies below 300 MHz	
RH	radius of a contour point in programs HARRA and PANB (10.2.2.)	m
RHD	round helical dipole (16.1.)	
RTEST	radius of the test segment center point (6.4.5.1., 10.2.2.)	m
$R_{\text{loss}}$	loss resistance of an antenna (4.5., 16.1.1.)	V/A
$R_{\text{rad}}$	radiation resistance of a transmitting antenna (4.5., 16.1.1.)	V/A
$\underline{R}_E$	reflection coefficient of the E-field of a TE-wave (5.2.4.)	1
$\underline{R}_H$	reflection coefficient of the H-field of a TM-wave (5.2.4.)	1
[R]	measurement row matrix (6.4.3.)	
s	distance from ground to feet of TS (5.1.2.)	m
S	surface of a body	m <sup>2</sup>
SAR	specific absorption rate, in W/m <sup>2</sup> or W/kg (4.3.)	VA/g
SUB	standard human test subject (5.4.1.)	
t	time	s
t	index, means tangential (to a surface) component (6.3.)	
$\vec{t}_{1,2}$	tangential unit vectors on a surface of a body (6.3.5.)	1
TE	transversal electric mode, horizontal polar. (5.2.4., 5.3.2.)	



SYMBOL	NAME AND DEFINITION	UNIT
TEM	transversal electro-magnetic mode, general case (5.2.4.)	
TM	transversal magnetic mode, vertical polarization (5.2.4., 5.3.2.)	
TS	test subject	
U	voltage	V
$U_{ind}$	induced voltage at the antenna terminals (5.2.2.)	V
V	volume of a body	$m^3$
VSWR	voltage standing-wave ratio, ratio of $U_{max}/U_{min}$ (16.1.)	1
$V_{eff}$	effective volume of an antenna, computational value (4.5.)	$m^3$
$V_s$	volume of the radiansphere = $\lambda^3/6 \pi^2$ (4.5.)	$m^3$
[V]	excitation matrix (6.4.1.)	
$\vec{W}_i$	testing function (6.4.1.)	
[Y]	admittance matrix (6.4.1., 10.2.2.)	
$Y_n(kr)$	Neumann function (Bessel function of second kind) (6.5.2.)	
Z	Impedance	V/A
ZH	height of a contour point in programs HARRA and PANB (10.2.2.)	m
ZTEST	height of the test segment center point (6.4.5.1., 10.2.2.)	m
$Z_0$	characteristic impedance of vacuum, $Z_0 = 377 \text{ Ohm}$	V/A
$Z_m$	characteristic impedance of a medium (5.3.2.)	V/A
[Z]	impedance matrix (6.4.1., 10.2.2.)	
$\alpha$	incident angle with respect to a body surface (5.2.4.)	°
$\beta$	phase factor (5.2.2.)	1
$a_n$	Fourier coefficient (6.5.2.)	
$\gamma$	reflection angle (glancing angle) of a wave to the ground (5.1.2.)	°
$\gamma_B$	Brewster angle, total refraction of a TM-wave (5.1.2, 5.3.2.)	°
$\underline{\Gamma}$	refraction coefficient of the air-medium interface at perpendicular (normal) wave incidence (4.2., 5.2.4.)	
$\delta$	penetration depth of a wave into a medium (4.2., 5.2.4., 6.2.)	m
$\delta E$	maximum field strength variation along antenna axis (5.2.2.)	dB
$\delta \Phi$	maximum phase variation of the field along antenna axis (5.2.2.) ( $\delta E$ and $\delta \Phi$ are measurements for the field homogeneity, 10.3.5.)	°

SYMBOL	NAME AND DEFINITION	UNIT
$\Delta U$	ratio actual induced voltage $U_{ind}$ to approximated induced voltage $\bar{U}_{ind}$ (from center field) in dB (5.2.2., mean error 10.2.5.)	dB
$\Delta_{s1}$	path difference for the first Fresnel Ellipsoid (5.3.1.)	m
$\Delta_{s2}$	path difference of a rough surface (Rayleigh criterion) (5.3.2.)	m
$\Delta_{s3}$	path difference of a plane wave along the body axis (5.3.3.)	m
$\Delta_{s3'}$	path difference of a spherical wave along body axis (5.3.3.)	m
$\Delta_{\psi 2}$	phase difference due to the reflection of the wave at a rough surface, Rayleigh criterion : $\Delta_{\psi 2} < \pi/2$ (5.3.2.)	°
$\epsilon$	total permittivity	As/Vm
$\epsilon_m$	permittivity of a medium (total permittivity)	As/Vm
$\epsilon_0$	dielectric constant, $\epsilon_0 = 8.854 \cdot 10^{-12}$ F/m or As/Vm	As/Vm
$\epsilon_r$	relative dielectric constant of a medium	1
$\theta_{e1}$	elevation angle of an incident wave above ground (5.1.2.)	°
$\theta_d$	refraction angle (5.3.2.)	°
$\theta_i$	incident angle of a wave (to the body axis) (5.1.2.)	°
$\theta_T$	angle of the test segment to the body axis (6.4.5.1.)	°
$\lambda$	wavelength	m
$\lambda_m$	wavelength of a wave in a medium (4.2.)	m
$\lambda_0$	wavelength of a wave in vacuum	m
$\mu$	total permeability	Vs/Am
$\mu_m$	permeability of a medium (total)	Vs/Am
$\mu_0$	permeability of vacuum, $\mu_0 = 4\pi \cdot 10^{-7}$ H/m or Vs/Am	Vs/Am
$\mu_r$	relative permeability of a medium	1
$\rho$	radius of a point on the surface of the body of revolution (6.4.)	m
$\rho_m$	distributed charges in a medium (charge density) (6.2.)	As/m <sup>3</sup>
$\sigma, \sigma_m$	conductivity of a medium in S/m or mho/m (4.2.)	A/Vm
$\sigma_{su}$	surface charge density on a body (6.3.)	As/m <sup>2</sup>
$\phi$	azimuthal rotation angle (in the horizontal plane) (5.1.2.)	°
$\Phi$	electric potential (6.3.3.)	V
$\psi$	phase of the reflection coefficient (5.3.2.)	°
$\Psi(z)$	current distribution function along the antenna axis (5.2.2.)	1
$\omega$	angular frequency, $\omega = 2\pi f$ in rad/s	1/s

Leer - Vide - Empty

## 4. SAFETY ASPECTS OF RADIO- AND MICROWAVES

### 4.1. INTRODUCTION AND HISTORICAL BACKGROUND

Body-mounted antennas are used in biotelemetry and walkie-talkies. Biotelemetry transmitters are applied on human test subjects and animals in order to record physiological and other data with minimum encumbrance for the test subject. Great efforts are made to reduce the influence of the measuring equipment on the data to be measured. In this chapter we are therefore not only interested in possible health hazards of radio transmitters but also in effects which may falsify the recorded data.

The subject is within the near-zone of a radiating source if body-mounted antennas are used. Due to the smallness of the antenna and due to the small antenna-body distance ( $d_{at}$ ), the power density ( $\vec{P}$ ) at the subject's surface may exceed the maximum permissible values of some safety standards. As an example the consequent application of the German Democratic Safety Standard [18] prohibits such transmitting devices if the radiated power exceeds a few mW.

The non-ionizing electromagnetic (EM) spectrum encompasses frequencies from 1 Hz to  $10^{19}$  Hz. In general, frequencies from about 0.03 MHz to 300 MHz are called radio frequencies (RF) and frequencies from 300 MHz to 300,000 MHz are designated as microwaves (MW). In analogy to the well established safety standards for ionizing radiation the purpose of the less known safety standards for non-ionizing radiation is to protect a large population from uncontrolled exposure. A safety standard is always a compromise between absolute safety and practical realization. The permissible limits should exclude health hazards based on the present state of science. Under certain, well-described conditions the safety limits may be exceeded willingly if the risks resulting from other factors can be considerably reduced. For example, the application of a powerful ECG telemetry transmitter for the monitoring of heart disease patients is justified if the physician in charge considers a permanent heart monitoring as urgent.

A meaningful application of the safety standard requires the knowledge of the risks and often also the history of the standard's development. Until about 1945 "low-power" non-ionizing EM radiation was generally considered completely harmless. It was known that dielectrical materials can be heated internally with high RF power, an effect which is applied in diathermy for the clinical warming-up of certain body regions (MOOR [60], SCHWAN [73]). During World War II the U.S. Department of Defense medical services

became interested and concerned about possible hazards associated with the development, operation and maintenance of the increasing numbers of radar sets and other RF emitting electronic equipment. The main reason for that interest was reports about human microwave cataractogenesis (see MILROY and MICHAELSON [59]), HIRSCH and PARKER [44]) in radar repairmen who have been exposed to power densities in excess of  $100 \text{ mW/cm}^2$ . After some investigations by the U.S. Navy and the U.S. Air Force, responsibility for research on biomedical aspects was delegated in 1957 to "Tri-Service-Program" directed by the USAF. This program, well described by MICHAELSON [58], included investigations on effects of exposure on whole-body, selective organs and tissues, single cells and enzyme systems, using various power levels, for pulsed and continuous waves in the frequency spectrum from 200 to 24,500 MHz. Basic work for the understanding of thermal effects was performed by SCHWAN and PIERSOL [74] on the field of power matching, absorption, penetration depth, etc.. Non-thermal effects such as field force effects on molecules (pearl chain formation, MUTH [61]), orientation of macromolecules (HELLER [43]), activation of membranes and neurons (e.g., LIVESHITS [55]), macromolecular resonance denaturation (e.g., BACH, LUZZIO and BROWNELL [4]) and many other effects have been investigated in that period. The listed non-thermal effects occurred only at high field intensities, so that the thermal effects were considered as dominant. A safe limit of  $10 \text{ mW/cm}^2$  power density was defined which is still valid now (ANSI 1974 [2]) in the USA and in most of the western countries.

The power density number of  $10 \text{ mW/cm}^2$  has the following origin: the metabolic processes of the human body amount to about  $1 \text{ W/kg}$  when averaged over the total body mass for the sleeping state (BELDING and HATCH [8], GUY [35]). This Basal Metabolic Rate (BMR) for the whole body may be exceeded by that of individual organs; for example, the heart muscle has a metabolic rate of  $33 \text{ W/kg}$ , the brain  $11 \text{ W/kg}$ , the liver  $6.7 \text{ W/kg}$ , the skeletal muscle  $0.7 \text{ W/kg}$  (GUY [35]). As a fundamental, limiting criterion an artificial power deposition of  $1 \text{ W/kg}$  averaged over the whole body was defined. Such an external heating increases theoretically the head core temperature by about  $0.15^\circ\text{C}$  and the body muscle temperature by about  $1^\circ\text{C}$  (EMERY et al. [22]). This heating is considered harmless since it is comparable with the heat produced by physical exercise. It was argued that since the BMR of the human body is in the order of 75 watts for a 70 kg man with a body surface of about  $1.9 \text{ m}^2$ , this represents an equivalent

areal heat production rate of about  $4 \text{ mW/cm}^2$ . Since half of the surface area would be available for single sided exposure to a MW field, by limiting the maximum continuous MW exposure on  $10 \text{ mW/cm}^2$ , one would expect no more than a doubling of the BMR in the body. (See limitations of this simplistic model in the next sections and TELL [77].) The philosophy of permissible heat loading concerns mainly the protection against destruction. Furthermore, clearly defined test conditions were chosen, e.g., in animal experiments an isolated test subject was exposed to a plane wave and great effort has been made to keep the field homogeneous. From the power density  $10 \text{ mW/cm}^2$  the equivalent free space field intensities were derived for near-field conditions (E-field  $200 \text{ V/m}$ , H-field  $0.5 \text{ A/m}$ ).

The Russian and generally the Eastern safety regulations are based on other considerations. The regulations concerning the power density are up to 10,000 times more stringent and the exposure duration is limited. As an example the GDR safety standard [18] demands that the power density in the MW region should not exceed  $10 \text{ } \mu\text{W/cm}^2$  at 8 h/day, and for the same exposure duration the E-field should not exceed  $2 \text{ V/m}$  in the frequency range 50 to 300 MHz. The H-field is not limited up to now, but since GUY [36] could prove that the H-field induced E-fields inside a human body are larger than the E-field induced E-fields in the frequency range 1 to 20 MHz, an appendix regarding permissible H-fields is to be expected. These very limiting safety standards are based mainly on effects studied in encephalography, biochemistry, cardiovascular pathophysiology etc. and are often connected with investigations in occupational medicine. Soviet investigators have stressed that the central nervous system is highly sensitive to all modes of radiation exposure. Their conceptional approach is based to a large extent on Pavlovian methods as can be seen from the many publications about changes in conditioned reflexes (GORDON, ROSCIN and BYCKOV [30]), see also summary of MICHAELSON [57]). Without discussing the details of the Eastern investigations it is evident that alterations of functions of complicated biological systems occur at much lower field intensities (nonthermal or microthermal effects) than material alterations or destruction. In the late 1960's the Eastern literature was reaching the American microwave community and initiated a broad research on low-level effects. One reason for this new interest was the introduction of microwave ovens in the USA, where the microwave leakage is in the range

from 0.7 to 20 mW/cm<sup>2</sup> (CONSUMER REPORTS [17]) in contrast to the reported effects at a power density level of 10  $\mu$ W/cm<sup>2</sup> to 5 mW/cm<sup>2</sup> (GORDON [30,31]). In 1971 GLASER [29] from the U.S. Electromagnetic Radiation Project Office began with a bibliography on reported effects and clinical manifestations attributed to MW and RF radiation. During this time the ninth supplement came out so that about 4,600 citations are available.

Some of the Eastern findings could not be reproduced in the West. Criticized were the insufficiently described test methods (see e.g. PROCEEDINGS WARSAW [69]). If more than one animal is kept in a cage for animal experiments, the field homogeneity may be disturbed by a factor of 100. Reflections from the cage walls and ground effects lead to enhanced absorption. If a rat is placed in a reflector corner, an averaged incident power density of 10 mW/cm<sup>2</sup> may lead to an absorption of 200 W/kg (GANDHI [26,27]). On the other hand it must be pointed out, that under working conditions, reflections exist and that no long-term investigations have been performed with controlled conditions. The stringent Eastern safety standards which have been prepared above all for the protection of workers in factories are reasonable from this point of view.

In the following sections the physical background of RF and MW absorption and recent investigations on biological effects will be presented in order to estimate safety recommendations for body-mounted antennas.

#### 4.2. ELECTRIC AND MAGNETIC PROPERTIES OF BIOLOGICAL MATERIALS

The investigations of the electric and magnetic properties were mainly performed during the last 30 years. Only the most important results can be discussed here; additional data and computation formulas can be found e.g., by TOLER and SEALS [79], SCHWAN and LI [75], JOHNSON and GUY [45].

Biological material is non-magnetic and can be characterized by their dielectric properties: conductivity  $\sigma$  and relative dielectric constant  $\epsilon_r$ . The dielectric properties depend on the material and the frequency. In TABLE 1 these dielectric properties and the properties of the electromagnetic waves in the media are shown for two typical biological material groups:

PROPERTIES OF ELECTROMAGNETIC WAVES IN TWO GROUPS OF BIOLOGICAL MEDIA								
	GROUP A Muscle, Skin, and Tissue with High Water Content				GROUP B Fat, Bone, and Tissue with Low Water Content			
Frequency $f$ [MHz]	40.7	100	300	915	40.7	100	300	915
Wavelength in Air $\lambda_0$ [cm]	738	300	100	32.8	738	300	100	32.8
Wavelength in Media $\lambda_m$ [cm]	51.3	27.0	11.9	4.5	187	106	41.0	13.7
Relative Dielectric Constant $\epsilon_r$ [1]	97.3	71.7	54.0	51.0	14.6	7.5	5.7	5.6
Conductivity $\sigma$ [mmho/m] or $\sigma$ [mS/m]	690	890	1370	1600	13-53	19-75	32-107	56-147
Depth of Penetration $\delta$ [cm]	11.2	6.66	3.89	3.04	118	60.4	32.1	17.7
Refl. Coeff. $\Gamma$ $ \Gamma $ [1] $\arg(\Gamma)$ [°]	0.91 +176	0.88 +175	0.83 +175	0.77 +177	0.62 +173	0.51 +168	0.44 +169	0.42 +173

TABLE 1 Properties of electromagnetic waves in two groups of biological media. (Source: JOHNSON and GUY [45]).



The dielectric behavior of the two groups of biological materials listed in TABLE 1 has been evaluated most thoroughly by SCHWAN and his associates [73,74,75]. The biological tissues are composed of cells encapsulated by thin membranes containing an intracellular fluid. The increase of the conductivity  $\sigma$  and the decrease of the relative dielectric constant  $\epsilon_r$  with increasing frequency can be explained for group A by the interfacial polarization across the cell membrane. The cell membranes, with a capacity of about  $1\text{f/cm}^2$ , act as insulating layers at low frequencies so that currents flow only in the extracellular medium. At higher frequencies the reactance decreases, resulting in increasing currents in the intracellular medium. The most noticeable change can be observed at about 100 MHz. A current density of about  $1\text{ mA/cm}^2$  produces a heat equal to that due to the BMR (SCHWAN [72]).

The depth of penetration  $\delta$  of RF and MW power into the material is defined as the distance required to reduce the power by  $e^2$ . The indicated values are valid only for a plane slab, an extended investigation of KRITIKOS and SCHWAN [52] on the distribution of heating potential inside lossy spheres has revealed hot spots in depths which may be larger than  $\delta$ . The hot spots appear inside only for spheres with radii from 0.1 to 8 cm and frequencies from 300 to 12,000 MHz and are of importance mainly in animal experiments (see e.g., GUY [35]).

The reflection coefficient  $\Gamma$  of the air-media interface will be important for the later computation of the scattering properties of a biological body. A  $\Gamma$  of  $0.88/+175^\circ$  (group A, TABLE 1) means that the reflected wave will be only about 1 dB less than whose reflected from a perfect conductor and will show the same phase (dB:  $20 \log E/E_0$ ,  $E_0$  reference E-field,  $E$  measured E-field, see chapter 5.1.2). For the computation of the absorption of electromagnetic energy in a multi-layer medium, also the reflection coefficients from one layer to the other are of importance as can be seen in the next section.

#### 4.3. ABSORPTION OF ELECTROMAGNETIC ENERGY IN BIOLOGICAL MATERIAL

The determination of the absorbed power in an arbitrarily shaped inhomogeneous biological medium needs a great computational effort. However, the multi-layer plane slab model is well investigated and may serve as a first approach for the absorption phenomena.

A simple plane slab model consists of two infinite layers of a certain thickness which are irradiated perpendicularly by a plane wave. (FIGURE 2: irradiation from the left, first layer = 3 cm fat, second layer = 10 cm muscle)

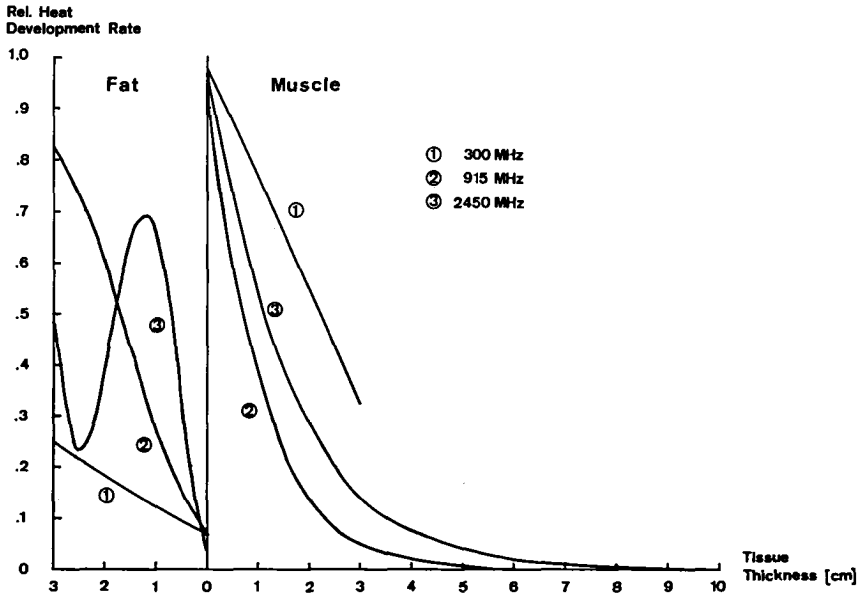


FIGURE 2 Relative Heat Development Rate (HDR) in a two-layer model.

(Source: TELL [76], SCHWAN and PIERSOL [74])

The power which is absorbed in a volume element  $V$  and which is converted into heat is given by the formula (1):

$$P_{abs} = \frac{1}{2} \int_V \sigma |\vec{E}(\vec{r})|^2 dV \quad (1)$$

The specific absorption rate (SAR) can be obtained by relating  $P_{abs}$  to the volume ( $W/cm^3$ ) or to the specific gravity ( $W/kg$ ). The electric field strength  $\vec{E}(\vec{r})$  can be computed by the reflection coefficients and the attenuation factors in the two layers. Since the impedances of the materi-

als are complex, a feasible method of solution is to apply the Smith Chart as demonstrated by TELL [76].

The SAR leads directly to the Relative Heat Development Rate (HDR) by dividing the obtained SAR's by the maximum obtained SAR (FIGURE 2). The heat actually produced could be computed by applying the laws of thermodynamics, but since thermal data (heat conduction, external cooling, etc.) are difficult to obtain with the required accuracy, thermographic methods are better suited (GUY, WEBB and SORENSEN [36]).

In FIGURE 2 it is interesting to see that the HDR in the fat layer depends directly on the intrinsic wavelength  $\lambda_m$ . At 915 MHz the fat layer is about  $\lambda_m/4$  (TABLE 1) and acts therefore as a  $\lambda/4$  impedance transformer. The result is a high HDR at the irradiated surface and a sharp rise just inside the muscle layer. At 300 MHz the heating in the fat is much less than in the muscle, and at 2,450 MHz the surface heating of the fat layer is about 68 percent of the maximum heating which occurs deeper within the fat.

This simple plane slab model is a good model for local application of a guided plane wave (diathermy applicators etc.), but does not adequately describe RF and MW absorption in complicated biological structures with irregular geometry, especially if the dimension of the body is comparable to the wavelength.

The absorption of EM energy in a three-dimensional body depends greatly on the body geometry and the wavelength. An adequate measure to describe this phenomenon is the Relative Absorption Cross-Section (RACS):

In FIGURE 3 a dielectric sphere with a radius  $a$  is shown which is irradiated by a plane wave (SCHWAN [72]). The RACS is defined as the ratio of absorbed power to the incident power. The incident power can be computed from the incident power density (in free space) multiplied by the shadow area  $\pi a^2$ ; the absorbed power can be computed by several methods or determined by thermal measurements. An RACS smaller than 1 means that a part of the incident power is reflected or transmitted through the sphere. An RACS greater than 1 means that the effective shadow area is greater than the physical area  $\pi a^2$  or, in other words, that EM power is extracted also from outer regions around the sphere.

Where are 3 different regions (FIGURE 3) : for small radius  $a$  (or for long wavelengths  $\lambda$ ) the RACS is small, but increases rapidly with size.

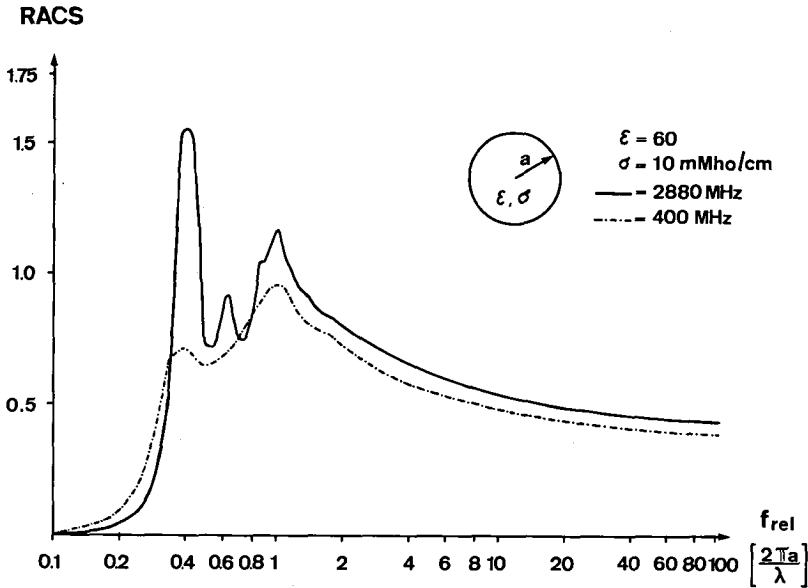


FIGURE 3 Relative Absorption Cross-Section (RACS) of a sphere of tissue-like dielectric properties as a function of the relative frequency  $f_{rel}$  (sphere circumference  $2\pi a$  / wavelength  $\lambda$ ) (Source: SCHWAN [72]).

For large radius  $a$  (or short wavelengths  $\lambda$ ) the RACS is about 0.5 since the sphere reflects a part of the incident power. High RACS's occur, if the circumference of the sphere is almost equal to the wavelength. For  $2\pi a/\lambda$  between 0.4 and 1.5 the RACS may exceed 1. In that resonant case not only is the absorption very high, but also the field homogeneity around the sphere is disturbed; an effect which will be important in the later field computation outside the irradiated body.

GANDHI et al. [25] continued RACS investigations with dielectric ellipsoids and various field polarizations. An ellipsoid with the axis  $a/b$  of 6.34 shows an RACS of about 4.2, if the incident E-field is polarized parallel to the main axis  $a$  and if the length  $L$  ( $2a$ ) of the ellipsoid is about  $\lambda/2$ .

Specific Absorption Rates (SAR, see above) of body elements were determined by GANDHI, HAGMANN and D'ANDREA [24] and are shown in FIGURE 4: A saline-filled man model was irradiated in free space with a power density of  $1 \text{ mW/cm}^2$ . The maximum averaged SAR for the whole body amounts to  $0.2 \text{ W/kg}$  and occur at 68 MHz for a model length of 1.75 m. The SAR of the leg and of the neck may reach  $0.4 \text{ W/kg}$  as can be seen from FIGURE 4.

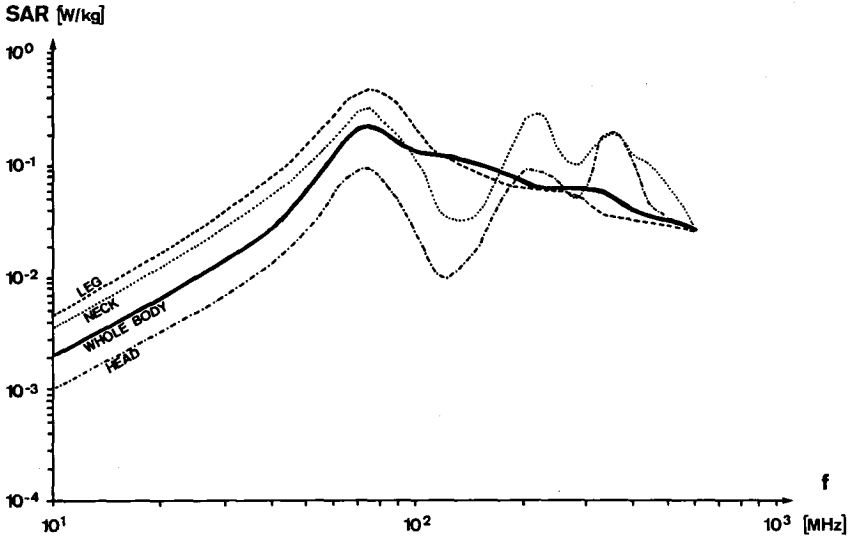


FIGURE 4 Specific Absorption Rate (SAR) for a 1.75m man model at an incident power density of  $1 \text{ mW/cm}^2$  in free space, vertical polarization. (Source: GANDHI, HAGMANN and D'ANDREA [24] )

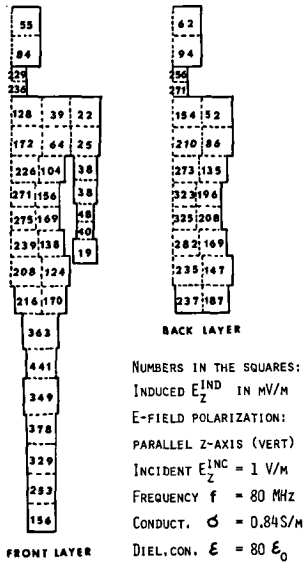


FIGURE 5

The z-component (vertical) of induced electric field. Incident EM-Wave: vertical polarization, incident  $E_Z^{inc}$  1 V/m, 80 MHz.

Compared with FIGURE 4 at an incident power density of  $1 \text{ mW/cm}^2$  and 70 MHz the maximum SAR's occur at the knee ( $0.4\text{-}0.5 \text{ W/kg}$ ) and in the neck ( $0.2 \text{ W/kg}$ ).

(Source: CHEN and GURU [15])

In FIGURE 5 the computed induced E-field components in the z-direction are shown in a body model irradiated by a vertical polarized EM-wave (CHEN and GURU [15]). The incident E-field is 1 V/m and the frequency 80 MHz. The highest induced E-field occurs in the knee region and is about 0.44 times the incident field. The computed SAR's agree with the measurement of GANDHI et al. [24,25]. High values are obtained mainly in the leg, the thigh and the neck. At horizontal polarization the largest SAR's occur at about 200 MHz and are located in the chest amounting to 0.4 W/kg at 1 mW<sup>2</sup> incident power density level (CHEN and GURU [15]). The dielectric properties  $\sigma$  and  $\epsilon$  in experiment and computation are similar to those of group A in TABLE 1. If the computer capacity is available, they could be varied for each cube for future refinement with more cubes.

Up to here the human body was considered to be in free space. The effects of the presence of reflecting surfaces and ground effects were studied by GANDHI et al. [24,26,27]. The SAR's for the whole body and some intact anatomical parts of a man for an incident power density of 1 mW/cm<sup>2</sup> is shown in FIGUR 6, where man is in good electrical contact with a high conducting ground plane:

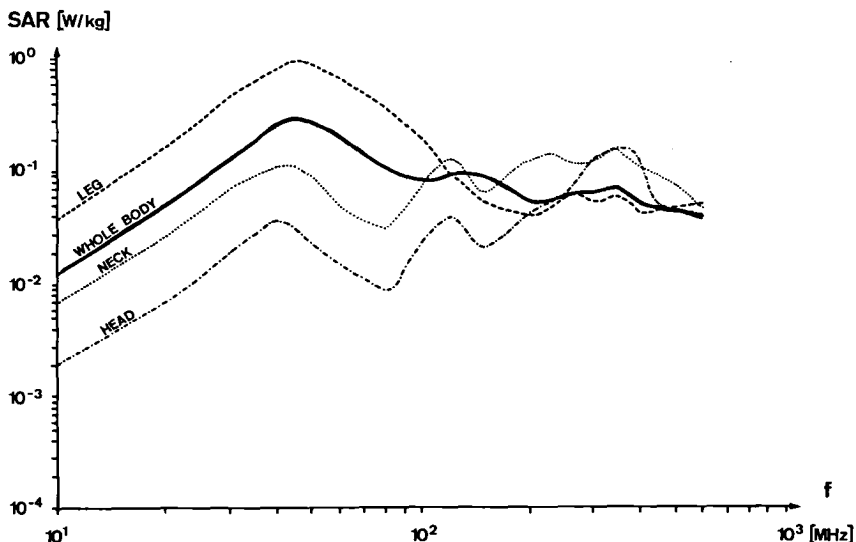


FIGURE 6 Specific Absorption Rate (SAR) for a 1.75 m man model in good electrical contact with a high conducting ground plane. The incident power density is 1 mW/cm<sup>2</sup>. (Source: GANDHI, HAGMANN and D'ANDREA [24])

The resonant frequency is now near 35 MHz, and the SAR's are about twice as high than in the ungrounded condition. The SAR of the whole body amounts to about 0.3 W/kg, the SAR of the leg to about 1 W/kg at an incident power density of 1 mW/cm<sup>2</sup>. The indicated SAR's are those integrated over basic anatomical structures and do not reveal the worst case.

A further increase of the SAR in the whole body can be observed when the man is placed in front of a flat reflector (1W/kg), in a 90° corner reflector (6W/kg) and in a corner reflector with ground contact (12W/kg) (all values related to a power density of 1 mW/cm<sup>2</sup>).

In the introduction it has been mentioned that the fundamental, limiting criterion was a power deposition of 1 W/kg which is equal to the BMR. At frequencies below 20 MHz and above 300 MHz the present U.S. safety standard of 10 mW/cm<sup>2</sup> fulfills this criterion. However, a more stringent safety standard seems to be reasonable for the resonance frequency range 20 to 300 MHz.

#### 4.4. OBSERVED BIOLOGICAL EFFECTS OF RF AND MW

Although some thousand recent investigations on biological effects are available (see bibliography of GLASER et al. [29]), the effects at low-power densities are not yet understood in a larger context. Most of the experiments were carried out with small animals at frequencies above 300 MHz, therefore the results of such investigations cannot be transferred directly onto large animals or humans. Some few examples should give an overview on the variety of the documented effects.

The teratogenic effects of MW in insects were studied by LIU, ROSENBAUM and PICKARD [56] by irradiating the pupae of the darkling beetle *Tenebrio Molitor* during its metamorphosis. A statistically significant increase in malformations in the adult insect was observed at power levels as low as 170 μW/cm<sup>2</sup>. The pupation time increased monotonically with the power density at a constant (2 h) irradiation duration. The damages increased linearly with the logarithm of the dosage, and the effects started at approximately 40 μW/cm<sup>2</sup> power density and 0.1 mWh/cm<sup>2</sup> energy density. Exposure of various durations (max. 16 h) and powers (max. 16 mW/cm<sup>2</sup>) strongly suggested that it is the total dosage which determines the level of teratological damage. Since irradiation at 16 mW/cm<sup>2</sup> is known to produce a

measured rise in pupal temperature of less than  $2^{\circ}\text{C}$ , and since heating by conventional thermal techniques appears not to be teratogenic, the effects seem to be not (macro-) thermal in origin.

A widely observed and accepted biological effect of low-average power EM energy is the auditory sensation evoked in an exposure to MW. Among other researchers GUY et al. [37] describe the effect as an audible clicking or buzzing sensation that originates from within and near the back of the head and that corresponds in frequency to the recurrence rate of the MW pulses. The loudness of the sensation correlates with the average incident power density. The threshold energy density per pulse is about  $40 \mu\text{J}/\text{cm}^2$  (corresponds to about  $0.01 \mu\text{Wh}/\text{cm}^2$ ) and is five order of magnitudes smaller than the permissible U.S. safety standard value of  $1 \text{ mWh}/\text{cm}^2$  for peak power averaged over any 6-minute period (ANSI [2]). However, it should be mentioned that the average power density for the threshold of  $120 \mu\text{W}/\text{cm}^2$  (about two order of magnitudes lower than the permissible U.S. safety standard value) requires a pulse width of 1 to  $32 \mu\text{s}$ , with peak power from  $1.25$  to  $40 \text{ W}/\text{cm}^2$ . The presented data are valid for  $2,450 \text{ MHz}$  for humans. Experiments at  $918 \text{ MHz}$  with cats have shown that depending on the pulse width ( $3$  to  $32 \mu\text{s}$ ) average energy densities of  $17$  to  $28 \mu\text{J}/\text{cm}^2$  per pulse, average densities of  $17$  to  $28 \mu\text{W}/\text{cm}^2$  and peak power density of  $0.8$  to  $5.8 \text{ W}/\text{cm}^2$  are required to produce the auditory effects. Although an energy density of  $40 \mu\text{J}/\text{cm}^2$  is capable of increasing the tissue temperature by only  $5 \cdot 10^{-6}^{\circ}\text{C}$ , the auditory effect could be explained by micro-thermal expansion of the liquid in the cochlea, producing a pressure wave similar to the normal input of acoustic signals.

Microwave-induced chronotropic effects in the isolated rat heart are described in a recent report by OLSEN, LORDS and DURNEY [68]. Continuous (CW) MW irradiation at  $960 \text{ MHz}$  causes bradycardia (lowered heart rate) in isolated, perfused rat heart maintained at  $20^{\circ}\text{C}$ . The observed bradycardia occurred at a power deposition of  $1.3$  to  $2.2 \text{ W}/\text{kg}$  that should have caused mild tachycardia (increased heart rate) based on the thermogenic properties of the irradiation. The observed bradycardia, moreover, exhibits neurologic features, because atropinized hearts showed strong tachycardia during irradiation, and hearts treated with propranolol showed significantly stronger bradycardia during irradiation than seen without drugs. It is assumed the MW interacts with the autonomic nervous system by changing the neurotransmitter release mechanism. Because the temperature rise was



limited to 0.1 °C, macrothermal mechanisms are not possible, but the possibility exists, that microheating, i.e., strong thermal gradients over small regions could be responsible for this chronotropic effect of MW. Similar effects, but at lower SAR in living rats, are reported by East European researchers [28,29,69].

A considerable body of literature has grown in the East European countries on transient functional changes following low dose RF and MW irradiation. A sample of clinical and experimental data is presented in TABLE 7.

A SAMPLING OF THE GENERAL BIOLOGICAL EFFECTS OF MICROWAVES AT POWER DENSITIES OF 10 mW/cm <sup>2</sup> OR LESS (EAST EUROPEAN SOURCES)	
Clinical Effects	Experimental Effects
I. General subjective complaints (sensations, fatigue, loss of appetite, asthenia, etc.)	I. Decreased physical endurance and retarded weight gain (rats).
II. Functional CNS and perceptual changes.	II. General inactivation of CNS electrical activity; domination of hypothalamic function; altered afferent function (rabbits, cats). Inhibition of conditioned reflexes; increased motor activity; weakening of excitation/inhibition reactions (rats, mice, birds). Morphological changes in nervous systems (rats, guinea pigs, rabbits) Altered reactivity in response to drugs (rats, rabbits).
III. Cardiovascular and associated autonomic changes.	III. Altered blood pressure and heart rate (rats, rabbits).
IV. Altered blood chemistry.	IV. Altered blood neuroendocrine chemistry (rats, rabbits).
V. Altered metabolism.	V. Altered amino acid and ascorbic acid metabolism (rats)
VI. Depressed endocrine function.	VI. Altered reproductive cycle; decreased viability of offspring (rats).
VII. Increased susceptibility to infectious diseases.	VII. Altered immune reactions (rabbits).

TABLE 7 A sampling of the general biological effects of MW power densities of 10 mW/cm<sup>2</sup> or less as reported by Soviet, Czechoslovakian and Polish researchers. (Source: GLASER and DODGE [28,19])

In the Warsaw Proceedings "Biological Effects and Health Hazards of MW Radiation" [69] and in the recent book by BARANSKI and CZERSKI [6] a review of the East European research is presented. GORDON, ROSCIN and BYCKOV [30] describe functional disturbances in the Central Nervous System (CNS), physiological alterations and behavioral changes which occur at power levels down to a few  $\mu\text{W}/\text{cm}^2$ . Various low-level effects may be considered as selective absorption of radiation at the interfaces of heterogeneous biological systems, e.g., hypothalamic-hypophyseal-suprarenal system. Electrophysical investigations of isolated nerves and muscle fibers in frogs at  $5 \mu\text{W}/\text{cm}^2$  have revealed slowed conduction of impulses, an increased synaptic delay, a lengthening of latent and refractory periods and changes in action potentials. DUMANSKI and SANDALA [20] investigated alterations in the EEG, in conditioned reflex activity (longer latent period, weakened reaction to positive stimuli) and in several metabolic processes in rats and rabbits after irradiation with less than  $10 \mu\text{W}/\text{cm}^2$  at 50 MHz and 12 h/day exposition. KALADA, FUKOLOVA and GONCAROVA [46] and others [69] demonstrated effects in occupational exposure. The effects are manifested by weakness, fatigue, headache, etc. and dysfunctions in the autonomic nervous system, which are apparently reversible.

As pointed out by many Western researchers some of the Eastern findings could not be reproduced in the West at the same low-power density level (see e.g., CHOU and GUY [16] and ROMERO-SIERRA, HALTER and TANNER [70]). However, there is an increasing number of investigations in the West which lead now to similar results (EEG-changes, altered conditioned reflexes, behavioral changes, pathological changes in nerve tissue and brain, increased sensitivity to drugs, etc.), and it has been well established that certain birds, fish and invertebrates can exhibit sensitivity at very weak fields of all kinds (see e.g., discussion by DODGE and GLASER [19]). Very little is known about RF- and MW receptors, the effect of irradiation on children and non-healthy persons, and the significance of long-term irradiation.

#### 4.5. HIGH FREQUENCY FIELDS FROM ELECTRICALLY SMALL ANTENNAS NEAR A BODY

The purpose of this section is to estimate the quantities of the E- and H-fields on the surface of a subject in close contact with a transmitting antenna and to compare these quantities with the safety standards.

Let us consider a small ( $2h < \lambda$ , see FIGURE 8) dipole antenna  $A_1$  radiating an RF power  $P_{\text{rad}}$ . In a large distance  $r$  ( $r \gg \lambda$ ) from the antenna one may assume that the propagating wave is plane, so that the E- and H-vectors are rectangular to each other and show the same phase. The amount of the vector power density  $\vec{P}$  and the amounts of the vectors  $\vec{E}$  and  $\vec{H}$  can be computed from  $P_{\text{rad}}$ ,  $r$  and the characteristic impedance of vacuum  $Z_0$ :

$$|\vec{P}| = |P_{\text{rad}}| / 4 \cdot r^2 \cdot \pi \quad (2)$$

$$\vec{P} = \vec{E} \times \vec{H} \quad (\text{Definition Poynting}) \quad (3)$$

$$Z_0 = (\mu_0 / \epsilon_0)^{1/2} = |\vec{E}| / |\vec{H}| \quad (4)$$

$$|\vec{E}| = (|\vec{P}| \cdot Z_0)^{1/2} \quad (5)$$

$$|\vec{H}| = (|\vec{P}| / Z_0)^{1/2}$$

In the vicinity of an actual antenna ( $r < \lambda$ ) the  $\vec{E}$ - and  $\vec{H}$ -vectors are neither rectangular to each other nor in phase.  $\vec{P}$  becomes a rotating vector of variable amount, and the time averaged power density  $|\vec{P}|$  is

$$|\vec{P}| = \frac{1}{2} |\text{Re}(\vec{E} \times \vec{H}^*)| \quad (6)$$

The total power density  $\vec{P}$  can be considered to be a superposition of a real power density  $\vec{P}_{\text{real}}$  and a reactive power density  $\vec{P}_{\text{reac}}$ . The energy associated with the reactive power  $P_{\text{reac}}$  pulses back and forth and represents stored energy (similar to the energy stored in an inductor or capacitor). The energy flow associated with the real power  $P_{\text{real}}$  is always positive in direction of propagation and represents a real energy flow. For the following estimation we define  $\vec{P}_{\text{real}}$  as the power density which is produced from a 'hypothetical point source' with the radiating power  $P_{\text{rad}}$ :

$$|\vec{P}_{\text{real}}| = |P_{\text{rad}}| / 4 \cdot r^2 \cdot \pi \quad (8)$$

An antenna can be considered as a resonator for the nominal frequency  $f_{\text{res}}$  which loses energy by radiation. In the vicinity of the antenna exists a large reactive power which is converted into radiating (real) power, and at about  $r = \lambda / 2\pi$  the radiating power dominates over the rapidly decreasing reactive power.

An electrically small antenna is defined as an aerial, one whose size is a small fraction of the wavelength. It is a capacitor or inductor, and is tuned to resonance by a reactor of opposite kind (WHEELER [83]). From this definition it is evident that an electrically small antenna will show a considerable amount of reactive power.

The 'Helical Normal-Mode Antenna' is today one of the most applied type of electrically small antennas for walkie-talkies and biotelemetry transmitters. The dipole version (see FIGURE 8) of the helical antenna consists of a helical conductor in the shape of a long cylinder with the diameter  $D_h (D_h \ll \lambda)$  and with the axial length  $2h (2h < \lambda/2)$ . The computation of the helical antenna and its features will be discussed in chapter 16.1. At the moment we have to know only, that the main radiation direction is radial to the axis and that the main polarization axis is parallel to the antenna axis (similar to a full-size dipole antenna).

With the theory of WHEELER [83,84,85] the ratio of real to reactive power can be computed in a situation as shown in FIGURE 8.

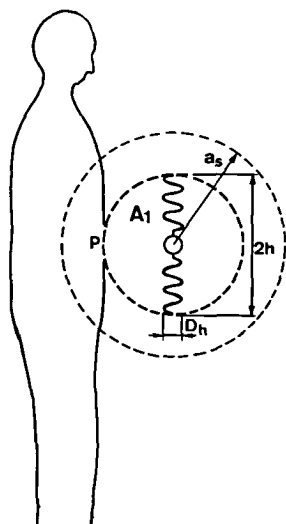


FIGURE 8

Model for the estimation of the near-field reactive power

- $A_1$  : helical dipole antenna
- $2h$  : physical antenna length ( $< \lambda$ )
- $D_h$  : diameter of the helical coil ( $\ll \lambda$ )
- $a_s$  : radius of the radiansphere (see definition in the text,  $a_s = \lambda / 2\pi$ )
- $\lambda$  : wavelength
- $P$  : point on the surface of the body, located in a distance  $h$  from the antenna

The 'radiansphere' is defined by WHEELER [84] as the boundary between the near field and the far field of a small antenna. Its circumference is  $\lambda$ , and the radius  $a_s$  is one radianlength ( $\lambda / 2\pi$ ), at which distance the three terms of the field (from R, L and C of the antenna impedance) are equal in

magnitude. The volume  $V_s$  of the radiansphere is:

$$V_s = \frac{4\pi}{3} \left( \frac{\lambda}{2\pi} \right)^3 = \frac{\lambda^3}{6\pi^2} \quad (9)$$

An electrically small antenna is somewhat smaller than the radiansphere, but it has a sphere of influence occupying the radiansphere. From the computation of radiation power factor an effective volume  $V_{eff}$  has been defined (WHEELER [85]) which is very roughly a value between the physical volume of the antenna and the volume of a sphere containing the antenna:

$$\frac{\pi D h^2}{4} \cdot 2h \ll V_{eff} < \frac{4\pi}{3} \cdot h^3 \quad (10)$$

The effective volume of a slender helical antenna is about  $2/3 \cdot h^3 \cdot \pi$ . The ratio between radiating power  $P_{rad}$  to reactive power  $P_{reac}$  is given by the ratio  $V_{eff}$  to  $V_s$  as discovered by WHEELER [83,85].

$$\frac{P_{reac}}{P_{rad}} = 4.5 \frac{V_s}{V_{eff}} \quad (11)$$

An antenna can also be considered as a resonant R-L-C network. The so-called Q-factor of such a network is defined by the ratio of the resonant frequency  $f_{res}$  to the bandwidth B and results from the ratio of stored power (in L and C) to real power (in R). The real power is the sum of the radiated power (in the radiation resistance  $R_{rad}$ ) and the dissipated power  $P_{loss}$  (in the loss resistances  $R_{loss}$ ):

$$Q = \frac{f_{res}}{B} = \frac{\text{stored power}}{\text{real power}} = \frac{P_{reac}}{P_{rad} + P_{loss}} \quad (12)$$

By combining equation (11) and (12) we obtain for the lossless antenna:

$$\frac{f_{res}}{B} = 4.5 \frac{V_s}{V_{eff}} = \frac{P_{reac}}{P_{rad}} \quad (13)$$

Equation (13) leads to the following interesting conclusions:

1. By decreasing the size of a distinct antenna type the bandwidth decreases considerably, if the resonant frequency is kept constant. This law (WHEELER [83]) is often not noticed in practical antennas, because the radiation resistance decreases and the loss resistance increases.
2. By decreasing the size of a distinct antenna, the reactive power in-

creases considerably, if the radiated power and the resonant frequency are kept constant. The Q of an actual antenna is about 5 to 30, so that the electrically small antenna represents a strong, concentrated reactive power source.

With the assumption that the total real and reactive power is contained in a sphere of radius  $h$  (FIGURE 8) and is distributed homogeneously, the averaged quantities of  $\vec{P}_{\text{real}}$ ,  $\vec{P}_{\text{reac}}$ ,  $\vec{H}$  and  $\vec{E}$  at the subject's surface point P can be estimated as follows:

- a) The radiated power  $P_{\text{rad}}$  can be computed from the electrical field-strength  $E_V$  in the far-field at the distance  $r$ : (BECKER [7])

$$P_{\text{rad}} \cong \frac{E_V^2 \cdot r^2}{45 \Omega} ; E_V \text{ in mV/m, } r \text{ in m, } P_{\text{rad}} \text{ in } \mu\text{W} \quad (14)$$

- b) The real power density  $\vec{P}_{\text{real}}$  originating from an assumed point source with the real radiating power  $P_{\text{rad}}$  is with equation (8) :

$$|\vec{P}_{\text{real}}| = P_{\text{rad}} / 4\pi h^2 \quad (15)$$

- c) The Q-factor can be obtained by measuring the resonant frequency  $f_{\text{res}}$  and the - 3 dB bandwidth  $B$ . For the lossless antenna we obtain the reactive power density  $\vec{P}_{\text{reac}}$  with equation (12) :

$$|\vec{P}_{\text{reac}}| = |\vec{P}_{\text{real}}| \cdot Q \quad (16)$$

For an antenna with high losses it is recommended to determine the losses with the efficiency measuring method or to compute the theoretical Q (see Appendix 16.1.)

- d) If we assume that the total reactive power is stored magnetically, the H-field component is about

$$|\vec{H}| \cong Q \cdot (|\vec{P}_{\text{real}}| / Z_0)^{1/2} \quad (17)$$

and if we assume that the total reactive power is stored electrically, the E-field component is about

$$|\vec{E}| \cong Q \cdot (|\vec{P}_{\text{real}}| \cdot Z_0)^{1/2} \quad (18)$$

The obtained results agree with actual measurements of helical antennas (TELL and O'BRIEN [78]) within a factor of 2. For generally small antennas an error factor of about 5 is to be expected, which is acceptable, because the threshold for biological effects is very variable.

Two typical examples should illustrate the significance of radiation of body-mounted antennas with respect to safety:

Mobile communication systems. Security personnel, police, traffic-control agents, the crew on railroad yards and many other groups are equipped more and more with body-mounted transmitters. The position of the antenna during transmission is close to the hip, chest or head, the standard power is 1 to 5 watts; the standard frequencies are about 170, 450 and recently also 900 MHz. For a 450 MHz walkie-talkie the general specifications are as follows: monopole antenna with a length of  $h=4$  cm, antenna-body distance  $d_{at}=4$  cm (situation as depicted in FIGURE 8), input power 5 W, antenna efficiency 50 percent and bandwidth 10 percent. From these data we compute a radiated power  $P_{rad} = 2.5$  W and a Q-factor of 10. The radiation intensities on the surface of the body computed with equation (15) to (18) are: real power density  $\vec{P}_{real} = 10$  mW/cm<sup>2</sup>, reactive power density  $\vec{P}_{reac} = 100$  mVA/cm<sup>2</sup> and maximum possible  $\vec{E}$  or  $\vec{H} = 2,000$  V/m or 5 A/m.

These intensities are comparable to the measurements of TELL and O'BRIEN [78] at a 3.8 W/450 MHz walkie-talkie equipped with a 15 cm helical antenna. At a distance of 5 cm a maximum power density of 24 mW/cm<sup>2</sup> was measured with an E-field probe (EDM-3 from NBS, see e.g., [9]).

If we assume a daily transmission duration of 20 minutes, the radiation of standard professional walkie-talkies exceeds the U.S. safety standard by a factor 1 to 10 and the East-European safety standard by a factor of 100 to 1,000. Macro-thermal effects are not to be expected, because the small irradiated area is well-cooled, but micro-thermal or non-thermal effects probably occur. The main risk is not only the high intensities, but the uncontrolled, frequent, world-wide application of walkie-talkies. The actual Polish regulation (see ref. 46) in BARANSKI and CZERSKI [6] requires that any candidate for work necessitating exposure to MW must undergo a medical examination and obtain a medical certificate for fitness, and periodic examination of MW workers are compulsory. It would be wise to collect medical data on personnel equipped with mobile communication systems in order to decide if similar examinations are necessary for such personnel.

Miniature biotelemetry transmitters. A common antenna for biotelemetry transmitters is a small coil around the housing. We assume the following data: RF-input power 1 mW, antenna diameters  $2h = 2$  cm, radiation efficiency 10 percent and a Q-factor of 30. With that data the real power density  $\vec{P}_{\text{real}}$  is about  $0.01 \text{ mW/cm}^2$  and the reactive power density  $\vec{P}_{\text{reac}}$  is about  $0.30 \text{ mVA/cm}^2$ .

The radiation intensities of miniature biotelemetry transmitters are between the safety standard limits of the U.S. and East Europe. The radiation duration is generally a few weeks, and often electrodes to sensitive body regions (EEG) are implanted. Often pulse position modulation (sharp peak power) is applied in animal experiments. Health hazards are not likely to occur, but micro-thermal gradients may cause biological effects which may lead to wrong physiological measuring data. Therefore, it would be wise to check the probable influence of the biotelemetry transmitter radiation with respect to artifacts.

The accurate computation of the E- and H-fields near an antenna and near or in the body is complicated and vary from one antenna type to the other. Near-field results of a slender monopole antenna have been presented by CHANG, HALBGEWACHS and HARRISON [13]. NYQUIST, CHEN and GURU [66] investigated the coupling of a 50 MHz  $\lambda/4$  dipole antenna with a man-model consisting of dielectrical cubes. At an antenna-body distance of 10 cm they computed a total power deposition of 0.28 W at an input power of 3.14 W. They concluded that an input power of 20 W results in potentially hazardous intensities comparable to a plane-wave irradiation with  $10 \text{ mW/cm}^2$ . It should be mentioned that a  $\lambda/4$  antenna is 1.5 m long so that the critical power level may be expected below 2 W for electrically small antennas.

Accurate near-field measurements in and outside the body still pose a problem. EGGERT, GOLTZ and KUPFER [21] developed the near-field strength meter NFM-1 which allows E-field measurements 10 cm away from a source with less than 15 percent error in the frequency range 10 to 350 MHz. BELSHER [9] developed the near-field electric energy density meter EDM-2 with a E-probe consisting of three orthogonal miniature dipoles. The probe is imbedded in a 2 cm  $\varnothing$  stick and allows E-field measurements with less than 10 percent error in the frequency range 10 to 500 MHz. GREENE [33,34] described an H-field probe and a near-field exposure synthesizer for the frequency range 10 to 40 MHz. The best method to determine the field inside a body is the thermographic recording of the absorption in a model (e.g., GUY, WEBB and SORENSEN [36]).



#### 4.6. CURRENT TRENDS IN INTERNATIONAL SAFETY STANDARD DEVELOPMENT

An overview on the present safety standards and on the actual existing exposures is given in FIGURE 9:

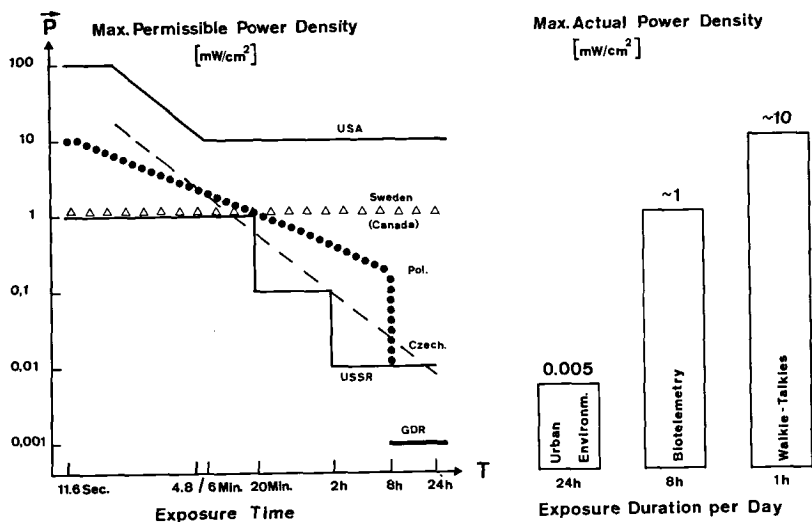


FIGURE 9 International safety standards and actual exposures. Some standards are related gradually to the duration, all are valid for partial and whole body exposure. The GDR limit is valid for pregnant and nursing women. The urban environmental exposure regards approximately 20,000 people in Washington and Chicago. Sources: MICHAELSON [57], DODGE and GLASER [19], ANSI [2], TGL [18], HANKIN et al. [39] and NEUKOMM [64].

The U.S. Safety Standard recommendations (ANSI [2]) apply to all radiation within the frequency range from 10 MHz to 100 GHz except for deliberate exposure of patients by or under the direction of practitioners of the healing arts. The recommendations pertain to both whole body and partial body irradiation. For normal environmental conditions the CW (continuous wave) radiation guide is  $10 \text{ mW/cm}^2$ , and the equivalent free-space electric and magnetic field strengths are approximately 200 V/m RMS and 0.5 A/m. For modulated fields, the power densities and the field strengths are averaged over any 0.1 hour period, and they should also not exceed an energy density of  $1 \text{ mWh/cm}^2$ . The US Army (MICHAELSON [57]) recommends further, that short exposures should not exceed  $100 \text{ mW/cm}^2$ , and that the exposure duration (in minutes) is limited by the expression  $6000/((x \text{ mW/cm}^2)^2)$ .

Sweden decreased step by step the maximum permissible power density from 10 mW/cm<sup>2</sup> (1970) over 5 mW/cm<sup>2</sup> (1973) to now 1 mW/cm<sup>2</sup>, and Canada intends to follow (DODGE and GLASER [19]).

The East European safety standards in FIGURE 9 apply for all occupational radiation in the frequency range 300 MHz to 300 GHz. Remarkable are the stepped curve (constant dosis) and the low values for permanent exposure. At lower frequencies somewhat higher values are permissible. A typical example for Eastern safety standards is presented in TABLE 10 with the German Democratic Republic's (GDR) safety standard:

FREQUENCY RANGE	MAXIMUM PERMISSIBLE FIELD INTENSITIES IN THE GERMAN DEMOCRATIC REPUBLIC (1978)			
	OCCUPATIONAL EXPOSURE TO IRRADIATION		COMMUNAL HYGIENE (RECOMMENDED)	
	GENERAL	PREGNANT AND NURSING WOMEN	OPEN TERRITORY	DWELLING HOUSES
60 kHz - 3 MHz	50 V/m	10 V/m per 8 h	10 V/m	10 V/m
3 MHz - 30 MHz	20 V/m	4 V/m per 8 h	4 V/m	0.4 V/m
30 MHz - 300 MHz	5 V/m	2 V/m per 8 h	2 V/m	0.2 V/m
300 MHz - 300 GHz	10 µW/cm <sup>2</sup> per 8 h	1 µW/cm <sup>2</sup> per 8 h	5 µW/cm <sup>2</sup> (pulsed, rot. antenna)	2 µW/cm <sup>2</sup> (pulsed, rot. antenna)
	100 µW/cm <sup>2</sup> per 2 h			
	1 mW/cm <sup>2</sup> per 0.3 h		1 µW/cm <sup>2</sup> (CW)	0.5 µW/cm <sup>2</sup> (CW)

TABLE 10 Maximum permissible field intensities for RF and MW irradiation in occupational exposure and communal hygiene in the GDR.

(Sources: DDR-Standard and appendix [18])

The actual exposure to RF and MW is shown in FIGURE 8 for three different categories. In urban areas with distributed Radio- and TV stations many thousand people are living day and night in EM fields. HANKIN et al. [39] investigated the power densities of UHF-TV stations and found that about 20,000 people in Washington, 20,000 people in Chicago and 3,000 people in Philadelphia are exposed to more than 4 µW/cm<sup>2</sup>. Up to now little data are available about hazardous effects, from the work of VREELAND, SHEPHERD and HUTCHINSON [82] it is known, however, that TV-stations may affect the correct operation of pacemakers. Mobile communication systems and especially the UHF walkie-talkies are of greater significance as discussed in section 4.5.. One may assume, that about 10 million people are exposed to more than 1 mW/cm<sup>2</sup> by such sources, and it is worth to mention that in the East European countries the power of professional walkie-talkies is legally limited to about 100 mW. Biotelemetry transmitters are relatively safe, but deserve attention to possible artifacts.

#### 4.7. RECOMMENDATIONS FOR SAFETY LIMITS FOR BODY-MOUNTED ANTENNAS

With the present poor knowledge about long-time effects of RF and MW on humans it is very difficult to state generalized recommendations. If very low permissible values are recommended, many sensible applications for biotelemetry and mobile communications have to be excluded. If very high values are recommended, we have to bear the responsibility for health hazards. Summarizing the facts collected in this chapter, we may come to the following conclusions:

##### Averaged permissible values related to the transmitting frequency:

Below 20 MHz the power absorption is about proportional to  $f^2$ , is determined mainly by the H-field, and at 10 mW/cm<sup>2</sup> the SAR's are well below 1 W/kg. A maximum power deposition of 10 mW/cm<sup>2</sup> and maximum near-field strengths of 200 V/m and 0.5 A/m are conservative limits.

Above 300 MHz the penetration depth is small, but local hot spots are possible under certain conditions. A maximum power density of 1 mW/cm<sup>2</sup> and maximum near-field strengths of 63 V/m and 0.16 A/m must not be exceeded.

In the resonance region of 20 to 300 MHz excessive local absorption is only possible, if the human body is irradiated by a remote source (whole body exposure), and if the power density is more than 1 mW/cm<sup>2</sup>. For partial body exposure, like irradiation from body-mounted antennas, a distribution of the available radiation power may be expected. For low-power transmitters (e.g., < 25 W) the maximum power density should not exceed 1 mW/cm<sup>2</sup> and the near-field strengths should not exceed 63 V/m and 0.16 A/m. For a high-powered transmitter the coupling conditions and the power distribution have to be investigated.

Peak power and dosis: The reported phenomena seem to be effects from the dosis and effects from the peak values. The above indicated maximum ratings are conservative for CW and for maximum 2 hour exposure per day. For shorter durations and pulse modulated sources the above indicated averaged power densities may be multiplied by a factor of 10 and the above indicated averaged field intensities may be multiplied by a factor of 3 in order to obtain the permissible peak values. For long-time exposure, however, the above indicated values should be divided by the factors 10 and 3, respectively.

Risk factors: Some of the risk factors are: conducting objects inside and outside the body (e.g., pace makers, electrodes, microphone cables, headphones, transducers), decreased state of health, extreme environmental conditions (heat), stress, immobility, pregnancy, etc. The present state of bio-research leads to the conclusion that some reversible biological effects may occur, but that real health hazards can be excluded at such low maximum safety limits. With respect to biotelemetry one has to take into account possible artifacts which may lead to wrong results. In animal experiments, especially with small animals, one should consider the wavelength/size ratio, the different biological functions (e.g., thermoregulation, metamorphosis) and the environmental (e.g., cage reflections) conditions.

Leer - Vide - Empty

## 5. ANALYSIS OF THE ANTENNA-BODY SYSTEM

### 5.1. DESCRIPTION OF THE GENERAL PROBLEM

#### 5.1.1. DEFINITION OF THE BASIC GOALS IN ANTENNA BODY MODELLING

Comparatively speaking, there are two kinds of antenna engineers. First, the experienced practitioner who develops in a short time an exotic, well-operating antenna, but who is not able to deliver computational data, because there are too many variable, undefined parameters. Second, the theoretically-trained engineer, who computes for assumed idealized conditions an excellent theoretical antenna which operates badly under the given difficult environmental conditions.

Similar to above the same dilemma is manifested in our modelling problem:

The antenna-body model should contain on one hand all significant parameters which describe a realistic situation, on the other hand the selected model should be computable with a reasonable effort.

The basic goals may be defined as follows:

The computation of the antenna-body model should explain the systematic relation among frequency, body geometry, relative position of the antenna to the body and transmission loss to a remote antenna.

The results of the computation should be verified by a sufficiently accurate measuring method.

The obtained results from both theory and experiment should deliver fundamental data for the development of efficient, electrically small, body-mounted antennas. With the test subject standing on the earth, the antenna-body system should radiate omnidirectionally in the horizontal plane.

#### 5.1.2. PARAMETER DESCRIPTION OF THE GENERAL ANTENNA-BODY SYSTEM

The general test situation is shown in Figure 11. Given is a test subject (TS), a body-mounted antenna ( $A_1$ ) and a remote antenna ( $A_2$ ). The TS is electrically isolated from ground by the small space (s) between ground and feet. The relative position of  $A_1$  to the TS is defined by the azimuthal rotation angle ( $\phi$ ), the relative antenna height ( $h_B$ ) and by the antenna-body distance ( $d_{at}$ ), which is the distance between the center of  $A_1$  and the surface of the TS. The absolute position of the antennas is de-

defined as follows: The transmitting distance ( $d$ ) is much greater than the wavelength ( $\lambda$ ) and  $d_{at}$ ; therefore we regard  $d$  as constant. The antenna height ( $h_1$ ) is the height of  $A_1$  above ground, the antenna height ( $h_2$ ) is the height of  $A_2$  above ground. The elevation angle ( $\theta_{e1}$ ) is the vertical angle of the beam  $\overline{A_1 A_2}$  to the horizontal ground; the incident angle ( $\theta_i$ ) is the vertical angle between the beam  $\overline{A_1 A_2}$  and the vertical body axis. The reflection angle ( $\gamma_B$ ) is the Brewster angle (later discussed in 5.3.2.).

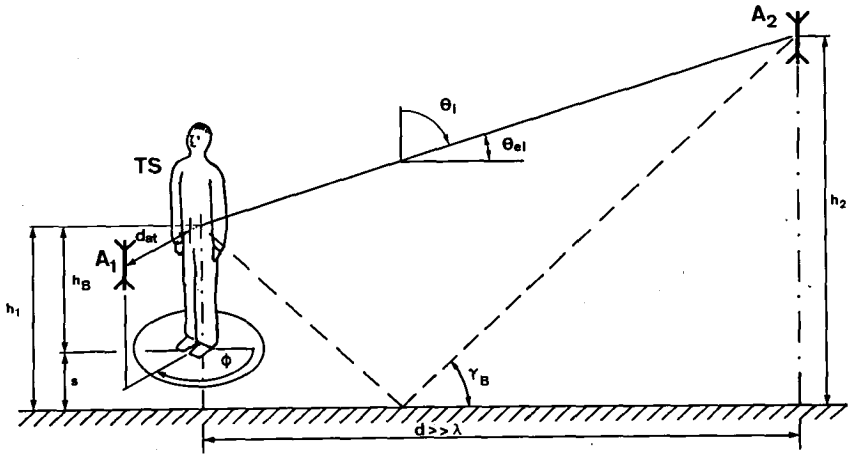


FIGURE 11 General test situation. Parameters described in the text.

The point of interest is the transmission from an EM signal from  $A_1$  to  $A_2$  when a body (TS) is near to the antenna  $A_1$ . Because we want to investigate the systematic influence of the TS and not the properties of a specific antenna type, we define the test situation closer :

The two antennas  $A_1$  and  $A_2$  have to fulfill the following requirements:

- The physical size of  $A_1$  should be smaller than any relevant dimension of the test set-up.
- $A_1$  should have only one dominant E-polarization axis ( $p_1$ )
- $A_1$  should radiate omnidirectionally in free space (e.g., radial radiation independent on the rotation angle of the axis of  $A_1$ )
- $A_1$  should not change its input impedance due to body proximity.
- $A_2$  should have a strict linear E-polarization ( $p_2$ )

As an additional regulation the input power ( $P_{in}$ ) at  $A_1$ , the absolute positions  $h_1, h_2, d$  and the polarization  $p_2$  are kept constant for each experiment performed at a given frequency ( $f$ ).

The reference field strength  $E_0$  is measured at  $A_2$ , when no subject is present.  $A_1$  is oriented for maximum radiation in direction of  $A_2$ ; in the first case (see FIGURE 11)  $p_1$  and  $p_2$  are vertical.

The actual field strength  $E$  is measured at  $A_2$  when the TS is positioned, varying  $d_{at}, h_B, \phi$  and  $p_1$ .

The "transmission loss" ( $Loss_B$ ) and the "transmission gain" ( $Gain_B$ ) is defined as follows:

$$Loss_B = -20 \log \left( \frac{|E|}{|E_0|} \right) \quad \text{in decibels [dB]} \quad (19)$$

$$Gain_B = 20 \log \left( \frac{|E|}{|E_0|} \right) \quad \text{in decibels [dB]} \quad (20)$$

$Loss_B$  is a measure for the negative (or positive) influence of the TS on the radiation characteristics of the antenna  $A_1$ .  $Loss_B$  is a function of many parameters which are discussed in TABLE 12. The main radiation pattern of the antenna-body system are described by  $Loss_B$  versus  $\phi$  and versus  $\theta_{el}$ .

Because  $E_0$  represents the maximum possible field strength for a given test antenna in the best practical conditions (near ground, but far away from a body), we call  $Loss_B$  of the free antenna ( $E_0$ ) "free-space level" (FSL):

$$\text{Free-space level (FSL)} = 0 \text{ dB} = \text{reference level } E_0 \quad (21)$$

The polarization  $p_2$  of  $A_2$  may also be horizontal (parallel to the ground). In that case the FSL (0 dB) is obtained by orienting  $p_1$  of  $A_1$  horizontal, so that  $p_1$  and  $p_2$  are parallel.

In the case of reverse transmission, that is, transmission from  $A_2$  to  $A_1$ , the FSL (0 dB) is calibrated to the electrical field strength  $E_0$  of the incident, plane wave in the region, where the TS is intended to be placed.

Finally, it is pointed out once more that  $E_0$  or the FSL is not identical with the field strength produced by an ideal isotropic radiator. At the moment we are not interested in the directional gain and in the efficiency of  $A_1$ ; such questions will be treated later in Appendix 16.1..

A list of  $Loss_B$  determining parameters are presented in TABLE 12:



A SAMPLE OF SIGNIFICANT PARAMETERS DETERMINING GENERALLY THE TRANSMISSION LOSS			
PARAMETER	SYMBOL	RANGE	DESCRIPTION OF THE PARAMETER AND ESTIMATION OF ITS INFLUENCE
Frequency	$f$	10-1000 MHz	At frequencies from 50-300 MHz the dimensions of the human body are in the same order of magnitude as the wavelength. Resonance phenomena of unknown influence are to be expected.
Wavelength	$\lambda$	0.3 - 30 m	
Polarization of $A_1$ and $A_2$	$p_1$	vert./hor./radial	The main resonance of the human body occurs at vertical polarization, a weaker resonance at horizontal polarization. Field irregularities outside the body may likely occur especially in the case of resonance for $p_1$ and $p_2$ vertical.
	$p_2$	vert./hor.	
Body-mounted antenna	$A_1$	$h < 0.15$ m	The requirements concerning length, polarization, omnidirectionality and impedance have been defined in 5.1.2. In the experiment $A_1$ has to be operated off-resonance in order to keep the impedance stable. An antenna for practical use, however, has to be tuned exactly on resonance for the provided mounting. Details are described in section 8. and 16.1.
Remote antenna	$A_2$	—	$A_2$ has no influence, if $A_2$ is a calibrated precision antenna with strict linear polarization $p_2$ .
Height of $A_1$ above ground	$h_1$	0.8 - 1.5 m	An $h_1$ of this range corresponds to $0.03\lambda$ up to $5\lambda$ . The radiation pattern in the vertical plane will show varying lobes for an elevation angle $\theta_{e1}$ of 5-20°. The electrical center of the antenna-body system is not known, so that errors of about 4 dB are likely due to ground reflections. See $\gamma_B$ below.
Height of $A_2$ above ground	$h_2$	fix 6.2 m	At frequencies above 20 MHz the $h_2$ has no influence, as long as $h_1$ , $d$ and thus $\theta_{e1}$ are kept constant.
Transmission distance	$d$	fix 31 m	As long as $d$ is greater than $\lambda$ and if $\theta_{e1}$ is kept constant, the distance $d$ has no influence. A small variation of the actual $A_1$ - $A_2$ distance with $d_{at}$ of $\pm 1$ m causes a 0.3 dB change.
Relative $A_1$ height	$h_B$	0.6 - 1.3 m	$h_B$ has an influence on $h_1$ and causes a secondary influence. The primary influence of $h_B$ is a subject of this study.
Azimuthal angle	$\phi$	0 - 360°	Experiments showed a large loss in the shadow zone at 180°. The influence of $\phi$ is a subject of this study.
$A_1$ -body-distance	$d_{at}$	0.05 - 4 m	Experiments showed a large loss at small $d_{at}$ . A large range variation of $d_{at}$ is a subject of this study.
Space TS to ground	$s$	0.2 - 1 m	Grounding effects will probably affect $Loss_B$ . The TS has to be isolated from the ground to minimize that influence.
Geometry of the TS	$L_B$	1.5 - 1.5 m	The length $L_B$ and the diameter $D_B$ of the TS might be related to the $\lambda/2$ resonances. A standard TS or phantom is required.
	$D_B$	0.2 - 0.5 m	
Material of the TS	$\epsilon_r$ $\sigma$	6 - 100 0.01-1.6 S/m	See section 4.2. The EM density is so high that the material might be of little significance at large $d_{at}$ .
Elevation angle	$\theta_{e1}$	5 - 20°	The elevation angle $\theta_{e1}$ should be kept constant. See discussion at $h_1$ above.
Brewster angle	$\gamma_B$	12 - 17°	The ground reflected vertically polarized wave is more than 10 dB smaller than the directly transmitted wave, if the Brewster angle $\gamma_B$ is adjusted properly. For details see section 5.3.2.

TABLE 12 A sample of significant parameters which generally determine the transmission loss ( $Loss_B$ ) in an antenna-body system.

## 5.2. PARAMETER EVALUATION AND MODELLING OF THE ANTENNA-BODY SYSTEM

### 5.2.1. TRANSFORMATION OF THE PROBLEM WITH THE RECIPROCITY THEOREM

The EM fields in the vicinity of an electrically small transmitting antenna  $A_1$  are of a complicated nature. If  $A_1$  is in the vicinity of the body, the near-fields are disturbed. The integral effects of the near-fields at the remote antenna  $A_2$  determine the transmission loss  $Loss_B$ . The computation of this problem is quite difficult and needs much additional input data concerning the specific antenna and the specific body.

Because we are only interested in the transmission loss from a point  $A_1$  to a point  $A_2$ , we may ask also for the transmission loss from a point  $A_2$  to a point  $A_1$ . If both losses are of the same magnitude, we had only to look at the more simple second case.

The reciprocity theorem (HEILMANN [42]) runs as follows:

Assumed are two arbitrary antennas  $A_1$  and  $A_2$  at arbitrary relative orientation and distance. If the same voltage is applied either to  $A_1$  or  $A_2$ , the same current will flow in the other antenna  $A_2$  or  $A_1$ .

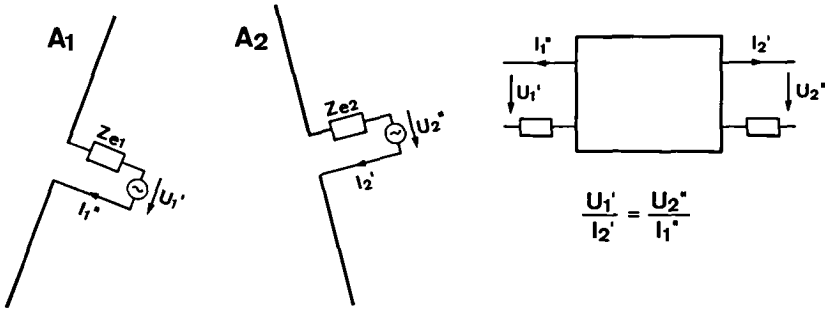


FIGURE 13 Test set-up for the verification of the reciprocity theorem (Source: HEILMANN [42]).

The reciprocity theorem is valid for any linear medium, where  $\mu, \epsilon$  and  $k$  are scalar, but arbitrary quantities. These electromagnetic parameters may depend on their locations, but are not functions of the field vectors.

In our model we can assume that the body material is linear (i.e., not dependent on the magnitude of the EM-field, no thermal alterations of the material) and isotropic (i.e., the properties do not depend on the direction of the EM field vectors). If both antennas are terminated with the same impedance, we may conclude that  $\text{Loss}_B$  is the same for  $A_1$ - $A_2$  and  $A_2$ - $A_1$  transmission.

As it will be shown in section 9.1.5. the reciprocity theorem is valid for our application. The verification measurements revealed a difference of less than 2 dB when the direction of transmission was reversed (transmitter and receiver changed over, antennas unchanged). This held true for all test bodies (see 5.4.1.), for all measurements at 100 to 1000 MHz, for all  $d_{at}$ 's above 0.05 m and for an applied input power  $P_{in}$  of 1 mW.

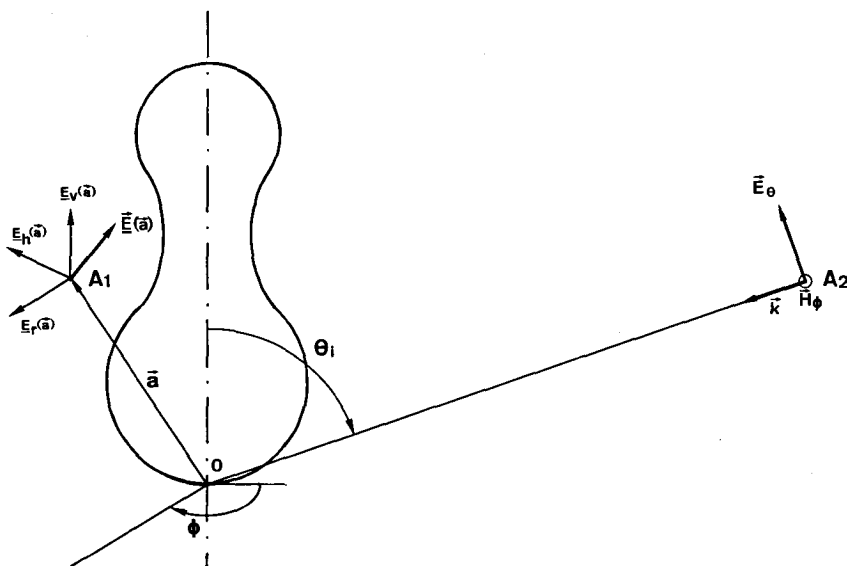


FIGURE 14 Transformed test situation. Antenna  $A_2$  generates a plane wave in the region of the body, the wave is scattered at the body and the disturbed wave is picked-up by antenna  $A_1$ .

The transformed problem, which we have to compute in this study is: a body is irradiated by a plane wave with an FSL field strength  $E_0$  at 0. We have to quantify the  $\vec{E}(\vec{a})$  vector components  $E_V$  (vertical),  $E_H$  (horizontal) and  $E_r$  (radial) around the body as a function of  $\vec{a}$  (FIGURE 14).

### 5.2.2. ANTENNA LENGTH AND FIELD HOMOGENEITY

In the test situation FIGURE 14 the monitored E-vector  $\vec{E}(\vec{a})$  is given by

$$\vec{E}(\vec{a}) = \vec{E}_{inc}(\vec{a}) + \vec{E}_{scat}(\vec{a}) \quad (23)$$

where  $\vec{E}_{inc}(\vec{a})$  is the incident E-vector from  $A_2$ , and  $\vec{E}_{scat}(\vec{a})$  is the scattered E-vector from the body. The total E-vector  $\vec{E}(\vec{a})$  is varying in direction, amount and phase for variable positions  $\vec{a}$ . Because the antenna  $A_1$  will have a certain length  $2h$  (FIGURE 15), the E-field irradiating  $A_1$  is not constant along the antenna axis.

Because the voltage induced at the terminals of the antenna  $A_1$  will become a measure for the transmission loss, we have to investigate the relation between  $\vec{E}(\vec{a})$ , antenna length  $2h$  and the induced voltage  $U_{ind}$ .

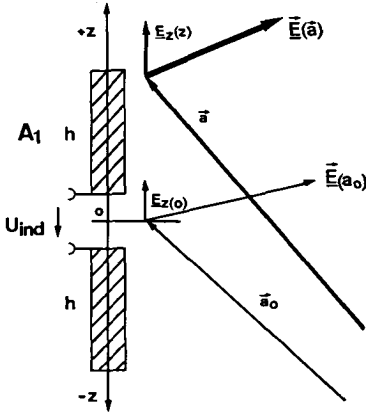


FIGURE 15

Induced voltage in a linear dipole antenna immersed in a inhomogeneous electrical field.

$\vec{E}(\vec{a})$  : variable applied E-field

$E_z(z)$  : z-component of  $\vec{E}(\vec{a})$   
for  $\vec{a}$  on the z-axis

$z$  : axis of the antenna

$2h$  : length of the antenna

$U_{ind}$  : induced voltage at the terminal of the antenna

$\vec{a}, \vec{a}_0$  : position vector (see also FIGURE 14)

Let us assume a linear dipole antenna  $A_1$  with the axis  $z$  and the length  $2h$  (FIGURE 15). Let us further assume that we know the current distribution function  $\Psi(z)$  along the  $z$ -axis for an incident plane wave (see e. g., HEILMANN [42]). The induced voltage  $U_{ind}$  is then given by:

$$U_{ind} = \int_{-h}^{+h} E_z(z) \Psi(z) dz \quad (24)$$

If the length  $2h$  of  $A_1$  is adequately small, the variations of  $E_z(z)$  along the  $z$ -axis are so small, that we are allowed to replace  $E_z(z)$  by the plane wave equivalent field strength  $E_z(o)$  of  $\vec{E}(\vec{a}_0) \cdot \vec{e}_z$ .

For a given antenna  $A_1$  a certain relation between the axial antenna length  $2h$  and the variability of the axial field  $\underline{E}_z(z)$  has to exist, if the above approximation should lead to induced voltages  $U_{ind}$  representing the field-strength. We assume the following:

- $A_1$  should measure the relative field strength  $\underline{E}_z(z)$  compared to an FSL reference field  $E_0$  with an accuracy of 2 dB.
- $A_1$  is small compared with the wavelength ( $2h < 0.2\lambda$ ).
- The total  $\vec{E}(\vec{a})$ -vector is polarized in z-direction, which is the main polarization axis  $p_1$  of  $A_1$ .
- We assume for the worst case a constant current distribution function  $\Psi(z) = \text{constant}$ . An  $\underline{E}_z$  at the ends of the antenna has the same weight on  $U_{ind}$  as an  $\underline{E}_z$  at the antenna center.
- We assume that  $\underline{E}_z(+h) = E_0 = 0$  dB and that  $|\underline{E}_z(z)|$  increases monotonously from  $-h < z < +h$ .  $\underline{E}_z(z)$  may be approximated as:

$$|\underline{E}_z(z)| = E(x) = a_0 + a_1x + a_2x^2, \quad x = \frac{z+h}{2h}, \quad 0 < x < 1 \quad (25)$$

- We assume that the phase angle  $\arg(\underline{E}_z(z))$  increases monotonously from  $-h < z < +h$  and depends linearly on  $z$ :

$$\arg(\underline{E}_z(z)) = \text{const.} + z \cdot \beta \cdot k; \quad 2h \cdot \beta \cdot k < \pi/2, \quad \beta = \text{const.} \quad (26)$$

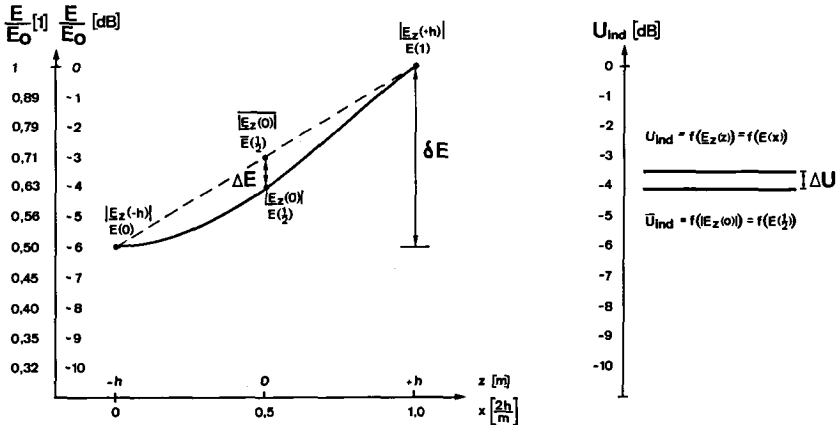


FIGURE 16 Relation among  $\delta E$ ,  $\Delta U$  and  $\Delta E$  in a worst-case situation as computed later in section 10. The assumed worst case E-field data are:

$$\begin{aligned} |\underline{E}_z(-h)| &= E(x=0) = \text{minimum at one antenna end} &= -6.00 \text{ dB} \\ |\underline{E}_z(0)| &= E(x=1/2) = \text{nominal center field} &= -4.08 \text{ dB} \\ |\underline{E}_z(+h)| &= E(x=1) = \text{maximum at other antenna end} &= 0.00 \text{ dB} \\ \overline{E}(0) &= \overline{E}(x=1/2) = \text{logarithmic mean value} &= -3.00 \text{ dB} \end{aligned} \quad (27)$$

The induced voltage  $U_{ind}$  at the antenna terminals is with (25)

$$U_{ind} = \int_{-h}^{+h} \underline{E}_z(z) dz = 2h \int_0^1 E(x) dx = 2h \left( a_0 + \frac{a_1}{2} + \frac{a_2}{3} \right) \quad (28)$$

The approximated induced voltage  $\bar{U}_{ind}$  with a constant (center) field is

$$\bar{U}_{ind} = \int_{-h}^{+h} \underline{E}_z(0) dz = 2h \int_0^1 E\left(\frac{1}{2}\right) dx = 2h \left( a_0 + \frac{a_1}{2} + \frac{a_2}{4} \right) \quad (29)$$

The logarithmic mean value  $|\underline{E}_z(0)|_{dB} = 20 \log \{ |\underline{E}_z(0)| / |\underline{E}_z(+h)| \}$  is

$$\begin{aligned} |\underline{E}_z(0)|_{dB} &= \bar{E}\left(\frac{1}{2}\right)_{dB} = \frac{1}{2} \left[ 20 \log 1 + 20 \log \left( \frac{a_0}{a_0 + a_1 + a_2} \right) \right] \\ &= 20 \log \left[ \sqrt{1 + \frac{a_1}{a_0} + \frac{a_2}{a_0}} / \left( 1 + \frac{a_1}{a_0} + \frac{a_2}{a_0} \right) \right] \end{aligned} \quad (30)$$

The logarithmic center field strenght  $|\underline{E}_z(0)|_{dB}$  is  $20 \log |\underline{E}_z(0)| / |\underline{E}_z(+h)|$ :

$$|\underline{E}_z(0)|_{dB} = E\left(\frac{1}{2}\right)_{dB} = 20 \log \left[ \left( 1 + \frac{a_1}{2a_0} + \frac{a_2}{4a_0} \right) / \left( 1 + \frac{a_1}{a_0} + \frac{a_2}{a_0} \right) \right] \quad (31)$$

From (28) and (29) we obtain the logarithmic difference  $\Delta U$ :

$$\Delta U = 20 \log U_{ind} - 20 \log \bar{U}_{ind} = 20 \log \left| \frac{1 + \frac{a_0}{2a_0} + \frac{a_2}{3a_0}}{1 + \frac{a_1}{2a_0} + \frac{a_2}{4a_0}} \right| \quad (32)$$

From (30) and (31) we obtain the logarithmic difference  $\Delta E$ :

$$\Delta E = 20 \log E\left(\frac{1}{2}\right) - 20 \log \bar{E}\left(\frac{1}{2}\right) = 20 \log \left| \frac{1 + \frac{a_1}{2a_0} + \frac{a_2}{4a_0}}{\sqrt{1 + \frac{a_1}{a_0} + \frac{a_2}{a_0}}} \right| \quad (33)$$

If we replace  $\frac{a_1}{a_0}$  by  $\alpha_1$  and  $\frac{a_2}{a_0}$  by  $\alpha_2$ , we obtain

$$\Delta U = 20 \log \left| \frac{1 + \frac{\alpha_1}{2} + \frac{\alpha_2}{3}}{1 + \frac{\alpha_1}{2} + \frac{\alpha_2}{4}} \right| \quad (34)$$

$$\Delta E = 20 \log \left| \frac{1 + \frac{\alpha_1}{2} + \frac{\alpha_2}{4}}{\sqrt{1 + \alpha_1 + \alpha_2}} \right| \quad (35)$$

As we can see from equation (35),  $\Delta E$  becomes zero for specific pairs of  $\alpha_1$  and  $\alpha_2$ , also when  $\Delta U$  is not zero. Therefore, the number  $\Delta E$  cannot be used as an indicator for  $\Delta U$ .

$\Delta U$ , however, varies only little for  $0 < \alpha_1, \alpha_2 < 1$ . As can be seen from (34),  $\Delta U$  increases with  $\alpha_2$  and decreases with increasing  $\alpha_1$ . A good measure for the maximum  $|\Delta U|$  can be obtained with  $|\delta E|$ , assuming that the  $E(x)$  function is of the type  $E(x) = a_0 + a_2 x^2$ . In FIGURE 16 such a function has been assumed with  $a_0 = 0.5$ ,  $a_2 = 0.5$  and thus  $\alpha_1 = 0$ ,  $\alpha_2 = 0$ . The obtained results  $\delta E$  and  $\Delta U$  are:

$$|\delta E| = 6 \text{ dB} \quad ; \quad |\Delta U| = 0.56 \text{ dB} \quad (36)$$

If we regard only the  $\Delta U/\alpha_2$  ratio of the same quadratic equation  $E(x) = a_0 + a_2 x^2$ , we obtain for a permissible  $|\Delta U|$  of 1 dB an  $\alpha_2$  of 2.3. Thus, the field strength variation  $\delta E$  along the antenna should not exceed :

$$|\delta E| = \left| |E_z(-h)|_{\text{dB}} - |E_z(+h)|_{\text{dB}} \right| < 20 \log \left( \frac{1}{1+2.3} \right) = 10 \text{ dB} \quad (37)$$

=====

The permissible phase variation  $\delta\phi$  along the antenna is limited by:

$$|U_{\text{ind}}| = \left| \int_{-h}^{+h} E \sin(\beta \cdot z \cdot k) dz \right| = \left| \frac{\hat{E}}{k} (\cos(2h\beta \cdot k)) \right| \quad (38)$$

If we require a resulting real-part variation of less than 10 dB (which causes a  $|\Delta U| < 1 \text{ dB}$ , see (37)), we obtain a phase variation limit  $\delta\phi$  of

$$|\delta\phi| = |\arg(E_z(-h)) - \arg(E_z(+h))| < \arccos(10^{-\frac{10}{20}}) = 71^\circ \quad (39)$$

=====

For the practical applications the field homogeneity requirements along a dipole test antenna  $A_1$  are completely specified by (38) and (39). Within these limits the field strength  $E_z(0)$  at the center of the antenna is representative for the whole field around the antenna, at an accuracy of better than 2 dB. Under these conditions the transmission loss  $\text{Loss}_B$  for  $p_1 = z$ -polarization can be computed as:

$$\text{Loss}_B = -20 \log \frac{|E_z(0)|}{|E_0|} \quad \begin{array}{l} E_0 = \text{FSL, } z = \text{polar. axis,} \\ E_z(0) = \text{center field strength} \end{array} \quad (40)$$

If equations (36) and (38) are not fulfilled, equation (24) has to be evaluated for both theoretical  $\text{Loss}_B$  and verification experiments.

### 5.2.3. RELATION OF BODY-DIMENSIONS TO WAVELENGTHS

In section 4.3. and FIGURE 3 it has been shown that the absorption of EM energy inside of a dielectric sphere depends on the ratio of the sphere-circumference  $2\pi a$  to the wavelength  $\lambda$  (see RACS).

With the Radar Cross Section (RCS) it should be shown that also the scattered fields outside a body depend on the same ratio. If a body is irradiated by an EM wave, a part of the EM energy will be absorbed as discussed in 4.3. and the remaining EM energy will be scattered in all directions. That part of EM-energy which will be back-scattered toward the EM-source can be quantified by the RCS. The RCS is defined as:

$$RCS = \frac{P_{scat}}{|\vec{P}|} = \lim_{R \rightarrow \infty} 4\pi R^2 \frac{|\vec{E}_{scat}|^2}{|\vec{E}_{inc}|^2} \quad (41)$$

$P_{scat}$  is the total scattered power,  $\vec{P}$  is the incident power density of the EM wave at the body,  $R$  is the distance between the remote source and the body,  $\vec{E}_{scat}$  is the back scattered E-field and  $\vec{E}_{inc}$  is the incident E-field. The RCS of a sphere is shown in FIGURE 17 versus the ratio  $2\pi a/\lambda$ .

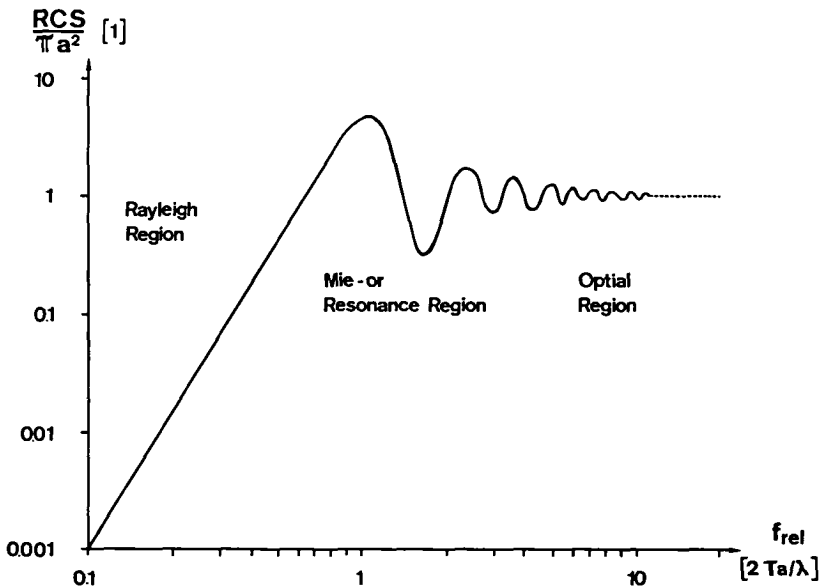


FIGURE 17 Radar Cross Section (RCS) of a sphere with the radius  $a$ , related to the shadow area  $\pi a^2$ , versus the relative frequency  $f_{rel}$  (sphere circumference  $2\pi a$ / wavelength  $\lambda$ ). (Source: BECKER [7]).



The shape of the human body can be approximated by an ellipsoid. From the literature it is known that the RCS of an ellipsoid is similar to the RCS of a sphere, if the largest circumference is equal and if the incident wave is polarized parallel to the main axis of the ellipsoid. In FIGURE 18 a simplified man-model is shown and the approximated main resonant frequency for vertical polarization is indicated:

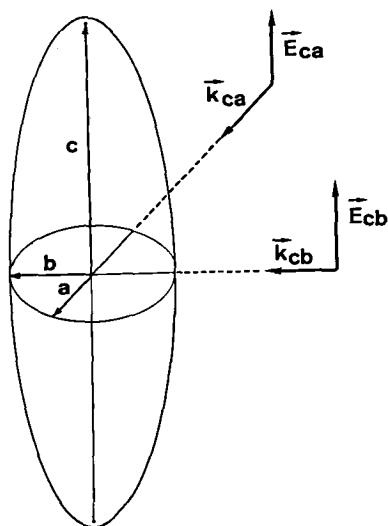


FIGURE 18 Simplified Man-Model

Vertical axis :  $2c = 1.8$  m

Sagittal axis :  $2a = 0.2$  m

Lateral axis :  $2b = 0.3$  m

Incident vertical polarized waves:

Sagittal incidence :  $\vec{E}_{ca}, \vec{k}_{ca}$

Lateral incidence :  $\vec{E}_{cb}, \vec{k}_{cb}$

Circumferences for vertical polarized incident waves:

$$C_{ca} \approx \pi(1.5(c+a) - \sqrt{c \cdot a}) = 3.77 \text{ m}$$

$$C_{cb} \approx \pi(1.5(c+b) - \sqrt{c \cdot b}) = 3.79 \text{ m}$$

Resonant frequency for maximum RCS

$$f_{res} \approx 80 \text{ MHz (vertical polar.)}$$

Comparing FIGURE 3 with FIGURE 17 we notice a certain relationship. If the absorption in a body and if the scattered field far away from the body is highly dependent on the circumference/wavelength ratio, we may assume that the scattered fields near the body are also affected by the same ratio:

- At frequencies below 40 MHz the RACS and the RCS are small. That means that the integral effect of the body on the incident EM-wave is small. However, local field disturbances in the vicinity of the body has to be expected, because the body is not transparent to EM-waves.
- At high frequencies above about 200 MHz the RACS and RCS are high but almost constant. The resonance effects may be neglected, and the three dimensional problem may be reduced to a two-dimensional problem, e.g., the scattering from an infinite cylinder.
- In the resonance region, that is about 40 to 200 MHz, both RACS and RCS are high and depend greatly on the frequency. Numerical field computations on a three dimensional model are urgently needed.

#### 5.2.4. INFLUENCE OF THE HUMAN BODY'S MATERIAL ON THE SCATTERED FIELD

The dielectric properties of biological materials have been discussed in section 4.2.. They depend on material and frequency, but, in general, the human body represents a dense, lossy medium. With respect to the field distribution around the irradiated body we have to look closer to the transmission of EM-energy through the body and the reflection of an EM-wave at the body's surface:

The transmission of EM-energy through the body can be estimated as follows: We assume a vertical, circular cylinder, which is irradiated by a plane, vertical polarized wave with the incident E-field  $\vec{E}_{inc}$  (FIGURE 19):

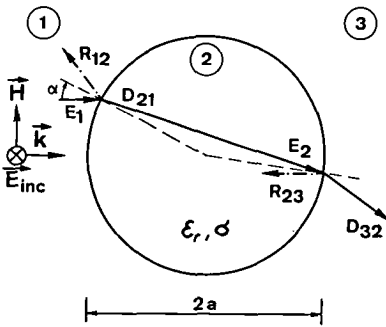


FIGURE 19 Transmission of EM-energy through a circular cylinder.

2a : diameter of the cylinder

1,3: medium air

2 : medium body, lossy material

$E_1$  : incident wave,  $|\vec{E}_{inc}| = 0$  dB

$R_{12}$ : reflected E-field in 1

$D_{21}$ : refracted E-field in 2

$E_2$  : attenuated E-field in 2

$R_{23}$ : reflected E-field in 2

$D_{32}$ : transmitted E-field in 3

The EM wave enters into medium 2 only for small angles  $\alpha$  and is refracted close to the center of the cylinder. The entered wave  $D_{21}$  is attenuated during the travelling through the body and amounts finally to  $E_2$ . The second refraction produced a small transmitted and scattered wave,  $D_{32}$ . Maximum transmission occurs at  $\alpha = 0^\circ$  and at low frequencies. For this case the complex computation of the EM transmission through a plane slab model of 2a thickness was performed by a computer, using the method of TELL [76]:

##### Input data:

Thickness plane slab : 2a = 0.25 m  
 Frequency : f = 75 MHz  
 Material :  $\epsilon_r = 50$  ,  $\sigma = 1.25$  S/m

##### Output data:

Reflection  $R_{12} = -0.8$  dB  
 Attenuated field  $E_2 = -38$  dB  
 Transmitted field  $D_{32} = -52$  dB

Without EM-transmission the Gaing(5.1.2.) in the shadow zone amounts up to -30 dB at extremely small  $d_{at}$ . Because the transmitted wave amounts to -52 dB, is scattered and is even smaller at higher frequencies, the transmitted wave through the human body has no effect on the transmission Loss<sub>B</sub>.

The reflection of the incident EM-wave at the surface of the human body determines the scattered field around the body. The EM-wave reflected at the air-body interface is described by the three reflection coefficients  $\underline{\Gamma}$  (see TABLE 1) and  $\underline{R}_E, \underline{R}_H$  (see also section 5.3.2. and FIGURE 24):

- $\underline{\Gamma}$  : reflection coefficient for the E-vector of an TEM-wave with rectangular incidence on the surface. The complex number  $\underline{\Gamma}$  is derived only from the intrinsic impedances of the interface media (for computation see e.g., TELL [76]). An average value for our frequency range is about 0.7-0.9 /  $\pm 175-177^\circ$  (TABLE 1).
- $\underline{R}_E$  : reflection coefficient for the E-vector of an TE-wave. Here the E-vector is parallel to the surface.  $\underline{R}_E$  is the ratio of  $\underline{E}_{ref}$  to  $\underline{E}_{inc}$  and  $-\underline{H}_{ref}$  to  $\underline{H}_{inc}$ . For a vertical body and a vertical polarized incident TE-wave (FIGURE 19)  $\underline{R}_E$  is about 1 /  $\pm 180^\circ$  (larger than  $\underline{\Gamma}$ ) for all angles  $\alpha > 10^\circ$ . (For reference see FIGURE 24, horizontal reflection at earth,  $\alpha = 90^\circ - \gamma$ ).
- $\underline{R}_H$  : reflection coefficient for the H-vector of an TM-wave. Here the H-vector is parallel to the surface.  $\underline{R}_H$  is the ratio of  $\underline{H}_{ref}$  to  $\underline{H}_{inc}$  and  $-\underline{E}_{ref}$  to  $\underline{E}_{inc}$ . For a vertical body and a horizontal polarized incident TM-wave,  $\underline{R}_H$  is near 1 /  $\pm 0^\circ$  for all angles  $\alpha$  smaller than  $70^\circ$ . Total refraction and signum change occur only at  $\alpha > 80^\circ$  and are of little significance on the integrally scattered fields. The average reflection coefficient for the E-vector is greater than  $\underline{\Gamma}$  and amounts to about 1 /  $\pm 180^\circ$ . (For reference see FIGURE 24, vertical reflection at earth,  $\alpha = 90^\circ - \gamma$ ).

The reflection coefficient  $\underline{\Gamma}$  represents at least for vertical polarization the smallest occurring reflection coefficient. The reflection coefficient for any incident E-vector at the interface air to a perfect conductor is -1. Compared with  $\underline{\Gamma}$  the amplitude of the body-reflected E-vector differs only within - 3 dB. This means that we are allowed to assume the human body as a perfectly conducting body, if we are only interested in the fields outside of the human body.

However, the penetration depth  $\delta$  of the EM-wave in the human body is not zero as in a perfect conductor. The surface charges and the surface currents (see section 6.) which are responsible for the scattered field are distributed in the outer layers but also with decreasing amplitude in deeper regions (TABLE 1). Therefore, the perfectly conducting man-model is only accurate for  $d_{at} > 50$  mm and verification measurements are needed.

### 5.3. GENERAL CONSIDERATIONS ON ANTENNA MEASUREMENTS

#### 5.3.1. ANTENNA MEASUREMENTS IN PROXIMITY TO THE GROUND

For the field measurements the TS has to be rotated together with the body-mounted antenna  $A_1$ , and the antenna-body distance  $d_{at}$  must be varied up to 4 m. Theoretically, antenna measurements with quasi-free-space conditions would be possible with anechoic chambers or elevated platforms. However, at measuring frequencies from 10 to 1000 MHz both methods are not suitable. Below 200 MHz an anechoic chamber has to be huge, and the common absorber pyramid plates has to be matched to the frequency (length of an absorber pyramid approximately  $\lambda/4$ !). An elevated platform is prohibitive due to material and stability problems. Thus, the measurements have to be performed in proximity to the ground, and we have to analyse the influence of the ground on the relative transmitted signal from  $A_1$  to  $A_2$ :

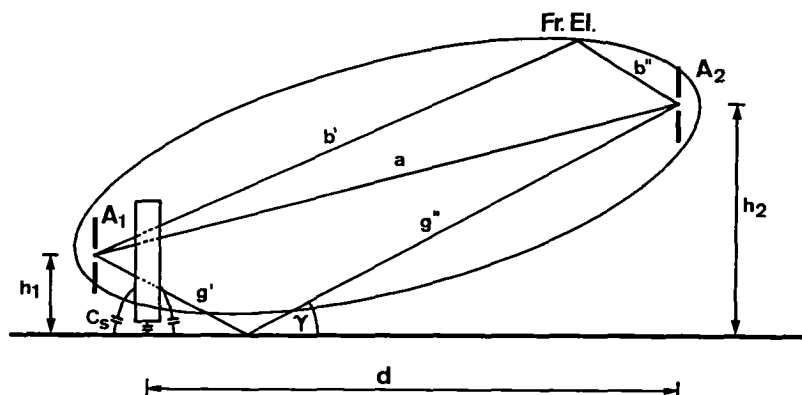


FIGURE 20 Effects in proximity to the ground in antenna measurements.

TS : Test subject                      Fr.El.: Fresnel Ellipsoid  $(b' + b'' - a) = \lambda/2$   
 $A_1$  : Body-mounted antenna     $C_s$  : stray capacitors from TS to ground  
 $A_2$  : Remote antenna               $\gamma$  : reflection angle (glancing angle)

At a small antenna height  $h_1$  (FIGURE 20) disturbing effects occur by:

- Capacitive coupling of the TS to the ground
- Entrance of material into the first Fresnel Ellipsoid

and depending on  $h_1, h_2$  and  $d$  :

- Ground reflections with significant interferences if  $(g' + g'' - a) = n \frac{\lambda}{2}$   
 and if the reflection coefficient of the ground is high.

The capacitive coupling of the TS to the ground depends on the space  $s$  and the material of both the TS and the ground. With great effort the stray capacitors  $C_s$  might be computed, but its effect on the scattered field around the TS would require a further study. Because such a study does not help much in the understanding of the antenna-body problem, it is not necessary to further scrutinize an investigation. In order to reduce the capacitive coupling, a constant space  $s$  of 0.2 m is now defined for the measurements. Verification measurements with varying  $s$  from 0.2 to 1 m will show that the capacitive coupling can be neglected with this restriction.

The first Fresnel Ellipsoid is defined as the geometrical locus for all points which satisfy the condition  $(b' + b'' - a) = \lambda/2$ . (FIGURE 20). If no obstacles interfere with the first Fresnel Ellipsoid, one speaks of optical line-of-sight propagation (BECKER [71]). The lower frequency limit  $f_{lim1}$  for this free propagation can be approximately determined for the data:

$$\begin{aligned} \text{Antenna height } h_1 &: 1.16 \text{ m} \\ \text{Antenna height } h_2 &: 6.2 \text{ m} \\ \text{Distance } d &: 31 \text{ m} \quad (d_{at} = 0) \end{aligned} \quad (42)$$

Assuming the ellipsoid touches the ground with the reflected beam  $g' + g''$  we obtain the path difference  $\Delta s_1$  and the frequency limit  $f_{lim1}$ :

$$\Delta s_1 = g' + g'' - a = \sqrt{(h_2 + h_1)^2 + d^2} - \sqrt{(h_2 - h_1)^2 + d^2} = 0.455 \text{ m} \quad (43)$$

$$f_{lim1} = c / 2\Delta s_1 = 330 \text{ MHz} \quad (44)$$

It has to be clearly stated that accurate absolute antenna measurements are not possible for frequencies below 350 MHz with such a test set-up. However, relative measurements with an accuracy of about 2 dB (experimental experience) are possible, if one looks carefully on the reflection angle  $\gamma$ .

### 5.3.2. REFLECTIONS FROM THE GROUND AND WAVE POLARIZATION

The following considerations are based on the condition that there is an optical line-of-sight propagation as discussed above.

The antenna measurements are performed on a very large lawn. Because the grass is not an ideal reflector, we have to find out the frequency limit  $f_{lim2}$  at which a certain grass thickness  $d_g$  changes from an EM smooth to an EM rough surface (Rayleigh criterion, BECKER [71]):

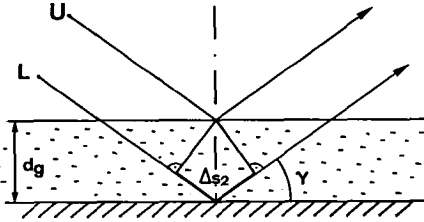


FIGURE 21 Phase difference of two beams, reflected on different heights.

$\lambda$  : reflection angle  
 $d_g$  : thickness of the reflecting layer (grass)  
 $U$  : upper beam  
 $L$  : lower beam  
 $\Delta s_2$  : path difference

In FIGURE 21 an EM-wave is shown which is reflected by the reflection angle  $\gamma$  from a grass surface. The upper beam  $U$  is reflected from the top of the grass layer, the lower beam  $L$  from the actual earth. We assume a reflection coefficient  $R_E$  of +1. The path difference  $\Delta s_2$  depend on  $\gamma$  and  $d_g$ :

$$\Delta s_2 = 2 \cdot d_g \cdot \sin \gamma \quad (45)$$

If the resulting phase difference  $\Delta \psi_2$  is near 0, the surface can be regarded as smooth. If  $\Delta \psi_2$  is larger than  $\pi$ , the surface is rough and represents a random scatterer. With the Rayleigh criterion  $\Delta \psi_2 < \pi/2$  we obtain finally the lower frequency limit  $f_{lim2}$  for a smooth surface:

$$f_{lim2} < \frac{c}{8 \cdot d_g \cdot \sin \gamma} \quad (46)$$

If we assume a thickness  $d_g \leq 0.05$  m and a reflection angle  $\gamma \leq 17^\circ$  we obtain:

$$f_{lim2} < 2500 \text{ MHz} \quad (47)$$

Thus we study the ground reflection at the smooth earth (FIGURE 22):

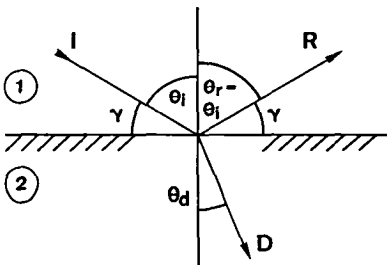


FIGURE 22 Reflection of a wave.

$I, \theta_i$  : incident wave and angle  
 $D, \theta_d$  : refracted wave and angle  
 $R, \theta_r$  : reflected wave and angle  
 $1$  : medium air ( $\epsilon_1, \mu_1, \sigma_1, m_1$ )  
 $2$  : medium earth ( $\epsilon_2, \mu_2, \sigma_2, m_2$ )  
 $m_1, m_2$  : refraction indices  
 $\gamma$  : reflection angle  $90^\circ - \theta_i$

The computation of reflection and refraction of waves at the interface of two media is completely described by e.g., BAGGENSTOS [5] and BECKER [7]. The derivation of the formulas is quite long, but well known so that only the significant final formulas should be indicated here.

The correlation of the refraction index  $m$ , the wave factor  $k$  and the characteristic impedance  $Z_m$  in a medium is given by BECKER [7] :

$$Z_m = \left( \frac{j\omega \mu_0 \mu_r}{j\omega \epsilon_0 \epsilon_r - \sigma} \right)^{1/2} = \frac{\omega \mu_0 \mu_r}{k} = \frac{\mu_r}{m} Z_0 \quad (48)$$

The correlation of the incident angle  $\theta_i$  with the refraction angle  $\theta_d$  and with the reflection angle  $\theta_r$  ( $\gamma = 90^\circ - \theta_r$ ) is:

$$\theta_i = \theta_r, \quad k_1 \sin \theta_i = k_2 \sin \theta_d, \quad m_1 \sin \theta_i = m_2 \sin \theta_d \quad (49)$$

The two different polarizations have to be treated separately (TABLE 23):

THE DIFFERENT REFLECTION OF A VERTICALLY AND A HORIZONTALLY POLARIZED WAVE	
VERTICAL POLARIZATION (TM-WAVE)	HORIZONTAL POLARIZATION (TE-WAVE)
<p>The E-vector is in the plane of incidence. The H-vector is parallel to the interface. Directly computable : reflection coefficient <math>R_H</math> of the H-vector :</p> $R_H = \frac{\mu_1 m_2^2 \cos \theta_i - \mu_2 m_1 \left( m_2^2 - m_1^2 \sin^2 \theta_i \right)^{1/2}}{\mu_1 m_2^2 \cos \theta_i + \mu_2 m_1 \left( m_2^2 - m_1^2 \sin^2 \theta_i \right)^{1/2}}$ <p>For <math>\mu_1 = \mu_2 = \mu_0</math> and <math>\sigma_1 = \sigma_2 = 0</math> :</p> $R_H = \frac{\tan(\theta_i - \theta_d)}{\tan(\theta_i + \theta_d)}$ <p>If <math>\theta_i + \theta_d = \pi/2</math>, the <math>R_H</math> becomes zero and there is no reflected wave. The glancing reflection angle <math>\gamma</math> (<math>\gamma = 90^\circ - \theta_i</math>) for which this extinction occurs is here defined as BREWSTER ANGLE <math>\gamma_B</math></p>	<p>The H-vector is in the plane of incidence. The E-vector is parallel to the interface. Directly computable : reflection coefficient <math>R_E</math> of the E-vector :</p> $R_E = \frac{\mu_2 m_1 \cos \theta_i - \mu_1 m_2 \left( 1 - \left( \frac{m_1}{m_2} \sin \theta_i \right)^2 \right)^{1/2}}{\mu_2 m_1 \cos \theta_i + \mu_1 m_2 \left( 1 - \left( \frac{m_1}{m_2} \sin \theta_i \right)^2 \right)^{1/2}}$ <p>For <math>\mu_1 = \mu_2 = \mu_0</math> and <math>\sigma_1 = \sigma_2 = 0</math> :</p> $R_E = - \frac{\sin(\theta_i - \theta_d)}{\sin(\theta_i + \theta_d)}$ <p><math>R_E</math> varies only a little and does not become zero. There is always a ground reflection.</p>

TABLE 23 Computation of the reflected wave for vertically and horizontally polarized incident waves. (Source: BECKER [7]).

The amounts and phases of the reflection coefficients  $R_H$  and  $R_E$  for a TM- and a TE-wave reflected by a realistic earth surface ( $\epsilon_2=10\epsilon_0, \sigma_2=1\text{mS/m}$ ) is shown in FIGURE 24:

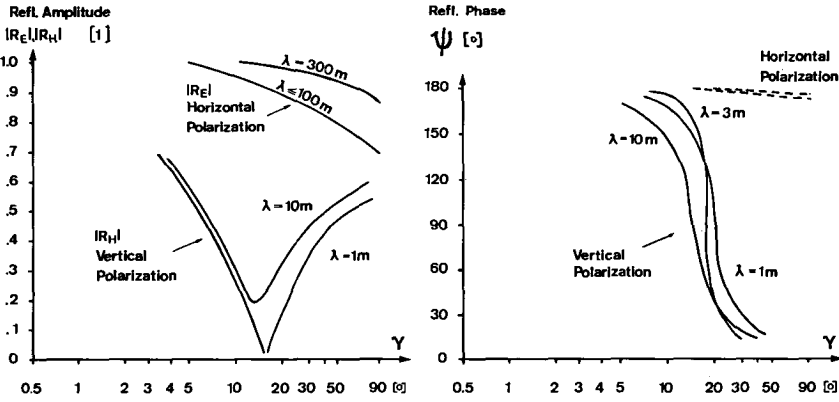


FIGURE 24 Amplitudes  $R_H$  and  $R_E$  (left) and phases  $\psi$  of  $R_H$  and  $R_E$  (right) versus the glancing reflection angle  $\gamma$  for an average earth surface. (Source: BECKER [7]).

If the conductivity is very low, the refraction index  $m_2$  and the Brewster angle  $\gamma_B'$  become for  $\epsilon_r = 10, \mu_r = 0, \sigma_2 = 0$ : ( $\gamma_B' = 90^\circ - \gamma_B$ )

$$m_2 = \sqrt{\epsilon_r} ; \gamma_B' = 90^\circ - \arctan m_2 = 17^\circ \quad (50)$$

which is close to the value depicted in FIGURE 24.

At vertical polarization the influence of the reflected wave is small, if the glancing reflection angle  $\gamma$  is near  $\gamma_B'$ . With the data in FIGURE 24 applied to the antenna configuration in FIGURE 20 we can compute according to BECKER [7] the influence of the reflected wave on the transmission from  $A_2$  to  $A_1$ . The field strength  $E_{\text{oeff}}'$  at  $A_1$  produced by the direct beam (a) from  $A_2$  is (input power  $P_{\text{in}}$ , antenna gain  $G_2$ ):

$$|E_{\text{oeff}}'| = \frac{(30 P_{\text{in}} G_2)^{1/2}}{d} \quad (51)$$

The actual  $E_{\text{oeff}}$  at  $A_1$  produced by the beams (a) and (g'+g'') is:

$$|E_{\text{oeff}}| \approx |E_{\text{oeff}}'| \left( 1 + 2|R_H| \cos(\psi + \frac{4\pi h_1 h_2}{\lambda d}) + |R_H|^2 \right)^{1/2} \quad (52)$$

If we insert the data (42), we obtain a  $\gamma$  of  $13.4^\circ$  and thus an  $|R_H|$  of less than 0.2 (FIGURE 24). At worst case  $\psi$  conditions and for all frequencies



between 30 to 1000 MHz the field strength  $E_{\text{oeff}}$  varies within :

$$0.8 |E_{\text{oeff}}'| < |E_{\text{oeff}}| < 1.2 |E_{\text{oeff}}'| \quad (53)$$

so that  $|E_{\text{oeff}}|$  differs from -2.0 to +1.6 dB. With respect to the transmission loss determination the effect of the ground reflected wave will be smaller, because the reference  $E_0$  will be determined for each measuring frequency, and because the direct and reflected E-vectors are not parallel.

At horizontal polarization the influence of the reflected wave might be important, if we look on FIGURE 24 and equation (52). With  $|R_E| = 1$  we obtain from (52) the interference equation:

$$|E_{\text{oeff}}| \approx |E_{\text{oeff}}'| \left| 2 \sin \left( \frac{2\pi h_1 h_2}{\lambda d} \right) \right| \quad (54)$$

With the data (42) we obtain at 323 MHz a maximum (+6 dB) and at 646 MHz an extinction (< -10 dB). Because  $h_1$  of  $A_1$  is not identical with the height of the antenna-body center, transmission loss measurements are very inaccurate at arbitrary frequencies. Reasonable measurements at horizontal polarizations are only possible at certain selected frequencies and only with large  $h_1$  and  $h_2$ . Because the horizontal polarization is of little significance for omnidirectionally radiating antenna-body systems, measurement at horizontal polarization will not be performed.

### 5.3.3. FIELD HOMOGENEITY ALONG THE BODY AXIS AT VERTICAL POLARIZATION

For the computation a homogeneous, plane wave has been assumed. For the measurements this is not absolutely true as can be seen from FIGURE 25:

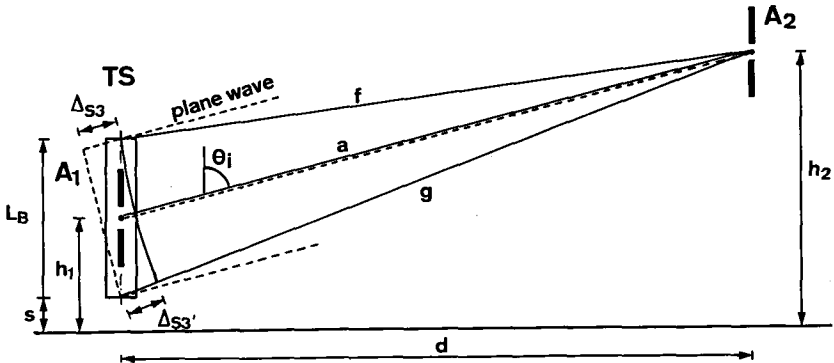


FIGURE 25 Field homogeneity along the body axis of the TS.

For this consideration we assume that  $A_1$  is on the vertical axis of the TS and that the following parameters are given:

$$\begin{aligned}
 p_1, p_2 &: \text{polarization} = \text{vertical} \\
 h_1 &: \text{nominal antenna height} = 1.16 \text{ m} \\
 h_2 &: \text{fixed antenna height} = 6.2 \text{ m} \\
 d &: \text{transmission distance} = 31 \text{ m} \\
 s &: \text{space TS to ground} = 0.2 \text{ m} \\
 L_B &: \text{length of the TS} = 1.8 \text{ m}
 \end{aligned} \tag{55}$$

For the computer computations (section 6.4., FIGURE 33) one assumes a plane wave (dashed lines in FIGURE 25) irradiating the TS with the nominal  $\theta_i$ :

$$\theta_i = \text{nominal incident irradiation angle} = 80.8^\circ \tag{56}$$

The program computes the phase difference among any field point and the origin 0 for the incident plane wave. In this case the path difference  $\Delta_{S3}$  of the plane wave along the axis of the TS amounts to :

$$\Delta_{S3} = L_B \cos \theta_i = 0.2878 \text{ m} \tag{57}$$

In the actual measurements (solid lines in FIGURE 25) the TS is irradiated by a spherical wave with an averaged incident angle  $\theta_i$ . The path difference  $\Delta_{S3}'$  of the spherical wave along the axis of the TS is:

$$\Delta_{S3}' = g - f = (d^2 + (h_2 - s)^2)^{1/2} - (d^2 + (h_2 - L_B - s)^2)^{1/2} = 0.2921 \text{ m} \tag{58}$$

The difference of the plane to the spherical wave is expressed by the difference of the path differences  $\Delta_{S3} - \Delta_{S3}'$ . If we allow a phase difference of  $\max. \pi/2$ , we obtain a maximum permissible frequency limit  $f_{\lim 3}$  for which the spherical wave can be still regarded as a plane wave:

$$f_{\lim 3} \leq \frac{c}{4|\Delta_{S3} - \Delta_{S3}'|} = 17,000 \text{ MHz} \tag{59}$$

In addition we have to fulfill the condition  $d > \lambda$ , i.e.,  $A_1$  has to be outside of the near-field of  $A_2$ . For small antennas we obtain the lower limit

$$f_{\lim 4} \geq \frac{c}{d} = 9.7 \text{ MHz} \tag{60}$$

Neglecting the ground reflections, we may assume a plane wave for both experiment and computation, if the operation frequency  $f$  is between:

$$9.7 \text{ MHz} < f < 17,000 \text{ MHz} \tag{61}$$

The effect of the ground on the field homogeneity ( $E_0(h_1)$ ) along the vertical axis is described in ARRL [3] for some selected cases. Generally, the field strength  $E_0(h_1)$  oscillates around the free space value  $E_0(\infty)$ , with minima and maxima spaced about  $\lambda/2$ . Because the field homogeneity is of fundamental interest for the later experiments, the field homogeneity along the vertical axis of the TS (without TS) has been measured by varying  $h_1$  from  $\lambda/8$  up to  $\lambda$  with the following method :

Electrically small dipole antennas  $A_1$  ( $2h = 0.1$  m) with autonomic RF-oscillators (see section 11.3.) were moved along the vertical axis with a special antenna manipulator (see section 11.2.). The field strength  $E_0(h_1)$  was measured with an LPD antenna  $A_2$  (see section 8.3.3.) and was calibrated to the field strength for  $h_1 = 1.2$  m. The obtained data are presented in TABLE 26:

VERTICALLY POLARIZED FIELD AMPLITUDE VARIATION AT VARIABLE ANTENNA HEIGHTS $h_1$						
FREQUENCY [MHz]	RELATIVE FREE-SPACE FIELD STRENGTH $E_0(h_1)$ IN DECIBELS AT HEIGHT					
	$h_1 = 0.8$ m	$h_1 = 1.0$ m	$h_1 = 1.2$ m	$h_1 = 1.4$ m	$h_1 = 1.6$ m	$h_1 = 1.8$ m
65	+ 0.5	+ 0.0	+ 0.0	- 0.0	- 0.5	- 0.5
74	+ 1.0	+ 0.5	+ 0.0	- 0.5	- 1.0	- 1.0
101	+ 1.5	+ 0.5	+ 0.0	+ 0.0	+ 0.0	+ 0.5
164	- 1.5	- 1.0	+ 0.0	+ 0.5	+ 1.5	+ 2.0

TABLE 26 Homogeneity of the field along the vertical axis of the TS at vertical polarization. Values of  $E_0(h_1)$  related to  $E_0$  at  $h_1 = 1.2$  m. (Measuring data obtained by the standard test set-up,  $h_2 = 6.2$  m,  $d = 31$  m ).

The maximum field strength variation amounts to  $\pm 2$  dB in a full  $\lambda/2$ - $h_1$  range (TABLE 26:  $f = 164$  MHz). If we apply the equations (52,53), there is a good agreement; the changing factor is  $R_H$ , but because  $s < h_1 < s + L_B$ , the reflection angle is  $11.6^\circ < \gamma < 14.8^\circ$  and thus  $|R_H| < 0.2$ . The variations of  $|E_0(h_1)|$  along the vertical axis are the same as given by equation 53 and amount to -2.0 to + 1.6 dB for all frequencies between 30 to 1000 MHz.

As a conclusion from this section 5.3. we may state:

- The test set-up allows antenna measurements with an accuracy of  $\pm 2$  dB in the proximity to ground at vertical polarization  $p_2$  of  $A_2$ .
- The TS must not be coupled with the ground.

## 5.4. ANTENNA-BODY MODELS FOR EXPERIMENT AND COMPUTATION

### 5.4.1. BODY MODELS

An adequate body model should respond to the investigated parameter like the original with a required accuracy but should be so simple that the phenomena can be computed with adequate effort.

The computation of the antenna-body model requires a stepwise increase of the complexity of the body model. In this study we start with a infinite model for two-dimensional computation and we end with a conducting model of human shape for three-dimensional computation.

The experiment with the antenna-body model requires a stepwise decrease of the complexity of the body model. The aim is twofold: at one side the body model should quantify the difference between original and model; on the other hand the model should allow the verification of the computation.

The development of the different body models is depicted in FIGURE 27:

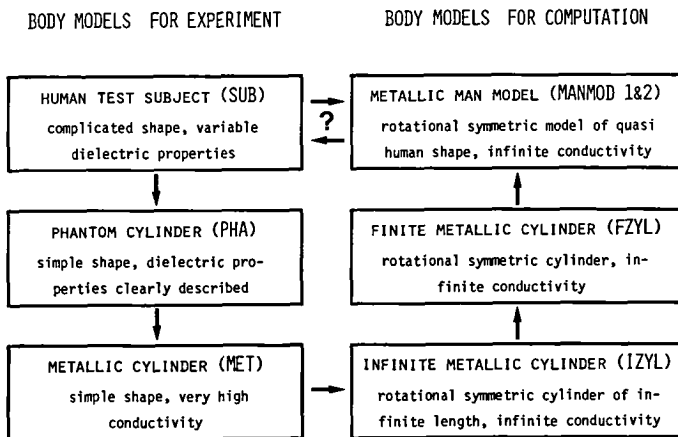


FIGURE 27 Body modelling for experiment and computation.

The different body models are specified as follows:

#### HUMAN TEST SUBJECT (SUB)

The same TS has been used for all experiments (dress without metallic parts)

Body length : 1.68 m

Averaged trunk diameter : 0.25 m

Lateral diameter : 0.3 m

Sagittal diameter : 0.2 m

### PHANTOM CYLINDER (PHA)

A cylindrical vessel has been constructed using a PVC tube filled with a kind of Ringer solution:

Cylinder length	: 1.8 m	Dielectric properties of the Ringer
Cylinder diameter	: 0.25 m	solution at 750 MHz:
Wall thickness	: 6.0 mm	Relative permittivity $\epsilon_r$ : 50
Relative $\epsilon_r$ of the wall:	2.7	Conductivity $\sigma$ : 1.25 S/m

The Ringer solution has been composed according to a prescription by GUY [38] and consisted of:

Glycol Ethandiol	$\text{HOCH}_2\text{-CH}_2\text{OH}$	48.2 liters
Destilled water	$\text{H}_2\text{O}$	35.4 liters
Natrium Chloride	$\text{NaCl}$	1.86 kg

### METALLIC CYLINDER (MET)

A cylindrical vessel without caps has been constructed with copper plates:

Cylinder length	: 1.8 m
Cylinder diameter	: 0.25 m
Wall thickness	: 1.0 mm

### INFINITE METALLIC CYLINDER (IZYL)

For the two-dimensional (off-resonance) computation a rotational symmetric cylinder of infinite length and infinite conductivity has been assumed:

Cylinder length	: infinite
Cylinder diameter	: 0.25 m (nominal value, used as a parameter)

### FINITE METALLIC CYLINDER (FZYL)

For the general three-dimensional computations a rotational symmetric cylinder with hemispherical caps and infinite conductivity has been assumed:

Cylinder length	: 1.8 m
Cylinder diameter	: 0.25 m
Caps diameter	: 0.25 m (other caps used as a parameter)

### METALLIC MAN MODEL (MANMOD 1 & MANMOD 2)

The sagittal and lateral projection of the human test subject (SUB) was used for modelling rotational symmetric, perfectly conducting body models. The shapes can be seen in FIGURE 28 and are described in section 16.2.4.

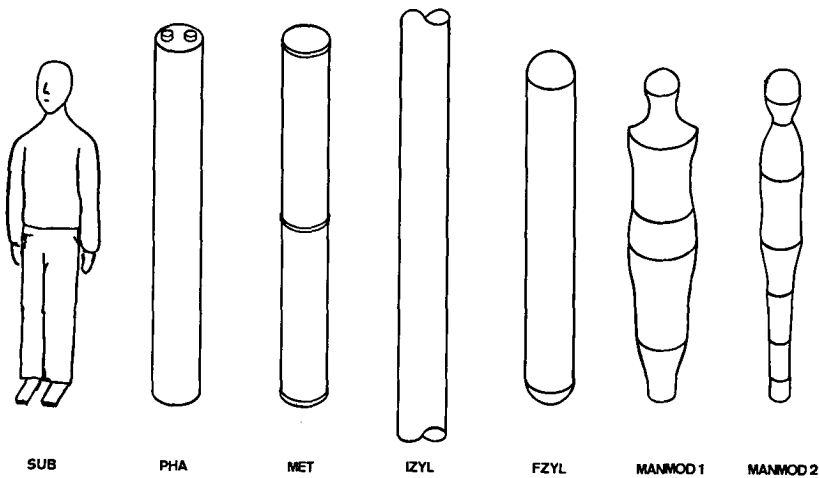


FIGURE 28 Body models used in experiments and computations

#### 5.4.2. ANTENNA-BODY MODELS FOR COMPUTATION

The off-resonance computation for frequencies above 200 MHz can be performed with a two-dimensional antenna-body model, using the body model IZYL. We assume a plane wave with  $\theta_i = 90^\circ$  which is scattered by a vertical cylinder of infinite length. The total field at an arbitrary point outside of the cylinder is the superposition of the incident field and the scattered field. This problem can be analytically solved by Bessel functions.

The general computation has to be performed with a three-dimensional antenna-body model, using the body models FZYL and MANMOD. We assume a plane wave with  $\theta_i = 80.8^\circ$  which is scattered by a rotational symmetric body. The total field at an arbitrary point outside of the cylinder is again the superposition of the incident field and the scattered field. This problem can only be solved by numerical methods, e.g., by the method of moments.

#### 5.4.3. ANTENNA-BODY MODELS FOR EXPERIMENT

The antenna-body model consists of the body models SUB, PHA and MET in a test set-up as shown in FIGURE 11. The parameters  $d$  (nominal 31 m),  $\theta_i$  (nominal  $80.8^\circ$ ) and  $\gamma_B'(12-17^\circ)$  should be kept as constant as possible during varying  $d_{at}$  and  $\phi$ . The antennas have to fulfill the requirements indicated in section 5.1.2..

Leer - Vide - Empty

## 6. FUNDAMENTAL THEORY FOR THE COMPUTATION OF SCATTERING FROM CONDUCTING BODIES

---

### 6.1. PURPOSE OF THE THEORY

The purpose of this theoretical section is to present all needed steps from the Maxwell equations up to the numerical solution concept. The theoretical background is described in BAGGENSTOS [5], VAN BLADEL [81], ANDRE-ASEN [1], KING and WU [50], HARRINGTON and MAUTZ [40] and BEVENSEE [10].

### 6.2. PENETRATION DEPTH OF THE EM FIELD IN CONDUCTING BODIES

Most of the computations of fields near a conducting body are based on the assumption that the body is a perfect conductor and that there is no field inside the body. This assumption should be proven for our application.

If the conducting body and the observer are not in relative motion to each other and if the conducting body is an isotropic and linear medium, the Maxwell equations within the conducting body can be written as:

$$\overrightarrow{\text{curl}} \vec{H} = \sigma_m \vec{E} + \epsilon_m \frac{\partial \vec{E}}{\partial t} \quad (101)$$

$$\overrightarrow{\text{curl}} \vec{E} = -\mu_m \frac{\partial \vec{H}}{\partial t} \quad (102)$$

$$\text{div} \vec{H} = 0 \quad (103)$$

$$\text{div} \vec{E} = \frac{\rho_m}{\epsilon_m} \quad (104)$$

In these equations  $\sigma_m$  is the conductivity of the medium,  $\epsilon_m$  is the dielectric constant  $\epsilon_r$  of the medium multiplied by the permittivity  $\epsilon_0$  of vacuum,  $\mu_m$  is the relative permeability  $\mu_r$  of the medium multiplied by the permeability  $\mu_0$  of vacuum and  $\rho_m$  is the electric charge density in the medium.

If static fields can be excluded, we obtain with (104) inserted in (101) :

$$\text{div} \overrightarrow{\text{curl}} \vec{H} = 0 = \frac{\sigma_m}{\epsilon_m} \rho_m + \frac{\partial \rho_m}{\partial t} \quad \text{and with}$$

$$\rho_m = \rho_{m_0} e^{-t/\tau} \quad \text{we obtain}$$

$$\tau = \frac{\epsilon_m}{\sigma_m} \quad (105)$$

Consider now a time interval  $T$  in which a change of the fields  $E$  and  $H$  should be observed. If this time interval  $T$  (usually a fraction of the



period time of the applied wave) is large in relation to  $\tau$ , that is here

$$\frac{T}{\tau} \gg 1 \quad (106)$$

when the electric charge density  $\rho_m$  in the medium can be assumed to be zero, since it disappears rapidly.

With the restriction (106) the Maxwell equations inside the medium are:

$$\overrightarrow{\text{curl}} \vec{H} = \sigma_m \vec{E} + \epsilon_m \frac{\partial \vec{E}}{\partial t} \quad (101)$$

$$\overrightarrow{\text{curl}} \vec{E} = -\mu_m \frac{\partial \vec{H}}{\partial t} \quad (102)$$

$$\text{div} \vec{H} = 0 \quad (103)$$

$$\text{div} \vec{E} = 0 \quad (107)$$

Using the curl function on (101) and (102) and the identity

$$-\nabla^2 = \overrightarrow{\text{curl}} \overrightarrow{\text{curl}} - \overrightarrow{\text{grad}} \text{div}$$

we obtain in a Cartesian coordinate system (x,y,z) the formula

$$\frac{\partial^2 F}{\partial x^2} + \frac{\partial^2 F}{\partial y^2} + \frac{\partial^2 F}{\partial z^2} + \mu_m \sigma_m \frac{\partial F}{\partial t} + \mu_m \epsilon_m \frac{\partial^2 F}{\partial t^2} = 0 \quad (108)$$

where F stands for  $E_x, E_y, E_z, H_x, H_y, H_z$ . The solution of this differential equation can be found in the case of a homogeneous body material with

$$F = F_0 e^{(-\vec{k}_m \cdot \vec{r} + j\omega t)} \quad \text{where} \quad (109)$$

$$k_m^2 = k_{mx}^2 + k_{my}^2 + k_{mz}^2 = j\omega\mu_m\sigma_m - \epsilon_m\mu_m\omega^2 \quad (110)$$

$$|\vec{k}_m| = \pm \sqrt{\omega\mu_m\sigma_m} \cdot \sqrt{j - \epsilon_m\omega/\sigma_m} \quad (111)$$

With the restriction (106) and with the period time T of the applied wave we obtain the maximum frequency  $f_{\max}$  at which the charge density within a well conducting medium (copper) may be still ignored:

$$\begin{aligned} T &= \frac{2\pi}{\omega} ; \quad \frac{\omega\epsilon_m}{2\pi\sigma_m} \ll 1 \\ \epsilon_m &\sim \epsilon_0 = 8.86 \cdot 10^{-12} \text{ A} \cdot \text{s} \cdot \text{V}^{-1} \cdot \text{m}^{-1} \\ \sigma_m &\sim 10^7 \text{ A} \cdot \text{V}^{-1} \cdot \text{m}^{-1} \\ f_{\max} &\sim 10^{18} \text{ Hz} \gg 1000 \text{ MHz} \end{aligned} \quad (112)$$

The wave factor  $\vec{k}_m$  from (111) becomes at frequencies well below  $f_{\max}$ :

$$\vec{k}_m \sim \pm \sqrt{j f \mu_m \sigma_m} (1 + j) \quad (113)$$

Considering a wave travelling in positive direction  $r$  within an isotropic medium, we may write:

$$-\vec{k}_m \cdot \vec{r} = -k_m \cdot r$$

The attenuated wave is described by (113) inserted in equation (109):

$$F = F_0 e^{-\sqrt{j f \mu_m \sigma_m} \cdot r} \cdot e^{j(\omega t - \sqrt{j f \mu_m \sigma_m} \cdot r)} \quad (114)$$

$F_0$  may be regarded as a component of  $\vec{E}$  or  $\vec{H}$  below the surface of the conducting body. The penetration depth  $\delta$ , defined as the distance which the propagating component will travel before the amplitude is decreased by a factor of  $e^{-1}$ , can be quantified as

$$\delta = \frac{1}{\sqrt{j f \mu_m \sigma_m}} \quad (115)$$

The lowest frequency in our investigation is 10 MHz. With a permeability  $\mu_m = \mu_0$  and with  $\delta$  we are now able to compute the maximum thickness of the field carrying surface layer of a well conducting medium. In a depth of 5 times  $\delta$  the fields are almost zero, and this layer thickness  $5\delta$  is :

$$5\delta = 5 \cdot \delta_{10 \text{ MHz}} \sim 0.2 \text{ mm (copper)} \quad (116)$$

This layer is much smaller than all dimensions of the body (see FIGURE 28) so that the field inside the conducting body models (copper) can be considered to be zero. This means that the computations on a perfectly conducting body will be also representative for an actual metallic body model as used for the experiments.

### 6.3. CHARGE- AND CURRENT-DENSITIES AT THE SURFACE OF A CONDUCTING BODY

#### 6.3.1. BOUNDARY-VALUE PROBLEM

We apply the Maxwell equations (101) and (102) on the fields near the surface of the medium and assume a thin layer  $5\delta$  in which the fields may exist. The deeper regions are field-free as calculated with (114). In the computational model FIGURE 29 we assume that:

- The E- and H- components within the test area  $\Delta A$  are finite
- The E- and H- components within  $\Delta l$  are constant in planes  $||$  surface.

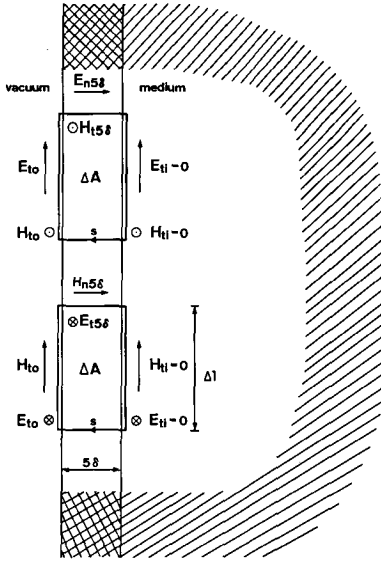


FIGURE 29 Interface between vacuum and a well-conducting medium.

$5\delta$  = thickness field-carrying layer

$\Delta l$  = length of the test area  $\Delta A$

$\Delta A$  = test area  $5\delta \cdot \Delta l$

$s$  = integration path

$E_{to}$  = E-comp. tangential outside

$E_{ti}$  = E-comp. tangential inside

$H_{to}$  = H-comp. tangential outside

$H_{ti}$  = H-comp. tangential inside

$E_{t5\delta}$  = E-comp. tangential in layer

$E_{n5\delta}$  = E-comp. normal in layer

$H_{t5\delta}$  = H-comp. tangential in layer

$H_{n5\delta}$  = H-comp. normal in layer

The integration along  $s$  contains the parts :

$$F_{to} \cdot \Delta l - F_{ti} \cdot \Delta l + \int_0^{5\delta} F_{n5\delta}(s) ds + \int_{5\delta}^0 F_{n5\delta}(s) ds$$

so that only  $F_{to} \cdot \Delta l$  is left. Thus, the integrations of (101) and (102) are:

$$E_{to} = - \frac{\mu_m}{\Delta l} \int_{\Delta A} \frac{\partial \vec{H}}{\partial t} \cdot d\vec{A} ; \vec{H} = H_{t5\delta}(s) \quad (117)$$

$$H_{to} = \frac{1}{\Delta l} \left( \int_{\Delta A} \sigma_m \vec{E} \cdot d\vec{A} + \epsilon_m \int_{\Delta A} \frac{\partial \vec{E}}{\partial t} \cdot d\vec{A} \right) ; \vec{E} = E_{t5\delta}(s) \quad (118)$$

For the integration of the Maxwell equations (103) and (104) we consider a subvolume  $\Delta V$  containing the field carrying layer (FIGURE 30) :

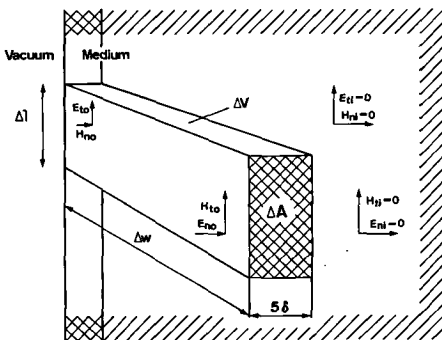


FIGURE 30 Interface between vacuum and medium (see also FIGURE 29 above).

$\Delta w$  = width of the subvolume  $\Delta V$

$\Delta V$  = subvolume  $\Delta A \cdot \Delta w$

$E_{no}$  = E-comp. normal outside

$E_{ni}$  = E-comp. normal inside

$H_{no}$  = H-comp. normal outside

$H_{ni}$  = H-comp. normal inside

- In analogy to the assumptions a) and b) we assume the field conditions:
- c) The E- and H-components within the test subvolume  $\Delta V$  are finite
  - d) The E- and H-components within  $\Delta l \cdot \Delta w$  are constant in planes  $\parallel$  surface.

The integrations of (103) and (104) over the layer thickness  $5\delta$  lead to :

$$H_{no} = 0 \quad (119)$$

$$E_{no} = \frac{1}{\Delta l \cdot \Delta w} \int_{\Delta V} \frac{\rho_m}{\epsilon_m} \cdot dV \quad (120)$$

We assume now that there is an outer wave travelling parallel to the surface. The Poynting vector  $\vec{P}$  is therefore parallel to the surface, and with FIGURE 30 we obtain the only tangential component  $P_t$  :

$$P_t = E_{to} \cdot H_{no} - E_{no} \cdot H_{to} \neq 0$$

Since  $H_{no}$  is zero (119) it remains :

$$P_t = - E_{no} \cdot H_{to} \quad \text{and} \quad E_{no} \neq 0, H_{to} \neq 0 \quad (121)$$

$E_{no} \neq 0$  means that the right side of (120) is not zero. Since we have proven with (105) that there are no charges  $\rho_m$  inside the medium at low frequencies, then charges have to exist on the surface of the medium:

$$E_{no} = \frac{\sigma_{su}}{\epsilon_m} \quad ; \quad \sigma_{su} = \text{surface charge density [C} \cdot \text{m}^{-2}] \quad (122)$$

$H_{to} \neq 0$  means that the right side of (118) is not zero. Thus currents flowing in the outer layer have to exist which can be expressed by:

$$H_{to} = J_t \quad ; \quad \vec{J} = \text{current density vector [A} \cdot \text{m}^{-1}] \quad (123)$$

The direction of  $J_t$  is tangential to the surface and perpendicular to  $H_{to}$ .

Now we consider a wave perpendicular (normal) to the surface. If we neglect the losses in the medium, there is no wave entering the medium and thus the wave will be totally reflected. This means that the Poynting vector has no normal component  $P_n$  (see FIGURE 29) :

$$P_n = E_{to} \cdot H_{to} = 0 \quad (\text{upper and lower case}) \quad (124)$$

Either  $E_{to}$  or  $H_{to}$  could be zero in order to fulfill (124). If  $H_{to}$  would be zero, no wave could exist outside the medium since  $H_{no}$  is already zero as proven by (119). Because the wave cannot vanish outside the medium, the other field component  $E_{to}$  has to be zero, and we obtain:

$$E_{to} = 0 \quad (125)$$

The conclusion of (119,122,123,125) is: at the surface of a good conductor the  $\vec{E}$ -field has only a component normal to the surface, produced by a surface charge density  $\sigma_{su}$ , and the  $\vec{H}$ -field has only a component tangential to the surface, produced by the surface current density  $\vec{J}$  normal to  $\vec{H}$ .

This surface charge density  $\sigma_{su}$  and the current density  $\vec{J}$  are the origins of the scattered fields from a conducting body which is irradiated by a wave.

### 6.3.2. THE EFFECT OF THE SURFACE CURRENT DENSITY $\vec{J}$

In FIGURE 31 a conducting body is depicted with the area element  $dS$ , containing the surface current density  $\vec{J}$  and the surface charge density  $\sigma_{su}$ :

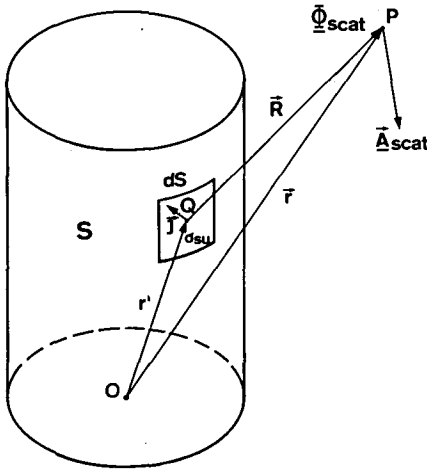


FIGURE 31 Conducting body with  $\vec{J}$  and  $\sigma_{su}$  produced by an incident wave, and scattered parameters.

O = Origin of coordinate system

Q = Source point

P = Observation point

$r'$  = Position of the source point

$r$  = Position of the observ. point

$\Phi^{scat}$  = Scattered electr. potential

$\vec{A}^{scat}$  = Scattered mag. vector pot.

$\vec{J}$  = Surface current density

$\sigma_{su}$  = Surface charge density

$dS$  = Area element on the body

The source is the current density  $\vec{J}$  in the area element  $dS$  positioned at  $Q(\vec{r}')$ . The effect is the scattered magnetic vector potential  $\vec{A}^{scat}$  at the remote observation point  $P(\vec{r})$ . Because the distance between the source and the observation point is comparable with the wavelength  $\lambda$ , a phase difference occurs which has to be treated by the time retardation  $t'$  :

$$R = |\vec{R}| = |\vec{r} - \vec{r}'|$$

$$t' = t - \frac{R}{c} \quad ; \quad t = \text{actual time} \quad (126)$$

$$t' = \text{time retardation}$$

The scattered magnetic vector potential  $\vec{A}^{scat}$  is defined as

$$\vec{A}^{scat}(\vec{r}, t) = \frac{\mu_0}{4\pi} \int_S \vec{J}(\vec{r}', t') \frac{1}{R} dS \quad (127)$$

From (109) and (123) we obtain the complex surface current density  $\vec{J}$  :

$$\vec{J}(\vec{r}', t') = \vec{J}(\vec{r}') e^{j\omega t'} \quad (128)$$

and using the retardation (126) we insert (128) in (127) :

$$\vec{A}^{\text{scat}}(\vec{r}, t) = \frac{\mu_0}{4\pi} \int_S \vec{J}(\vec{r}') e^{j\omega(t-R/c)} \frac{1}{R} dS$$

Introducing the wave factor  $k$  for free space (111)

$$k = 2\pi/\lambda = \omega/c \quad (129)$$

the exponential function becomes

$$e^{j\omega(t-R/c)} = e^{jk(t \cdot c - R)}$$

and if we delete the time dependency we obtain finally :

$$\vec{A}^{\text{scat}}(\vec{r}) = \frac{\mu_0}{4\pi} \int_S \vec{J}(\vec{r}') e^{-jkR} \frac{1}{R} dS \quad (130)$$

### 6.3.3. THE EFFECT OF THE SURFACE CHARGE DENSITY $\sigma_{su}$

The treatment of the effect of the charge density  $\sigma_{su}$  is analogous to 6.3.2..

The source is the charge density  $\sigma_{su}$  in the area element  $dS$  positioned at  $Q(\vec{r}')$ . The effect is the scattered electric (scalar) potential  $\phi^{\text{scat}}$  at  $P(\vec{r})$ .

The scattered electric potential  $\phi^{\text{scat}}$  is defined as

$$\phi^{\text{scat}}(\vec{r}, t) = \frac{1}{4\pi\epsilon_0} \int_S \sigma_{su}(\vec{r}', t') \frac{1}{R} dS \quad (131)$$

and analogous to 6.3.2., we obtain with deleted time dependency :

$$\phi^{\text{scat}}(\vec{r}) = \frac{1}{4\pi\epsilon_0} \int_S \sigma_{su}(\vec{r}') e^{-jkR} \frac{1}{R} dS \quad (132)$$

### 6.3.4. THE FIELD OUTSIDE OF THE CONDUCTING MEDIUM

With the magnetic vector potential  $\vec{A}^{\text{scat}}$  (130) and the electric potential  $\phi^{\text{scat}}$  (132) the field strengths of the scattered  $\vec{E}^{\text{scat}}$  and  $\vec{H}^{\text{scat}}$  are:

$$\vec{H}^{\text{scat}} = \frac{1}{\mu_0} \overrightarrow{\text{curl}} \vec{A}^{\text{scat}} \quad (133)$$

$$\vec{E}^{\text{scat}} = - \frac{\partial \vec{A}^{\text{scat}}}{\partial t} - \overrightarrow{\text{grad}} \phi^{\text{scat}} \quad (134)$$

The total fields outside of the conducting medium are the superpositions of the incident and the scattered fields:

$$\vec{E}^{\text{tot}} = \vec{E}^{\text{inc}} + \vec{E}^{\text{scat}} \quad (135)$$

$$\vec{H}^{\text{tot}} = \vec{H}^{\text{inc}} + \vec{H}^{\text{scat}} \quad (136)$$

The index 'tot' means total outer field, 'inc' stands for the incident field and 'scat' stands for the scattered field.

The combinations of (134)(135) and (133)(136) lead to :

$$\vec{E}^{\text{tot}} = \frac{\partial \vec{A}^{\text{scat}}}{\partial t} - \vec{\text{grad}} \phi^{\text{scat}} + \vec{E}^{\text{inc}} \quad (137)$$

$$\vec{H}^{\text{tot}} = \frac{1}{\mu_0} \vec{\text{curl}} \vec{A}^{\text{scat}} + \vec{H}^{\text{inc}} \quad (138)$$

#### 6.3.5. DETERMINATION OF THE CURRENT DENSITY $\vec{J}$ AND THE CHARGE DENSITY $\sigma_{\text{su}}$

From equations (119) and (123) we know that at the margin of the conductor only the tangential H-components are existing. Since the coordinate system is not yet chosen, we define  $\vec{H}_t$  as a H-vector parallel to the test area  $dS$ .

$$\vec{H}_t^{\text{tot}} = \vec{H}_t^{\text{inc}} + \vec{H}_t^{\text{scat}} \quad (139)$$

$$\mu_0 \vec{H}_t^{\text{tot}} = \mu_0 \vec{H}_t^{\text{inc}} + \mu_0 \vec{H}_t^{\text{scat}}$$

With the equation (123) and the relation:

$$\begin{aligned} \mu_0 \vec{H}_t^{\text{scat}} &= \text{Induction } \vec{B}^{\text{scat}} = \vec{\text{curl}}_t \vec{A}^{\text{scat}} = \vec{J}_t \mu_0 \\ \vec{\text{curl}}_t &= \text{tangential components of } \vec{\text{curl}} \end{aligned} \quad (140)$$

we obtain finally

$$\vec{J} = \frac{\vec{\text{curl}}_t \vec{A}^{\text{scat}}}{\mu_0} + \vec{H}_t^{\text{inc}} \quad (141)$$

Equation (141) is a transcendental differential equation for the two tangential components of  $\vec{J}$ .

Similar as above we obtain the normal component of  $\vec{E}$  at the margin of the conductor with equations (122) and (137) :

$$\vec{\text{grad}}_n, A_n, E_n = \text{normal component of } \vec{\text{grad}}, \vec{A}, \text{ and } \vec{E} \quad (142)$$

$$E_n^{\text{tot}} = - \frac{\partial A_n^{\text{scat}}}{\partial t} - \vec{\text{grad}}_n \phi^{\text{scat}} + E_n^{\text{inc}} \quad (143)$$

By inserting (122) we obtain a transcendental differential equation :

$$\frac{\sigma_{su}}{\epsilon_0} = - \frac{\partial \vec{A}_n^{scat}}{\partial t} - \overrightarrow{\text{grad}}_n \phi^{scat} + \vec{E}_n^{scat} \quad (144)$$

Equation (134) can be rearranged considering (109) :

$$\vec{E}^{scat}(\vec{r}) = - j\omega \vec{A}^{scat}(\vec{r}) - \overrightarrow{\text{grad}} \phi^{scat}(\vec{r}) \quad (145)$$

and with (135) and (125) are

$$\begin{aligned} \vec{E}^{inc} &= \vec{E}^{tot} - \vec{E}^{scat} \\ \vec{E}_t^{inc} &= \vec{E}_t^{tot} - \vec{E}_t^{scat} \quad \text{with } \vec{E}_t^{tot} = 0 \end{aligned} \quad (146)$$

we obtain with  $\vec{A}_t$ ,  $\overrightarrow{\text{grad}}_t$  = tangential components of  $\vec{A}$  and  $\overrightarrow{\text{grad}}$

$$\vec{E}_t^{scat}(\vec{r}) = j\omega \vec{A}_t^{scat}(\vec{r}) + \overrightarrow{\text{grad}}_t \phi^{scat}(\vec{r}) \quad (147)$$

We may apply now (147) on a local coordinate system  $\vec{t} = \hat{t}_1, \hat{t}_2$  on the surface of the conducting body where the sources are located. Thus, we build the scalar product  $\vec{t}$  with  $\vec{E}^{inc}$  as follows :

$$\vec{t} \cdot \vec{E}^{inc}(\vec{r}) = \vec{t} \cdot \left( j\omega \vec{A}^{scat}(\vec{r}) + \overrightarrow{\text{grad}}_t \phi^{scat}(\vec{r}) \right) \quad (148)$$

By inserting (127) and (132) the equation (148) can be shaped in a form of an integral equation which does no more contain  $\vec{A}$  and  $\phi$  :

$$\vec{t} \cdot \vec{E}^{inc}(\vec{r}) = \frac{j\omega\mu_0}{4\pi} \vec{t} \cdot \left( \int_S \vec{J}(\vec{r}') \frac{e^{-jkR}}{R} dS + \frac{1}{j\omega\mu_0\epsilon_0} \overrightarrow{\text{grad}}_t \int_S \sigma_{su}(\vec{r}') \frac{e^{-jkR}}{R} dS \right) \quad (149)$$

The current density vector  $\vec{J}$  and the surface charge density  $\sigma_{su}$  are not independent of each other but are linked by the continuity equation:

$$\frac{\partial}{\partial t} \rho(\vec{r}, t) = - \text{div } \vec{J}(\vec{r}, t) \quad (150)$$

In our case the continuity equation becomes

$$\frac{\partial}{\partial t} \sigma_{su}(\vec{r}, t) = - \text{div}_t \vec{J}(\vec{r}, t) \quad (151)$$

By inserting (109) and (122) in equation (151) we obtain

$$\sigma_{su}(\vec{r}') = - \frac{1}{j\omega} \text{div}_t \vec{J}(\vec{r}') \quad (152)$$



The surface current density  $\underline{\sigma}_{su}$  is now expressed by a function of  $\vec{J}$  for each position  $r'$  of the area element  $dS$ . With the free-space wave factor

$$k^2 = \omega^2 \epsilon_0 \mu_0 \quad (153)$$

we combine (149) with (152). We obtain two equations for the tangential components of the incident E-field as functions of  $\vec{J}$  only :

$$\begin{aligned} \vec{t} \cdot \vec{E}^{inc}(\vec{r}) = \\ \frac{j\omega\mu_0}{4\pi} \vec{t} \cdot \left( \int_S \vec{J}(\vec{r}') \frac{e^{-jkR}}{R} dS + \frac{1}{k^2} \vec{\text{grad}}_t \int_S \frac{e^{-jkR}}{R} \text{div}_t \vec{J}(\vec{r}') dS \right) \end{aligned} \quad (154)$$

=====

The general scattering problem is a very complicated mathematical boundary - value problem which so far has resisted exact analytical treatment except in such special cases as the sphere and the infinite cylinder. For all other cases only numerical methods can be applied.

#### 6.4. SCATTERING FROM BODIES OF REVOLUTION WITH THE METHOD OF MOMENTS

##### 6.4.1. GENERALIZED NETWORK PARAMETERS FOR BODIES OF REVOLUTION

The integral equation (154) can be solved numerically by the method of moments (HARRINGTON [41]). In the years 1968 and 1969 a theory and some computer programs have been developed for the scattering from bodies of revolution by HARRINGTON AND MAUTZ [40]. The following is a summary of this report as it applies to the present problem. The first step is the determination of the generalized network parameters:

The equation (154) can be rewritten in the simpler form:

$$\vec{E}_t^{inc} = L(\vec{J}) \quad (155)$$

where  $L(\vec{J})$  is the integro-differential operator and which corresponds to the right side of equation (154).  $L(\vec{J})$  is also similar to (148) :

$$\begin{aligned} L(\vec{J}) &= [j\omega \vec{A} + \vec{\text{grad}} \phi]_t \\ \vec{A} &= \vec{A}^{scat} \quad (\text{see (130)}) \\ \phi &= \phi^{scat} \quad (\text{see (132)}) \end{aligned} \quad (156)$$

A solution of (155) gives the current  $\vec{J}$  on the surface  $S$ . Usually we are interested in some functional of  $\vec{J}$ , which can be computed once  $\vec{J}$  is known.

In order to effect a solution by the method of moments, let the inner product be defined as : (see definition of  $\langle f, g \rangle$  in HARRINGTON [41])

$$\langle \vec{W}, \vec{J} \rangle = \int_S \vec{W} \cdot \vec{J} \, dS \quad (157)$$

Both  $\vec{W}$  and  $\vec{J}$  are tangential vectors on  $S$ . A set of expansion functions  $\{\vec{J}_j\}$  is next defined, and the current on  $S$  is approximated by

$$\vec{J} = \sum_j I_j \vec{J}_j \quad (158)$$

$I_j$  are constants to be determined. Equation (158) is substituted into (155) which, because of the linearity of  $L$ , reduces to

$$\vec{E}_{tinc} = \sum_j I_j L(\vec{J}_j) \quad (159)$$

A set of testing functions  $\{\vec{W}_i\}$  is defined, and the inner product of (159) with each  $\vec{W}_i$  is taken. The result is

$$\sum_j I_j \langle \vec{W}_i, L\vec{J}_j \rangle = \langle \vec{W}_i, \vec{E}_{inc} \rangle \quad i = 1, 2, 3, \dots \quad (160)$$

The index 't' has been dropped from  $\vec{E}_{inc}$  because the inner product involves only tangential components. We now define the generalized network matrices

$$[Z] = [\langle \vec{W}_i, L(\vec{J}_j) \rangle] \quad (161)$$

$$[V] = [\langle \vec{W}_i, \vec{E}_{inc} \rangle] \quad (162)$$

$$[I] = [I_i] \quad (163)$$

and rewrite the set (160) as

$$[Z] [I] = [V] \quad (164)$$

$[Z]$  is the generalized impedance matrix, and  $[Y] = [Z]^{-1}$  is the generalized admittance matrix. The inverse of (164)

$$[I] = [Y] [V] \quad (165)$$

gives the coefficients  $I_j$  of the current expansion (158) and hence is an approximate solution of the problem.

The impedance elements of (161) are explicitly using (156) and (157) :

$$Z_{ij} = \int_S \vec{W}_i \cdot (j\omega \vec{A}_j + \vec{\text{grad}} \phi_j) \, dS \quad (166)$$

The subscript  $j$  denotes that  $\vec{A}_j$  and  $\phi_j$  are potentials due to  $\vec{J}$  and  $\sigma_{su}$ . In order to match the equations in 6.3. to those used in [40] we replace

$$\begin{aligned}\vec{\text{grad}} \phi &= \vec{\nabla} \phi \\ \text{div } \vec{J} &= \vec{\nabla} \cdot \vec{J}\end{aligned}\quad (167)$$

Regarding  $\vec{W}_i$  as a current density from  $\sigma_{su}$ , we rewrite (152) with (167)

$$\sigma_{su_i} = \frac{-1}{j\omega} \vec{\nabla} \cdot \vec{W}_i \quad (169)$$

Now (166) can be written as

$$Z_{ij} = j\omega \int_S (\vec{W}_i \cdot \vec{A}_j + \sigma_{su_i} \phi_j) \quad (170)$$

Equation (170) is more convenient for computation than (166) or (154).

So far the discussion has been for an arbitrary conducting body. Now we restrict considerations to the surface  $S$  generated by revolving a plane curve about the  $z$ -axis. The surface and the coordinate systems are shown in FIGURE 32:

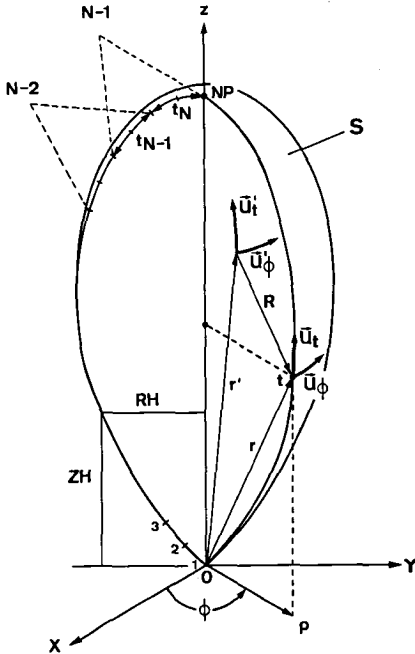


FIGURE 32 Body of revolution and coordinate systems.

$S$  = surface of the body

$NP$  = number of points describing the generating curve

$RH$  = radius parameter of gen.curve

$ZH$  = height parameter of gen.curve

$t_N$  = tangent unit elements,  $N = \frac{NP-1}{2}$

$t$  = length variable along the curve generating  $S$

$\rho$  = radius of a point on  $S$

$\phi$  = angle of a point on  $S$

$z$  = height of a point on  $S$

$\vec{u}_t$  = local tangential coord. syst.

$\vec{u}_\phi$  = local tangential coord. syst. (suffix ' = source point)

$\triangle^{N-1}$  = triangle function (182),  $N-1$  peaks at  $1, 2, \dots, N-1$ .

The body of revolution is described by the generating curve given by the curve parameters RH and ZH. The variable 't' is now a tangential length variable along the curve generating the surface S. We desire the expansion (158) to be general enough to approximate an arbitrary  $\vec{J}$  on S. Hence, independent sets of functions are defined as

$$\vec{J}_{mj}^t = \vec{u}_t f_j(t) e^{jm\phi} \quad (171)$$

$$\vec{J}_{mj}^\phi = \vec{u}_\phi f_j(t) e^{jm\phi} \quad (172)$$

where  $u_t$  and  $u_\phi$  are unit vectors t-directed and  $\phi$ -directed, respectively. The  $f_j(t)$  has been chosen in both sets to be the same, but it is not necessary to do so [40]. The current expansion (158) now becomes

$$\vec{J} = \sum_{m,j} (I_{mj}^t \vec{J}_{mj}^t + I_{mj}^\phi \vec{J}_{mj}^\phi) \quad (173)$$

For testing functions, choose

$$\vec{W}_{ni}^t = \vec{u}_t f_i(t) e^{-jn\phi} \quad (174)$$

$$\vec{W}_{ni}^\phi = \vec{u}_\phi f_i(t) e^{-jn\phi} \quad (175)$$

which differ from (171,172) only in the sign of the exponent. The  $\vec{W}_n$  are orthogonal to  $\vec{J}_m$ ,  $m \neq n$ , over 0 to  $2\pi$  on  $\phi$ , and also to  $L(\vec{J}_m)$  (the field from  $\vec{J}_m$ ). Hence, all impedance elements are zero except those for which  $m = n$ , and each mode  $n$  can be treated separately. This is the major simplification introduced by the rotational symmetry of the body. For the computation of non-rotational symmetric bodies, such as shown in FIGURE 18, the further procedure had to be already changed here.

The use of (171)(172)(174) and (175) to evaluate the elements of (170) results in the partitioned matrix equation

$$\begin{bmatrix} [Z_n^{tt}] & [Z_n^{t\phi}] \\ [Z_n^{\phi t}] & [Z_n^{\phi\phi}] \end{bmatrix} \begin{bmatrix} [I_n^t] \\ [I_n^\phi] \end{bmatrix} = \begin{bmatrix} [V_n^t] \\ [V_n^\phi] \end{bmatrix} \quad (176)$$

Here the elements of the Z submatrices are

$$(Z_n^{tt})_{ij} = \langle \vec{W}_{ni}^t, L(\vec{J}_{nj}^t) \rangle, \text{ etc. for } t\phi, \phi t \text{ and } \phi\phi \quad (178)$$

The elements of the I submatrices are the coefficients in (173), and the elements of the V submatrices are

$$\begin{aligned}(V_n^t)_i &= \langle \vec{W}_{ni}^t, \vec{E}_{inc} \rangle \\ (V_n^\phi)_i &= \langle \vec{W}_{ni}^\phi, \vec{E}_{inc} \rangle\end{aligned}\quad (179)$$

Note that, for N terms in the Fourier series of  $\phi$ , there are N sets of matrix equations (176).

The solution to (176) can be also written in partitioned form as

$$\begin{bmatrix} [I_n^t] \\ [I_n^\phi] \end{bmatrix} = \begin{bmatrix} [Y_n^{tt}] & [Y_n^{t\phi}] \\ [Y_n^{\phi t}] & [Y_n^{\phi\phi}] \end{bmatrix} \begin{bmatrix} [V_n^t] \\ [V_n^\phi] \end{bmatrix}\quad (180)$$

The Y submatrices must in general be obtained after inversion of the entire Z matrix and are not the inverse of the corresponding Z submatrices. However, as shown in [40], the -n mode matrices are related to the +n mode matrices, so that only the  $n \geq 0$  mode matrices need to be inverted.

Finally, for an explicit solution one has to choose the t expansion functions  $f_i(t)$ . A triangle expansion function gives a piecewise-linear approximation which converges rapidly:

$$f_i(t) = \frac{1}{\rho} T(t - t_i) \quad (181)$$

$$T(t) = 1 - |t| \quad \text{for } |t| < 1 \quad \text{and } 0 \quad \text{for } |t| > 1 \quad (182)$$

When using these functions, distance and frequency are scaled so that the  $t_i$ 's are one unit apart. The generating curve is determined by NP body points (FIGURE 32). There are  $(NP-1)/2 = N$  tangential units, and if one triangle function covers 2 units, there are N-1 peaks at 1,2,3...N-1.

#### 6.4.2. IMPEDANCE MATRICES

##### 6.4.2.1. EVALUATION OF THE IMPEDANCES

The generalized impedances for a body of arbitrary shape is the integral over all source points ( $dS'$ ) and the integral over all field points ( $dS$ ) :

$$Z_{ij} = \int_S dS' \int_S dS \left[ j\omega\mu_0 \vec{W}_i \cdot \vec{J}_j + \frac{1}{j\omega\epsilon_0} (\vec{\nabla}' \cdot \vec{W}_i) (\vec{\nabla} \cdot \vec{J}_j) \right] \frac{e^{-jkR}}{4\pi R} \quad (183)$$

For bodies of revolution the integrals have the t-elements 0 to N and the  $\phi$ -

elements 0 to 2 $\pi$ . The radius R (see FIGURE 32) can be expressed by  $\vec{r} - \vec{r}'$ :

$$R = \left[ \rho^2 + \rho'^2 - 2\rho\rho' \cos(\phi - \phi') + (z - z')^2 \right]^{1/2} \quad (184)$$

The inner products in (183) are of the type

$$\vec{\nabla} \cdot \vec{J} = \frac{1}{\rho} \frac{\partial}{\partial t} (\rho J_t) + \frac{1}{\rho} \frac{\partial}{\partial \phi} (J_\phi) \quad (185)$$

Four types of impedances are defined by (178). To evaluate them, we use (171)(172) and (174)(175) to obtain the  $\vec{W} \cdot \vec{J}$  terms in (183) as

$$\vec{W}_{ni}^p \cdot \vec{J}_{nj}^q = e^{jn(\phi - \phi')} f_i(t') f_j(t) \vec{u}_p' \cdot \vec{u}_q \quad (186)$$

where p and q represent permutations of t and  $\phi$ . The unit vector inner products in terms of the body coordinates defined by FIGURE 32 are

$$\begin{aligned} \vec{u}_t' \cdot \vec{u}_t &= \sin v \sin v' \cos(\phi - \phi') + \cos v \cos v' \\ \vec{u}_t' \cdot \vec{u}_\phi &= -\sin v' \sin(\phi - \phi') \\ \vec{u}_\phi' \cdot \vec{u}_t &= \sin v \sin(\phi - \phi') \\ \vec{u}_\phi' \cdot \vec{u}_\phi &= \cos(\phi - \phi') \end{aligned} \quad (187)$$

Here v is the angle between the t direction and the z axis, being positive if  $\vec{u}_t$  points away from the z-axis. Changing  $(\phi - \phi')$  to a new variable, and expressing the sine and cosine terms of (187) as exponentials, one  $\phi$  integration of (183) can be performed. The remaining  $\phi$  integration defines the Green's function :

$$g_n = \int_0^{2\pi} d\phi \frac{e^{-jkR_0}}{R_0} \cos n\phi \quad (188)$$

where  $R_0$  is given by (184) with  $\phi' = 0$ . With  $f_i$  given by (181), the resultant expression for the impedance elements (178) are (only  $(Z_n^{tt})_{ij}$  shown):

$$\begin{aligned} (Z_n^{tt})_{ij} &= \int_0^N dt' \int_0^N dt \left[ j\omega\mu_0 T(t'-i) T(t-j) (\sin v \sin v' \frac{g_{n+1} + g_{n-1}}{2} \right. \\ &\quad \left. + \cos v \cos v' g_n) + \frac{1}{j\omega\epsilon_0} T'(t'-i) T'(t-j) g_n \right] \end{aligned} \quad (189)$$

Here  $T'$  is the derivative of the triangle function

$$\begin{aligned} T'(t) &= 1, \quad -1 < t < 0 \\ &= -1, \quad 0 < t < 1 \\ &= 0, \quad |t| > 1 \end{aligned} \quad (190)$$

The integrations of (189) involve many different integrands, and to reduce the number of integrations the following approximations are made. For the  $t$ -integration, the  $T$  function is approximated by four pulses of amplitude  $1/4, 3/4, 3/4, 1/4$ , and the derivative of  $T$  (denoted here as  $T'$ ) is represented exactly by four pulses of amplitude  $1, 1, -1, -1$ . The functions  $\rho$ ,  $\sin v$ , and  $\cos v$  are assumed constant over each pulse, equal to their values at the midpoints of the pulses. For the  $t'$  integration, the  $T$  function is approximated by four impulse functions of strengths  $1/8, 3/8, 3/8, 1/8$ , and the derivative of  $T$  is approximated by four impulse functions of strengths  $1/2, 1/2, -1/2, -1/2$  ( $T_1, T_2, T_3, T_4$  and  $T'_1, T'_2, T'_3, T'_4$ ).

The midpoints of the pulses and the pulse Green's functions are defined :

$$t_p = i + \frac{p-2.5}{2} ; \quad t_q = j + \frac{q-2.5}{2} \quad (191)$$

$$G_n = 2 \int_{j+\frac{q-3}{2}}^{j+\frac{q-2}{2}} dt \int_0^\pi d\phi \frac{e^{-jkR_p}}{R_p} \cos n\phi \quad (192)$$

$$R_p = \left[ \rho^2 + \rho_p^2 - 2\rho\rho_p \cos \phi + (z - z_p)^2 \right]^{1/2} \quad (193)$$

In terms of these definitions and approximations, the matrix elements of (189) reduce to:

$$(Z_n^{tt})_{ij} = \sum_{p=1}^4 \sum_{q=1}^4 \left[ j\omega\mu_0 T_p T_q (\sin v_p \sin v_q \frac{G_{n+1} + G_{n-1}}{2} + \cos v_p \cos v_q G_n) + \frac{1}{j\omega\epsilon_0} T'_p T'_q G_n \right] \quad (194)$$

$$(Z_n^{t\phi})_{ij} = \sum_{p=1}^4 \sum_{q=1}^4 \left[ -\omega\mu_0 T_p T_q \sin v_p \frac{G_{n+1} - G_{n-1}}{2} + \frac{n}{\omega\epsilon_0} T'_p \frac{T_q}{\rho_q} G_n \right]$$

$$(Z_n^{\phi t})_{ij} = \sum_{p=1}^4 \sum_{q=1}^4 \left[ +\omega\mu_0 T_p T_q \sin v_q \frac{G_{n+1} - G_{n-1}}{2} - \frac{n}{\omega\epsilon_0} \frac{T_p}{\rho_p} T'_q G_n \right]$$

$$(Z_n^{\phi\phi})_{ij} = \sum_{p=1}^4 \sum_{q=1}^4 \left[ j\omega\mu_0 T_p T_q \frac{G_{n+1} - G_{n-1}}{2} + \frac{n^2}{j\omega\epsilon_0} \frac{T_p}{\rho_p} \frac{T_q}{\rho_q} G_n \right]$$

Here  $\rho_p, v_p, \rho_q, v_q$  are the  $\rho$  and  $v$  evaluated at  $t_p$  and  $t_q$  respectively.

Finally, the  $G_n$  (192) was prepared for the numerical computation by dividing the integration interval 0 to  $\pi$  into  $M$  equal intervals. In the actual computer program the  $G_n$ 's were further divided by  $k$  in order to make

them insensitive to the absolute size of the body. In addition, the  $T_p$  and the  $T'_p$  were modified, as can be seen in the description of the computer program A by HARRINGTON and MAUTZ [40].

#### 6.4.2.2. LIMITATIONS OF THE NUMERICAL COMPUTATIONS OF THE IMPEDANCES

The computer program HARRA is based on the above theory. It will be discussed later in section 10.2.. The purpose of the program HARRA is to compute the four Z-matrices (194) and its inverse four Y-admittance matrices (164). The Y-matrices for each mode  $n$  from 0 to  $n_{nn}$  (192) are stored in a file for the later use by following programs computing the scattering.

Because the solution for the Y-matrices are obtained by matrix inversions, the matrix size has to be limited to a reasonable value in order to save computation time and storage capacity. The body shape will be approximated by 20 tangents ( $N=20$ ), thus one obtains 4 matrices of the size  $19 \times 19$  for each mode. The integral intervals of the  $G_n$ 's of 0 to  $\pi$  will be divided into 20 subintervals ( $M=20$ ).

With these specifications accurate Y-matrices up to the mode  $n=6$  can be obtained for a conducting model of man up to frequencies of 400 MHz. The proof for these statements will be presented in the program description in section 10.3.1.

#### 6.4.3. MEASUREMENT MATRICES

Any linear measurement of the field from the current  $\vec{J}$  on the body  $S$  can be expressed as a linear functional of  $\vec{J}$ , that is

$$\text{measurement} = \int_S \vec{E}^r \cdot \vec{J} \, dS \quad (195)$$

where  $\vec{E}^r$  is a known function. For a moment solution, the current is given by a superposition  $J = \sum I_j \vec{J}_j$ , and (195) reduces to

$$\text{measurement} = [R] [I] \quad (196)$$

where  $[I]$  is the matrix (163) and  $[R]$  is a measurement row matrix:

$$[R] = [ < \vec{J}_j, \vec{E}^r > ] \quad (197)$$

$[R]$  is similar to the excitation matrix  $[V]$  (162), and with the matrix solution (165) substituted in (196), one has

$$\text{measurement} = [R] [Y] [V] \quad (198)$$



For bodies of revolution, the expansion for  $\vec{J}$  can be separated into  $t$  and  $\phi$  directed components, according to (173). It is then convenient to partition  $[R]$  into  $t$  and  $\phi$  component terms as

$$\begin{aligned}(R_n^t)_i &= \langle \vec{J}_{ni}^t, \vec{E}^r \rangle \\ (R_n^\phi)_i &= \langle \vec{J}_{ni}^\phi, \vec{E}^r \rangle\end{aligned}\quad (199)$$

The analogous partition for excitation  $[V]$  is given by (179). Now one can rewrite (198) in the partitioned form as

$$\text{measurement} = \begin{bmatrix} [R_n^t] & [R_n^\phi] \end{bmatrix} \begin{bmatrix} [Y_n^{tt}] & [Y_n^{t\phi}] \\ [Y_n^{\phi t}] & [Y_n^{\phi\phi}] \end{bmatrix} \begin{bmatrix} [V_n^t] \\ [V_n^\phi] \end{bmatrix} \quad (200)$$

where the  $Y$  submatrices are obtained after the  $Z$  matrix is inverted and are not the inverses of the corresponding  $Z$  submatrices.

An important special case is that of radiation field measurements. HARRINGTON [41] has shown that the radiation field from currents  $\vec{J}$  on  $S$  is given by (201) :

$$\vec{E} \cdot \vec{u} = \frac{-j\omega\mu_0}{4\pi r} e^{-jkr} [R] [I] \quad (201)$$

where the elements of  $[R]$  are given by (197) with

$$\vec{E}^r = \vec{u} e^{-j\vec{k} \cdot \vec{r}} \quad (202)$$

This is a unit plane wave with polarization vector  $\vec{u}$  and propagation vector  $\vec{k}$ . An arbitrary plane wave is a superposition of two orthogonal components :

$$\vec{E}_\theta = \text{'vertical' polarization (see 5.3.2.)} \quad (203)$$

$$\vec{E}_\phi = \text{'horizontal' polarization (see 5.3.2.)} \quad (204)$$

Hence, one can treat the general case as two applications of (202), one for  $\vec{u} = \vec{u}_\theta$  and the other for  $\vec{u} = \vec{u}_\phi$ . To distinguish between the two cases let us denote the measurement matrices as follows: (205), (206)

$\theta$ -polarized case

$$(R_n^{t\theta})_i = \langle \vec{J}_{ni}^t, \vec{E}_\theta^r \rangle$$

$$(R_n^{\phi\theta})_i = \langle \vec{J}_{ni}^\phi, \vec{E}_\theta^r \rangle$$

$\phi$ -polarized case

$$(R_n^{t\phi})_i = \langle \vec{J}_{ni}^t, \vec{E}_\phi^r \rangle \quad \theta: (205)$$

$$(R_n^{\phi\phi})_i = \langle \vec{J}_{ni}^\phi, \vec{E}_\phi^r \rangle \quad \phi: (206)$$

The excitation matrices can now be evaluated as follows. Let

$$\vec{E}_\theta^r = \vec{u}_\theta^r e^{jk(\rho \sin \theta_r \cos \phi + z \cos \theta_r)} \quad (207)$$

where  $\theta_r$  and  $\phi_r = 0$  are the angles to the field point of measurement. The inner products required in (205) are given by

$$\begin{aligned} \vec{u}_t \cdot \vec{u}_\theta^r &= \cos \theta_r \sin v \cos \phi - \sin \theta_r \cos v \\ \vec{u}_\phi \cdot \vec{u}_\theta^r &= -\cos \theta_r \sin \phi \end{aligned} \quad (208)$$

Using the integral formula for Bessel functions

$$J_n(\rho) = \frac{j^n}{2\pi} \int_0^{2\pi} e^{-j\rho \cos \phi} e^{-jn\phi} d\phi \quad (209)$$

one can evaluate the  $\phi$  integrations in (205), obtaining

$$(R_n^{t\theta})_i = 2\pi j^{n+1} \int_0^N dt \rho f_i(t) e^{jkz \cos \theta_r} [\cos \theta_r \sin v \frac{J_{n+1} - J_{n-1}}{2} + j \sin \theta_r \cos v J_n] \quad (210)$$

$$(R_n^{\phi\theta})_i = -2\pi j^{n+1} \int_0^N dt \rho f_i(t) e^{jkz \cos \theta_r} \cos \theta_r \frac{J_{n+1} + J_{n-1}}{2j}$$

and one can similarly evaluate the  $\phi$  integration for the  $\phi$  case :

$$(R_n^{t\phi})_i = 2\pi j^{n+1} \int_0^N dt \rho f_i(t) e^{jkz \cos \theta_r} \sin v \frac{J_{n+1} + J_{n-1}}{2j} \quad (211)$$

$$(R_n^{\phi\phi})_i = 2\pi j^{n+1} \int_0^N dt \rho f_i(t) e^{jkz \cos \theta_r} \frac{J_{n+1} - J_{n-1}}{2}$$

where  $J_n$  is

$$J_n = J_n(k\rho \sin \theta_r) \quad (212)$$

For computations, the  $\rho f_i(t)$  in (210) and (212) were the triangle functions (182). For plane-wave excitation of the body the excitation matrix  $[V]$  is

$$(V_n^{pq})_i = (R_{-n}^{pq})_i \quad (213)$$

where  $pq$  represents  $t\theta$ ,  $\phi\theta$ ,  $t\phi$ , or  $\phi\phi$ . Equation (213) means that the  $V_i$  are given by (210) and (211) with  $n$  replaced by  $-n$  and  $\theta_r$  by  $\theta_t$ .



The method of solution (BEVENSEE [10]) is an extension of the method by HARRINGTON and MAUTZ [40] discussed above in sections 6.4.1. to 6.4.3.. The formulas (155) up to (163) can be summarized as follows:

The operation equation

$$\vec{E}_t^{inc} = L(\vec{J}) , \quad L(\vec{J}) = (j\omega\vec{A} + \vec{\nabla}\phi)_t \quad (214)$$

is solved by expanding

$$\vec{J} = \sum_j I_j \vec{J}_j \quad (215)$$

for the  $n^{th}$  azimuthally varying mode by a set of functions :  $\vec{J}_j = \vec{u} f_j e^{jn\phi}$  ( $\vec{u}$  = unit vector in the  $t$ - or  $\phi$ -direction on the surface of the body) and by a set of functionals  $\vec{W}_j = \vec{u} f_j e^{-jn\phi}$  in succession :

$$\langle \vec{W}_i, \vec{E}_t^{inc} \rangle = \sum_j \langle \vec{W}_i, L(\vec{J}_j) \rangle I_j , \quad i = 1, 2, \dots, N \quad (216)$$

The  $\langle \rangle$  denotes a spatial integral over the localized range of the  $W_i$ -function. Defining  $Z_{ij}$  as  $\langle \vec{W}_i, L(\vec{J}_j) \rangle$  one obtains the network representation of (214) as :

$$V_i = \sum_j Z_{ij} I_j , \quad V_i = \langle \vec{W}_i, \vec{E}_t^{inc} \rangle \quad (217)$$

Analogously, a test segment, subscript T , is inserted to measure the scattered field  $\vec{E}^{scat} = L(\vec{J})$  as (BEVENSEE [10])

$$\langle \vec{W}_T, \vec{E}^{scat} \rangle = \langle \vec{W}_T, -L(\vec{J}) \rangle = -\sum_j \langle \vec{W}_T, L(\vec{J}_j) \rangle I_j \quad (218)$$

Defining the measurement matrix  $[ZM]$  as  $(ZM)_{1j} = -\langle \vec{W}_T, L(\vec{J}_j) \rangle$  , where the index '1' means test segment 1 and 'j' the source element (166), one has

$$\langle \vec{W}_T, \vec{E}^{scat} \rangle = \sum_j (ZM)_{1j} I_j \quad (219)$$

and the electric field in the T-direction along the test segment is approximately

$$\vec{E}_T^{scat} = \frac{1}{\langle \vec{W}_T \rangle} \sum_j (ZM)_{1j} I_j \quad (220)$$

As the area  $\langle \vec{W}_T \rangle$  of the test segment approaches zero,  $\vec{E}_T^{scat}$  approaches the correct scattered field value.

The computation of the fields at a point near the conducting body (see FIGURE 33) involves the following steps:

First, the [Z] matrices (194) and its inverse [Y] matrices have to be computed for all needed modes. This computation is only dependent on the dimensions of the body and the applied frequency but not on the irradiation angle  $\theta_i$  or the polarization.

Second, the [R] matrices (210) and (211) have to be computed for a specific incident wave in order to obtain the excitation matrices [V] and the coefficient [I] of the current expansion (164).

Third, at a given test point a test segment is defined by five points and four sections of equal length DTEST (FIGURE 33). This test segment is first positioned along the spherical radius vector  $\vec{a}_r$  (for IT = 1, as shown in FIGURE 33) to measure the  $\vec{a}_r$ - and  $\vec{a}_\phi$ -components of the  $\vec{E}$  field. It is then positioned along the spherical  $\vec{a}_\theta$ -vector (for IT = 2) to measure the  $\vec{a}_\theta$ - and  $\vec{a}_\phi$ -components of the  $\vec{E}$  field. The two measured  $E_\phi$  fields approach each other as the test segment length 4DTEST approaches zero; their discrepancy gives an estimate of the accuracy obtained with this segment.

The total E-field  $\vec{E}^{\text{tot}}$  along an  $\vec{a}$ -vector is the superposition of  $\vec{E}^{\text{inc}}$  and  $\vec{E}^{\text{scat}}$  (see (135)). The  $\vec{E}^{\text{inc}}$ -components are obtained by using the subroutine PLANE (which computes the [R] and [V] matrices, see (213)) applied a second time on the test segment. The  $\vec{E}^{\text{scat}}$ -components are computed with a new subroutine NEARZ which is well described by BEVENSEE [10]

The matrix elements of [ZM] (220) are determined similar to the elements of [Z] (194) but with an altered Green's function  $G_{nT}$ . If we denote a surface element on the body as  $2 y_0 \cdot x_0$  ( $2 y_0 = 2$  tangent units as in FIGURE 32,  $x_0 =$  circumference unit  $\rho_q \pi / M$ ,  $M =$  number of  $\pi$  intervals), the  $G_{nT}$  for the test segment may be written in the form

$$G_{nT}^{(1)} = \frac{1}{2 \rho_q y_0} \int_{-y_0}^{+y_0} dy \int_0^{x_0} dx \frac{1 + jk[x^2 + (y - y_a)^2 + \Delta_a^2]^{1/2}}{[x^2 + (y - y_a)^2 + \Delta_a^2]^{3/2}} \quad (221)$$

where  $dx = \rho_q d\phi$ ,  $x, y =$  center of a local coordinate system at the center of the  $j^{\text{th}}$  source element,  $y_a =$  tangential distance from the test section and  $\Delta_a =$  projection distance from the test section (see FIGURE 34). Equation (221) can be evaluated as follows:



unless  $\Delta_a/\lambda > 1$  and also  $4 \text{ DTEST}/\lambda < 1/4$ , where 4 DTEST is the full length of the test segment in FIGURE 33.

The remainder of NEARZ is essentially the same as in program A and HARRA (6.4.2.2.) except that the measurement matrix [ZM] is computed for the test segment instead of the impedance matrix [Z] of the body.

The output of the source program HARRDF (BEVENSEE [10]) consists of the field components  $E^{\text{inc}}, E^{\text{scat}}, E^{\text{tot}}$  in the directions of  $\vec{a}_\theta, \vec{a}_r$  and  $(2x) \vec{a}_\phi$  for  $\phi = 0^\circ$ , a selected incident angle  $\theta_i$  and the selected mode  $n$ .

The extended program PANB computes these quantities for all needed modes  $n$  and for  $\phi = 0, 5, 10, \dots, 180^\circ$ . The contribution of each mode is summed separately, and one obtains the complete  $E^{\text{tot}}$  in  $\vec{a}_\theta, \vec{a}_r$  and  $\vec{a}_\phi$  (mean value) directions. After coordination transformation the  $E^{\text{tot}}(\phi)$  are available in vertical, horizontal and radial directions. The amounts of  $E^{\text{tot}}(\phi)$  related to  $|E|$  of the incident plane wave deliver the chosen transmission Loss<sub>B</sub> for the three polarization axes  $p_i$  of the antenna  $A_i$  in FIGURE 11.

#### 6.4.5.2. LIMITATIONS OF THE NEAR-FIELD COMPUTATIONS

The basic limitations are already given by the computation of the [Z] matrices with program HARRA (see discussion in section 6.4.2.2.)

A further problem is to select the "best" segment length. If the segment is short, one would measure fluctuating components of the tangential fields, since the boundary condition of  $E_t = 0$  (125) is only satisfied in an integral sense with respect to the triangle functions. If the segment is long, one obtains an averaged value of the surrounding fields of the test point. Near field computations of a point field with a test segment tend to be inaccurate unless both these conditions are fulfilled:

- a.) Minimum distance of the test segment center to the body surface  $> \lambda$ .
- b.) Test segment length  $< \lambda/4$ .

The accuracy of the obtained results will be discussed in section 10.3.. In general, the field components can be computed with less than 2 dB error for a human-sized conducting model, if the frequency is below 500 MHz and if the distance of the test segment (antenna-body distance  $d_{at}$ ) from the surface is larger than 0.1 m. It is required to investigate the influence of each additional mode  $n$  and to perform two computations with different test segment lengths, in our case 0.08 and 0.2 m, to check fluctuations.

## 6.5. SCATTERING FROM LONG CIRCULAR CYLINDERS: AN ANALYTICAL APPROACH

### 6.5.1. PURPOSE OF THE ANALYTICAL APPROACH

The numerical computation of a finite body of revolution according to section 6.4. is primarily limited by computation time and storage capacity of the computer. Tremendous efforts are needed if the frequency is above 400 MHz and if the antenna-body distance is smaller than 0.1 m.

On the other hand, as shown in section 5.2.3., the human body is large compared with the wavelength at frequencies above 200 MHz if we consider the radar cross section as a measure for quasi-off-resonance behavior.

If we neglect the resonance phenomena and are looking only on the total field at vertical polarization at frequencies above 200 MHz, the three-dimensional problem can be converted in a more simple two-dimensional problem. Thus, the adequate model is an infinite, circular cylinder, which is irradiated by a plane wave at an angle  $\theta_i = 90^\circ$ . The theory to solve this problem originates from KING and WU [50] and VAN BLADEL [81].

### 6.5.2. METHOD OF SOLUTION

The scattered fields associated with a circular cylindrical scatterer can be determined by separation of variables. The configuration of interest is shown in FIGURE 35, the body model is the IZYL defined in 5.4.1.:

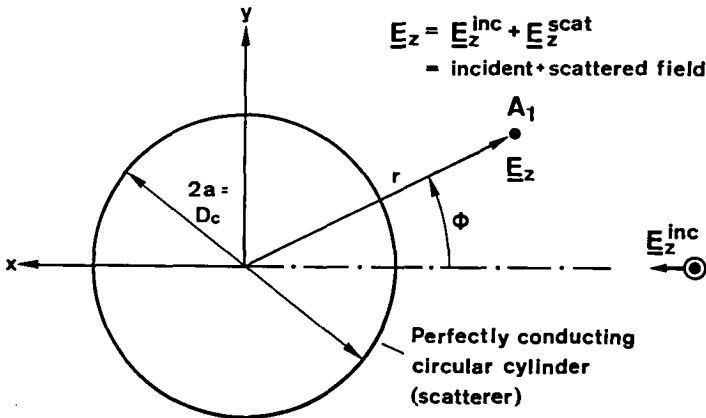


FIGURE 35 Two-dimensional model of man for analytical computation (IZYL). Vertical infinite cylinder in a vertical polarized incident plane wave:  $D_c$  = cylinder diameter,  $A_1$  = antenna positioned at  $r, \phi$ ,  $E_z^{inc}$  = incident  $\vec{E}$



For the following computation it is convenient to operate with the angle  $\phi'$  and the cylinder radius  $a$  :

$$\phi' = \phi + \pi ; a = D_c/2 \quad (223)$$

The incident  $\vec{E}$ -wave has only a  $z$ -component and is of the type :

$$\underline{E}_z^{inc} = e^{-jkx} = e^{-jkr \cos \phi'} \quad (224)$$

The incident field is expanded in a Fourier series in  $\phi'$  whose  $r$ -dependent coefficients are found by insertion in the wave equation to satisfy Bessel's equation. Thus, with  $\underline{E}_z^{inc}$  finite at  $r = 0$

$$\underline{E}_z^{inc} = \sum_{n=-\infty}^{\infty} j^{-n} J_n(kr) e^{jn\phi'} \quad (225)$$

where  $J_n(kr)$  is a Bessel function of order  $n$ . The scattered field must have a Fourier series of the form

$$\underline{E}_z^{scat} = \sum_{n=-\infty}^{\infty} \underline{\alpha}_n j^{-n} H_n^{(2)}(kr) e^{jn\phi'} \quad (226)$$

where  $H_n^{(2)}(kr)$  is a Hankel function of the second kind and order  $n$ . The value of  $\underline{\alpha}_n$  follows directly from the boundary condition (125) :

$$\underline{E}_z = \underline{E}_z^{inc} + \underline{E}_z^{scat} = 0 \quad \text{at } r = a \quad (227)$$

according to which the  $\underline{\alpha}_n$  are

$$\underline{\alpha}_n = - \frac{J_n(ka)}{H_n^{(2)}(ka)} \quad (228)$$

The above formulas by KING and WU [50] and VAN BLADEL [81] are now evaluated for near-field conditions with respect to the computer program PANA (see also program description in section 7.3. and listings in 16.2.1.)

A series of complex parameters can be expressed as

$$\sum_{n=-\infty}^{+\infty} \underline{c}_n = \underline{c}_n + \sum_{n=1}^{+\infty} (\underline{c}_n + \underline{c}_{-n}) \quad (229)$$

In equation (225) the  $\underline{c}_n$  and  $\underline{c}_{-n}$  are

$$\begin{aligned} \underline{c}_n &= j^{-n} J_n(kr) e^{jn\phi'} \\ \underline{c}_{-n} &= j^{-n} J_{-n}(kr) e^{-jn\phi'} = j^n (-1)^n J_n(kr) e^{-jn\phi'} \end{aligned} \quad (230)$$

With the relations  $(-j)^n = (j)^{-n}$  and  $e^{jn\phi'} = \cos \phi' = e^{-jn\phi'}$ ,  $\underline{E}_z^{inc}$  becomes

$$\underline{E}_z^{inc} = J_0(kr) + 2 \sum_{n=1}^{+\infty} j^{-n} J_n(kr) \cos n\phi' \quad (231)$$

The series for  $\underline{E}_z^{scat}$  is evaluated as follows:

$$\begin{aligned} \underline{c}_n &= \underline{\alpha}_n j^{-n} H_n^{(2)}(kr) e^{jn\phi'} \\ \underline{c}_{-n} &= \underline{\alpha}_{-n} j^n H_{-n}^{(2)}(kr) e^{-jn\phi'} \\ H_{-n}^2(kr) &= e^{-jn\pi} H_n^{(2)}(kr) \end{aligned} \quad (232)$$

Because  $(-1)^n = (e^{j\pi})^n$ ,  $(-1)^n e^{jn\pi} = (e^{j2\pi})^n = +1$ , the  $\underline{\alpha}_{-n}$  becomes

$$\underline{\alpha}_{-n} = - \frac{(-1)^n J_n(ka)}{e^{-jn\pi} H_n^{(2)}(ka)} = (-1)^n e^{jn\pi} \underline{\alpha}_n = \underline{\alpha}_n \quad (233)$$

and the  $\underline{c}_{-n}$  becomes

$$\underline{c}_{-n} = \underline{\alpha}_n j^n e^{-jn\pi} H_n^{(2)}(kr) e^{-jn\phi'} \quad (234)$$

With the relations  $e^{-jn\pi} = (-1)^n$ ,  $j^n e^{-jn\pi} = j^{-n}$  one obtains for  $\underline{E}_z^{scat}$

$$\underline{E}_z^{scat} = \underline{\alpha}_0 H_0^2(kr) + 2 \sum_{n=1}^{+\infty} \underline{\alpha}_n H_n^{(2)}(kr) j^{-n} \cos n\phi' \quad (235)$$

The combined fields from (231) and (235) represent the solution  $\underline{E}_z(r, \phi')$  at the location of the antenna  $A_1$ .

For the computer program the Hankel function may be replaced by the expression:

$$H_n^{(2)}(kr) = J_n(kr) - j Y_n(kr) \quad (236)$$

where  $J_n$  is a Bessel function of the first kind and order  $n$ , and  $Y_n$  is a Bessel function of the second kind and order  $n$  or a Neumann function.

### 6.5.3. LIMITATIONS OF THE ANALYTICAL NEAR-FIELD COMPUTATION

The convergence of the series (231) and (235) is quite slow ( $r \gg a$ ) for big values of  $ka$ . Whereas six terms (modes  $n$ ) give satisfactory results for  $ka = 3$ , over 1000 terms are needed for  $ka = 100$  (KING and WU [50]). Our  $ka$  is about 3 at 1000 MHz, and accurate near-field data are possible with  $n \leq 25$ .

Leer - Vide - Empty

## 7. TWO-DIMENSIONAL COMPUTATION OF SCATTERING FROM AN INFINITE CIRCULAR CYLINDER

### 7.1. COMPUTATIONAL MODEL AND GOALS

The antenna-body model consists of a perfectly conducting, circular cylinder of infinite length (FIGURE 28: Model IZYL), a small antenna  $A_1$  polarized parallel to the cylinder axis with the coordinates  $r$  (radius) and  $\phi$  (azimuthal angle), and an incident plane wave with the E-field polarized parallel to the cylinder axis. The computational situation is shown in FIGURE 35, and the method of solution is described in section 6.5..

The selection of this model follows from the analysis in section 5.2.3. and 5.2.4. The vertical IZYL represents a standing human TS at frequencies above 200 MHz, irradiated by a plane wave with the incident angle  $\theta_i = 90^\circ$ .

The model allows the computation of all vertical polarized E-field components and should give a preliminary answer about the correlation among antenna-body distance  $d_{at}$ , azimuthal angle  $\phi$ , frequency  $f$ , cylinder diameter  $D_c$  and transmission Gain<sub>B</sub>.

### 7.2. COMPUTER PROGRAM PANA: NEAR-FIELD PATTERN COMPUTATION OF THE INFINITE CYLINDER IZYL

#### 7.2.1. COMPUTATIONAL FORMULAS AND PARAMETERS

The total field (vertical component always)  $\underline{E}(r, \phi')$  at the antenna  $A_1$  is determined by the formulas (223) to (236) in section 6.5.. With  $\phi' = \phi + \pi$ :

$$\underline{E}(r, \phi') = \underline{E}^{inc}(r, \phi') + \underline{E}^{scat}(r, \phi') \quad (= 0 \text{ at } r = a) \quad (227)$$

$$\underline{E}^{inc}(r, \phi') = J_0(kr) + 2 \sum_{n=1}^{+\infty} j^{-n} J_n(kr) \cos n\phi' \quad (231)$$

$$\underline{E}^{scat}(r, \phi') = \alpha_0 \underline{H}_0^{(2)}(kr) + 2 \sum_{n=1}^{+\infty} \alpha_n \underline{H}_n^{(2)}(kr) j^{-n} \cos n\phi' \quad (235)$$

$$\alpha_n = - \frac{J_n(ka)}{\underline{H}_n^{(2)}(ka)} \quad ; \quad a = D_c/2 \quad (228)$$

$$\underline{H}_n^{(2)}(kr) = J_n(kr) - j Y_n(kr) \quad (236)$$

The transmission Gain<sub>B</sub> (see definition (20) in section 5.1.2.) is then:

$$\text{Gain}_B = 20 \log \left| 1 + \frac{E_{\text{scat}}(r, \phi')}{E_{\text{inc}}(r, \phi')} \right| \quad (237)$$

In the program the variables and parameters are denoted as follows:

INPUT	PARAMETER NAME	MEANING	UNITS
*	A (REAL)	a, radius of the cylinder	[m]
	AK (REAL)	ka	
	DAT (REAL)	dat, antenna-body distance	[m]
*	DMAX1 (REAL)	maximum dat for ARP	[m]
*	DMAX2 (REAL)	maximum dat for DRP	[m]
*	DMIN1 (REAL)	minimum dat for ARP	[m]
*	DMIN2 (REAL)	minimum dat for DRP	[m]
	EZI (COMPL)	E <sub>inc</sub>	
	EZSC (COMPL)	E <sub>scat</sub>	
*	F (INTEG)	f, integer number for the frequency	[MHz]
	G (REAL)	Gain <sub>B</sub>	[dB]
	HNKR (COMPL)	H <sub>n</sub> , Hankel function, second kind	
	JN (REAL)	J <sub>n</sub> , Bessel function, first kind	
	K (REAL)	k, wave propagation factor	
	LAM (REAL)	λ, wavelength	[m]
*	M1 (INTEG)	maximum mode n for ARP	
*	M2 (INTEG)	maximum mode n for DRP	
*	MR1 (INTEG)	number of dat for ARP	
*	MR2 (INTEG)	number of dat for DRP	
	PHI (INTEG)	φ, integer azimuthal angle, 0, 5, 10, ... 180	[°]
	PHH (REAL)	φ', φ + π	[°]
	RK (REAL)	kr	
	YN (REAL)	Y <sub>n</sub> , Bessel function, second kind	

TABLE 36 Variables and parameters used in program PANA

(ARP: Azimuthal radiation pattern, DRP: Directive radiation pattern)

### 7.2.2. PROGRAM DESCRIPTION PANA

The listing of the program PANA is enclosed in Appendix 16.2.1. It consists of one main program and one subroutine BESS. The main program consists of two parts preceded by an input section.

PANA 44 to 60 : Input and preliminary computations

PANA 61 to 98 : Computation of the azimuthal radiation pattern

PANA 100 to 143 : Computation of the directive radiation pattern

The input data set consists of the following punched cards (PANA 174-179):

NAMES INPUT PARAMETER				FORMATS INPUT PARAMETER				SAMPLE INPUT PARAMETER			
DMIN1	DMAX1	MR1	M1	F6.2	F6.2	I4	I4	0.05	0.25	05	12
DMIN2	DMAX2	MR2	M2	F6.2	F6.2	I4	I4	0.05	1.00	20	25
A				F7.3				0.125			
F				I3				150			
:				:				:			
F				I3				250			

TABLE 37 Input parameter set (punched cards PANA 174-179)

Card No. 1 : data for the azimuthal radiation pattern

Card No. 2 : data for the directive radiation pattern

Card No. 3 : data for the cylinder radius

Card No. 4+i : data for the frequencies to be computed ( $i=0,1,2,\dots$ )

In the present program the azimuthal radiation pattern computation (part 1) consists of the computation of the  $\phi$ -dependence of  $\text{Gain}_B$  for five (MR1) fixed  $d_{at}$ 's of 0.05 to 0.25 m in the  $\phi$ -range 0 to  $180^\circ$ . The spacing of the  $\phi$ -steps is determined to  $5^\circ$  due to the statement

DO 2 I=1,37

PANA 81

The maximum number of  $d_{at}$ 's (MR1) is limited by the output procedure PANA 69-71; the values of the  $d_{at}$ 's may vary from 0.01 to 9.99 m (PANA 70).

In the present program the directive radiation pattern computation (part 2) consists of the computation of the  $d_{at}$ -dependence of  $\text{Gain}_B$  at the irradiated side ( $\phi=0^\circ$ ) and in the shadow zone ( $\phi=180^\circ$ ) of the cylinder. The  $d_{at}$ 's vary from 0.05 to 1.00 m in 0.05 m steps, determined by the input cards. The maximum number of  $d_{at}$ 's (MR2) is limited only by the computational time; the values of the  $d_{at}$ 's may vary from 0.01 to 9.99 m (PANA 109).

The program computes the two radiation patterns for as many frequencies as frequency input cards are added in the data set. If the last frequency is executed, the program stops due to the statements:

IF(EOF (1)) 52,53  
52 STOP

PANA 55  
PANA 145

The radius a (A) is limited by PANA 64 and 104 and may vary from 0.005 to 4.999 m. The frequency f (F) may vary from 1 to 999 MHz (PANA 62 and 101).

The computation of the first  $G_{inb}$  for the azimuthal radiation pattern starts with the defining of AK (PANA 60), selecting the first  $d_{at}$  (PANA 78 and 79) and selecting the first  $\phi=0^\circ$  (PANA 81 and 82). The corresponding RK is given by PANA 88 and the PHH by PANA 83. The maximum mode number M1 is transferred to M, and the computation parameters M, AK, RK, PHH are transferred to the subroutine BESS for the computation of  $G_{inb}$  (G) :

CALL BESS(M,AK,RK,PHH,EZI,EZSC,V,G) PANA 89

The subroutine BESS will be discussed below. The result G ( $G_{inb}$ ) is returned from the subroutine and is checked for correct size in printing (PANA 90) and plotting (PANA 92). With the statements

DO 3 L=1.31	PANA 85
3 D1(L)=1H	PANA 86
KK=IFIX(G+30.5)	PANA 93
D1(KK)=1R0+J)	PANA 94

the number J (first J=1) of the J-th  $d_{at}$  is plotted as an amplitude marker in the  $G_{inb}$  versus  $\phi$  diagram in FIGURE 38.

The computation of the first  $G_{inb}$  for the directive radiation pattern uses the same AK and starts with the defining of the first  $d_{at}$  (PANA 124) and the first PHH (PANA 118). The corresponding RK is computed in PANA 131 and 132. The following computation of  $G_{inb}$  in the subroutine BESS and the plotting of  $G_{inb}$  as an amplitude marker in the  $G_{inb}$  versus  $d_{at}$  diagram is similar to above with the exception that a (\*) is printed. The complete diagram is shown in FIGURE 39.

The subroutine BESS uses the routine BESYN of the library BRUSLIB VIMCODE C306. Because other Bessel routines might be used in other computer centers, a few comments are helpful. In FORTRAN IV the transfer of the parameter 0 causes difficulties. Thus, the mode numbers  $n = 0, 1, 2, \dots, M$  are changed into  $MP1 = 1, 2, 3, \dots, M+1$  (PANA 153). The statement

CALL BESYN(-AK,MP1,JN,YN) PANA 154

executes the computation of  $J_n(ka)$  and  $Y_n(ka)$  for the modes  $0, 1, 2, \dots, MP1-1$ . With PANA 156 one obtains the  $\alpha_n$  of (228) in array AN(I). Similarly

CALL BESYN(-RK,MP1,JN,YN) PANA 157

executes the computation of  $J_n(kr)$  and  $Y_n(kr)$ . Finally, the  $E_{inc}$  and  $E_{scat}$  are computed in PANA 158-167. The returned G in PANA 169 represents  $G_{inb}$  of equation (237) for the selected r and  $\phi'$ .

### 7.2.3. PROGRAM LIMITATIONS AND ACCURACY

The convergence of the series in equation 231 and 235 is quite slow for large values of  $kr$  and similar in equation 228 for large values of  $ka$ . The minimum required modes  $n_{\min}$  to solve equation 237 accurately depends therefore primarily on the maximum frequency  $f$  and the maximum  $d_{at}$ . The subroutine BESS allows the computation of maximum 99 modes, and since the computational time increases with  $n$ ,  $n_{\min}$  should be evaluated as follows:

For large values of  $d_{at}$ 's (or distance  $r$ )  $G_{\text{aing}}$  should approach 0 dB for  $\phi = 180^\circ$  (shadow zone). If the chosen  $n_{\min}$  is too small,  $G_{\text{aing}}$  increases first monotonously with increasing  $d_{at}$  as expected; it begins to oscillate for larger  $d_{at}$ 's, and finally the program stops with an error message.

Introducing the additional statements:

GOTO 5	before PANA 61
5 CONTINUE	before PANA 100
IJ=IJ+2	before PANA 118

the program executes only the directive radiation pattern computation for  $\phi = 180^\circ$ . At a given frequency  $f$ , a given radius  $a$  and a chosen minimum mode number  $n_{\min}$  ( $M2$ ) the largest correctly computed  $d_{at}$  can be seen in the  $G_{\text{aing}}$  versus  $d_{at}$  diagram (e.g., FIGURE 39, bottom, if  $M2$  would be  $<12$ ).

In our application it was found that even for the maximum frequency 999 MHz a mode number of 25 ( $M2 = 25$ ) is sufficient for  $d_{at}$  below 2 m, with  $a = 0.125$  m and an accuracy of better than 0.1 dB.

The dimensions of the input parameters depend mainly on the selected output formats and have been discussed in 7.2.2.. The units are [m] and [MHz]:

DMIN1 : 0.01	DMIN2 : 0.01	A	: 0.005-4999	
DMAX1 : 9.99	DMAX2 : 9.99	F	: 1 - 999	
MR1 : 1-5	MR2 : 1-∞	No. of F	: 1 - ∞	(238)
M1 : 1-99	M2 : 1-99	$\Delta\phi$ steps	: 1 - ∞ (PANA 81)	

Scaled model computations are possible with a factor  $c_{\text{scale}}$ :

$F_{\text{model}}$	=	$F_{\text{actual}} \cdot c_{\text{scale}}$	
$A_{\text{model}}$	=	$A_{\text{actual}} \div c_{\text{scale}}$	(239)
$R_{\text{model}}$	=	$R_{\text{actual}} \div c_{\text{scale}}$	( $R = d_{at} + a$ )

The execution of the program PANA on a CDC 6500 computer requires a storage of 20,000 to 60,000 octal, depending on the compiler. The standard program (with 3 frequencies) requires 30 s execution time.



### 7.3. COMPUTED RESULTS OF THE TWO-DIMENSIONAL MODEL IZYL

#### 7.3.1. AZIMUTHAL AND DIRECTIVE RADIATION PATTERNS OF ANTENNA-IZYL MODEL

Samples for the frequency 567 MHz (FIGURES 38 and 39) and 150 MHz (FIGURES 40 and 41) are presented here; additional samples are in Appendix 16.2.1..

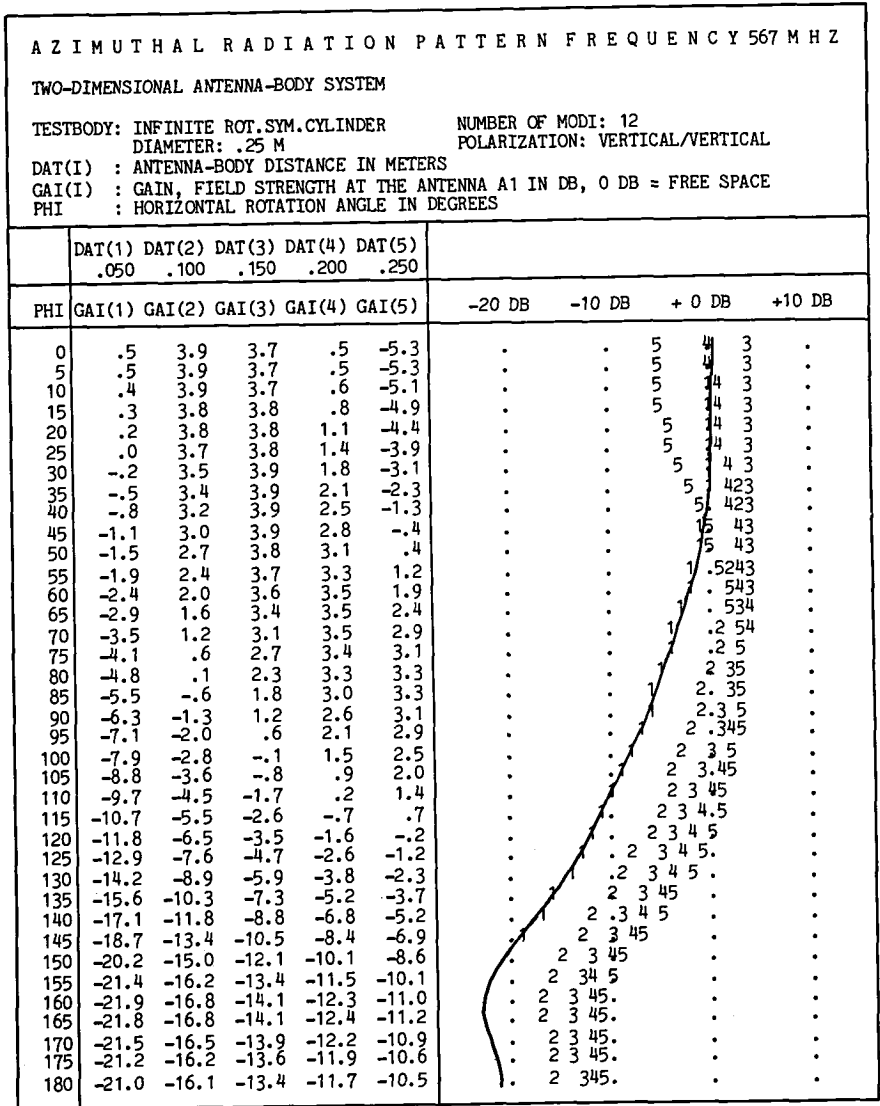


FIGURE 38 Azimuthal radiation pattern at 567 MHz (result of program PANA)  
Left: Gain<sub>B</sub> for 5 dat's and  $\phi = 0 - 180^\circ$ , right: Gain<sub>B</sub> versus  $\phi$  for 5 dat's.

In FIGURE 38 and 39 the diameter of the IZYL is 0.25 m and the frequency is 567 MHz. The azimuthal radiation pattern (FIGURE 38) shows a clear minimum of the gain (GAI(I)) at  $\phi = 160-165^\circ$ , decreasing with decreasing  $d_{at}$  (DAT(I)). The directive radiation pattern (FIGURE 39) at  $\phi = 0^\circ$  reveals a gain oscillation, with maxima at  $d_{at}$  of about  $\lambda/4 + n \cdot \lambda/2$ .

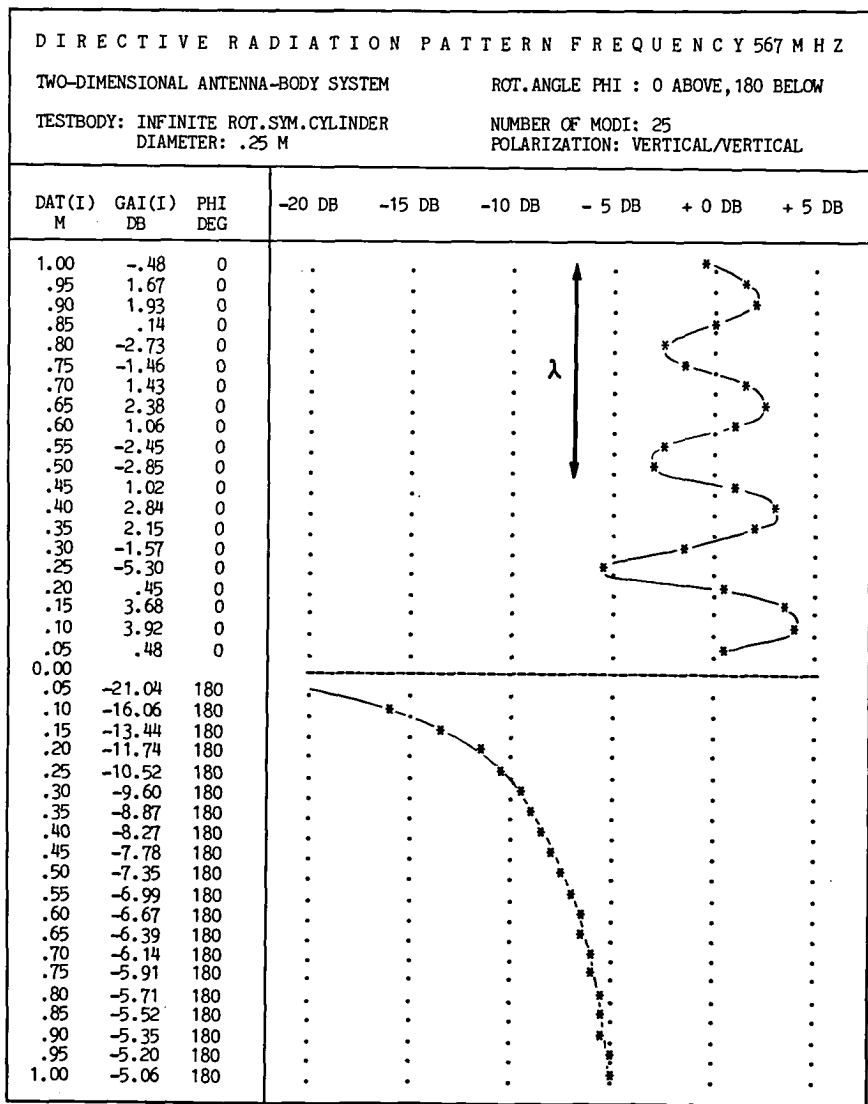


FIGURE 39 Directive radiation pattern at 567 MHz (result of program PANA).

· Above: Gain<sub>B</sub> versus  $d_{at}$  at  $\phi = 0^\circ$ , below: Gain<sub>B</sub> versus  $d_{at}$  at  $\phi = 180^\circ$ .

In FIGURE 40 and 41 the same IZYL is shown at a frequency of 150 MHz. This frequency is just below the application range of this two-dimensional computational model. The data obtained with this model should be compared with the data from the three-dimensional model in section 10.4..FIGURE 40 shows the azimuthal- and FIGURE 41 the directive radiation pattern:

AZIMUTHAL RADIATION PATTERN FREQUENCY 150 MHZ										
TWO-DIMENSIONAL ANTENNA-BODY SYSTEM										
TESTBODY: INFINITE ROT.SYM.CYLINDER						NUMBER OF MODI: 12				
DIAMETER: .25 M						POLARIZATION: VERTICAL/VERTICAL				
DAT(I) : ANTENNA-BODY DISTANCE IN METERS										
GAI(I) : GAIN, FIELD STRENGTH AT THE ANTENNA A1 IN DB, 0 DB = FREE SPACE										
PHI : HORIZONTAL ROTATION ANGLE IN DEGREES										
	DAT(1)	DAT(2)	DAT(3)	DAT(4)	DAT(5)					
	.050	.100	.150	.200	.250					
PHI	GAI(1)	GAI(2)	GAI(3)	GAI(4)	GAI(5)	-20 DB	-10 DB	+ 0 DB	+10 DB	
0	-8.2	-3.3	-.8	.8	1.9	.	. 1	2 3.45	.	.
5	-8.2	-3.3	-.8	.8	1.9	.	. 1	2 3.45	.	.
10	-8.3	-3.4	-.8	.8	1.8	.	. 1	2 3.45	.	.
15	-8.3	-3.4	-.9	.7	1.8	.	. 1	2 3.45	.	.
20	-8.4	-3.5	-1.0	.6	1.7	.	. 1	2 3.45	.	.
25	-8.6	-3.7	-1.1	.5	1.6	.	. 1	2 3.45	.	.
30	-8.7	-3.8	-1.2	.4	1.5	.	. 1	2 3.45	.	.
35	-8.9	-4.0	-1.4	.2	1.4	.	. 1	2 3.45	.	.
40	-9.1	-4.2	-1.6	.0	1.2	.	. 1	2 3.45	.	.
45	-9.4	-4.5	-1.9	-.2	1.0	.	. 1	2 3.45	.	.
50	-9.7	-4.7	-2.1	-.4	.8	.	. 1	2 3.45	.	.
55	-10.0	-5.0	-2.4	-.7	.5	.	. 1	2 3.45	.	.
60	-10.3	-5.4	-2.7	-1.0	.2	.	. 1	2 3.45	.	.
65	-10.7	-5.8	-3.1	-1.4	-.1	.	. 1	2 3.45	.	.
70	-11.1	-6.2	-3.5	-1.7	-.5	.	. 1	2 3.45	.	.
75	-11.6	-6.6	-3.9	-2.2	-.9	.	. 1	2 3.45	.	.
80	-12.1	-7.1	-4.4	-2.6	-1.3	.	. 1	2 3.45	.	.
85	-12.6	-7.6	-4.9	-3.1	-1.8	.	. 1	2 3.45	.	.
90	-13.1	-8.2	-5.5	-3.7	-2.3	.	. 1	2 3.45	.	.
95	-13.7	-8.7	-6.0	-4.2	-2.9	.	. 1	2 3.45	.	.
100	-14.3	-9.3	-6.6	-4.8	-3.5	.	. 1	2 3.45	.	.
105	-14.9	-10.0	-7.3	-5.5	-4.1	.	. 1	2 3.45	.	.
110	-15.6	-10.6	-7.9	-6.2	-4.8	.	. 1	2 3.45	.	.
115	-16.2	-11.3	-8.6	-6.8	-5.5	.	. 1	2 3.45	.	.
120	-16.8	-11.9	-9.3	-7.5	-6.2	.	. 1	2 3.45	.	.
125	-17.4	-12.5	-9.9	-8.2	-6.9	.	. 1	2 3.45	.	.
130	-18.0	-13.1	-10.5	-8.8	-7.5	.	. 1	2 3.45	.	.
135	-18.5	-13.6	-11.0	-9.4	-8.1	.	. 1	2 3.45	.	.
140	-18.9	-14.0	-11.5	-9.8	-8.6	.	. 1	2 3.45	.	.
145	-19.1	-14.3	-11.8	-10.2	-9.0	.	. 1	2 3.45	.	.
150	-19.4	-14.6	-12.1	-10.4	-9.3	.	. 1	2 3.45	.	.
155	-19.5	-14.7	-12.2	-10.6	-9.5	.	. 1	2 3.45	.	.
160	-19.6	-14.8	-12.3	-10.7	-9.6	.	. 1	2 3.45	.	.
165	-19.6	-14.8	-12.3	-10.7	-9.6	.	. 1	2 3.45	.	.
170	-19.6	-14.8	-12.3	-10.7	-9.6	.	. 1	2 3.45	.	.
175	-19.6	-14.8	-12.3	-10.7	-9.6	.	. 1	2 3.45	.	.
180	-19.6	-14.8	-12.3	-10.7	-9.6	.	. 1	2 3.45	.	.

FIGURE 40 Azimuthal radiation pattern at 150 MHz (result of program PANA).  
Left: Gain<sub>B</sub> for 5 d<sub>at</sub>'s and  $\phi = 0 - 180^\circ$ , right: Gain<sub>B</sub> versus  $\phi$  for 5 d<sub>at</sub>'s.

The azimuthal radiation pattern (FIGURE 40) shows a clear minimum of the gain (GAI(I)) at  $\phi = 180^\circ$ , decreasing with decreasing  $d_{at}$  (DAT(I)). The minimum gain amounts to -19.6 dB, compared with -21.9 dB at 567 MHz. FIGURE 41 shows at  $\phi = 0^\circ$  a maximum gain at  $d_{at} = \lambda/4$  (0.375 m). The shadow zone  $\phi = 180^\circ$  is within 1.5 dB identical with those at 567 MHz.

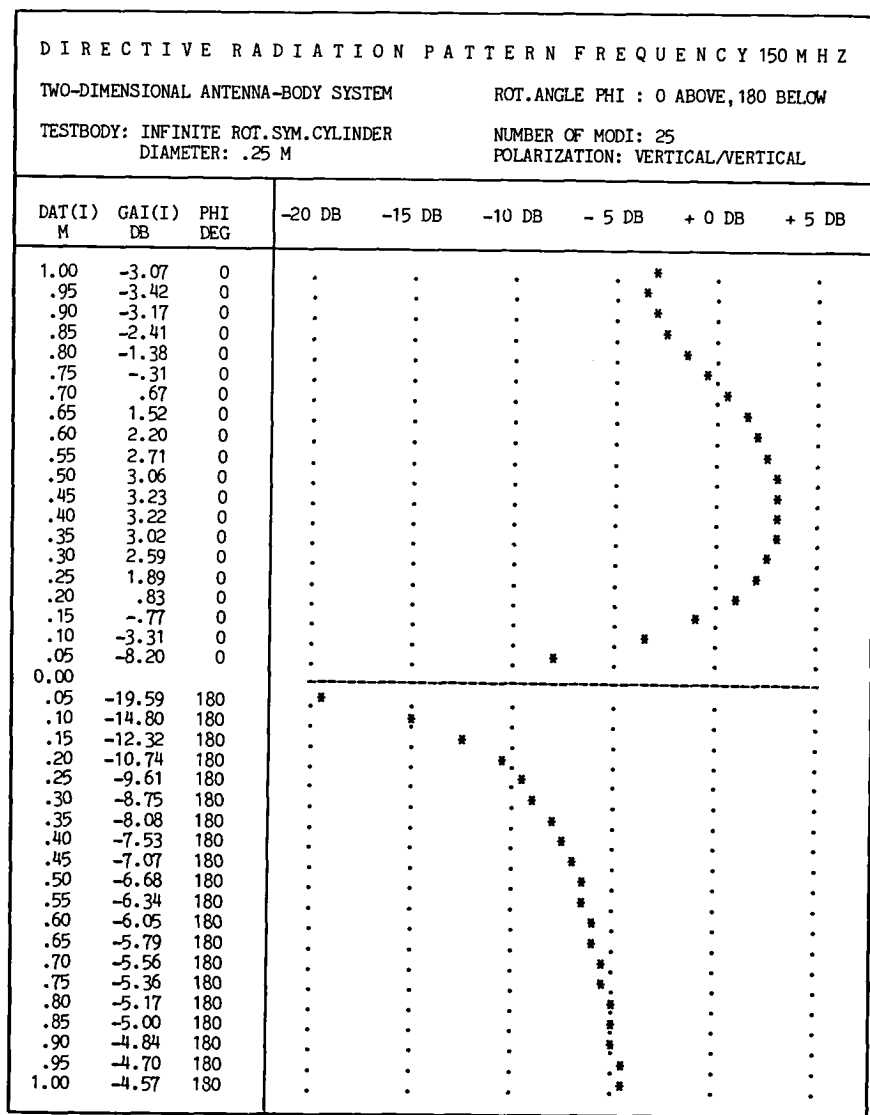


FIGURE 41 Directive radiation pattern at 150 MHz (result of program PANA).  
Above: Gain<sub>g</sub> versus  $d_{at}$  at  $\phi = 0^\circ$ , below: Gain<sub>g</sub> versus  $d_{at}$  at  $\phi = 180^\circ$ .

### 7.3.2. MINIMUM GAIN DEPENDING ON FREQUENCY AND CYLINDER RADIUS

The minimum Gain<sub>B</sub> occurs at frequencies above 300 MHz not at  $\phi = 180^\circ$  but at about  $165^\circ$  as shown in FIGURE 42 (dashed lines: model not accurate). Small diameter changes are of little significance at all  $d_{at}$ 's (FIGURE 43).

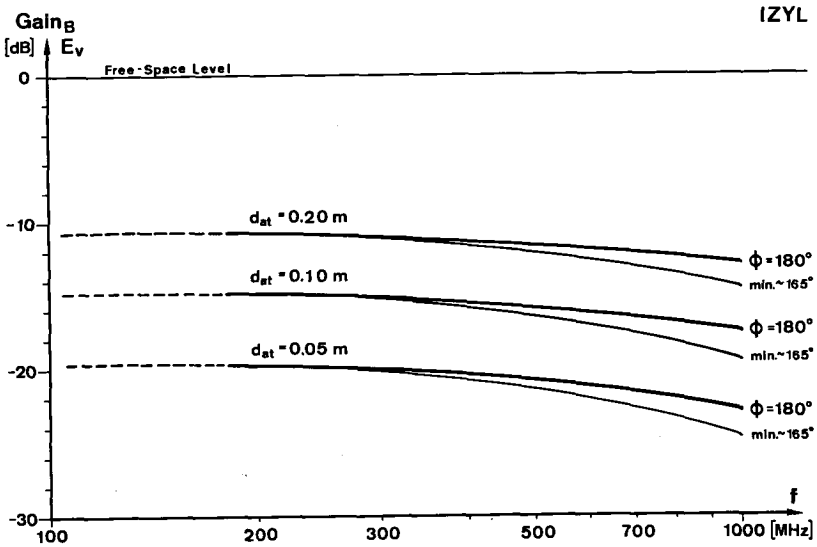


FIGURE 42 Gain<sub>B</sub> versus  $f$  in the shadow zone of the IZYL.

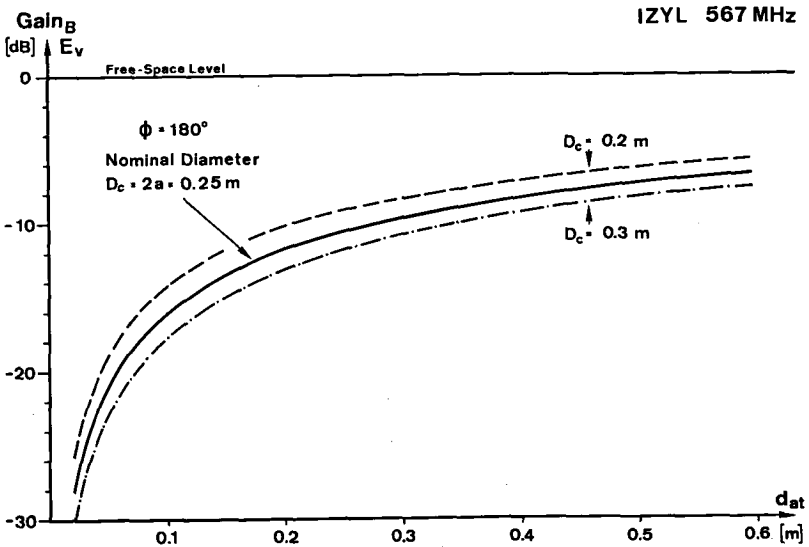


FIGURE 43 Gain<sub>B</sub> versus  $d_{at}$  for different cylinder diameters  $D_c$  ( $\phi = 180^\circ$ ).

## 8. MEASURING METHOD

### 8.1. PURPOSE OF THE EXPERIMENT

The experiments should answer the following questions:

Assumption verification : The computational models are based on assumptions which need to be verified. The main assumptions, as discussed in section 5.2., are reciprocity, quasi-perfect conductivity, and simplified body shape.

Off-resonance model verification : The two-dimensional computation of the radiation characteristics of the IZYL-antenna model (section 7.) delivers data for frequencies above 200 MHz. The experiment at frequencies above 200 MHz should deliver near-field data for large scale  $d_{at}$  and  $\phi$  variation. If an acceptable correlation between experiment and computation exists, an extension of the theory on three dimensional computation of conducting bodies is reasonable.

Resonance phenomena : The analysis of the antenna-body system (section 5.2.3.) predicts resonance effects at about 40 to 200 MHz. The experiment should verify this prediction.

Practical body-mounted antennas : A practical body-mounted antenna is usually a monopole antenna mounted on a transmitting device. If the housing of the transmitter is small (e.g., maximum dimension about 0.25 m), the counterpoise for the monopole antenna is not ideal (too small) for frequencies below 300 MHz. Thus, the experiment should also deliver data for standardized transmitting devices operating in proximity to the body in the entire regarded frequency range.

### 8.2. DESCRIPTION OF THE ANTENNA-BODY TEST SET-UP

Real-size antenna-body experiments have to be performed outdoors and in proximity to the ground. The reasons for this decision and the problems dealing with ground reflections have been discussed in section 5.3.. The outdoor FR experiments are performed on a military airport (AMF Dübendorf). With respect to RF-emissions one has to act very cautiously. Not only the RF-power emitted at the measuring frequency has to be kept within permissible limits but also unwanted harmonic distortions have to be controlled. On the other hand there are at any frequency distortions from the outside. Our experiment requires a signal/noise (S/N) ratio of > 30 dB

since the effect to be studied are up to 25 dB below the maximum field strength level. Further, one is obliged to apply small radiation sources (electrically small antennas, limited counterpoise) with a generally limited efficiency. Thus, the accurate measuring frequency and the necessary RF-power cannot be determined in advance.

Quartz-stabilized RF-generators for all measuring frequencies are out of question. The manufacturing of miniaturized transmitters is too expensive (especially for frequencies above 200 MHz), the frequency is fixed and the power can only be controlled within small margins (see section 11.3.).

Free-oscillating RF-generators tend to be unstable with respect to power and frequency, need a careful tuning in order to avoid harmonic distortions and get detuned if the antenna environment is disturbed. Thus, such transmitting devices are not suited for our experiments.

In order to choose arbitrary antennas, frequencies and power levels, a dummy system (FIGURE 44) is used instead of an autonomic RF-generator. The monopole antenna  $A_1$  and its counterpoise represent an idealized field point source (transmitting case) or a small field probe (receiving case).  $A_1$  is connected by a long coaxial cable to a precision RF-generator or in the receiving case to a field strength meter.

Let us first consider  $A_1$  as a transmitting antenna. Remote feeding causes severe problems concerning radiation from the feeding coaxial cable, if  $A_1$  is a monopole with an electrically small ( $< \lambda/2$  diameter) counterpoise. For the experiments  $A_1$  has to be approached up to 0.05 m to the test body. As a consequence, the counterpoise in FIGURE 44, No. 2, represents the maximum acceptable size with a diameter of 70 mm and a length of 100 mm. If no precautions would be taken, the outer sleeve of the cable would become a part of the counterpoise at frequencies below 500 MHz. Radiating currents on the outer sleeve of the cable would make accurate field measurements impossible. Methods for attenuating such sleeve currents are described in ARRL [3], KRUPKA [53] and ROTHAMMEL [71]. Usually a  $\lambda/4$  hollow cylinder is mounted around the coax, opened towards the antenna and contacted with the coax on the opposite cylinder side. Such a  $\lambda/4$  RF choke is efficient if the diameter is about 3-times the coax diameter. A smaller RF-choke can be obtained if the feeding coax cable is shaped in a coil (FIGURE 44, No. 4) of an electrical length of  $\lambda/4$ . The design of such a helical RF-choke is similar to that of a helical antenna and will be discussed in 8.3.2.. Be-

cause the helical RF-choke radiates itself a certain amount of RF power, it is covered by an absorbing tube (FIGURE 44, No.5.). The remaining surface waves on the feeding coax are attenuated by covering the whole coax with absorber material in the proximity of the antenna  $A_1$ . Finally load variations for the coax and the generator are prevented by inserting a 20 dB attenuator (FIGURE 44, No.3) below the antenna's foot point.

The complete antenna test set-up is shown in FIGURE 44. It follows the specifications evaluated in section 5.3. and allows measurements of vertical polarized E-fields in the frequency range 10-1000 MHz. The dummy system discussed above has a shape of a circular cylinder of 70 mm diameter and is supported by an antenna holder (No.6.). Depending on the frequency the test antenna  $A_1$  (No.1.) is a helical monopole as shown or a whip (see 8.3.1.). The revolving stage (No.7.) rotates the test-body together with the antenna  $A_1$ . A directive, broadband antenna (8.3.3.)  $A_2$  (No.8.) completes the antenna test set-up.

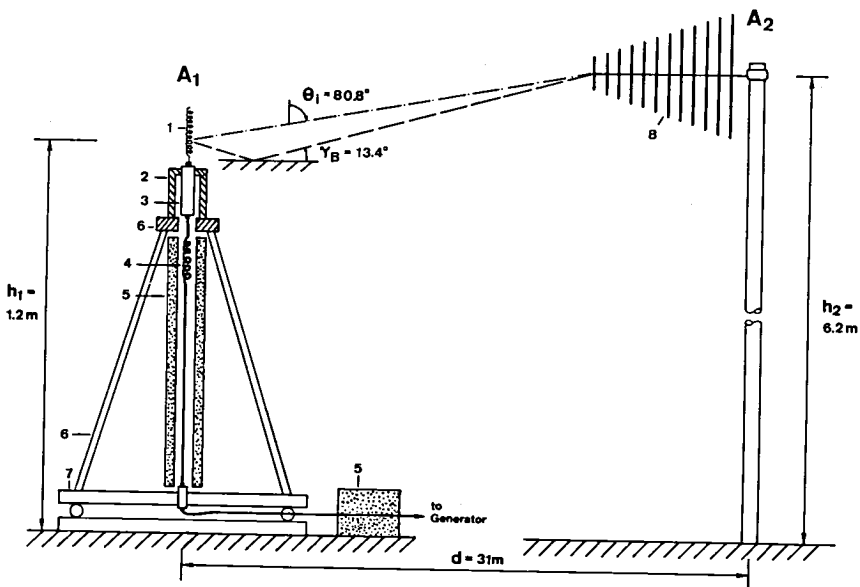


FIGURE 44 Measuring antenna test set-up

- |                                      |                           |
|--------------------------------------|---------------------------|
| 1: test (body-mounted) antenna $A_1$ | 5: EM absorber material   |
| 2: electrical counterpoise for $A_1$ | 6: wooden antenna holder  |
| 3: 20 dB attenuator in series        | 7: wooden revolving stage |
| 4: matched RF-choke                  | 8: remote antenna $A_2$   |



For the computational models the transmission distance  $d$  has been defined in section 5.1.2. as follows:

$$\left. \begin{array}{l} \text{Transmission distance } d \\ \text{for computational models} \end{array} \right\} : \begin{array}{l} \text{Horizontal distance between} \\ \text{the center of the body and } A_2 \end{array} \quad (240)$$

For the experiment it is better to keep the distance between  $A_1$  and  $A_2$  constant, thus we define the experimental transmission distance  $d$ :

$$\left. \begin{array}{l} \text{Transmission distance } d \\ \text{for experiments} \end{array} \right\} : \begin{array}{l} \text{Horizontal distance between} \\ \text{the centers of } A_1 \text{ and } A_2 \end{array} \quad (241)$$

Essentially there is no difference between (240) and (241), because  $d_{at}$  is small compared with  $d$  and because we are not interested in the absolute phase of the fields. However, the reference field strength  $E_0$  is more constant when the antennas and the cables are not moved.

The experiments require rotation of the antenna-body system ( $\phi = \text{variable}$ ,  $d_{at} = \text{parameter}$ ) and translation of the body in respect to the antenna  $A_1$  ( $d_{at} = \text{variable}$ ,  $\phi = \text{parameter}$ ). These two experiments are shown schematically in FIGURE 45:

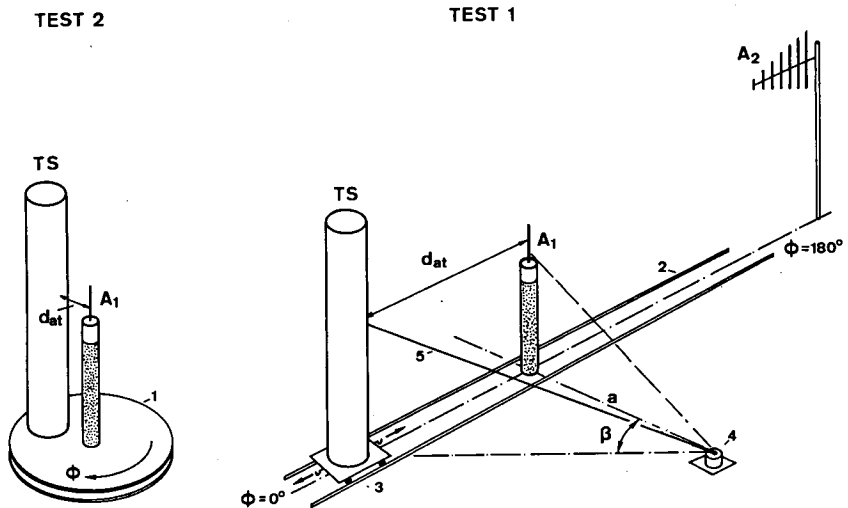


FIGURE 45 Rotation and translation of test bodies

- |                             |  |
|-----------------------------|--|
| 1: wooden revolving stage   | 4: displacement transducer<br>(rubber band goniometer) |
| 2: plastic trackway section | 5: rubber thread                                       |
| 3: wagon                    |  |

### 8.3. ANTENNAS AND FEEDING

#### 8.3.1. BODY-MOUNTED ANTENNA $A_1$

Theoretically the body-mounted antenna  $A_1$  should fulfill the following requirements as defined in section 5.1.2. :

- The radiation intensity should be constant, but the efficiency is not of interest.
- The physical size of  $A_1$  should be smaller than any relevant dimension of the test set-up.
- Only one dominant E-polarization axis  $p_1$  should exist.
- The antenna should radiate omnidirectionally.
- The impedance and thus the radiation should not change due to body proximity.

In practice there are physical and technical limitations:

- The efficiency should be so high, that the radiation of  $A_1$  is much higher (30 dB) than the leakage radiation of all involved equipment. Such an efficiency can only be obtained if  $A_1$  is operated near resonance.
- An antenna length  $h$  of 0.15 m is acceptable for the purpose of the experiment. This antenna length corresponds to  $\lambda/4$  at 500 MHz. Thus, efficient, resonant (no external tuning), electrically small antennas have to be used for all frequencies below 500 MHz.
- A strict linear polarization is difficult to obtain with resonant electrically small antennas. Any internal frequency tuning element leads to certain field irregularities.
- Omnidirectional radiation in a horizontal plane depends not only on the antenna but also on the feeding cable. A dipole antenna is not suited because the cable had to be mounted rectangular to the antenna axis. Thus, monopole antennas have to be used with a limited counterpoise.
- If an antenna has to be operated near resonance; the impedance depends on body proximity, because the bandwidth of any electrically small antenna is narrow (see section 4.5.).

The normal mode helical monopole (16.1.) offers a good compromise for antenna lengths  $h > \lambda/20$ . The polarization is elliptical, with a dominant vertical E-component which is larger than that of an equal-sized whip.

Ant. Type No.	Resonant Frequency $f_{res}$ [MHz]	Approx.-3 dB Bandwidth min/max [MHz]	Antenna length $h$ [mm]	Antenna diameter $D_h$ [mm]	Number of turns $N_h$	Wire diam. $d_w$ [mm]
AT1 hel.	$120 \pm 3$	110 - 125	185	11.5	42	1.5
AT2 hel.	$180 \pm 3$	170 - 185	155	12.0	26	2.0
AT3 hel.	$210 \pm 2$	190 - 215	145	12.0	24	2.0
AT4 hel.	$298 \pm 2$	260 - 310	145	12.0	13	2.0
AT5 hel.	$363 \pm 4$	335 - 403	130	12.0	8	2.0
AT6 whip	$490 \pm 5$	450 - 560	150	-	-	1.5
AT7 whip	$630 \pm 5$	605 - 700	110	-	-	2.0
AT8 whip	$1060 \pm 8$	960 - 1150	75	-	-	1.0

TABLE 46 Monopole antennas  $A_1$  for field experiments. The resonant frequency  $f_{res}$  and the bandwidth have been measured with a network analyser, when  $A_1$  was mounted on the counterpoise, with RF-choke, but without attenuator, and in an anechoic chamber.

The specifications of the experimental antennas  $A_1$  are shown in TABLE 46. It should be mentioned that these data may vary from the theoretical data in section 16.1., because the antennas  $A_1$  are operated on the later used limited counterpoise.

### 8.3.2. RF-CHOKES

The purpose of the RF-chokes is to attenuate surface currents on the feeding coaxial cable. They are constructed from an RG-58 coaxial cable, wrapped in a helical shape. The specifications are shown in TABLE 47:

RF Choke No	Operating Range $f_c$ [MHz]	Choke length $l_c$ [mm]	Choke diameter $d_c$ [mm]	Cable length $l_f$ [mm]	Number of turns $n_c$	Cable diam. $d_f$ [mm]
CH1	50 - 150	100	20	1000	14	6
CH2	100 - 200	70	16	700	12	6
CH3	150 - 200	50	16	500	8.5	6
CH4	200 - 250	37	16	330	6	6
CH5	250 - 350	22	16	220	4	6
CH6	350 - 500	13	16	130	3	6

TABLE 47 RF-chokes for field experiments.  $f_c$  theoretical values.

The effectiveness of the coax-line RF-chokes in TABLE 47 decreases at higher frequencies because of the distributed capacitance among the turns. Since they have to be mounted in absorbing tubes (attenuation of the choke radiation), the Q-factor is not very high, resulting in a favourable broad band range, but with further decreases effectiveness. There is a simple method to test RF-chokes: when the complete antenna test set-up according to FIGURE 44 is assembled for the selected test frequency, the received field strength should not change more than 2 dB if the coaxial feeding cable is touched by hand at any location along the cable.

### 8.3.3. REMOTE ANTENNA A<sub>2</sub>

Because the helical antennas A<sub>1</sub> are elliptically polarized and we have to measure only the vertical polarized E-field component, the remote antenna A<sub>2</sub> has to be strictly linear polarized. In addition A<sub>2</sub> should be a directive antenna with broadband characteristics. It was found that a logarithmic periodic antenna (LPD) fulfills these requirements best. The chosen Cross LPD (R. GRANER, AMF) operates from 100 to 1000 MHz with a directive gain of about 6 dB (aperture angle  $\pm 60^\circ$ ). By simple line-switching the vertical polarization and the horizontal polarization can be measured independently, which is needed to check the radiation properties of A<sub>1</sub> before the actual experiment can be started.

## 8.4. MEASURING EQUIPMENT

### 8.4.1. REVOLVING STAGE FOR ANTENNA-BODY ROTATION

In cooperation with R. GRANER from the AMF a revolving stage and an electronic plotter control unit has been developed. It consists of

- revolving stage with basement, stage, engine and angle sensors  
(see FIGURE 48, shown with inverted separate stage).
- angle data transmitter, combined with remote control of the stage rotator and with an intercom system
- plotter control unit with angle display, synchronizer and x-y driver  
(see FIGURE 49).

This equipment allows the automatic plotting of azimuthal gain charts when combined with the RF-equipment and the power supply for the stage engine. The control unit synchronizes on the zero marker (FIGURE 48) and plots one full 0-360° E/ $\phi$  sequence with 1° resolution on an ordinary x-y recorder in a rectangular diagram as recommended by CEI Publication 138.

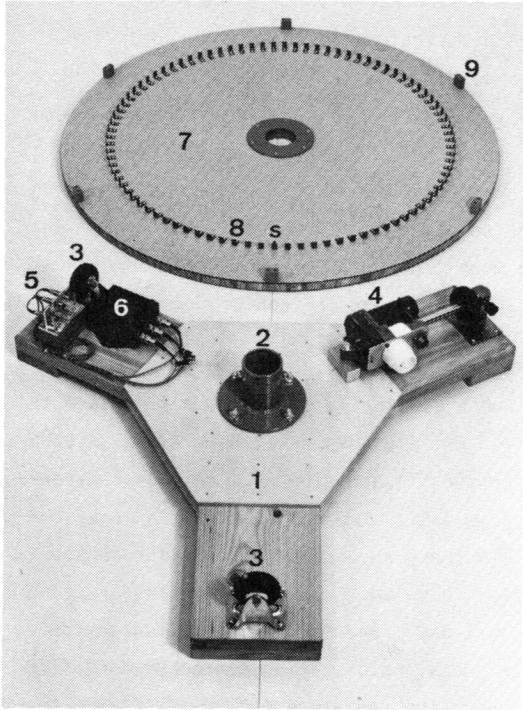


FIGURE 48 Revolving stage  
1 : basement  
2 : hollow axle (for antenna coaxial cable with rotational N-connector)  
3 : supporting wheels  
4 : engine with driving wheel (24 V DC)  
5 : angle sensors with sensor protection bolts  
6 : line driver and intercom station  
7 : stage platform (upside down)  
8 : angle markers (s: synchronization marker)  
9 : angle marker protection

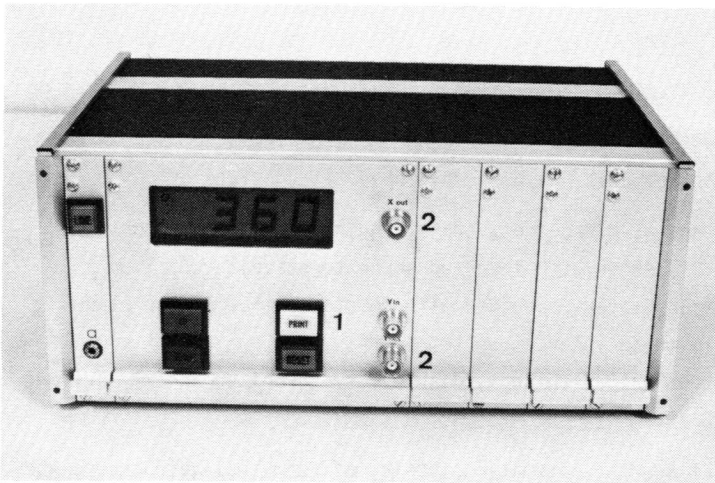


FIGURE 49 Plotter control unit  
1 : command switch : next revolution = plot diagram  
2 : x-y driver output

#### 8.4.2. TRACKWAY FOR ANTENNA-BODY TRANSLATION

According to FIGURE 45 a trackway was constructed in order to move the heavy test subject (phantom weight 90 kg !) continuously toward the stationary antenna  $A_1$ . A wooden basement of 5 meter length equipped with plastic rails was mounted on the  $\phi$ -coordinates  $0-180^\circ$  and later  $90-270^\circ$ . A small, ball-bearing equipped wagon carried the test subjects, with the footpoint spaced  $s=0.2\text{m}$  appart from the ground. By help of deflection pulleys, mounted each 10 meters away from  $A_1$  on the trackway axis, and long plastic strings the wagon could be precisely moved manually.

The monitoring of  $d_{at}$ , which is the distance from the center of  $A_1$  and the nearest surface of the test body, is not easy. First, this distance has to be actually measured and not e.g., the position of the wagon, because of practical accuracy considerations. Second, the space between  $A_1$  and TS should not be disturbed by measuring devices, because any metallic or dielectric material causes field disturbances. Third, an accuracy of  $\pm 10\text{ mm}$  is required at least in the low  $d_{at}$  regions.

The rubber band goniometry, developed by NEUKOMM [65] for the biomechanical research, solves this difficult problem with little effort. A low torque conductive plastic potentiometer is mounted rectangularly to the trackway axis in the distance  $a=2\text{ m}$  from the vertical  $A_1$  axis. (FIGURE 45, No. 4.). At the vertical axis of the potentiometer a beryllium bronze arm of  $0.1\text{mm}$  thickness and  $100\text{ mm}$  length is attached. The arm can be bent up and down without angular changes or significant forces on the axle. From this arm a thin rubber thread ( $\phi < 0.3\text{mm}$ ) is stretched (about  $1\text{ N}$  tensil force) to the test point on the TS and fixed with self-adhesive tape (see FIGURE 45, No. 5. ). The linear motion  $d_{at}$  is thus transformed into an angular motion  $\beta$  according to

$$\beta = \arctg(d_{at}/a) \quad (242)$$

There is a non-linear, but one-to-one correspondence between  $\beta$  and  $d_{at}$ . In a linear  $\beta$  presentation the interesting range  $0 < d_{at} < 0.35\text{ m}$  corresponds to  $0 < \beta < 10^\circ$  but contains also the large range  $0.35 < d_{at} < 2.38\text{m}$  corresponding to  $10 < \beta < 50^\circ$ . The accuracy in the low  $d_{at}$  range is better than  $10\text{ mm}$ , because the hysteresis of the rubber band goniometer is less than  $0.3^\circ$ , the resolution is quasi-infinite (better than  $0.01^\circ$ ). The non-linearity of the potentiometer of  $0.5\%$  F.S. would cause moderate errors in (242), thus the  $\beta$ -scale is calibrated directly in the actual  $d_{at}$ -scale.

The mechanical  $\beta$  signal is converted by the potentiometer into a proportional electrical tension, and with the built-in impedance converter the signal is transmitted over a long shielded cable to the x-input of the plotter. If the field strength signal is on the y-input of the plotter, one obtains a calibrated  $E/d_{at}$  plot with  $0 < d_{at} < 2.3$  m for  $\phi = 0^\circ$  and  $\phi = 180^\circ$ . Of course, the switching from  $\phi = 0^\circ$  to  $\phi = 180^\circ$  requires a tip down of the  $A_1$  antenna tower and to connect the rubber thread on the reverse side of the test body when it has been rolled over with the wagon. The  $d_{at}$ -scale has to be calibrated once by means of markers on the middle line of the trackway.

#### 8.4.3. FIELD MEASURING EQUIPMENT

Besides the mentioned antennas and  $\phi/d_{at}$  recording devices the following materials have been applied in the experiments:

- Field-strength measuring unit: main unit RHODE + SCHWARZ VHF-UHF ESUM BN 15076/5/P with the plug-in units 25-230 MHz, 160-470 MHz, and 850-1300 MHz. The effective accuracy (as tested) is  $\pm 0.5$  dB in the +5 to -20 dB range and  $\pm 2$  dB in the -20 to -35 dB range. (0 dB = 80 % full scale of the recorder output, operating on the self calibrated "linear" range of the ESUM)
- RF-Generator : HEWLETT PACKARD 8640B, 25-1000 MHz. The stability of the amplitude is specified to  $\pm 0.1$  dB and could be checked by a free space recording before and after an experiment at a specific frequency (over-all test revealed a stability of  $\pm 0.5$  dB at frequencies above 200 MHz, depending mostly on the antenna  $A_1$ )
- X-Y-Recorder: BRYANS 26000 A3. The accuracy is specified to  $\pm 1$ mm which could be affirmed by a test,
- Absorber material: blocks of  $0.3 \times 0.3 \times 1$  m. Standard absorbers of the PTT antenna development division, efficient above about 100 MHz. Has been used to attenuate sleeve currents on the feeding coaxial cable (see FIGURES 44 and 53).
- Coaxial cables: double shielded coax of 9 mm diameter with N-connectors. Standard materials of the AMF antenna development division. At frequencies below 30 MHz the RF-radiation leakage cannot be neglected if inefficient antennas and cable lengths in excess of 40 m are used.

### 8.5. ANTENNA SET-UP TESTING AND EXPERIMENTAL PROCEDURE

Field measurements with non-resonant antennas in proximity to the ground require careful preliminary tests in order to exclude artifacts. With a human test subject TEST 1 (FIGURE 45,  $\phi = 0.90, 180, 270^\circ$ ,  $d_{at} = 0$  to 4 m) and TEST 2 (FIGURE 45,  $d_{at} = 0.035, 0.077, 0.135$  m) have been performed at the frequencies 25, 50, 75, 100, 150, 200, 300, 400, 600, 700, 800 and 900 MHz. In October 1976 a further experiment with the three test bodies SUB, PHA and MET (see specifications in section 5.4.1) was performed according TEST 1 (FIGURE 45,  $\phi = 0$  and  $180^\circ$ ,  $d_{at} = 0.035$  to 2 m) at 11 frequencies from 74 to 897 MHz. TABLE 50 shows the preliminary test preparations, TABLE 51 the antenna parameter and TABLE 52 the experiment check list.

1. LABORATORY PREPARATIONS
1.1. Computation and construction of antennas $A_1$ 1.2. Network analysis in anechoic chamber (TABLE 46) 1.3. Construction and testing of RF-chokes (TABLE 47) 1.4. Construction of rubber band goniometer with lawn anchor 1.5. Goniometer test with 100 m cable and strong RF disturbances
2. MEASURING SET-UP PREPARATIONS
2.1. Warming-up of RF equipment and recorder, initial calibration 2.2. Trackway mounting with levelling rod under 100 kg load 2.3. Goniometer mounting with levelling rod. (In this test series is $a=1m$ , corresponding to $d_{at} : 2 m \cong \beta : 63.43^\circ$ ) 2.4. Calibration of the $d_{at}$ scale with reference markers on trackway 2.5. Verification of the $d_{at}$ accuracy when rubber thread is attached on phantom at $h_1 = 1.2$ m.
3. TRANSMISSION TEST (for each measuring frequency)
3.1. Search for a free RF-channel 3.2. Evaluation of antenna $A_1$ and RF choke, sleeve current tests. 3.3. Checking if no obstacles are around within a radius of 50 m. 3.4. Polarization and reciprocity test: Transmitter out on $A_1$ , polarization $A_2 =$ vertical , reading: Receiver input on $A_1$ , polarization $A_2 =$ vertical , reading: Receiver input on $A_1$ , polarization $A_2 =$ horizontal , reading: Transmitter out on $A_1$ , polarization $A_2 =$ horizontal , reading: 3.5. RF-leakage test: $A_1$ replaced by a $50 \Omega$ terminator Transm. out on $A_1$ cable, polar. $A_2 =$ vertical , reading: Receiv. in on " " " " = vertical , reading: Receiv. in on " " " " = horizontal , reading: Transm. out on $A_1$ cable, polar. $A_2 =$ horizontal , reading:

TABLE 50 Preliminary test preparations and checks



The accuracy of the data obtained in the following antenna-body experiments depends directly on the results of the transmission test 3.4. and 3.5. in TABLE 50. The field strength at vertical polarization should be at least 15 dB higher than the field strength at horizontal polarization, and should be at least 20 dB higher than the noise or the residual signal picked-up when  $A_1$  (transmitting and receiving case) is replaced by a  $50\ \Omega$  terminator. The reciprocity test reveals RF-leakage in the control center, theoretically the transmission in both directions should give the same reading. These important antenna parameters are listed in TABLE 51 :

Freq [MHz]	$A_1$ No.	RF choke No.	$A_1$ = transmitting antenna				$A_1$ = receiving antenna			
			$A_2$ : verti.		$A_2$ : horiz.		$A_2$ : verti.		$A_2$ : horiz.	
			ANT [dB]	TERM [dB]	ANT [dB]	TERM [dB]	ANT [dB]	TERM [dB]	ANT [dB]	TERM [dB]
74	AT1	2x CH1	25	3	13	0	17	25	18	20
101	AT1	3x CH1	25	10	0	0	26	15	0	0
125	AT1	2x CH1	25	0	6	0	25	0	6	0
158	AT2	CH1	25	0	4	0	26	0	3	2
205	AT3	CH2	25	2	9	0	25	7	9	0
250	AT4	CH3	25	0	2	0	25	0	3	0
300	AT4	CH3	25	3	5	0	24	7	5	0
400	AT5	CH4	25	0	0	0	25	0	0	0
562	AT6	CH5	25	3	11	0	24	0	7	0
700	AT7	CH6	25	0	0	0	25	0	5	0
897	AT8	CH6	25	0	2	0	25	0	0	0

TABLE 51 Antenna parameter of the test set-up used in the later antenna-body experiments. ANT: specified antenna  $A_1$  connected to generator or receiver, TERM:  $A_1$  replaced by a  $50\ \Omega$  terminator. Frequency 74 allows no accurate measurements (but qualitative measurements for  $A_1$  = transmitting antenna), 101 MHz is at the border line of the applicability.

If we compare TABLE 51 with TABLE 46, one can predict that the frequency

300 MHz may cause difficulties, because AT4 resonates at 298 MHz. A change in the proximity of the antenna (body) will effect an important change of the antenna impedance. The specifications at 74 MHz are not satisfactory not only due to AT1, but also due to the lower frequency limit of 100 MHz of the remote antenna A<sub>2</sub>.

The check list for the actual antenna-body experiment (TEST 1 in FIGURE 45) is shown in the next TABLE 52 :

4. ANTENNA-BODY EXPERIMENT CHECK LIST (for each measuring frequency)	
4.1.	Final calibration of RF-equipment and recorder
4.2.	Repetition of points 3.4. and 3.5. according TABLE 50
4.3.	Zero calibration of the goniometer
4.4.	Calibration of the FSL (free-space level) on + 15 dB for A <sub>1</sub> = transmitting antenna and A <sub>2</sub> = vertical polarization
4.5.	Experiments with the test bodies MET, PHA and SUB in the d <sub>at</sub> -interval 0.035 up to 2 m: (A <sub>2</sub> =always vertical polarization)
4.5.1.1.	MET, $\phi = 0^\circ$ , A <sub>1</sub> = transmitting antenna
2.	A <sub>1</sub> = receiving antenna
4.5.2.1.	PHA, $\phi = 0^\circ$ , A <sub>1</sub> = transmitting antenna
2.	A <sub>1</sub> = receiving antenna
4.5.3.1.	PHA, $\phi=180^\circ$ , A <sub>1</sub> = receiving antenna
2.	A <sub>1</sub> = transmitting antenna
4.5.4.1.	MET, $\phi=180^\circ$ , A <sub>1</sub> = transmitting antenna
2.	A <sub>1</sub> = receiving antenna
4.5.5.1.	SUB, $\phi=180^\circ$ , A <sub>1</sub> = receiving antenna
2.	A <sub>1</sub> = transmitting antenna
4.5.6.1.	SUB, $\phi= 0^\circ$ , A <sub>1</sub> = transmitting antenna
2.	A <sub>1</sub> = receiving antenna
4.6.	When all test bodies are dislocated, reading of the FSL for A <sub>1</sub> = transmitting antenna.
4.7.	Reading of the goniometer at d <sub>at</sub> = 0.

TABLE 52 Antenna-body experiment check list (shortened)

The procedure for TEST 2 (FIGURE 45) is similar to TABLE 50, 51, and 52. In FIGURE 53 a picture is shown of such a TEST 2. The measured results are discussed in the next section together with the theoretical predictions. The sketch in FIGURE 54 is not only a joke : the directive gain from the bodies of three men amounts to about 4 to 6 dB as measured with a MOTOROLA HT 220 walkie-talkie with a 4 inch helix at 174 MHz.

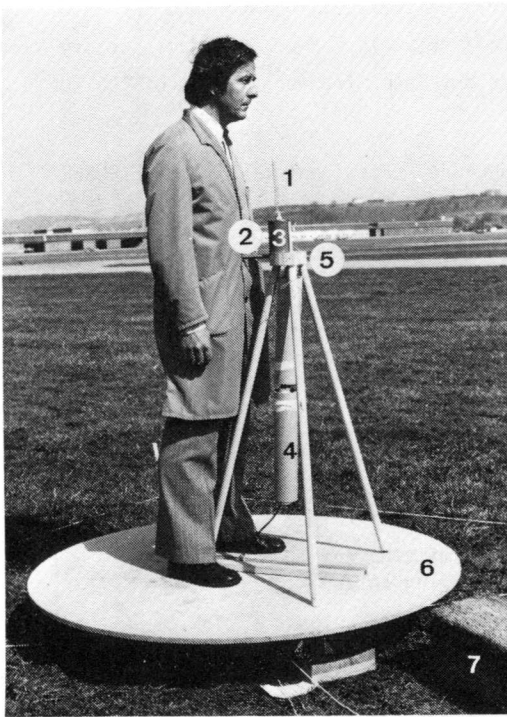


FIGURE 53

Test set-up for azimuthal radiation experiments

- 1: test antenna  $A_1$
- 2: spacer ( $d_{at}$  = parameter)
- 3: electrical counterpoise with attenuator
- 4: absorber tubes (RF-choke within the tubes)
- 5: wooden antenna holder
- 6: wooden revolving stage
- 7: absorber blocks on feeding coaxial cable

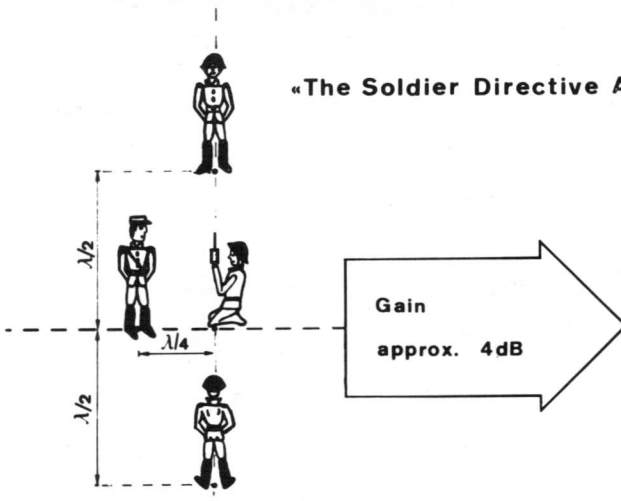


FIGURE 54 "The soldier directive antenna". An application of the Gain obtained at  $d_{at} = \lambda/4$  at  $\phi = 0^\circ$  and  $d_{at} = \lambda/2$  at  $\phi = 90^\circ$  and  $270^\circ$ .

## 9. COMPARISON OF EXPERIMENTAL DATA WITH THEORETICAL DATA

### 9.1. INVESTIGATED PARAMETERS

#### 9.1.1. EFFECT OF FREQUENCY AND BODY MATERIAL

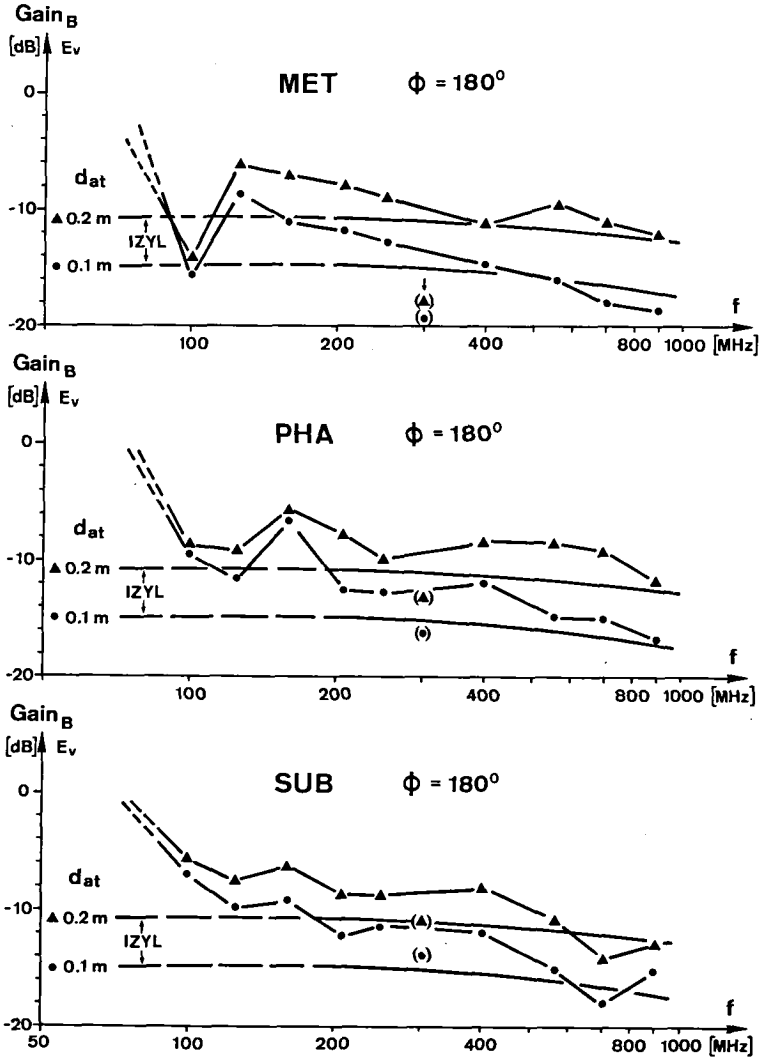


FIGURE 55  $G_{dB}$  versus  $f$  in the shadow zone from the three test bodies MET, PHA, SUB (measured data) compared with the computed data from IZYL. Parameter:  $d_{at} = 0.1$  and  $0.2$  m.  $E_v$ : E-field strength, vertical polarization.

FIGURE 55 is a comparison between the experimental data for the three test bodies MET, PHA, SUB and the computational data for the IZYL (see definition of the bodies in 5.4.1.). Shown are the data for the constant parameter  $d_{at} = 0.1$  m and  $0.2$  m in the shadow zone  $\phi = 180^\circ$ , obtained from the  $G_{in}/d_{at}$  experiment in FIGURES 56, 57 and 58.

The experiment, performed according to the check lists in 8.5., includes the experimental frequencies (74), 101, 125, 158, 205, 250, (300), 400, 562, 700 and 897 MHz. The results at (74) and (300) MHz are not accurate enough for a quantitative consideration, the reasons are mentioned below TABLE 51 and in section 9.2..

The computational data for the infinite cylinder (IZYL) are valid only for frequencies above 200 MHz for finite bodies of more than 1.8 m length, as explained in section 7.1.. The most interesting result is the parallelism of the  $G_{in}$  curves for  $d_{at} = 0.1$  m and  $0.2$  m. The difference is almost constant versus the frequency and amounts to  $4 \pm 0.5$  dB.

The experimental data reveal a similar tendency. For all test bodies the gain difference between  $d_{at} = 0.1$  m and  $d_{at} = 0.2$  m amounts to  $4 \pm 3$  dB and often to  $4 \pm 1$  dB. Thus, one may assume for a first approach that the measuring accuracy is better than  $\pm 3$  dB.

The experimental data oscillate around the computed data, at frequencies below 200 MHz with a considerable amplitude and above 200 MHz with a much smaller amplitude. The experimental data reveal clearly four regions:

- $\lambda/2$  resonance at 74 to 101 MHz (exp. data of insufficient accuracy)
- $3 \lambda/4$  anti-resonance at about 101 to 125 MHz
- $\lambda$  second resonance at about 125 to 158 MHz
- $> \lambda$  off-resonance at frequencies above 200 MHz.

The MET and PHA have the same length of 1.8 m, the SUB is only 1.68 m long. It seems that the body material does not influence the resonant frequencies much, and that the anti-resonance is especially weaker in lossy materials.

Above 200 MHz the difference between experiment and theory is less than  $\pm 3$  dB for all three test bodies. Taking into account that field measurements in the shadow zone are very difficult due to the large field gradients, the correlation is encouraging.

9.1.2. EFFECT OF ANTENNA-BODY DISTANCE AND BODY MATERIAL

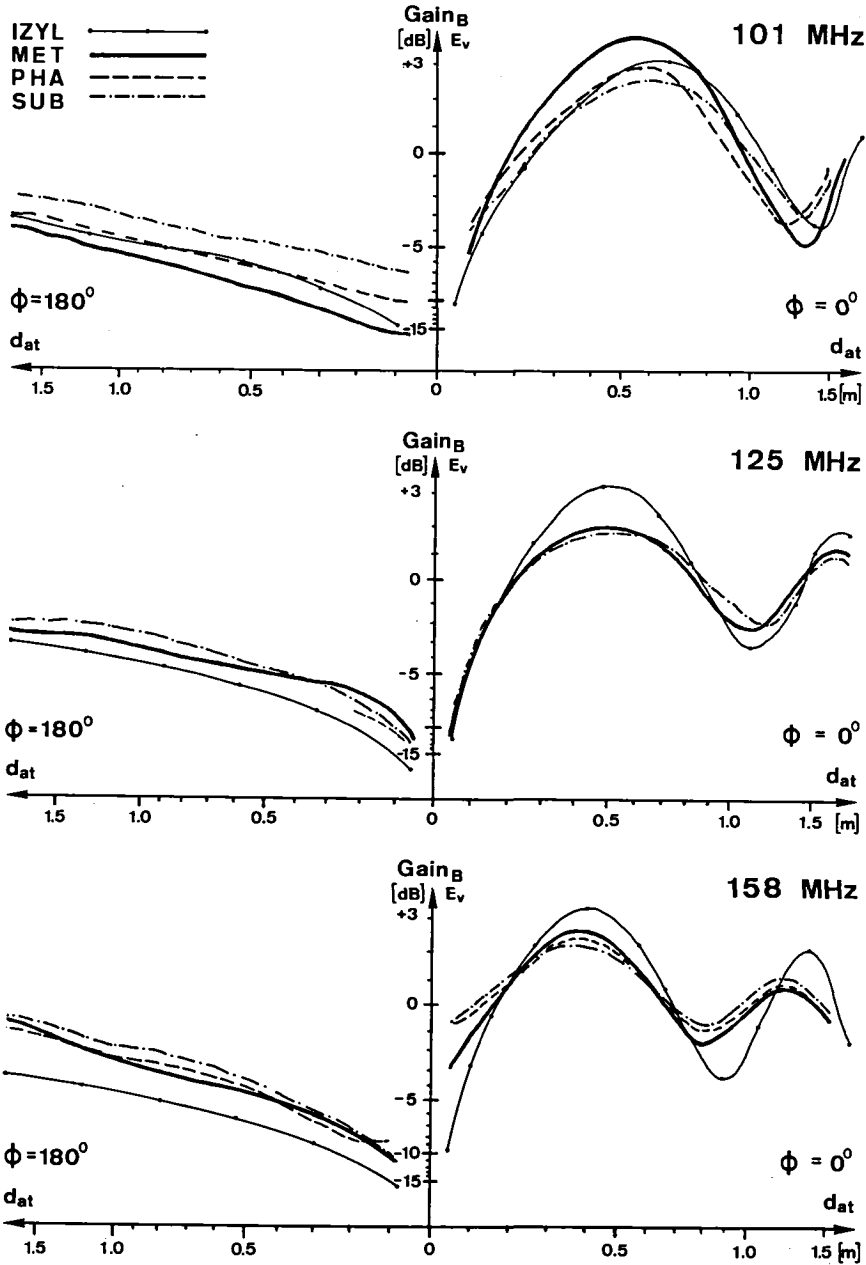


FIGURE 56 Gain<sub>B</sub> versus d<sub>at</sub> at  $\phi = 0$  and  $180^\circ$  from the three test bodies MET, PHA, SUB (measured data) compared with the computed data from IZYL.

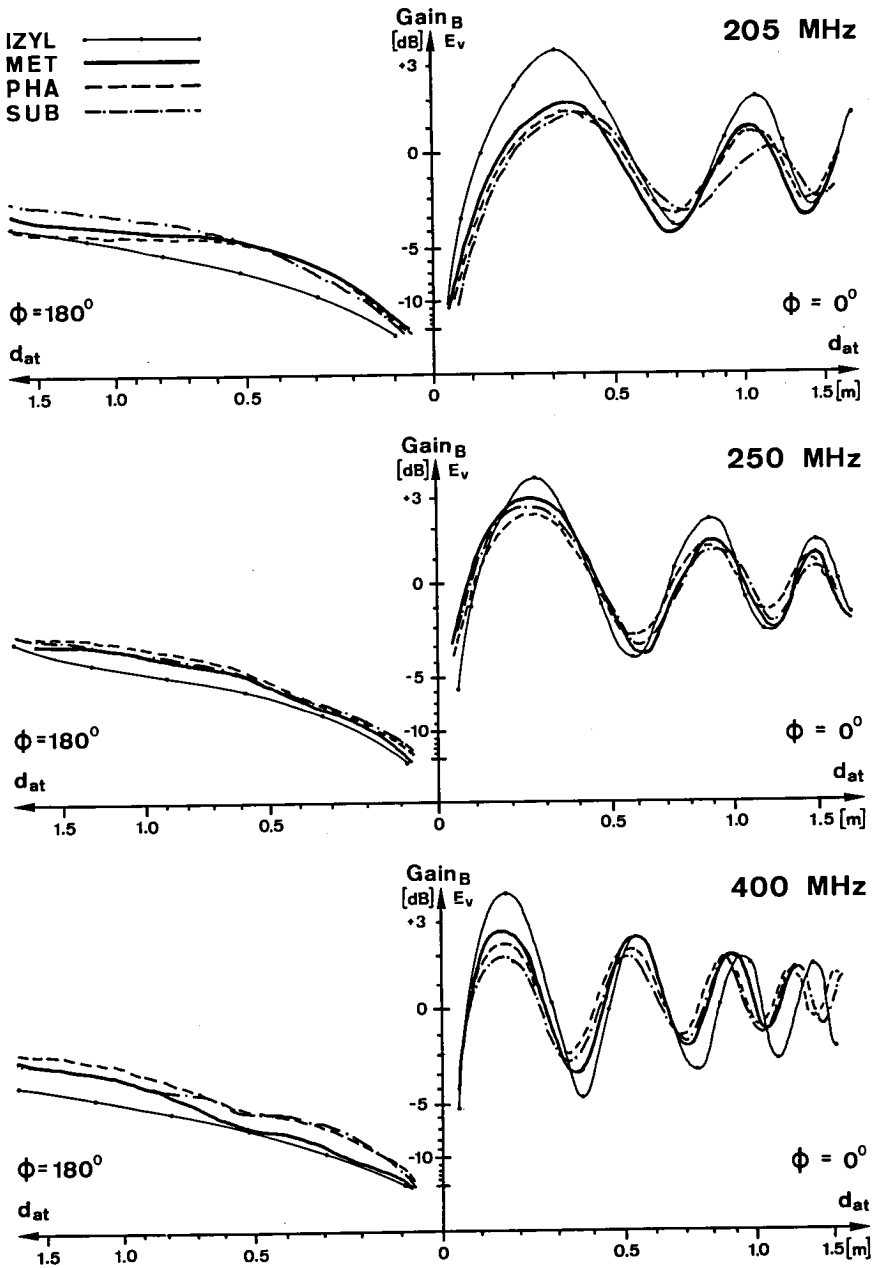


FIGURE 57  $G_{B}$  versus  $d_{at}$  at  $\phi = 0$  and  $180^\circ$  from the three test bodies MET, PHA, SUB (measured data) compared with the computational data from IZYL (continuation of FIGURE 56).

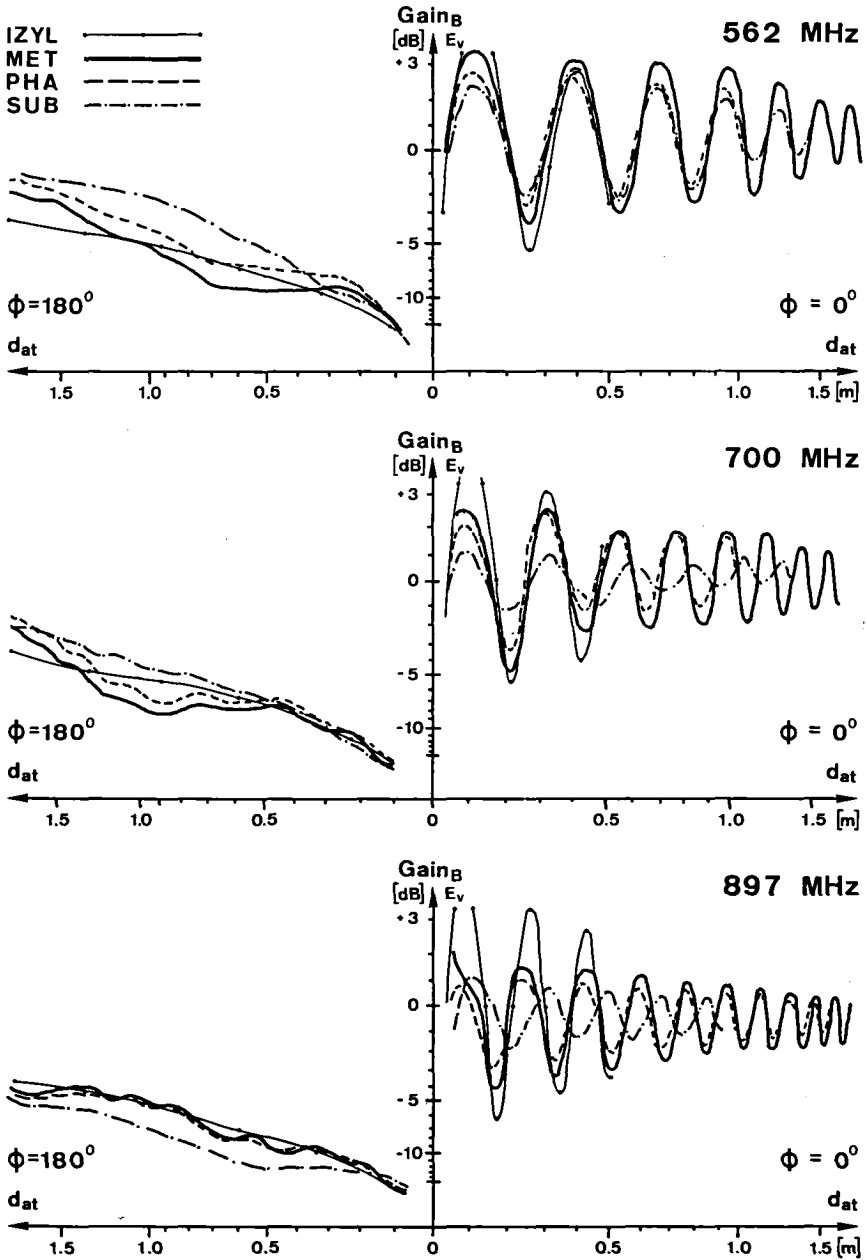


FIGURE 58 Gain<sub>B</sub> versus d<sub>at</sub> at  $\phi = 0$  and  $180^\circ$  from the three test bodies MET, PHA, SUB (measured data) compared with the computational data from IZYL (continuation of FIGURES 56 and 57).



FIGURES 56,57 and 58 are comparisons between the experimental data for the three test bodies MET,PHA,SUB and the computational data for the IZYL.

The experiments include the experimental frequencies 101, 125, 158, 205, 250, 400, 562, 700 and 897 MHz and were performed according to the check lists in section 8.5..

The computational data for the infinite cylinder (IZYL) are valid only for frequencies above 200 MHz, as explained in section 7.1.. The  $G_{\text{dB}}$  decreases with decreasing  $d_{\text{at}}$  in the shadow zone  $\phi = 180^\circ$  and oscillates around the FSL in the irradiated zone  $\phi = 0^\circ$ , with maxima at  $d_{\text{at}} \sim n\lambda/4$ ,  $n = 1,3,5,\dots$  and minima at  $d_{\text{at}} \sim n\lambda/2$ ,  $n = 0,1,2,\dots$

The experimental data agree qualitatively with the theoretical data for all frequencies and antenna-body distances. The quantitative agreement depends on the frequency range:

- Resonance region below 200 MHz. At  $\phi = 0^\circ$  the differences are smaller than 2 dB, except for 158 MHz at  $d_{\text{at}}$  below 0.1m. At  $\phi = 180^\circ$  the differences amount up to about 5 dB at  $d_{\text{at}}$  above 0.2m. Generally,  $G_{\text{dB}}$  decreases from SUB to PHA to MET. The somewhat larger differences at very small  $d_{\text{at}}$ 's seem to be caused by near-field effects.
- Off-resonance region between 200 and 400 MHz. There is an excellent agreement between experiment and theory. Generally, the accuracy is better than 3 dB for all  $d_{\text{at}}$ 's and  $\phi$ 's. There are no significant differences between the three test bodies.
- High frequencies above 400 MHz. It should be mentioned that the test antenna  $A_1$  has a length of  $\sim \lambda/4$  in this frequency region, so that  $A_1$  cannot be regarded as an actual point source. However, the difference amounts to less than 4 dB. The data for MET and PHA are very similar but differ from SUB, leading to the hypothesis that the shape of the body becomes more important than the body material.

The  $G_{\text{dB}}$  versus  $d_{\text{at}}$  diagrams demonstrate clearly a formerly unknown, systematical relation between these two quantities.

Analogous experiments at  $\phi = 90^\circ$  and  $270^\circ$  revealed similar results as shown at  $\phi = 0^\circ$ , with maxima at  $d_{\text{at}} \sim n\lambda/2$ ,  $n = 1,3,\dots$  as predicted. An application of these maxima at 0, 90 and  $270^\circ$  is shown in FIGURE 54. Similar effects occur also, if a person approaches a mobile receiver (FM, 80-120 MHz) when tuned to a weak radio station (Try it with your radio !).

### 9.1.3. EFFECT OF THE AZIMUTHAL ANGLE

If one speaks of the influence of the human body on the radiation pattern of body-mounted antennas, one means generally the azimuthal radiation pattern. Such experiments were performed by many authors, e.g., BUCHANAN, MOORE and RICHTER [12], KING and WU [50], etc.. Generally, the published results differed greatly, offering hypotheses about directive properties of the human body and impedance changes.

After the discovery of the dominant  $d_{at}$  effect, the azimuthal radiation pattern is well explainable in the off-resonance region. FIGURE 59 shows a typical azimuthal radiation pattern recording for  $d_{at}=0.035$ ,  $0.077$  and  $0.135$  m compared with the computed results at  $d_{at}=0.050$  and  $0.150$  m :

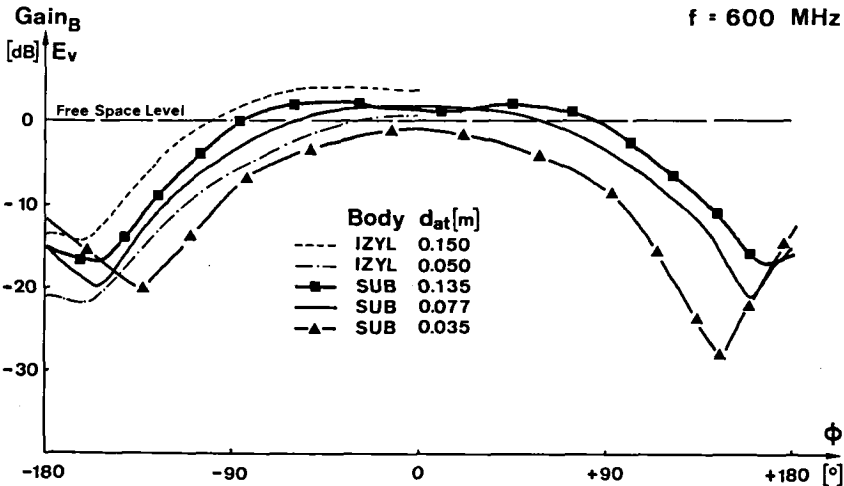


FIGURE 59 Azimuthal radiation pattern at 600 MHz. Gaining  $B$  versus  $\phi$  for the human test subject SUB compared with the computational data from IZYL.

The experimental data SUB,  $d_{at}=0.077$  and  $0.135$  m are in between the computational data from IZYL,  $d_{at}=0.05$  and  $0.15$  m. Thus, the agreement between experiment and computation is better than 3 dB for  $d_{at}$  above  $0.05$  m. The antenna-body system is an efficient directive antenna with a front-to-back ratio of up to 20 dB and a gain up to 2-3 dB. The main- and side-lobes are completely controlled by  $d_{at}$  for a given  $\phi$  (FIGURES 59, 38 and the other computer results in Appendix 16.2.1.). The experimental difference in gain and  $\phi$ , and the asymmetric shape of the curve at  $d_{at}=0.035$  m may be caused by the asymmetry of the SUB and by an inclination of  $A_1$ .

A summary of the results obtained by TEST 2 (see FIGURE 45) is shown in TABLE 60. Listed are the minimum Gaining measured with the human test subject SUB at  $d_{at} = 0.035, 0.077$  and  $0.135$  m and the minimum Gaining computed from IZYL :

MINIMUM GAIN AT VERTICAL POLARIZATION IN SHADOW ZONE FOR SUB AND IZYL													
Frequency [MHz]	25	50	75	100	150	200	300	400	500	600	700	800	900
SUB, Gaining $d_{at} = 0.035$ m [dB]	0	-8	+2	-4	-18	-20	-23	-20	-22	-28	-23	-21	-26
SUB, Gaining $d_{at} = 0.077$ m [dB]	0	-3	+4	-7	-13	-17	-21	-19	-18	-21	-21	-18	-24
SUB, Gaining $d_{at} = 0.135$ m [dB]	0	-4	--	-5	-12	-11	-15	-18	-17	-17	-21	-16	-20
IZYL, Gaining $d_{at} = 0.100$ m [dB]	-	-	-	-	-	-15	-15	-16	-17	-17	-18	-18	-19

TABLE 60 Minimum Gaining at vertical polarization in the shadow zone  $135^\circ < \phi < 225^\circ$ . Comparison between measured data (SUB) and computational data (IZYL) at different antenna-body distances  $d_{at}$ .

The experimental minima occur somewhere between  $135 < \phi < 225^\circ$ . They are symmetrical for  $d_{at} > 0.05$  m (see also FIGURE 59, the most asymmetrical recording of the whole test series). In contrast, the computed minima are always near  $\pm 165^\circ$  (see also section 10.4.) in the IZYL-model. Nevertheless, the IZYL data agree within 3 dB with the averaged experimental data at  $d_{at} 0.077$  and  $0.135$  m. Taking into account the small signals (up to -26 dB below FSL), and the large field gradients, the agreement is satisfactory for frequencies above 200 MHz (IZYL-model limit).

#### 9.1.4. EFFECT OF THE BODY MATERIAL

In the analysis 5.2.4. it was shown that the reflection coefficient for TEM, TE and TM waves is close to -1 for the E-vector and that probably differences occur only due to larger penetration depth  $\delta$ . In fact, the experimental results prove these hypotheses. The differences among MET, PHA and SUB are generally below  $\pm 3$  dB (FIGURES 56,57,58 and also 55) at  $d_{at}$  above 0.1 m. Below 200 MHz and at extreme small  $d_{at}$ 's there are somewhat larger differences caused perhaps by  $\delta$ , but also by the different shapes of the bodies. From the practical point of view, these differences

are of little interest, as long as the antenna-body distance is above approximately 0.050 m. Smaller  $d_{at}$  are only sensible with much smaller antennas, but one should take into account that  $\text{Gain}_B$  becomes very small and that the antenna gets detuned due to the extreme body proximity.

#### 9.1.5. VERIFICATION OF THE RECIPROCITY THEOREM

The complete test series TEST 1 in section 9.1.2. was performed for both transmission directions ( $A_1$  = transmitting antenna /  $A_2$  = receiving antenna and  $A_1$  = receiving antenna /  $A_2$  = transmitting antenna). The transmission loss (or  $\text{Gain}_B$ ) differed only within  $\pm 2$  dB (usually  $\pm 0.5$  dB). This holds true for all three test bodies, for all frequencies above 100 MHz and for all antenna-body distances above 0.05 m. The RF-power was always below 1 mW; it might be that at higher power levels with considerable heating effects significant differences could occur, but such power levels are beyond our application.

#### 9.2. DISCUSSION OF THE LIMITATIONS OF EXPERIMENT AND COMPUTATION

The agreement between experiment and theory is  $\pm 3$  dB at frequencies above 200 MHz and antenna-body distances above 0.1 m. Taking into account the large signal range from -26 dB up to +4 dB, the agreement is more than satisfactory. A difference of  $\pm 3$  dB around the -20 dB level corresponds to a power variation of only  $\pm 1\%$ , related to 0 dB = FSL = 100 %.

The relative simple IZYL model explains the off-resonance effects at frequencies above 200 MHz, at  $d_{at}$  above 0.1 m and for all test bodies.

The assumptions in section 5.2. could be verified. The reciprocity theorem is valid for our application as shown in 9.1.5.. The human body can be regarded as a perfectly conducting body with respect to scattering, at least for  $d_{at}$  above 0.05 m as shown in 9.1.1. and 9.1.2..

Experimental data at frequencies between 100 and 900 MHz (except 300 MHz) could be measured accurately at distances from 4 m up to 0.1 m. The lower frequency limit is mainly determined by the performance of the test antenna  $A_1$  and also by the remote antenna  $A_2$ . The main problem is the bad efficiency of electrically small antennas when operated off - resonance. Measurements with antennas tuned on resonance tend to be inaccurate as can be seen in FIGURE 55 at 300 MHz: the extreme loss with MET is caused by detuning effects due to body proximity, less accentuated with PHA and

SUB. The experimental lower limit for  $d_{at}$  is determined by the antenna dimensions and by the extremely low signal level in the shadow zone.

A problem related to all frequencies below 300 MHz is the insufficient counterpoise of the monopole antennas  $A_1$ . With the precautions in FIGURE 44 the resulting radiation from the feeding coaxial cable could be attenuated. A better solution with dipole antennas and built-in RF-generators will be shown in section 11.3..

The IZYL-antenna model has proven its usability for two-dimensional off-resonance computations at vertical E-field polarization at  $\theta_i = 90^\circ$ . An extension of the computations for frequencies at or below resonance, for arbitrary polarizations and arbitrary wave incidence is only possible with a finite body-antenna model. Such three-dimensional computations and experiments of verifications will be performed in the next sections.

## 10. THREE-DIMENSIONAL COMPUTATION OF SCATTERING FROM FINITE BODIES OF REVOLUTION

---

### 10.1. COMPUTATIONAL MODELS AND GOALS

The antenna-body models consist of perfectly conducting, finite bodies of revolution (FIGURE 28: Body models FZYL, MANMOD1 and MANMOD2), a small antenna  $A_1$  positioned at  $h_B, d_{at}$  and  $\phi$ , and an incident plane wave with an irradiation angle  $\theta_i$  to the vertical axis of the body. The computational situation is shown in the FIGURES 14 and 33: the E-field vector of the incident wave may be  $\theta$ -polarized ('vertical', def. 203) or  $\phi$ -polarized ('horizontal', def. 204); the E-field components at  $A_1$  are computed in  $\vec{a}_\theta$ ,  $\vec{a}_r$  and  $\vec{a}_\phi$  directions by help of test segments located at RTEST and ZTEST, rotated with the angle  $\phi$  around the z-axis. With these data one obtains the vertical, radial and horizontal field components  $E_v, E_r$  and  $E_h$  at  $A_1$ .

The method of solution is described in section 6.4. and is based on the extended works of HARRINGTON and MAUTZ [40] and BEVENSEE [10]. The purpose of the following (very expensive) computation is to collect numerical data in the important frequency range 10 to 500 MHz (extended resonance region of man) with regard to near-field components which influence  $G_{ain}$ . The parameters of interest are the body geometry (actual shape of the body), frequency  $f$ , antenna-body distance  $d_{at}$ , azimuthal angle  $\phi$ , antenna polarization  $p_1$  and  $p_2$ , incident irradiation angle  $\theta_i$  and the relative antenna height  $h_B$ .

### 10.2. COMPUTER PROGRAMS FOR NEAR-FIELD COMPUTATIONS

#### 10.2.1. GENERAL OVERVIEW

Due to storage capacity- and computational time limits the computation is split-up into three independent programs connected by one file:

- Program HARRA : computation of the Y-matrices
- Program PANB : computation of near-field data for some  $A_1$ -positions
- Program PANC : computation of the field homogeneity along  $A_1$ .

These programs are written in Fortran IV for a CDC 7600 computer and require a minimum storage capacity of 160,000 octal in the core memory. The data are stored in a COLLECT FILE, catalogued in HARRA, read and extended in PANB and read in PANC. There is only an auxiliary print output in HARRA and PANB, because the final data are plotted by a special routine.

The following subroutines are used several times in program HARRA,PANB:

- Subroutine LINEQ : replaces a 19 by 19 matrix Z by its inverse
- Subroutine PLANE : provides the measurement matrices for the body of revolution and for the test segments
- Subroutine PROGA : prepares the matrix variables in order to accommodate the Y-matrices read from the file
- Subroutine REORD : arranges a number of values in descending order (needed if no plotter is available)
- Subroutine NEARZ : computes the coordinates for the test segments, similar to the body coordinates in HARRA.

The complete programs and output samples are enclosed in Appendix 16.2.. Not enclosed is the plot routine, because its application is limited to the ETH computer center. The procedure to compute the near-field data can be summarized as follows:

- definition of the body geometry and frequency in HARRA
- computation of the Y-matrices for some modes and storage in a collect file in HARRA
- definition of the test segments (location and length) in PANB
- computation of the near-fields for each mode, manual test of the convergence of the results in PANB
- summation of contribution of each mode and for each azimuthal angle, manual checking of the minimum number of needed modes in PANB
- coordinate transformation of the results in order to obtain the E-field components in vertical, radial and horizontal direction, separate storage of the data in the collect file in PANB
- auxiliary output of Gaing for some significant cases in PANB
- reading of the file data, final processing and plotting or
- reading of the file data, final processing of the field homogeneity and printing in PANC.

#### 10.2.2. PARAMETER DESCRIPTION

The input parameters are described in TABLE 61; the body parameters for FZYL, MANMOD1 and MANMOD2 are enclosed in the listings of PANC in Appendix 16.2.4.. CAUTION: For convenience the computational frequency is ten times smaller than the actual frequency, and all computational dimensions are ten times larger than actual. This means that the input data

have to be scaled to the computational data. The output tables describing the body parameters, the tables with the complex field data for each test segment for the convergence test and the tables showing the contribution of each mode are presented in the computational scale. However, the final graphical outputs and the final result tables about the field homogeneity are presented in the actual scale.

INPUT PARAMETER	MEANING	UNITS
BK (REAL)	Computational wave factor = $2\pi/\lambda_{\text{actual}} * 0.1$ .	[1/m]
DTEST (REAL)	Test segment length, see FIGURE 33, computational DTEST = actual size * 10 .	[m]
F (REAL)	Computational frequency = $f_{\text{actual}} * 0.1$ in HARRA. Only used for data card identification.	[MHz]
F (REAL)	Actual frequency used in PANC.	[MHz]
KK (INTEGER)	Number of computed modes. KK=8 means that the modes 0,1,2,...7 are executed, if the corresponding Y-matrices are available.	
NN (INTEGER)	Mode number. NN is the same as n appearing in (194).	
NNPHI (INTEGER)	Number of azimuthal angle $\phi$ steps in the range from 0° to 180°. The standard NNPHI is 37.	
NP (INTEGER)	Number of points describing the generating curve, see FIGURE 32. The arc length $t_{\text{tot}}$ along this curve is divided in $(NP-1)/2 = N$ tangential unit elements $t$ from one peak of a triangle function to the next peak. It is <u>not</u> necessary that the body points are equally spaced. Standard NP is 41.	
NPHI (INTEGER)	Number of equal subdivisions of the body $\phi$ axis from 0 to $\pi$ . The standard NPHI is 20.	
NT (INTEGER)	Number of irradiation angles. The standard NT is 1, but the program is prepared for larger NT's.	
NTEST (INTEGER)	Number of test points ( $A_1$ positions $dat$ 's and $hg$ 's). The standard NTEST is 9 for PANB and 5 for PANC.	
RH (REAL)	Radius of the points describing the generation curve, see FIGURE 32. The computational RH is the actual body radius * 10.	[m]
RTEST (REAL)	Radius from the body axis to the test point, see FIGURE 33. The computational RTEST is the actual radius * 10.	[m]
RUN (INTEGER)	Control variable. If RUN = 1, program PANB computes the scattering from the direct incident wave , if RUN = 2, of the ground reflected wave.	
ZH (REAL)	Height of the points describing the generation curve, see FIGURE 32. The computational ZH is the actual height * 10.	[m]
ZTEST (REAL)	Height $hg$ of the test point, see FIGURE 33. The computational ZTEST is $h_{\text{Bactual}} * 10$ .	[m]

TABLE 61 Input parameter names used in programs HARRA, PANB and PANC



OUTPUT AND FILE PARAMETER NAMES		MEANING	UNITS
DA	(REAL)	length of the body in z-axis, actual scale	[m]
DAV	(REAL)	logarithmic difference $\delta E, p_1$ vertical or hor.	[dB]
DAR	(REAL)	logarithmic difference $\delta E, p_1$ radial	[dB]
DI	(REAL)	antenna-body distance $dat$ , from body point No. 22, def. at PANB 336, actual scale	[m]
DU	(REAL)	diameter of the body, at body point No. 20, def. at PANB 332, actual scale	[m]
DPV	(REAL)	phase variation $\delta\phi$ along the antenna axis, $p_1$ vertical or horizontal	[°]
DPR	(REAL)	phase variation $\delta\phi$ along antenna axis, $p_1$ rad.	[°]
EAV	(REAL)	logarithmic difference $\Delta U, p_1$ vertical or hor.	[dB]
EAR	(REAL)	actual to averaged $U_{ind}$ $p_1$ radial	[dB]
EPH	(COMPLEX)	E-field $\vec{a}_\phi$ -direction amplitude of one mode, of	[V/m]
ERAD	"	" $\vec{a}_r$ " one test point, for $\phi =$	
ETH	"	" $\vec{a}_\theta$ " $00, \theta_i, E_{inc}$ and $E_{inc}$	
EPTOT	(COMPLEX)	E-field $\vec{a}_\phi$ -direction added amplitudes up to	[V/m]
ERTOT	"	" $\vec{a}_r$ " the last computed mode,	
ETTOT	"	" $\vec{a}_\theta$ " else identical to above	
EHTOT	(COMPLEX)	E-field horizontal field strength components	[V/m]
ESTOT	"	" radial including all modes for	
EVTOT	"	" vertical all $\phi$ 's, one test point	
GHTOT	(REAL)	E-field horizontal amounts of the components	[V/m]
GSTOT	"	" radial in dB, including all modes	
GVTOT	"	" vertical for all $\phi$ 's, one test p.	
PHTOT	(REAL)	Phase horizontal phases of the field com-	[°]
PSTOT	"	of radial ponents GHTOT, GSTOT and	
PVTOT	"	E-field vertical GVTOT	
H0	(REAL)	relative antenna height $h_B$ , actual size	[m]
IT	(INTEGER)	control variable for test segment orientation	
ITE	(INTEGER)	index test point	
L	(INTEGER)	index irradiation angle	
M	(INTEGER)	index mode	
NST	(INTEGER)	number of stored final data: NTEST*NNPHI(H,S,V)	
NZ	(INTEGER)	number of stored Y-elements: $(NP-3)^2(Y1,Y2,Y3,Y4)$	
POL	(INTEGER)	control variable: $1=E_{\theta}^{inc}, 2=E_{\phi}^{inc} (p_2)$	
SYH	(COMPLEX)	stored final data, horizontal components	[V/m]
SYS	(COMPLEX)	stored final data, radial components	[V/m]
SYV	(COMPLEX)	stored final data, vertical components	[V/m]
TJ	(REAL)	arc length along generating curve to the $j$ th triangle function (HARRA), computational scale	[m]
X1	(REAL)	irradiation angle $\theta_i$ or $180^\circ - \theta_i$ , (RUN 1,2)	[°]
Y1-4	(COMPLEX)	Y-matrices elements $(Y_{ij}^{tt}), (Y_{ij}^{tt}), (Y_{ij}^{t\phi}), (Y_{ij}^{\phi\phi})$ , first run $n=0$ , next run $n=1, 2, \dots, NN$	
Z	(COMPLEX)		
S164M07	(FILE)	S = code MANMOD 2, 164 = 164 MHz, M07 = max. mode 7	
S164D9	(FILE)	S = code MANMOD 2, 164 = 164 MHz, D9 = 9 dat's	
F100D5	(FILE)	F = code FZYL, 100 = 100 MHz, D5 = 5 dat's	

TABLE 62 Output and file parameter names in programs HARRA, PANB, PANC

### 10.2.3. PROGRAM DESCRIPTION HARRA

The computer program HARRA is based on the theory in section 6.4.1. and 6.4.2.. In the presented form (Appendix 16.2.2.) it computes the Z-matrices for the body MAMMOD2 for the actual frequency 164 MHz, performs the matrix inversion and stores the Y-matrices Y1 to Y4 for the modes 0 to 7 in the collect file AMAT2 with the code name S164M07.

The source program is the program A developed and well described by HARRINGTON and MAUTZ [40]. It runs on an IBM computer. Because our computer center is equipped with a CDC-computer, the source program has been altered to the present program HARRA. The modifications regard mainly the structure of the program parts, the conversion of some characters and the file generation. Only the input and file procedure are discussed here; details can be studied in the above mentioned source program description.

Punched card data about mode number, number of body points,  $\phi$ -subdivisions, k-factor and frequency (computational scale) is read early in the main program:

```
50 READ (1,51) NN, NP, NPHI, BK, F          HARRA 47
51 FORMAT (3I3, E14.7, F8.2)                HARRA 48
```

The number F is only used for punched card data identifications and is not used for computations. Because we need all modes from 0,1,2,...7 in our example, there are 8 data cards, only differing in the first number for NN. If the last mode is executed, the program stops due to the statement:

```
      IF (EOF (1)) 52,49                     HARRA 49
49 CONTINUE                                  HARRA 50
52 STOP                                      HARRA259
```

Punched card data about the body contour (MANMOD2) is read later:

```
      READ (1,53) (RH(I),I=1,NP)             HARRA 51
      READ (1,53) (ZH(I),I=1,NP)             HARRA 52
53 FORMAT (10F8.4)                           HARRA 53
```

For each mode a complete set of data is required. With an earlier reading of the number NP only one reading of the body data would be required, but for a better overview on the program the presented procedure is more convenient.

For each mode the Y-matrices are computed and printed separately. The

output (see example in Appendix 16.2.2.) consists of the listing of the input data, the 19 arc lengths along the generation curve and 4 Y-matrices of 19 x 19 complex elements (see theory in section 6.4.2.2.). The Y-matrices are stored on the collect file according to:

PERMF,AMAT2.	(first run)	HARRA	4
PUBLIC, COLLECT.	(first run)	HARRA	7
COLLECT,N=AMAT2.	(first run)	HARRA	8
CATALOG,AMAT2.	(first run)	HARRA	9
or			
ATTACH,AMAT2,PW..	(following runs)	HARRA	13
PUBLIC, COLLECT.	(following runs)	HARRA	16
COLLECT,M=AMAT2.	(following runs)	HARRA	17
PROGRAM HARRA (...TAPE 6 = DISK)			HARRA 21
WRITE (6) (Z(I),I=1,NZ)			HARRA242
ADD, S164M07, DISK, RO.			HARRA334
LIST			HARRA335
END			HARRA336

Due to the LIST statement all existing names of the files in AMAT2 are listed.

#### 10.2.4. PROGRAM DESCRIPTION PANB

The computer program PANB is based on the theory in section 6.4.5.. In the presented form (Appendix 16.2.3.) it reads the Y-matrices from the collect file, computes the current densities on the body of revolution MANMOD2 for the specified incident wave, computes the incident, the scattered and the total E-field at a specified test segment near the body, determines the field components in vertical, radial and horizontal directions, delivers some tables for accuracy considerations, prints an auxiliary output and stores the final data in the same collect file AMAT2 with the code name S164D9 (or in a new collect field HOMOG with the code name F100D5, see description program PANC).

The source program is the program HARRDF, developed and well described by BEVENSEE [10]. HARRDF is an extension of the program D by HARRINGTON and MAUTZ [40], so that both reports have to be consulted for a detailed understanding. HARRDF runs on an IBM computer and delivers the field components in  $\vec{a}_\theta$ ,  $\vec{a}_r$  and  $\vec{a}_\phi$  directions at one test point, for  $\phi = 0^\circ$  and for each single mode. The source program has been altered to the present program PANB. The modifications regard mainly the structure of the pro-

gram parts, the preceding computation of the Y-matrices (now in HARRA), the conversion of some characters (CDC-notations), the  $\theta_i$ -handling, the extension on the computation of the  $\phi$ -dependence, the summation of the contributions of each mode, the coordinate transformation of the results, the output procedure and the file generation. A major problem was the reduction of the storage requirement from the original 662,513 octal to 160,000 octal. Only the input and some important procedures are discussed here; the principle of the method is described in section 6.4.5. and the computational details in the above mentioned reports.

Punched card data about the number of modes, number of body points,  $\phi$ -subdivisions, number of incident angles, number of test points, number of azimuthal steps, k-factor and wave origin is read early in the main program in computational scale:

50 READ (1,51) KK, NP, NPHI, NT, NTEST, BK, RUN	PANB 62
51 FORMAT (6I3, E14.7, 2X, I2)	PANB 63

Usually only one corresponding data card is necessary, but more than one is possible similar to the input section in program HARRA. Next the card data about the body contour (MANMOD 2) are read:

READ (1,53) (RH(I), I=1, NP)	PANB 67
READ (1,53) (ZH(I), I=1, NP)	PANB 68
53 FORMAT (10F8.4)	PANB 69

Next an integer array TEXT(9) is filled with the letters for the words "VERTIKAL", "HORIZONTAL", "RADIAL", "DIREKTE EINSTRABLUNG" (means direct irradiation) and "REFLEKTIERTE EINSTRABLUNG" (means irradiation by a wave reflected from the ground) to be used in the output tables. The input data appear first in the output listing due to the statements

JA=RUN*3+1	PANB 79
⋮	⋮
WRITE (3,46) (ZH(I), I=1, NP)	PANB 91

The irradiation angle  $\theta_i$  is set to  $80.78^\circ$  (direct wave, RUN = 1) and  $103.36^\circ$  (reflected wave, RUN = 2) due to the statements

DT = 0.394	[DT = PI/(NT-1) ]	PANB 111
DO 1 J=1, NT	[DO 1 J=1, NT ]	PANB 112
THR(J) = DT*(J-1) + 1.410	[THR(J) = DT*(J-1)]	PANB 113
IF(RUN.EQ.2) THR(J) = DT*J+1.410		PANB 114

For equally spaced  $\theta_i$ -steps the [statements] must be used and all arrays concerning the  $\theta_i$ -variable (L=1, NT) have to be changed (PANB 39 to 50).

After some initial computations the punched card data about the 9 test points are read :

```
      READ (1,49) (RTEST(J), ZTEST(J), DTEST(J), J=1,NTEST      PANB 173
49 FORMAT (3F8.4)                                           PANB 174
```

For a given mode subroutine PLANE is called with its 5<sup>th</sup> argument IT=1 to compute the incident plane wave components VVR(1,J) on the J<sup>th</sup> field triangle on the body:

```
      CALL PLANE (VVR,THR,NP,NT,1,R,ZS,SV,CV,T,TR)           PANB 199
```

In contrast to the source program the Y-matrices are read from the collect file, called by PROGA which prepares only the matrices accommodations.

```
      CALL PROGA                                           PANB 200
127 READ (6) (Y(I),I=1,NZ)                               PANB 202
```

In the DO 41 loop E3(L,J) and E3(L,J+NM) measure the current densities for the L<sup>th</sup> incident angle of the  $E_0^{inc}$  ( $p_2$  = vertical, see FIGURE 33) while E4(L,J) and E4(L,J+NM) measure corresponding current densities of the  $E_0^{inc}$  ( $p_2$  = horizontal, see FIGURE 33) in  $\vec{t}$  and  $\vec{\phi}$  directions (FIGURE 32):

```
      E3(L,J) = E3(L,J) + Y(J1)*VVR(1,I1)-Y(J2)*VVR(1,I2)    PANB 221
      E4(L,J) = E4(L,J) - Y(J1)*VVR(1,I3)+Y(J2)*VVR(1,I4)    PANB 222
```

With  $J_t$  and  $J_\phi$  the current densities per unit length in azimuth and along  $t$ , respectively, at the peak of the J<sup>th</sup> triangle, for a certain  $\theta^{inc}$ ,

$$E_\theta^{inc} \quad J_{Jt}(\phi) \quad \left\{ \begin{array}{ll} \frac{E3(L,J)}{RH(J2)} & NN = n = 0 \\ \frac{E3(L,J)}{RH(J2)} 2 \cos n\phi & n \geq 1 \end{array} \right. \quad (240)$$

$$\text{polarization} \quad J_{J\phi}(\phi) \quad \left\{ \begin{array}{ll} 0 & n = 0 \\ \frac{E3(L,J+NM)}{RH(J2)} j 2 \sin n\phi & n \geq 1 \end{array} \right. \quad (241)$$

These formulas are similar for  $E_\phi^{inc}$  polarization (see BEVENSEE [10]) and can be used to compute the current density  $\vec{J}$  in equation 128 at any point on the body surface, if one sums the contributions of all modes for each azimuthal angle separately.

In the following discussions only the  $E_\theta^{inc}$  polarization will be considered, but all the data from  $E_\phi^{inc}$  are computed, printed and stored. With E3(L,J)

stored for a given mode, for each incident angle  $l$ , and for each triangle function  $J$ , the scattered field for that mode can be determined from them for all test segments in succession. Thus, the DO loop 7100 over the test segments, NEARZ determines the near-field matrix  $ZM$  for a given test segment, and PLANE yields its sampled incident field for all angle of incidence. Both test segment orientations for  $IT=1$  and  $IT=2$  are treated:

DO 706 IT=1,2

PANB 251

The test segment fields are approximated according to equation 220. The  $ESC(IT,1)$  and  $ESC(IT,2)$  at PANB 257 are proportional to the scattered field mode amplitudes in the  $\vec{a}_r$  and  $\vec{a}_\phi$ -directions for  $IT=1$ , and in the  $\vec{a}_\theta$  and  $\vec{a}_\phi$ -directions for  $IT=2$ , respectively. From statement 702 to 711 the incident, the scattered and the total E-fields in  $\vec{a}_r$  (ERAD),  $\vec{a}_\theta$  (ETH) and twice in  $\vec{a}_\phi$  (EPH) - directions are computed and printed for the regarded mode  $M$ , irradiation angle  $L$ , test segment  $ITE$  and both wave polarizations. The use of the two EPH's will be discussed in section 10.3.4.2..

With the advice of BEVENSEE [10] the program has been extended to compute the total field components for different azimuthal angles. The key formulas are: (ERAD:ETR, ETH:ETH, EPH: ETP1 and ETP2 inside the program)

$$E_r^{tot}(r_T, z_T, \phi) = \sum_{M=0}^{KK-1} ETR(M, ITE, L) \begin{matrix} \cos M\phi, E_\theta^{inc} \\ j \sin M\phi, E_\phi^{inc} \end{matrix} \quad (242)$$

$$E_\theta^{tot}(r_T, z_T, \phi) = \sum_{M=0}^{KK-1} ETH(M, ITE, L) \begin{matrix} \cos M\phi, E_\theta^{inc} \\ j \sin M\phi, E_\phi^{inc} \end{matrix} \quad (243)$$

$$E_\phi^{tot}(r_T, z_T, \phi) = \sum_{M=0}^{KK-1} ETP_2^1(M, ITE, L) \begin{matrix} j \sin M\phi, E_\theta^{inc} \\ \cos M\phi, E_\phi^{inc} \end{matrix} \quad (244)$$

These computations are performed by the statements

909 DO 506 M=1, KK

PANB 361

NN = M-1

PANB 362

ERTOT = ERTOT + ETR(M, ITE, L)\*COPHI(M, J)

PANB 363

ETTOT = ETTOT + ETT(M, ITE, L)\*COPHI(M, J)

PANB 364

EPTOT = EPTOT + ETP(M, ITE, L)\*SIPHI(M, J)

PANB 365

where ETP is the averaged value of the two EPH's and the trigonometric functions COPHI and SIPHI are the previously computed numbers:

EPR = (ETP1R+ETP2R)/2 \$ EPI = (ETP1I+ETP2I)/2

PANB 295

ETP(M, ITE, L) = COMPLX(EPR, EPI)

PANB 296

COPHI(M, J) = COS(NN\*PHI(J))

PANB 189

SIPHI(M, J) = U\*SIN(NN\*PHI(J))

PANB 190

In order to monitor the contribution of each mode (see later in section 10.3.4.1.) the continuously summed up field components are listed in the output for  $\phi = 0, 90$  and  $180^\circ$ . The sample output shows the results for one  $\theta_j$ , the 9 test points ( $h_b = \text{constant} = 1 \text{ m}$ ,  $d_{at} = \text{DIST} = \text{parameter}$ ), for  $E_\theta^{\text{inc}}$  and for the actual frequency 164 MHz, according to:

40 CONTINUE	PANB 330
F=3000.*BK/(2*PI)	PANB 331
:	:
IF(J.EQ.19) WRITE (3,545) NN,ERTOT,EPTOT,ETTOT	PANB 376
913 CONTINUE	PANB 378

From the last ERTOT, EPTOT, ETTOT the corresponding field components are computed in vertical, horizontal and radial directions : EVTOT, EHTOT and ESTOT. They are also stored as SYV(JDI), SYH(JDI) and SYS(JDI) :

JDI=0	PANB 350
JDI=JDI+1	PANB 379
EVTOT = ERTOT * COTN(ITE) - ETTOT * SITN(ITE)	PANB 380
SYV(JDI) = EVTOT	PANB 381
EHTOT = EPTOT	PANB 382
SYH(JDI) = EPTOT	PANB 383
ESTOT = ERTOT * SITN(ITE) + ETTOT * COTN(ITE)	PANB 384
SYS(JDI) = ESTOT	PANB 385

The numbers COTN(ITE) and SITN(ITE) are the sin and cos of the  $\alpha$ -vector already computed in PANB 177 for the different test points. Next the field components are scaled in dB and the phase angles are computed:

PP = CMPLX(1.0E-32, 1.0E-32)	PANB 333
QQ = 1.0E-32	PANB 334
IF(CABS(EVTOT).LT.QQ) EVTOT = PP	PANB 386
:	:
GVTOT(ITE,L,J) = 20.*ALOG10(CABS(EVTOT))	PANB 389
:	:
PVTOT(ITE,L,J) = ATAN2(REAL(EVTOT),AIMAG(EVTOT))*PR	PANB 392
:	:
504 CONTINUE	PANB 396

For the later use of the results in the plot programs or in PANC, the complex original data are stored in the collect file:

ATTACH,AMAT2,PW..	PANB 4
CALL,S164M07,P=AMAT2,B=DISK. (for Y-matrices)	PANB 5
PROGRAM PANB (...TAPE 6 = DISK, TAPE 7 = RESULT)	PANB 13
WRITE (7) (SYV(I),I=1,NST)	PANB 397
WRITE (7) (SYH(I),I=1,NST)	PANB 398
WRITE (7) (SYS(I),I=1,NST)	PANB 399
ADD, S164D9, RESULT,RO. (or S100D5 for later PANC)	PANB 768

The remaining of the program PANB is concerned with the graphical output of the amplitude and the phase of Gaing. Due to the statements

DO 918 I=1,3  
J = (I\*18)-17

PANB 400  
PANB 401

only the results for  $\phi=0, 90$  and  $180^\circ$  are printed. By changing these cards into DO 918 I=1,37 and J=I all azimuthal results would be printed. Only the  $p_1$ =vertical polarization is executed by the output procedure. By changing PANB 402, 403 and 431 and duplicating the program from PANB 404 to 463 (change labels) one also obtains the other  $p_1$ -data. The  $E_\phi^{inc}$  output ( $p_2$ =horizontal) is already incorporated in the program due to the DO loop 912 in PANB 239, but not shown in the sample output.

Similarly, the results for the next program PANC are computed for all  $p_1$  and  $p_2$ . The only difference is, that the results are stored in the collect file HOMOG, and that only 5 test points are needed.



### 10.2.5. PROGRAM DESCRIPTION PANC

The computer program PANC is an extension to program PANB and is based on the investigation in section 5.2.2.. It reads the vertical polarized E-data of P1, P4, P5, the radial polarized E-data of P1, P2, P3 and the horizontal polarized E-data of P1 (see FIGURE 63) for all azimuthal angles  $0 \leq \phi \leq 180^\circ$  ( $J = 1$ , NNPHI) from the collect file HOMOG. It computes the horizontal E-data of P6 and P7, so that the fields at the center and at the ends of a dipole antenna of  $2h=0.1\text{m}$  are available for  $p_1 = \text{vertical/radial}$  at  $p_2 = \text{vertical}$  and  $p_1 = \text{horizontal/radial}$  at  $p_2 = \text{horizontal}$ . Then it computes the amplitude variation  $\delta E$  and the phase variation  $\delta\phi$  along the antenna polarization axes, the logarithmic difference  $\Delta U$  between the induced voltage computed by  $E_{\text{center}} \cdot 2h$  and the numeric integral  $\int_{-h}^{+h} E(\xi) \cdot d\xi$  where  $\xi = p_1$ , and prints all data versus  $\phi$  in tables which can be directly applied for field homogeneity considerations and antenna design. The sample program is specified for the body model FZYL at 100 MHz and  $d_{\text{at}}=0.1\text{m}$ . The listing of the program and results for the frequencies 65,75,100,125,300 and 425 MHz are enclosed in Appendix 16.2.4..

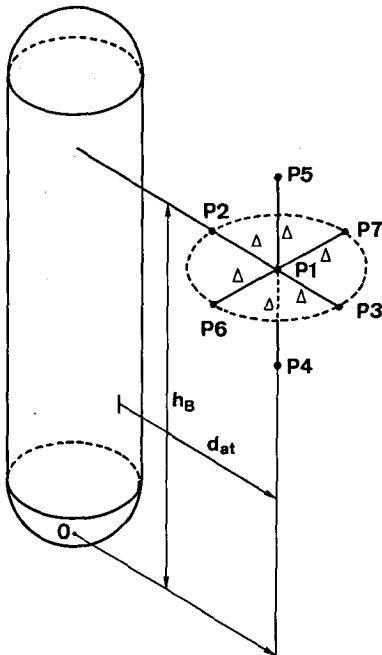


FIGURE 63

Body model FZYL and antenna A1 with its center at P1.

Antenna polarization  $p_1$ :

$p_1 = \text{vertical}$  : P4, P1, P5

$p_1 = \text{radial}$  : P2, P1, P3

$p_1 = \text{horizontal}$ : P6, P1, P7

Antenna length  $2h = 2\Delta = 0.1\text{m}$

Antenna height  $h_B = 1\text{m}$

Ant.body dist.  $d_{\text{at}} = 0.1\text{m}$

Body diameter  $D_B = 0.25\text{m}$

Body length  $L_B = 1.8\text{m}$



In the DO loop 700 the J-dependent variables ITE1 for P1, ITE2 for P2,.. ITE5 for P5 are computed by the statements PANC 97 to 101. For each azimuthal angle  $0 \leq \phi \leq 180^\circ$  ( $J=1, \text{NNPHI}$ ) the amounts of the fields at P1,P5,P4 (vertical components) and at P1,P3,P2 (radial components) are computed according to

```

AMV1 = CABS(SYV(ITE1)) $ AMR1 = CABS(SYS(ITE1))      PANC 114
AMV5  "    ITE5  $ AMR3  "    ITE3      PANC 115
AMV4  "    ITE4  $ AMR2  "    ITE2      PANC 116

```

The phases of the fields at these points are computed due to

```

PV1 = ATAN2(REAL(SYV(ITE1)),AIMAG(SYV(ITE1))) * PR    PANC 117
:
```

The phase differences  $\delta\phi$  along the p<sub>1</sub>-vertical/radial axes is computed by:

```

DPV1 = ABS(PV5-PV4) $ DPV2 = 360.-DPV1              PANC 123
:
```

```

IF(ABS(DPV2).LT.ABS(DPV1)) DPV1 = DPV2 $ DPV = ABS(DPV1) PANC 125
:
```

Then the dB-values of the fields are computed according to

```

AV1 = 20.*ALOG10(AMV1) $ AR1 = 20.*ALOG10(AMR1)      PANC 133
:
```

The numerical integration of the E-field along the antenna axis is simply the sum of  $(\text{AMV5}+\text{AMV1})\cdot h/2 + (\text{AMV4}+\text{AMV1})\cdot h/2$  and corresponds to the actual induced voltage  $U_{\text{ind}}$  (see section 5.2.2.). The mean induced voltage  $\bar{U}_{\text{ind}}$  is  $\text{AMV1}\cdot 2h$ . The logarithmic difference  $\Delta U$  in dB is  $20 \log (\bar{U}_{\text{ind}}/U_{\text{ind}})$  :

```

EAV = 20.*ALOG10(((4.*AMV1)/(AMV5+AMV4+2.*AMV1)))    PANC 136
EAR  "    "    R1    R3    R2    R1                  PANC 137

```

The amplitude variation  $\delta E$  is computed according to

```

DAV = ABS(AV5-AV4) $ DAR = ABS(AR3-AR2)              PANC 138

```

After the checking of the size of AV1 and AR1 (PANC 139 and 142) the results  $\phi$ , E(dB) center,  $\phi$  center,  $\Delta U$ ,  $\delta E$  and  $\delta\phi$  are printed for p<sub>1</sub>=vertical and radial at p<sub>2</sub>=horizontal due to the statement PANC 145.

In the second run POL=2 (PANC 58) the p<sub>2</sub>=horizontal data are read from the collect file by the same statements PANC 59,60 and 61. After the output statements the field data are rearranged as follows in DO loop 700:

```

IH1 = J-2 $ IH2 = J+2 $ NC = NNPHI-1                PANC 94
IF(J.EQ.1) IH1 = J+2 $ IF(J.EQ.2)   IH1 = J          PANC 95
IF(J.EQ.NC) IH2 = J   $ IF(J.EQ.NNPHI) IH2 = J-2      PANC 96

```

At POL = 2 the vertical components SYV(J) are not used. In order to apply the same procedure as for POL = 1 the horizontal components around the center point P1 ( $\phi = \pm 10^\circ$ , see FIGURE 64) P1(J-2), P1(J) and P1(J+2) are transferred into the vertical component arrays of P1, P5 and P4:

IF(POL.EQ.1) GOTO 4	PANC 103
SYV(ITE1) = SYH(ITE1)	PANC 104
SYV(ITE5) = SYH(IH1)	PANC 105
SYV(ITE4) = SYH(IH2)	PANC 106
4 CONTINUE	PANC 107

Now the amplitude difference D1 and D2 (FIGURE 64) is computed and the approximated amounts at P6 (now called P5) and P7 (now called P4) are determined, and the phase difference  $\delta\phi$  is obtained by  $\delta\phi' \cdot \text{FAC}$  :

IF(POL.EQ.1) GOTO 5	PANC 127
D1 = AMV1-AMV5 \$ D2 = AMV1-AMV4	PANC 128
AMV5 = AMV1-D1*FAC \$ AMV4 = AMV1-D2*FAC	PANC 129
IF(AMV5.LT.QQ) AMV5 = QQ \$ IF(AMV4.LT.QQ) AMV4 = QQ	PANC 130
DPV = DPV*FAC	PANC 131
5 CONTINUE	PANC 132

The rest of the procedure is analogous to the computation of the field parameters at  $p_2 = \text{vertical}$ .

The output consists of two tables. The first table contains the field data  $p_1 = \text{vertical/radial}$  at  $p_2 = \text{vertical}$  , and the second table contains the field data  $p_1 = \text{horizontal/radial}$  at  $p_2 = \text{horizontal}$ . The model body and the antenna positions are explained in the table head. The data are ranging from  $0 \leq \phi \leq 180^\circ$ . The output parameters are:

GAIN CENTER DB	= amount of the field at P1 in [dB]
PHASE CENTER DEG	= phase of the field at P1 in [ $^\circ$ ]
MEAN ERROR DB	= logarithmic difference $\Delta U$ in [dB]
MAXIMUM GAINVAR DB	= logarithmic difference $\delta E$ in [dB]
MAXIMUM PHASEVAR DEG	= phase variation $\delta\phi$ in [ $^\circ$ ]

The results of PANC are discussed in section 10.3.5.1.

### 10.3. INVESTIGATION OF PROGRAM LIMITATIONS AND COMPUTATIONAL ACCURACY

#### 10.3.1. PROGRAM LIMITATIONS

The limitations of the program HARRA and PANB are defined by BEVENSEE [10] and HARRINGTON and MAUTZ [40] and are interpreted as follows:

- The programs are written for perfectly conducting bodies of revolution in free space.
- The wave-number  $k = 2\pi/\lambda$  should be such that the peaks of the triangle functions are not more than  $\lambda/2\pi$  apart. For a given  $\lambda$  this condition determines the number NP (number of points describing the generation curve). The arc length along the generation curve  $t_{tot}$  (see FIGURE 32) is divided in HARRA by  $(NP-1)/2 = N$  tangential unit elements  $t$  of equal lengths. This length should not be larger than  $\lambda/2\pi$  in order to prevent field oscillation between two peaks of the triangle functions. If we assume the standard NP of 41 and an arc length of the human body of  $t_{tot} = 2\text{ m}$ , we obtain the maximum permissible frequency  $f_{lim5}$ :

$$f_{lim5} = \frac{(NP-1)/2 \cdot c}{t_{tot} \cdot 2\pi} = 500 \text{ MHz} \quad (243)$$

- The number of subdivisions of the  $\phi$ -axis, NPFI, should be large enough so that  $\pi(n_{max})/NPFI < 1 \text{ rad}$ ,  $n_{max}$  being the number of the last azimuthal mode employed. In addition,  $(2\pi/\lambda) (\pi/NPFI) \cdot \rho_{max} < 1 \text{ rad}$ ,  $\rho_{max}$  being the maximum radial cylindrical coordinate of the body contour. These conditions are interpreted as follows:
- We assume a plane wave at  $\theta_i = 90^\circ$ ,  $\vec{k} \parallel x$ -axis. The  $\phi$ -axis is subdivided in  $\pi \cdot n_{max}/NPFI$  sectors with the arc length  $w$  and the angle  $\phi_w$ . The phase along  $w$  should not vary more than  $\lambda/2\pi$  in order to prevent field oscillations within a sector. For small  $\phi_w$  the projection of  $w$  to the  $\vec{k}$ -axis amounts to  $w \cdot \sin \phi$ . The maximum permissible  $n_{max}$  for a given  $f = 300 \text{ MHz}$ ,  $\rho_{max} = 0.125 \text{ m}$  and  $NPFI = 20$  for all sectors amounts to:

$$n_{max} = \frac{\lambda \cdot NPFI}{2\pi \cdot \pi \cdot \rho_{max}} \cdot \frac{1}{\sin \phi} = 8 \quad (244)$$

Equation (244) is valid for all  $\phi$ . If we consider the interesting special case  $\phi = 0^\circ$  (or  $180^\circ$ ) and  $d_{at} < 0.2 \text{ m}$ , the sectors with  $\phi$  near  $0^\circ$  (or  $180^\circ$ ) are of greater influence than those with  $\phi$  near  $\pi/2$ . Thus,  $n_{max}$  may be as large as 10 for 500 MHz without large accuracy loss.

- The convergence of the computed current densities to their correct values along the surface increases with NP and NPHI and should be rapid if both circumferences ( $2 \cdot t_{\text{tot}}$  and  $\rho_{\text{max}} \cdot 2\pi$ ) remain  $< \lambda$ . In our case with  $\theta_i \sim 90^\circ$  the body radius sets the limit. With a  $\rho_{\text{max}} = 0.125$  m the convergence may worsen at frequencies above 380 MHz.
- Near-field computations of a point field with a test segment tend to be inaccurate unless both these conditions are fulfilled:
  - a.) minimum distance of the test segment center to the body surface  $> \lambda$
  - b.) test segment length  $< \lambda/4$ .

When the test segment is very near to the body surface it usually does not measure the point field accurately. But if it has a length equal to one of the triangle functions it measures, at the position of that triangle function, the integral of electric field according to the network equation obtained with that function. The length of a triangle element is about 0.09 m (actual) and the length of a test segment is  $4 \cdot D_{\text{TEST}} = 0.08$  and 0.20 m (actual) which is smaller than  $\lambda/4$  at frequencies below 375 MHz. The distance of the test segment to the body surface, however, is generally much smaller than  $\lambda$  ( $d_{\text{at}}$  from 0.05 m to about 1 m). Thus, computations have to be performed with different test segment lengths, at test frequencies around the wanted frequency and the influence of each mode has to be monitored.

The program PANC is limited on  $d_{\text{at}} = 0.1$  m but is valid for all frequencies. For other  $d_{\text{at}}$ 's see the program description in 10.2.5..

### 10.3.2. COMPUTATIONAL TIME LIMITATIONS

With the standard NP of 41 and the standard NPHI of 20 one obtains for each mode 4 matrices of the size  $19 \times 19$  (complex elements). The computational time depends on the matrix inversion time and thus on the matrix size and on the number of modes. As an example program HARRA requires for the computation of 9 modes at the computational frequency 16.4 MHz 325 sec on a CDC 6500. The execution of program PANB at the same frequency for 7 test points with the modes 0 to 7 requires 320 sec. The execution of program PANC needs only about 5 sec. Thus, one should limit  $n_{\text{max}}$  on the absolutely needed number (increases with  $d_{\text{at}}$  and frequency, see 10.3.4.1.), and one should limit the number of test segments, especially those with large  $d_{\text{at}}$ .

### 10.3.3. STORAGE CAPACITY LIMITATIONS

The original program by BEVENSEE [10] requires a total storage of 662,513 octal which exceeds the permissible limit of 160,000 octal of the ETH computer by a factor of 4. With the assistance of BEVENSEE and the specialists at the computer center the storage requirement could be reduced. The main steps of reduction were:

- Separate computation of the Y-matrices in HARRA
- Reduction of the ZM-matrix from  $(2 \times 10,000)$  to  $(2 \times 76)$
- Reduction of NT to 2, KK to 13 and NTEST to 9
- Reduction of the VVR from  $(2 \times 14,400)$  to  $(2 \times 760)$ , Y from  $(10,000)$  to  $(1,444)$ , and G from  $(30,603)$  to  $(4764)$
- Extensive use of the COMMON BLANK and COMMON/A

The reduction of the array sizes and the COMMON operations is critical with respect to writing over the reserved array lengths. Several debugging procedures are needed which cannot be discussed here.

The final storage requirements of the programs in Appendix 16.2. are:

- Program HARRA: 61,200 octal (specified 70,000)
- Program PANB : 121,600 octal (specified 130,000)
- Program PANC : < 10,000 octal (specified 70,000)

### 10.3.4. INVESTIGATION OF THE COMPUTATIONAL ACCURACY

#### 10.3.4.1. MINIMUM MODE NUMBER KK

The preliminary study in section 7.2.3. has shown that up to 25 modes contribute to the total field at  $f \leq 1000$  MHz and  $d_{at} \leq 2$  m. It is not possible to compute so many modes due to the limitations mentioned above. With the following method the absolutely needed minimum KK is evaluated:

Program PANB offers for  $p_1$  = vertical and horizontal a table denoted as "Einfluss der Anzahl der berücksichtigten Modi auf  $E_{tot}$ " (see Appendix 16.2.3.) For each test segment the values for ERTOT, EPTOT and ETTOT are listed for the azimuthal angles  $\phi = 0, 90$  and  $180^\circ$  as the summation from the modes 0 to M, where  $0 \leq M \leq (KK-1)$ . In each column one checks first if the (KK-1) result is  $> 10^{-3}$  and if the (KK-2) result differs not more than  $\pm 1\%$ . Then one chooses that result in the column which is not more than  $\pm 5\%$  different from the (KK-1) result and notes the corresponding minimum M.

TABLE 65 shows the evaluation of the minimum mode number from the data in Appendix 16.2.3. for the actual frequency 164 MHz and for 5 % relative accuracy.

TEST SEGMENT No. $d_{at}$ [m]	ERTOT-comp.at 0° 90° 180°			EPTOT-comp.at 0° 90° 180°			ETTOT-comp.at 0° 90° 180°			Recom- mended KK (M+1)
	M	M	M	M	M	M	M	M	M	
1    0.08	3	1	3	0	3	(3)	1	2	3	$\geq 4$
2    0.13	2	2	3	0	3	(3)	2	2	2	$\geq 4$
3    0.18	3	4	3	0	3	(4)	2	2	3	$\geq 4$
4    0.28	3	4	4	0	3	(4)	3	3	3	$\geq 5$
5    0.38	3	2	4	0	3	(4)	4	3	4	$\geq 5$
6    0.53	4	4	4	0	3	(4)	4	4	4	$\geq 5$
7    0.68	4	4	5	0	5	(5)	4	4	6	$\geq 7$
8    0.83	6	5	6	0	5	(6)	5	4	6	$\geq 7$
9    1.03	7	6	6	0	7	(7)	6	6	7	$\geq 8$

TABLE 65 Determination of the minimum mode number KK for 5 % relative accuracy at 9  $d_{at}$ 's at the actual frequency 164 MHz and model MANMOD2.

In general it is sufficient to monitor the results at  $\phi = 180^\circ$ . In the example in TABLE 65 (164 MHz,  $p_1$  = vertical,  $\theta_1 = 80.8^\circ$ ) the horizontal component EPTOT is very small ( $10^{-7}$ ) so that those differences are of little meaning. Very roughly the minimum KK increases linearly with  $d_{at}$  and frequency. The computational data in section 10.4. at  $d_{at}$  from 0.1 to 0.4 m were computed with the NN and KK listed in TABLE 66, checked according to TABLE 65 at a 2% level below 300 MHz and 5% level above 300 MHz.

FREQUENCY RANGE	MAXIMUM NN in HARRA	SELECTED KK in PANB
1 to 30 MHz	4 ok	5 ok
50 to 100 MHz	5 ok	6 ok
101 to 200 MHz	7 ok	8 ok
250 to 300 MHz	9 ok	10 ok
350 to 500 MHz	10 ~ok	11 ~ok
600 to 800 MHz	12 (?)	13 (?)

TABLE 66 Mode number NN and KK versus frequency at  $d_{at}$  from 0.1 to 0.4 m. At frequencies below 500 MHz the relative accuracy is better than 5 %, the absolute accuracy (FSL = 100 %) is better than 0.2 %.



#### 10.3.4.2. DIFFERENCE BETWEEN THE TWO AZIMUTHAL FIELD COMPONENTS

Program PANB computed the azimuthal field components EPH twice (for  $E_{inc}$ ,  $E_{scat}$  and  $E_{tot}$ , for  $\phi = 0^\circ$ ), first for  $IT=1$  (test segment oriented along the  $\vec{a}_r$ -vector) and then for  $IT=2$  (test segment oriented along the  $\vec{a}_\phi$ -vector) for both incident polarizations ETHETA INC ( $p_2$ =vertical) and EPHI INC ( $p_2$ =horizontal). The results are listed after the output of the body contour (see Appendix 16.2.3.) as follows:

$\theta$  SIG  $\theta\theta$  MAG  $S\theta\theta$  SIG  $\phi\phi$  MAG  $S\phi\phi$  MODE NN = 0

RTEST = 1.7500 ZTEST = 10.0000 DTEST = 0.2000

EINC ETHETA INC  
ERAD(x,x), EPH (x,x), ETH(x,x), EPH (x,x)  
ESCAT ETHETA INC  
ERAD(x,x), EPH (x,x), ETH(x,x), EPH (x,x)  
ETOT ETHETA INC  
ERAD(x,x), EPH (x,x), ETH(x,x), EPH (x,x)

etc. for EPHI INC

RTEST = 2.2500 ZTEST = 10.0000 DTEST = 0.2000

etc. for all RTEST up to

RTEST = 11.2500 ZTEST = 10.0000 DTEST = 0.2000

and the same output is now repeated for all modes up to MODE NN = 7

The data in Appendix 16.2.3. were used as an indicator for the computational accuracy. The results, obtained with the following method, are listed in TABLE 67 :

EPH1 = first EPH ( $IT=1$ ), EPH2 = second EPH ( $IT=2$ ), (245)  
Data from ETOT and ETHETA INC ( $E_{tot}$  and  $p_1$  = vertical)

Error in  $\%$  =  $||EPH1| - |EPH2|| \cdot 1000 E_0$  (246)

The results in TABLE 67 are therefore related to the free-space level = 1000  $\%$  = 0 dB. Generally, the error increases with decreasing  $d_{at}$ , and the first modes determine the final accuracy. Below 500 MHz an increase of the error could not be noticed depending on the frequency . In normal conditions (see next section) the total error is well below 1 %.

TEST SEGMENT No.	SEGMENT dat [m]	Difference between the two EPH in ‰ at 164 MHz. Mode:							
		NN = 0	NN = 1	NN = 2	NN = 3	NN = 4	NN = 5	NN = 6	NN = 7
1	0.08	0	1.926	0.257	0.029	0.016	<0.03	~ 0	~ 0
2	0.13	0	0.273	0.103	0.045	0.021	~ 0	~ 0	~ 0
3	0.18	0	0.011	0.065	0.041	0.024	~ 0	~ 0	~ 0
4	0.28	0	0.061	0.060	0.024	<0.03	~ 0	~ 0	~ 0
5	0.38	0	0.053	0.047	0.012	~ 0	~ 0	~ 0	~ 0
6	0.53	0	0.034	0.036	<0.03	~ 0	~ 0	~ 0	~ 0
7	0.68	0	0.029	0.017	~ 0	~ 0	~ 0	~ 0	~ 0
8	0.83	0	0.026	<0.03	~ 0	~ 0	~ 0	~ 0	~ 0
9	1.03	0	<0.03	~ 0	~ 0	~ 0	~ 0	~ 0	~ 0

TABLE 67 Computational error in ‰ versus mode number NN and versus dat at the actual frequency 164 MHz and model MANMOD 2.

Considering the results in TABLE 67 one could conclude that the computational accuracy is satisfactory for all applications, but this is not absolutely true. The exceptions are mentioned in 10.3.4.3..

#### 10.3.4.3. DIFFERENCE BETWEEN RESULTS AT DIFFERENT TEST SEGMENT LENGTHS

Due to the approximation method by BEVENSEE [10] (see description in 6.4. 5.1. and program limitations in 10.3.1.) problems may occur at some few frequencies at small dat. Without checking carefully the result according to the method in 10.3.4.2. the computational error had to be specified to about 10 %. With the following method inaccurate results can be detected easily:

All computations are performed twice, first with a test segment length of 0.08 m (DTEST=0.2) and second with 0.2 m (DTEST=0.5). The results of the test points are plotted versus the frequency (all results in section 10.4. contain the computational data from both test segments). At some arbitrary frequencies discrepancies occur between the two results (see FIGURE 80,82). If the difference exceeds 1 dB, the results are checked according to 10.3.4.2.. Up to now the inaccuracy was always manifested by a large EPH difference, in all of the 11 problematic cases of about 100 complete near-field computations. The computations are repeated at a new frequency, differing from the "disturbed" frequency by about 2 %. There is no strict rule to prevent "disturbed" frequencies, but dat's below 0.2 m, frequencies above 300 MHz and complicated body shapes are risk factors.

### 10.3.5. FIELD HOMOGENEITY AROUND A NEAR FIELD POINT

#### 10.3.5.1. SIGNIFICANCE OF THE FIELD HOMOGENEITY AND COMPUTATIONAL DATA

The body-mounted antenna  $A_1$  is not infinitesimally small. Thus, the induced voltage at the antenna terminals (receiving case) depends generally not only on the field at the (computed) antenna center, but also on the field along the antenna axis. The study in section 5.2.2. concluded in the statements:

If the amount of the E-field can be described by a polynome of second degree and if the phase of the E-field changes monotonously along the antenna axis, the logarithmic difference  $\Delta U$  (i.e., the ratio induced voltage from center field / induced voltage from actual field, see 5.2.2.) is less than 1 dB, if the following conditions are fulfilled:

$$\delta E = \begin{array}{l} \text{variation of the amount of the E-field along} \\ \text{the antenna axis in direction of the regarded } p_1 \end{array} < 10 \text{ dB} \quad (37)$$

$$\delta \phi = \begin{array}{l} \text{phase variation of the E-field along the an-} \\ \text{tenna axis in direction of the regarded } p_1 \end{array} < 71^\circ \quad (38)$$

In section 10.2.5. the near-field data along the  $p_1$ -axis vertical, radial and horizontal were computed at the center and at the ends of a dipole antenna of the length  $2h = 0.1$  m, with test segment lengths of 0.08 m. The test segments at  $+h$  and  $-h$  are separated by a gap of 0.02 m, so that oscillations (if existing) can be detected without computational artifacts which may occur at smaller test segments (10.3.1.). The quantities  $\Delta U, \delta E$  and  $\delta \phi$  were computed for  $d_{at} = 0.1$  m,  $h_b = 1.0$  m,  $\theta_1 = 80.8^\circ$  and for the body model FZYL at several frequencies (see TABLE 68, 69 and the results in Appendix 16.2.4.).

The computational results confirm the validity of equation (37) and (38). At  $p_1$  = vertical and radial the  $\delta E$  and  $\delta \phi$  are below the critical level and thus  $\Delta U$  remains smaller than 1 dB. With  $p_1, p_2$  = horizontal the antenna  $A_1$  is oriented perpendicular to the  $E^{\text{tot}}$  wavefront at about  $\phi = 80$  to  $100^\circ$ , resulting in large phase changes and thus large  $\Delta U$ . The significant data of the homogeneity investigation are summarized in TABLE 70 for the frequencies 65, 75, 100, 125, 150, 300 and 425 MHz.

AZIMUTHAL RADIATION PATTERN FREQUENCY 150 MHZ										
HOMOGENEITY CHECK OF THE FIELD ALONG A 0.1 METER DIPOLE ANTENNA										
TESTBODY: ROT.SYM.CYLINDER					FIELD POINT		INCIDENT WAVE			
AXIAL LENGTH = 1.80 M					DAT = .10 M		POLAR. = VERTICAL			
DIAMETER = .25 M					HB =1.00 M		THETA = 80.8 DEG			
PHI DEG	VERTICAL POLARIZED ANTENNA					RADIAL POLARIZED ANTENNA				
	GAIN CENTER DB	PHASE CENTER DEG	MEAN ERROR DB	MAXIMUM GAINVAR DB	MAXIMUM PHASEVAR DEG	GAIN CENTER DB	PHASE CENTER DEG	MEAN ERROR DB	MAXIMUM GAINVAR DB	MAXIMUM PHASEVAR DEG
0	-3.6	151.9	.00	.4	2.8	1.4	40.8	-.26	4.1	.2
5	-3.6	152.0	.00	.4	2.8	1.4	40.8	-.25	4.1	.2
10	-3.7	152.4	.00	.4	2.7	1.4	40.9	-.25	4.1	.1
15	-3.7	153.2	.00	.4	2.7	1.4	41.1	-.25	4.1	.0
20	-3.9	154.2	.00	.4	2.6	1.3	41.3	-.25	4.1	.2
25	-4.0	155.4	.00	.4	2.5	1.3	41.6	-.25	4.1	.4
30	-4.1	157.0	.00	.4	2.3	1.2	41.9	-.25	4.1	.7
35	-4.3	158.8	.00	.4	2.1	1.2	42.3	-.24	4.0	.9
40	-4.6	160.8	.00	.4	1.9	1.1	42.7	-.24	4.0	1.2
45	-4.8	163.1	.00	.4	1.7	1.1	43.0	-.23	4.0	1.5
50	-5.1	165.7	.00	.4	1.5	1.0	43.4	-.23	4.0	1.8
55	-5.4	168.5	.00	.3	1.2	.9	43.8	-.23	4.0	2.1
60	-5.8	171.5	.00	.3	.9	.8	44.1	-.22	3.9	2.4
65	-6.2	174.8	.00	.3	.7	.7	44.4	-.22	3.9	2.6
70	-6.6	178.3	.00	.3	.4	.6	44.7	-.22	4.0	2.8
75	-7.1	178.0	.00	.3	.0	.5	44.8	-.21	4.0	3.0
80	-7.6	174.0	.00	.2	.3	.4	44.9	-.21	4.0	3.0
85	-8.2	169.8	.00	.2	.6	.3	44.8	-.21	4.0	3.0
90	-8.8	165.3	.00	.1	.9	.1	44.7	-.21	4.0	2.9
95	-9.5	160.5	.00	.1	1.2	.0	44.5	-.21	4.0	2.8
100	-10.2	155.3	.00	.0	1.4	-.1	44.2	-.21	4.1	2.5
105	-10.9	149.8	-.00	.1	1.7	-.2	43.7	-.21	4.1	2.2
110	-11.6	143.9	-.00	.2	1.8	-.3	43.2	-.21	4.1	1.7
115	-12.4	137.4	-.00	.3	1.9	-.3	42.6	-.21	4.1	1.3
120	-13.2	130.4	-.00	.4	1.9	-.4	42.0	-.21	4.1	.8
125	-13.9	122.9	-.00	.5	1.7	-.4	41.4	-.21	4.1	.3
130	-14.6	114.9	-.01	.6	1.3	-.5	40.7	-.21	4.1	.2
135	-15.2	106.6	-.01	.7	.8	-.5	40.0	-.22	4.1	.7
140	-15.6	98.1	-.01	.8	.1	-.5	39.4	-.22	4.0	1.2
145	-15.9	89.9	-.01	.8	.6	-.5	38.8	-.22	4.0	1.6
150	-16.1	82.3	-.01	.9	1.3	-.5	38.3	-.22	4.0	1.9
155	-16.2	75.5	-.01	.9	2.0	-.5	37.8	-.23	3.9	2.2
160	-16.2	69.8	-.01	.8	2.5	-.5	37.4	-.23	3.9	2.4
165	-16.2	65.4	-.01	.8	2.8	-.5	37.1	-.23	3.9	2.6
170	-16.1	62.2	-.01	.8	3.1	-.5	36.9	-.23	3.9	2.7
175	-16.1	60.3	-.01	.8	3.2	-.5	36.8	-.23	3.9	2.8
180	-16.1	59.7	-.01	.8	3.3	-.5	36.7	-.23	3.9	2.8

TABLE 68 Field homogeneity at 150 MHz at  $d_{at} = 0.1$  m and  $p_2 = \text{vertical}$ .  
Left:  $p_1 = \text{vertical}$ , right:  $p_1 = \text{radial}$ ; dB-values related to 0 dB = FSL.  
Gain center:  $G_{inb}$  [dB], Phase center:  $\phi$  [°], Mean error:  $\Delta U$  [dB],  
Maximum gainvar:  $\delta E$  [dB], Maximum phasevar:  $\delta \phi$  [°].

AZIMUTHAL RADIATION PATTERN FREQUENCY 150 MHZ										
HOMOGENEITY CHECK OF THE FIELD ALONG A 0.1 METER DIPOLE ANTENNA										
TESTBODY: ROT.SYM.CYLINDER					FIELD POINT		INCIDENT WAVE			
AXIAL LENGTH = 1.80 M					DAT = .10 M		POLAR. = HORIZONTAL			
DIAMETER = .25 M					HB =1.00 M		THETA = 80.8 DEG			
PHI DEG	HORIZONTAL POLARIZED ANTENNA					RADIAL POLARIZED ANTENNA				
	GAIN CENTER DB	PHASE CENTER DEG	MEAN ERROR DB	MAXIMUM GAINVAR DB	MAXIMUM PHASEVAR DEG	GAIN CENTER DB	PHASE CENTER DEG	MEAN ERROR DB	MAXIMUM GAINVAR DB	MAXIMUM PHASEVAR DEG
0	-4.7	16.8	.10	0.0	0.0	*****	*****	*****	*****	*****
5	-4.7	17.1	.10	.4	2.6	-19.4	36.2	-.18	2.7	17.1
10	-4.8	17.9	.10	.8	5.2	-13.4	36.6	-.18	2.7	16.8
15	-5.0	19.1	.09	1.2	7.9	-9.9	37.2	-.18	2.6	16.5
20	-5.3	20.9	.09	1.6	10.5	-7.4	38.1	-.18	2.6	16.0
25	-5.7	23.3	.08	2.0	13.2	-5.5	39.3	-.18	2.6	15.4
30	-6.1	26.1	.08	2.5	15.9	-4.0	40.7	-.18	2.6	14.6
35	-6.6	29.5	.07	3.0	18.8	-2.8	42.3	-.18	2.5	13.8
40	-7.2	33.5	.07	3.5	21.7	-1.8	44.1	-.17	2.5	12.8
45	-8.0	38.0	.06	4.1	24.8	-.9	46.1	-.17	2.5	11.8
50	-8.8	43.2	.05	4.8	28.4	-.1	48.3	-.17	2.4	10.7
55	-9.8	49.0	.04	5.6	32.6	.6	50.6	-.17	2.4	9.5
60	-11.0	55.8	.03	6.6	38.1	1.1	53.0	-.17	2.3	8.2
65	-12.3	63.6	.00	7.9	46.2	1.6	55.6	-.17	2.3	6.9
70	-13.9	73.1	-.07	9.4	59.5	2.0	58.2	-.17	2.3	5.5
75	-15.9	85.3	-.28	10.5	82.8	2.3	60.9	-.17	2.2	4.2
80	-18.1	102.5	-.89	8.9	116.6	2.5	63.7	-.17	2.2	2.8
85	-20.3	128.7	-1.96	4.1	142.9	2.7	66.5	-.17	2.2	1.4
90	-21.0	164.7	-2.44	1.6	149.0	2.8	69.3	-.17	2.1	.0
95	-19.3	-162.4	-1.61	7.2	134.2	2.8	72.1	-.17	2.1	1.4
100	-16.8	-140.5	-.69	11.1	101.8	2.7	74.8	-.17	2.1	2.7
105	-14.4	-125.9	-.26	11.3	70.4	2.6	77.5	-.17	2.1	4.0
110	-12.4	-115.4	-.10	9.8	51.2	2.4	80.1	-.17	2.1	5.3
115	-10.8	-107.1	-.03	8.2	40.1	2.2	82.6	-.17	2.1	6.6
120	-9.3	-100.3	.01	7.0	33.0	1.8	85.0	-.17	2.1	7.7
125	-8.1	-94.5	.03	5.9	28.1	1.3	87.3	-.17	2.1	8.8
130	-7.1	-89.4	.05	5.1	24.2	.8	89.5	-.17	2.1	9.9
135	-6.2	-85.1	.06	4.4	21.0	.1	91.4	-.17	2.1	10.9
140	-5.4	-81.2	.07	3.7	18.2	-.7	93.3	-.17	2.1	11.8
145	-4.7	-77.9	.08	3.1	15.6	-1.7	94.9	-.17	2.1	12.5
150	-4.2	-75.1	.08	2.6	13.2	-2.9	96.3	-.17	2.1	13.3
155	-3.7	-72.8	.09	2.1	10.9	-4.3	97.5	-.17	2.1	13.9
160	-3.4	-70.9	.09	1.7	8.7	-6.1	98.6	-.17	2.1	14.4
165	-3.1	-69.4	.10	1.2	6.5	-8.6	99.4	-.17	2.1	14.8
170	-2.9	-68.3	.10	.8	4.3	-12.0	99.9	-.17	2.1	15.0
175	-2.8	-67.7	.10	.4	2.1	-18.0	100.3	-.18	2.1	15.2
180	-2.7	-67.5	.10	0.0	0.0	*****	*****	*****	*****	*****

TABLE 69 Field homogeneity at 150 MHz at  $dat = 0.1$  m and  $p_2 = \text{horizontal}$ .  
Left:  $p_1 = \text{horizontal}$ , right:  $p_1 = \text{radial}$ ; dB-values related to 0 dB = FSL.  
Gain center :  $G_{\text{dB}}$  [dB]. Phase center:  $\phi$  [°], Mean error:  $\Delta U$  [dB],  
Maximum gainvar:  $\delta E$  [dB], Maximum phasevar:  $\delta \phi$  [°].

The maximum ratings of the computed field homogeneity parameters are listed in TABLE 70 :

FRE- QUEN- CY [MHz]	Maximum ratings $p_2 = \text{VERTICAL}$						Maximum ratings $p_2 = \text{HORIZONTAL}$					
	$p_1 = \text{VERTICAL}$			$p_1 = \text{RADIAL}$			$p_1 = \text{HORIZONTAL}$			$p_1 = \text{RADIAL}$		
	$\Delta U$ [dB]	$\delta E$ [dB]	$\delta \Phi$ [°]	$\Delta U$ [dB]	$\delta E$ [dB]	$\delta \Phi$ [°]	$\Delta U$ [dB]	$\delta E$ [dB]	$\delta \Phi$ [°]	$\Delta U$ [dB]	$\delta E$ [dB]	$\delta \Phi$ [°]
65	0.1	1.0	10	0.3	4.5	4	8.7	29.9	200	0.2	2.1	7
75	0.2	3.8	18	0.3	4.3	2	7.6	25.0	194	0.2	2.1	8
100	0.0	1.3	3	0.3	4.5	2	5.4	18.1	180	0.2	2.3	11
125	0.0	1.9	5	0.4	4.5	3	3.7	13.5	165	0.2	2.5	14
150	0.0	0.8	3	0.3	4.1	3	2.4	11.3	149	0.2	2.7	17
300	0.0	1.2	8	0.5	5.1	31	>10	>20	222	0.3	2.2	45
425	0.1	1.7	19	1.0	5.9	65	3.1	13.3	100	0.3	2.3	50

TABLE 70 Maximum ratings from the field homogeneity computations.

The data concern the model FZYL with the antenna position  $d_{at} = 0.1$  m and  $h_b = 1.0$  m, related to a  $2h = 0.1$  m dipole antenna  $A_1$ .

The field homogeneity is satisfactory except for  $p_1 = p_2 = \text{horizontal}$  which is not suited for omnidirectional transmission. From the data in TABLE 70 one can conclude that all further computations have only to be performed for the center test point which is representative for the field around the test point, if  $d_{at}$  is larger than 0.1 m and if the frequency is below 500 MHz.

#### 10.3.5.2. COMPUTATIONAL DATA FOR ANTENNA DESIGN

With the knowledge of the amplitude- and especially the phase conditions along a certain antenna axis the design of radiation systems become possible which perform better than an usual antenna in the proximity to a body. If we look at TABLE 68 at  $p_1 = \text{radial}$  we notice a field amplification effect produced by the body. There is strong radial field around the body, differing only from +1.4 to -0.5 dB at  $0 < \phi < 180^\circ$ . The  $\delta E$  and the  $\delta \Phi$  are within reasonable limits (4 dB and  $30^\circ$ ), so that an excellent antenna with omnidirectional radiation characteristics could be designed. In the following study the near-field data are discussed and compared with experimental data; a special radial antenna will be shown in 13.3.3..

Leer - Vide - Empty

## 10.4. RESULTS FROM THREE-DIMENSIONAL COMPUTATIONS ON ANTENNA-BODY MODELS

### 10.4.1. OVERVIEW OF INVESTIGATED PARAMETERS AND EXPLANATIONS

In the following sections the influence of certain parameters on the near-field will be demonstrated by computer plots. Unless otherwise specified, the regarded body model is the finite conducting cylinder (FZYL), the irradiation angle  $\phi$  amounts to  $80.8^\circ$ ,  $p_2$  is vertical ( $E_\theta^{inc}$ ) and the relative antenna height  $h_B$  is 1.0 m. The field data are related to the free-space level  $FSL = 0$  dB and specify the E-field in dB in direction of the investigated polarization axis  $p_1$  = vertical, radial or horizontal.

The computations were performed according to section 10.2. and 10.3., and the results were checked according to 10.3.4..The accuracy of the following data is better than  $\pm 1\%$ , corresponding to  $\pm 1$  dB at signal levels above - 21 dB, at frequencies from 10 to 500 MHz. All data have been computed with two different test segment lengths (0.08 m and 0.2 m, actual scale) and generally both results are plotted, as can be noticed by the thicker or double lines in the plots. The accuracy of the frequencies above 500 MHz is in the region of 5% F.S. and was not further investigated, because the previous computational model presented in section 7. covers the frequency range from 200 to 1000 MHz, and because the interesting effects occur below 500 MHz. In addition, more accurate computations above 500 MHz are prohibitive due to storage and computational time limitations (see limitations in section 10.3.2. and 10.3.3.).

The following sections treat the specific effects:

- 10.4.2. Effect of the frequency on vertical and radial field
- 10.4.3. Effect of the antenna-body distance
- 10.4.4. Effect of the azimuthal angle
- 10.4.5. Effect of the irradiation angle
- 10.4.6. Effect of the relative antenna height
- 10.4.7. Effect of the frequency on the azimuthal radiation patterns
- 10.4.8. Effect of the frequency on the directive radiation patterns
- 10.4.9. Effect of different body shapes on the fields in the shadow zone
- 10.4.10. Effect of different body shapes on azimuthal radiation patterns

### 10.4.2. EFFECT OF THE FREQUENCY ON VERTICAL AND RADIAL FIELD

FIGURE 71 provides a first impression. The  $G_{dB}$  data are shown for 4  $d_{at}$ 's of 0.1, 0.2, 0.3 and 0.4 m in the shadow zone  $\phi = 180^\circ$  at  $p_1, p_2$  = vertical.



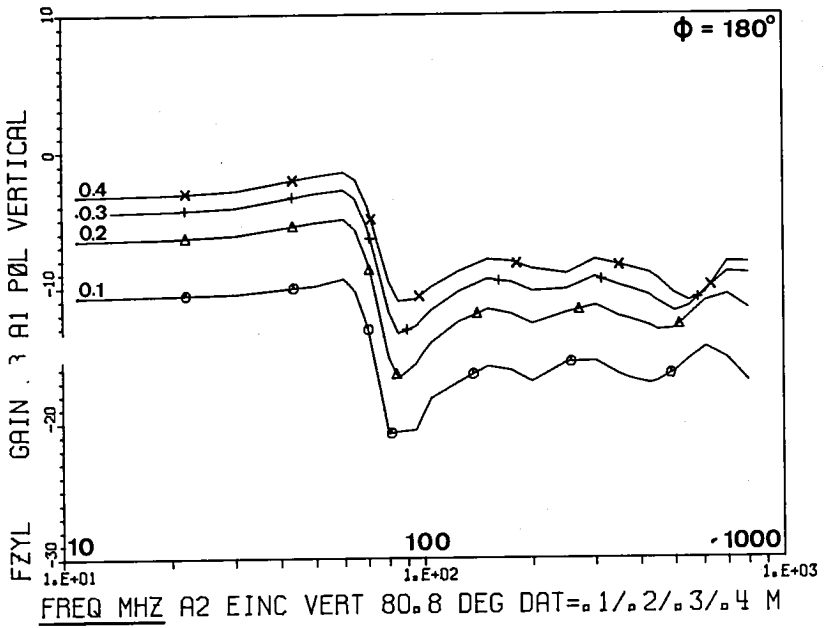


FIGURE 71 Vertical field component  $E_v$  versus frequency, parameter  $dat$ .

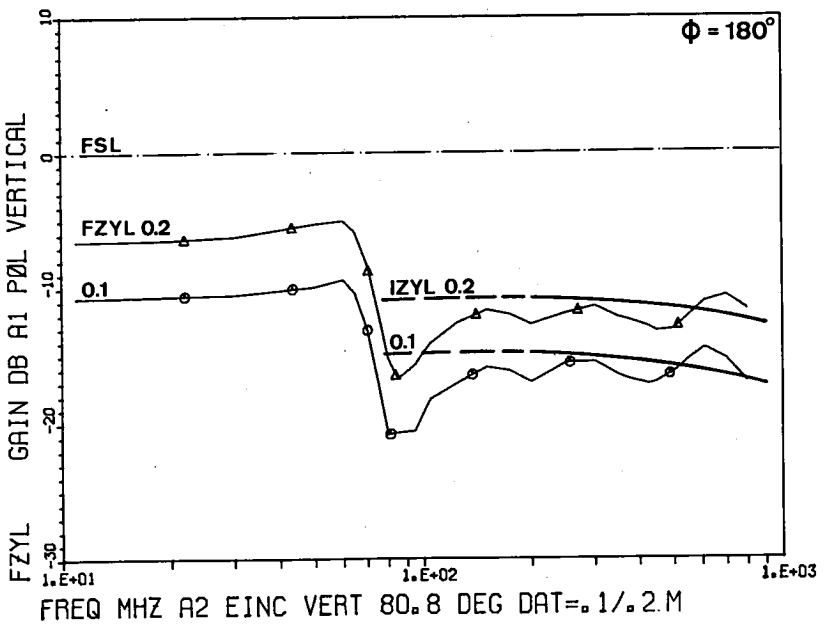


FIGURE 72 Comparison between IZYL and FZYL computation (same parameters).

Unless otherwise specified one always considers the E-field components  $E_v$ ,  $E_r$  and  $E_h$  in the shadow region  $\phi = 180^\circ$ . In FIGURE 71 one distinguishes 5 frequency regions similar to those noticed in the experiments in section 9.

- $< \lambda/2$  below resonance at frequencies below 50 MHz
- $\lambda/2$  first resonance at about 65 MHz
- $3\lambda/4$  anti-resonance at about 80 to 110 MHz
- $\lambda$  second resonance at about 140 MHz
- $> \lambda$  off-resonance at frequencies above 200 MHz

If we compare the FZYL results with the previous IZYL results in FIGURE 72 one observes an oscillation of the FZYL data around the IZYL data with an amplitude of maximum 2.5 dB at frequencies above 200 MHz. This means that both computational methods agree at higher frequencies. From the practical point of view this agreement is disappointing for two reasons: first, there is no theoretical chance to operate with vertical polarized antennas above 75 MHz due to the high transmission losses, second, the experimental data do not agree with the computational data below 150 MHz.

Fortunately, an astonishing radial field effect occurs in the resonance region which provides new hope for both application and experiment :

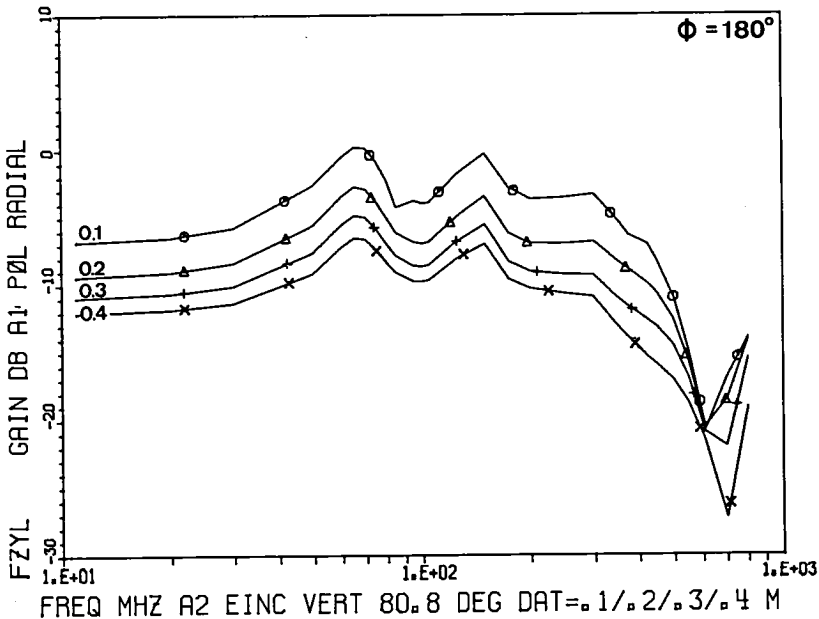


FIGURE 73 Radial field component  $E_r$  versus frequency  $f$ , parameter  $d_{at}$ .

As can be seen in FIGURE 73 a radial field component  $E_r$  is developed at frequencies from about 40 to 300 MHz, caused by a vertical polarized incident wave and the body. In the proximity to the body this  $E_r$  is very strong (-4 to 0 dB at  $d_{at}=0.1$  m) and decreases with increasing  $d_{at}$ . Below 30 MHz the  $E_r$  is small (< -12 dB at  $d_{at}>0.3$  m) and above 500 MHz the  $E_r$  is extremely small (< -16 dB at  $d_{at}>0.3$  m). The significance of the strong  $E_r$  is demonstrated in the next section.

#### 10.4.3. EFFECT OF THE ANTENNA-BODY DISTANCE

Let us consider first the vertical ( $E_v$ ) and radial ( $E_r$ ) field component within the resonance region at 150 MHz and at  $\phi=0^\circ$  (irradiated zone) and at  $\phi=180^\circ$  (shadow zone). FIGURE 74 shows the dependence of the field components from the antenna-body distance  $d_{at}$  :

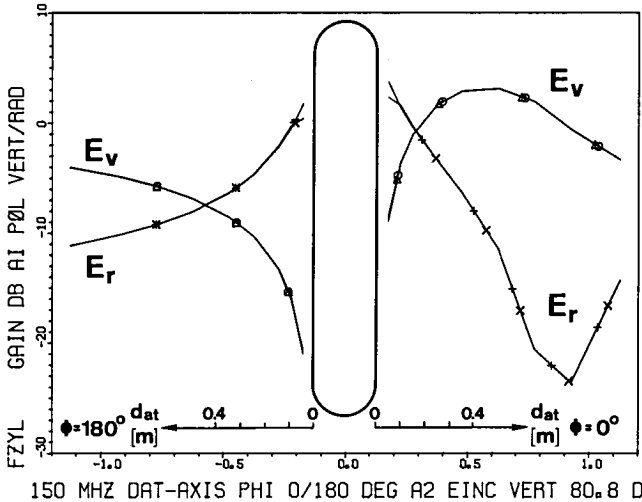


FIGURE 74 Vertical ( $E_v$ ) and radial ( $E_r$ ) field component versus  $d_{at}$ .

Parameter:  $E_v$  and  $E_r$  at  $A_1$  at  $\phi=180^\circ$  (left) and  $0^\circ$  (right)

Constant : frequency = 150 MHz,  $p_2$  = vertical,  $\theta_i = 80.8^\circ$ ,  $h_B = 1.0$  m

At  $\phi=0^\circ$  the  $E_r$  becomes larger than  $E_v$  at  $d_{at}<0.15$  m and at  $d_{at}=0.05$  m  $E_r$  is about 12 dB larger than  $E_v$ . The situation is even more extreme at  $\phi=180^\circ$ ; the  $E_r$  becomes larger than  $E_v$  at  $d_{at}<0.42$  m and at  $d_{at}=0.05$  m  $E_r$  is about 22 dB larger than  $E_v$ ! This effect explains the discrepancy of the experimental results at small  $d_{at}$ , because the transverse sensitivity of a probe antenna  $A_1$  is rarely below -15 dB. It is not possible to measure an  $E_v$  of only -20 dB, if there is also an  $E_r$  of about 0 dB.

#### 10.4.4. EFFECT OF THE AZIMUTHAL ANGLE

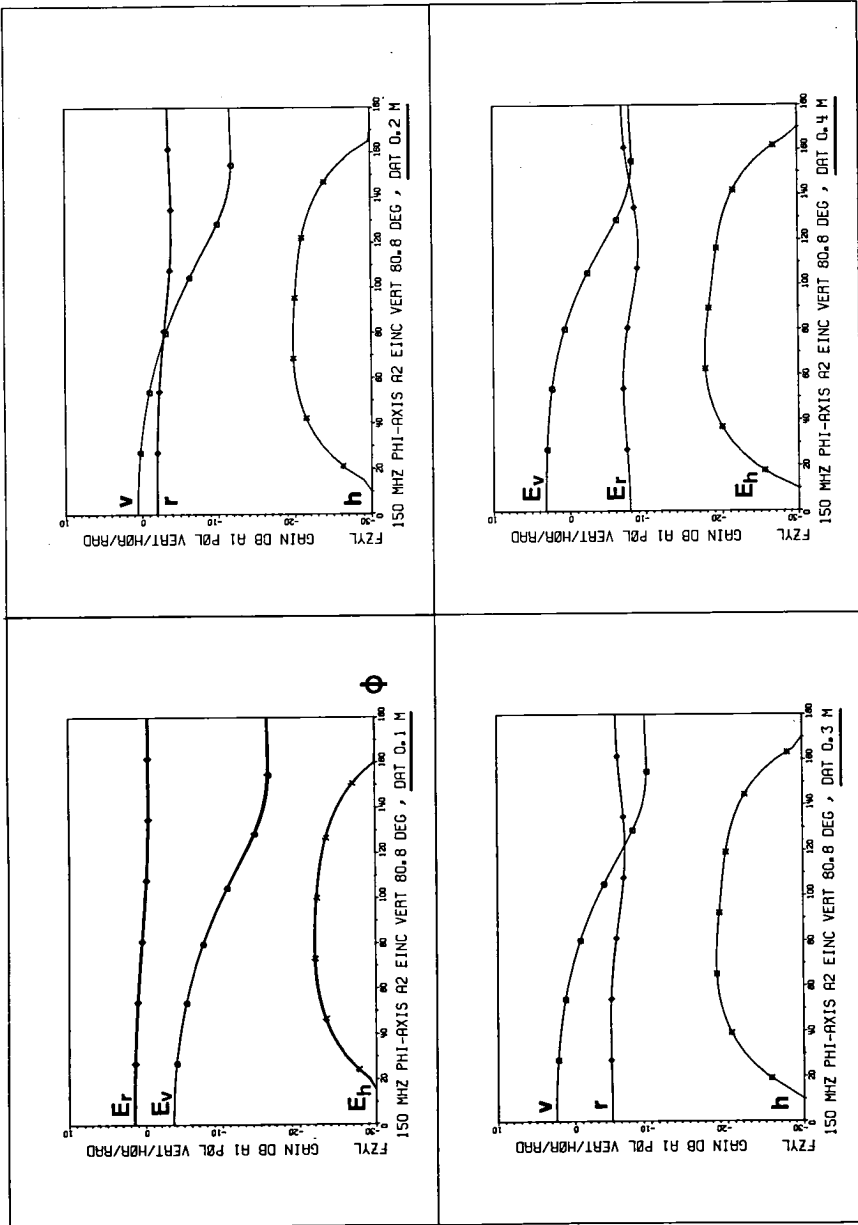


FIGURE 75 Vertical ( $E_v$ ), radial ( $E_r$ ) and horizontal ( $E_h$ ) field components versus azimuthal angle  $\phi$ . Parameter:  $E_v, E_r, E_h$  and  $d_{at} = 0.1, 0.2, 0.3, 0.4$  m. Constant: frequency = 150 MHz,  $p_2$  = vertical,  $\theta_1 = 80.8^\circ$ ,  $h_b = 1.0$  m. The  $E_r$  component is almost constant throughout the full  $\phi = 0-180^\circ$  range.

# 10.4.5. EFFECT OF THE IRRADIATION ANGLE

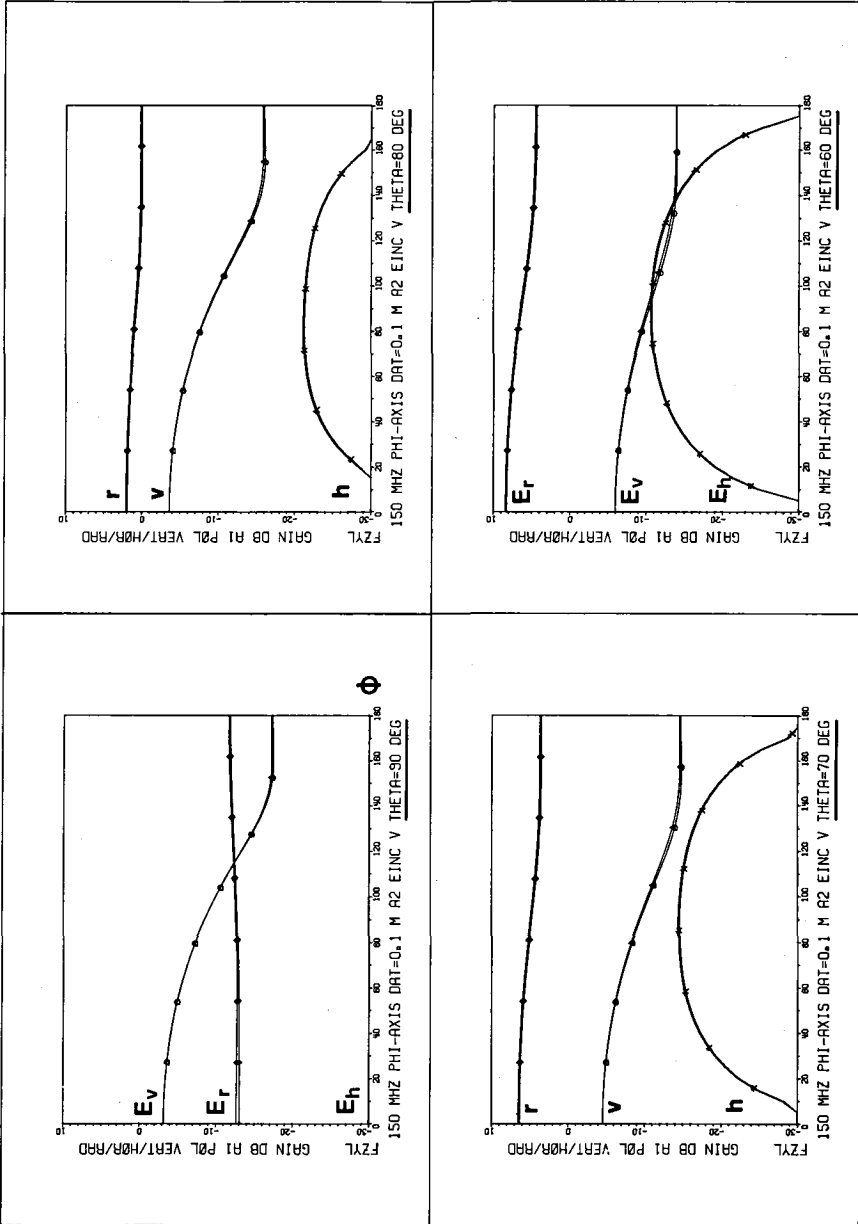


FIGURE 76 Vertical ( $E_v$ ), radial ( $E_r$ ) and horizontal ( $E_h$ ) field components at constant  $d_{at} = 0.1$  m versus  $\phi$  for different irradiation angles  $\theta_i = 90, 80, 70$  and  $60^\circ$ . Constant:  $f = 150$  MHz,  $p_2 =$  vertical,  $h_g = 1.0$  m.  $E_r$  increases with decreasing  $\theta_i$ ,  $E_v$  remains about constant,  $E_h$  disappears at  $\theta_i = 90^\circ$ .

# 10.4.6. EFFECT OF THE RELATIVE ANTENNA HEIGHT

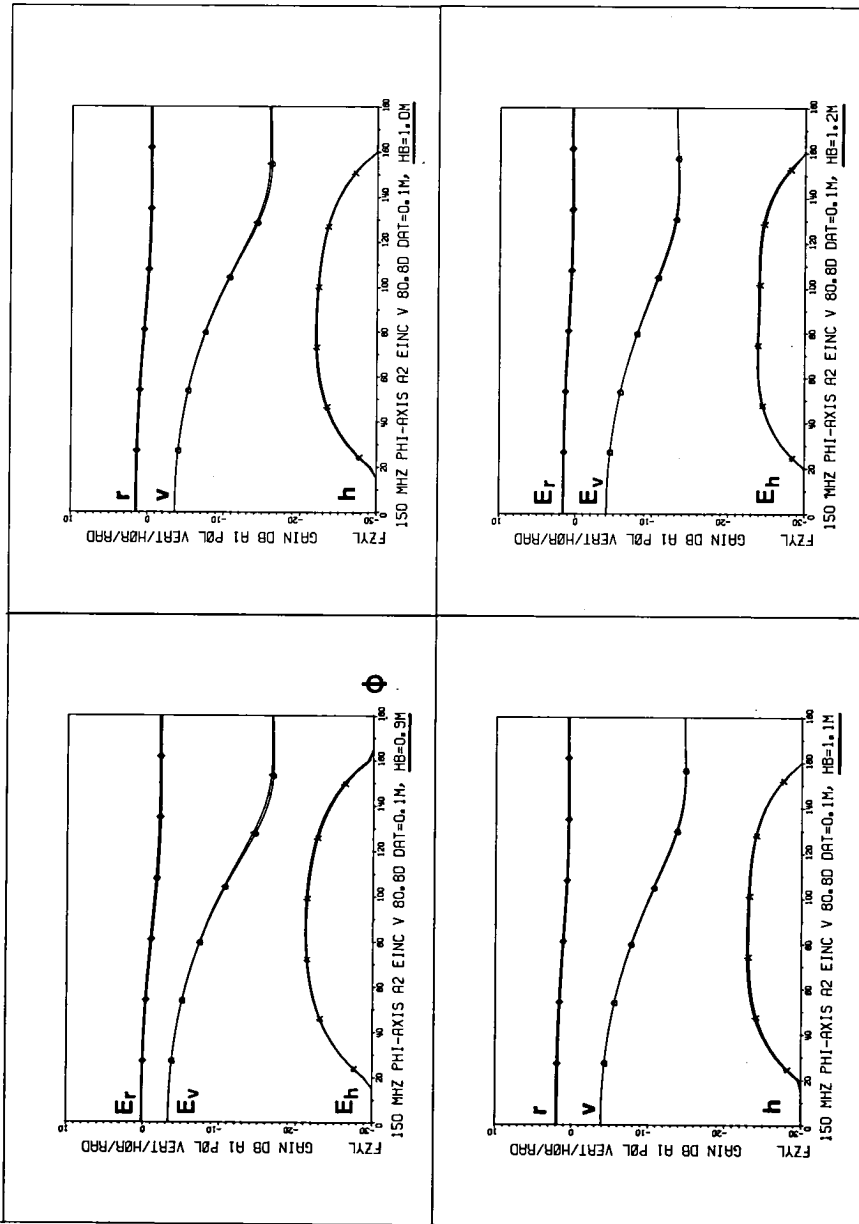


FIGURE 77 Vertical ( $E_v$ ), radial ( $E_r$ ) and horizontal ( $E_h$ ) field components at constant  $d_{at} = 0.1$  m versus  $\phi$  for different relative antenna heights  $h_B = 0.9, 1.0, 1.1$  and  $1.2$  m. Constant:  $f = 150$  MHz,  $p_2 = \text{vertical}$ ,  $\theta_i = 80.8^\circ$ . Even at  $h_B = 0.9$  (body center) all field components are only little influenced by  $h_B$ .

# 10.4.7. EFFECT OF THE FREQUENCY ON THE AZIMUTHAL RADIATION PATTERN

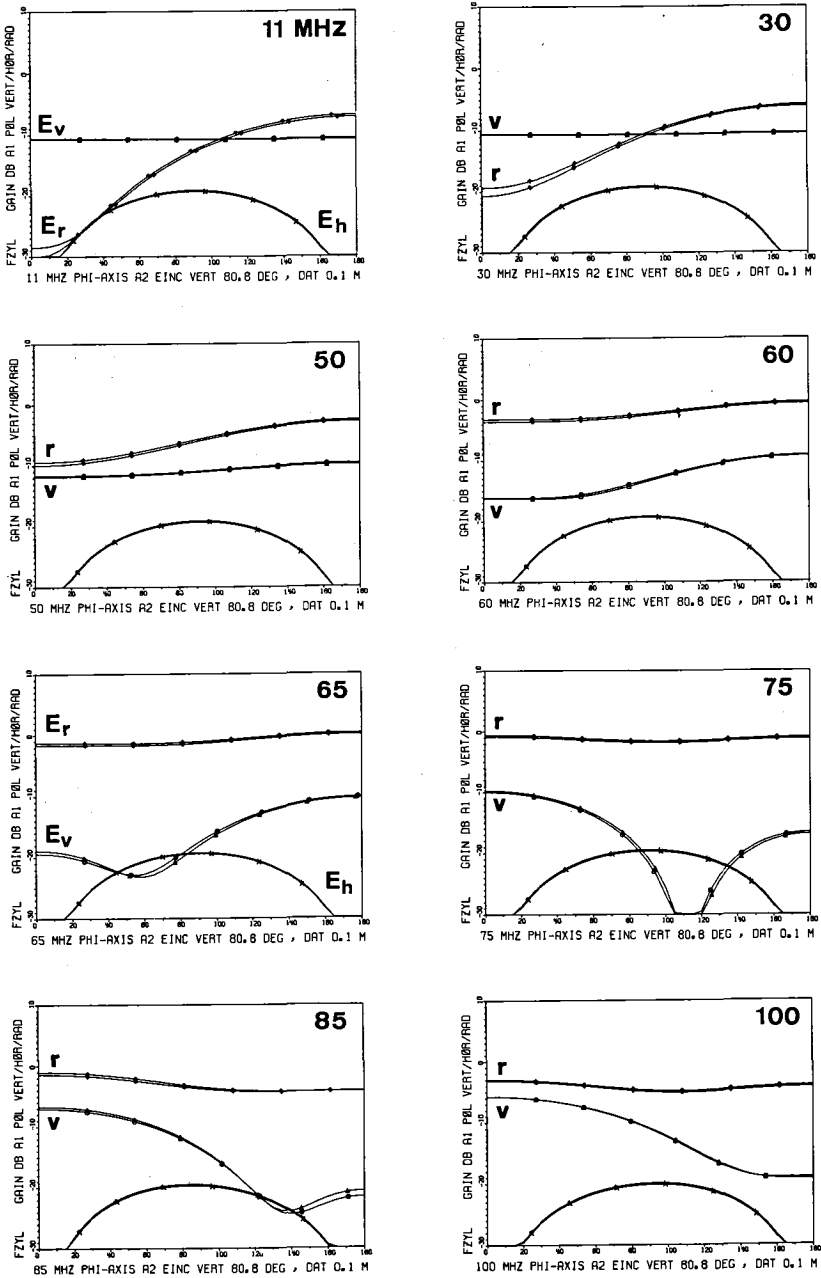


FIGURE 77a Field components  $E_v$ ,  $E_r$  and  $E_h$  versus  $\phi$  with the parameter  $f$  11 to 100 MHz. Constant:  $d_{at} = 0.1$  m,  $p_2 = \text{vertical}$ ,  $\theta_i = 80.8^\circ$ ,  $h_b = 1.0$  m.

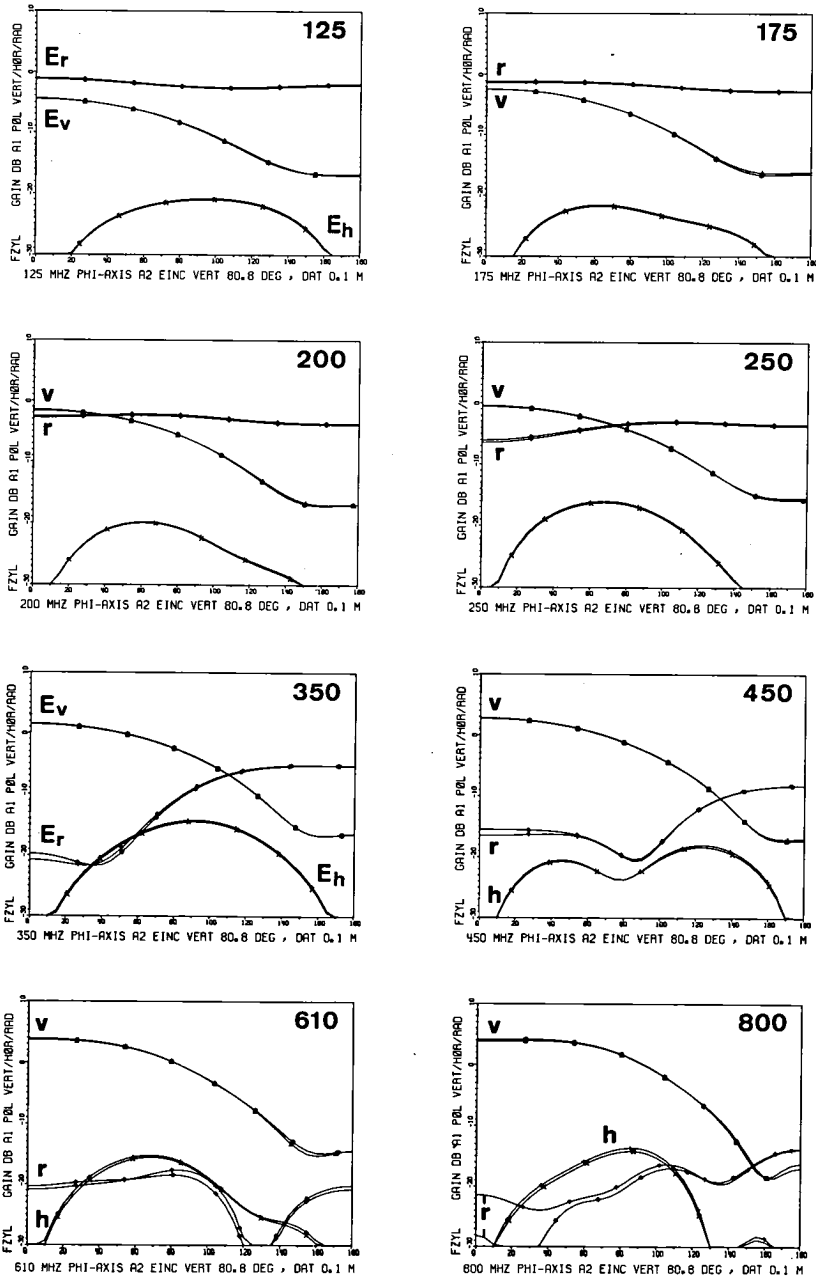


FIGURE 77b Field components  $E_v$ ,  $E_r$  and  $E_h$  versus  $\phi$  with the parameter  $f$  125 to 800 MHz. Constant:  $d_{at} = 0.1$  m,  $p_2 = \text{vertical}$ ,  $\theta_j = 80.8^\circ$ ,  $h_g = 1.0$  m.



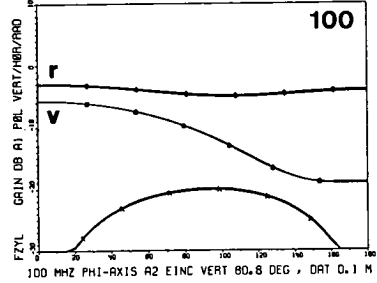
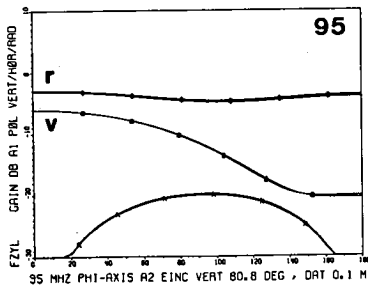
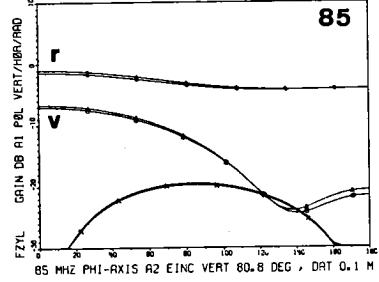
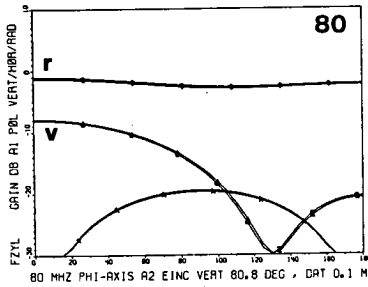
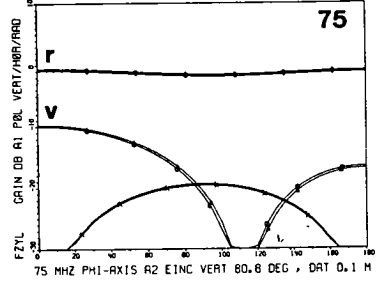
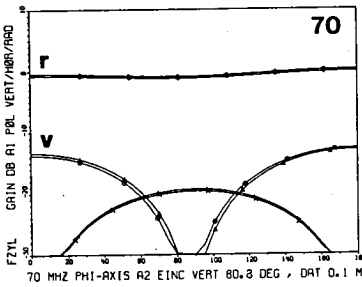
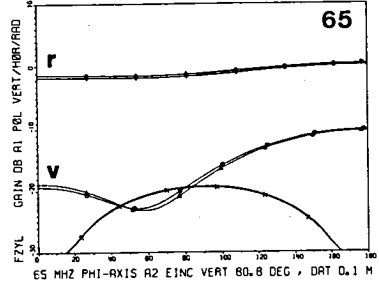
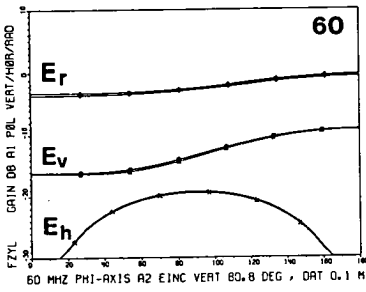


FIGURE 77c Field components  $E_v$ ,  $E_r$  and  $E_h$  versus  $\phi$  with the parameter  $f$  60 to 100 MHz. Constant:  $d_{at} = 0.1$  m,  $p_2 = \text{vertical}$ ,  $\theta_i = 80.8^\circ$ ,  $h_B = 1.0$  m.

FIGURES 77a and 77b show the azimuthal radiation pattern with constant  $d_{at}$  of 0.1m in the full frequency range 11 to 800 MHz, FIGURE 77c in the resonance frequency range 60 to 100 MHz.

#### Vertical E-field component $E_v$

- Below resonance: at frequencies below 50 MHz  $E_v$  depends not on  $\phi$ . Although the far-field scattering (RCS, see section 5.3.2.) is small, the attenuation of the near-field is considerable (-11 dB). However, omnidirectional transmission is possible with a reasonable transmission loss.
- Above first resonance: at frequencies above 60 MHz  $E_v$  depends much on  $\phi$ . Generally  $E_v$  decreases with increasing  $\phi$  and the maximum difference amounts to 12 dB at 125 MHz up to 23 dB at 800 MHz from  $0 < \phi < 180^\circ$ . Thus, omnidirectional transmission is difficult due to the large  $E_v$  variation and due to the small  $E_v$  (minimum: -19 dB/800 MHz). Compared with the IZYL data the FZYL data vary not more than 2.5 dB above 125 MHz.

#### Radial E-field component $E_r$

- Below resonance: at frequencies below 50 MHz  $E_r$  depends much on  $\phi$ . Generally  $E_r$  is very small at  $\phi = 0^\circ$  (-30 dB at 11 MHz, but increases with  $f$  up to -10 dB at 50 MHz) and is relatively high at  $\phi = 180^\circ$  (-7 dB at 11 MHz and -3 dB at 50 MHz).  $E_r$  increases with  $\phi$ , and the maximum difference within  $0^\circ < \phi < 180^\circ$  amounts to 23 dB at 11 MHz and 7 dB at 50 MHz.  $E_r$  becomes permanently larger than  $E_v$  above 50 MHz and is therefore suited for omnidirectional transmission above 50 MHz.
- Above first resonance: at frequencies from (60)-200 MHz  $E_r$  depends not much on  $\phi$  and is always larger than -4 dB. These properties of  $E_r$  are ideal for omnidirectional transmission. Above 250 MHz  $E_r$  depends on  $\phi$ , first decreases  $E_r$  at  $\phi = 0^\circ$ , becomes small at  $0 < \phi < 180^\circ$  and above 500 MHz (Appendix 16.2.5.) the minimum  $E_r$  becomes very small (-30 dB).

#### Horizontal E-field component $E_h$

- At all frequencies the  $E_h$  depends much on  $\phi$  and is smaller than -14 dB.

#### Resonance region 60 to 100 MHz

- Vertical  $E_v$  component: with increasing frequency the minimum shifts from  $\phi = 0^\circ$  to  $\phi = 180^\circ$ . The minimum occurs at about 73 MHz (at about  $\phi = 90^\circ$ ) and is smaller than -30 dB. The maximum  $E_v$  amounts to -7 dB at 100 MHz,  $\phi = 0^\circ$ .
- Radial  $E_r$  component:  $E_r$  depends little on  $\phi$  and is always  $> 4.5$  dB.

# 10.4.8. EFFECT OF THE FREQUENCY ON THE DIRECTIVE RADIATION PATTERN

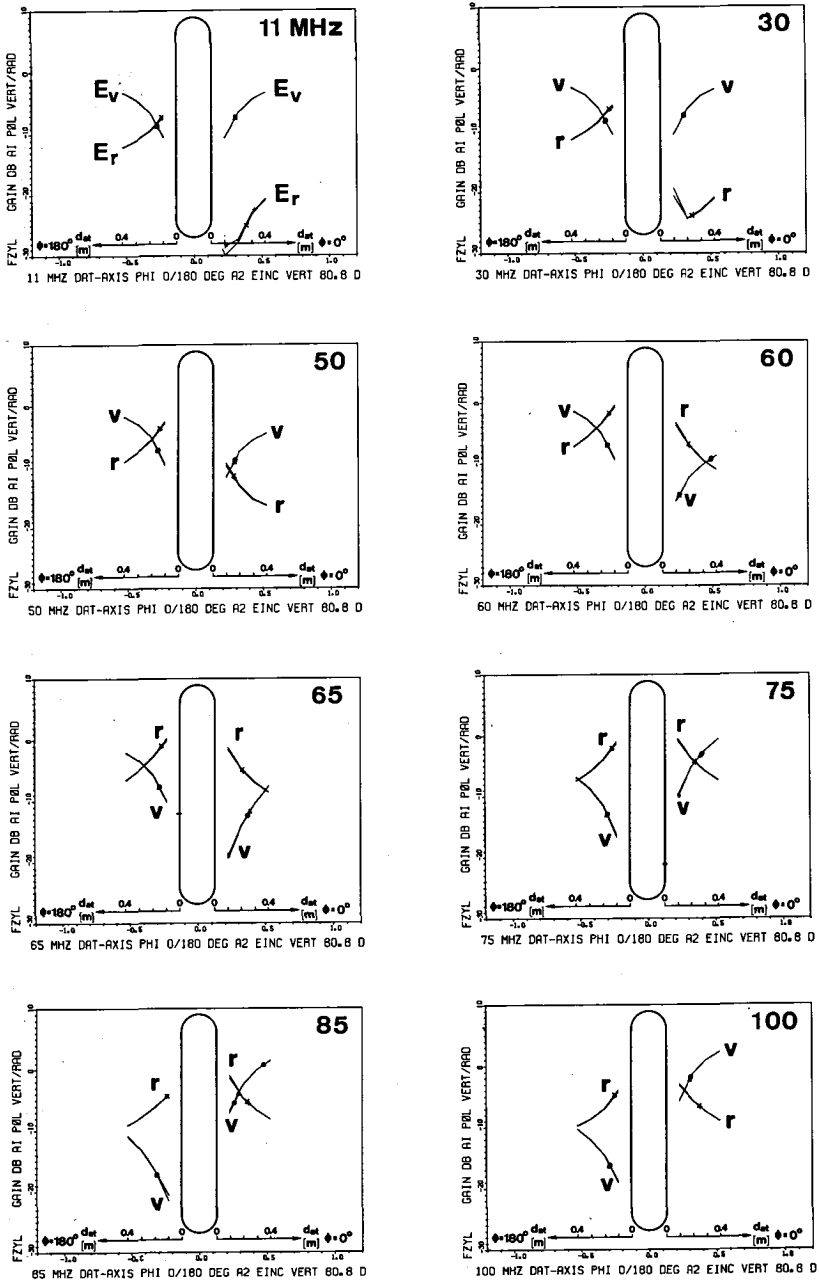


FIGURE 78a Field components  $E_v$  and  $E_r$  versus  $d_{at}$  at  $\phi = 0$  and  $180^\circ$ , with the parameter  $f$  11 to 100 MHz. Constant:  $p_2 = \text{vertical}$ ,  $\theta_i = 80.8^\circ$ ,  $h_g = 1.0 \text{ m}$ .

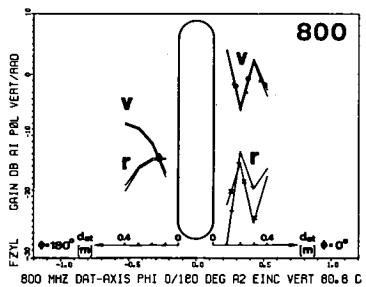
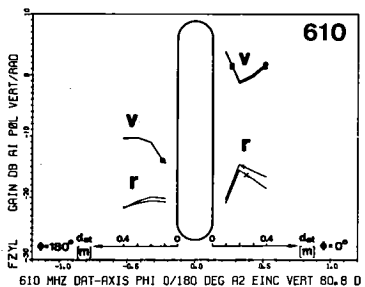
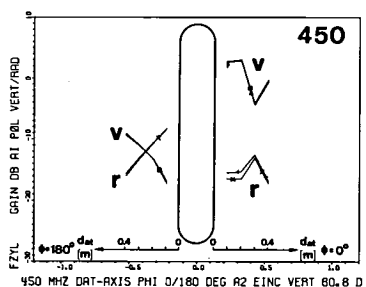
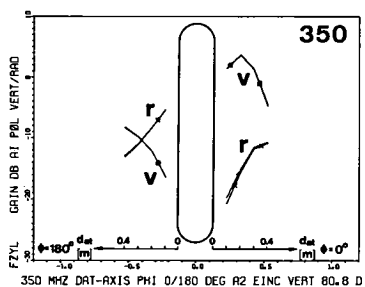
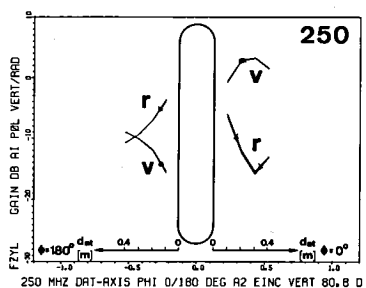
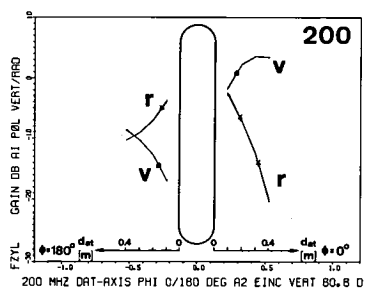
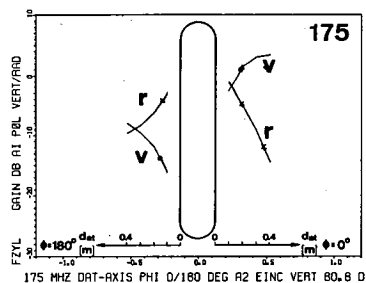
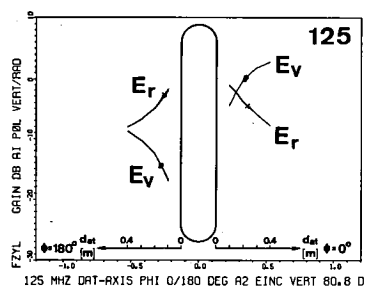


FIGURE 78b Field components  $E_v$  and  $E_r$  versus  $d_{at}$  at  $\phi = 0$  and  $180^\circ$ , with the parameter  $f$  125 to .800 MHz. Constant:  $p_2$  = vertical,  $\theta_i = 80.8^\circ$ ,  $h_B = 1.0$  m.

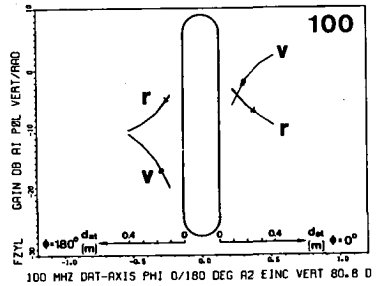
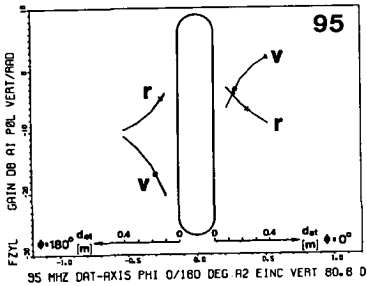
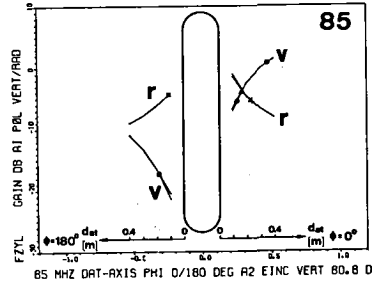
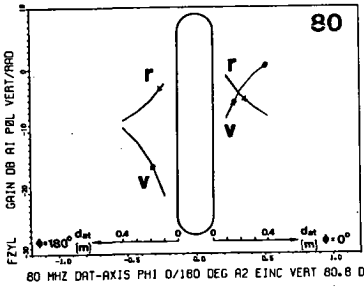
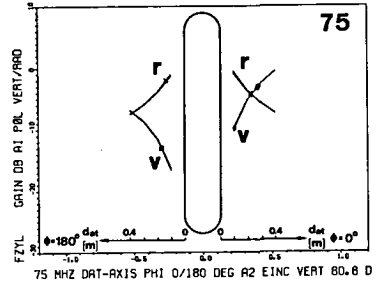
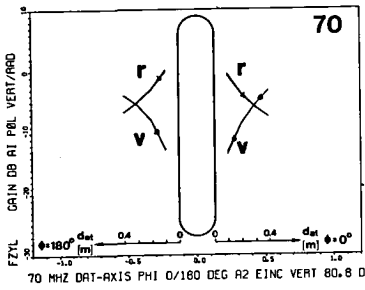
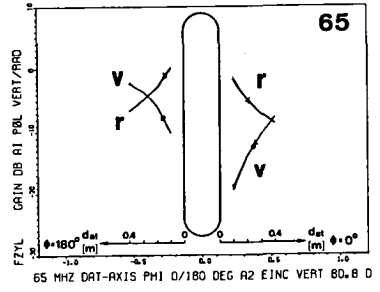
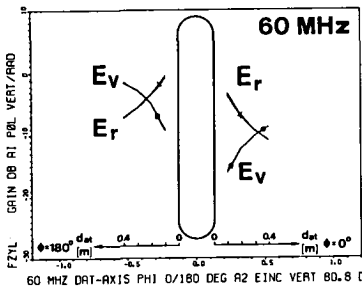


FIGURE 78c Field components  $E_v$  and  $E_r$  versus  $d_{at}$  at  $\phi = 0$  and  $180^\circ$ , with the parameter  $f$  60 to 100 MHz. Constant:  $p_2 = \text{vertical}$ ,  $\theta_i = 80.8^\circ$ ,  $h_b = 1.0 \text{ m}$ .

FIGURES 78a and 78b show the directive radiation pattern at  $\phi = 0^\circ$  and  $180^\circ$  at variable  $d_{at}$  in the full frequency range from 11 to 800 MHz, FIGURE 78c in the resonance frequency range 60 to 100 MHz.

#### Vertical E-field component $E_V$

- Below resonance : Below 30 MHz the  $E_V$ 's at  $\phi = 0$  and  $180^\circ$  are symmetrical, are largest with large  $d_{at}$  (-3 dB at  $d_{at} = 0.4$  m) and decrease with decreasing  $d_{at}$  (-11 dB at  $d_{at} = 0.1$  m). Above 50 MHz the two  $E_V$ 's become asymmetric but still decrease with decreasing  $d_{at}$ . Thus, the body shows no directive characteristics, and the body has little influence on  $E_V$  as long as  $d_{at}$  is larger than 0.4 m.
- Above first resonance: At frequencies above 125 MHz  $E_V$  is always smaller at  $\phi = 180^\circ$  than at  $\phi = 0^\circ$ . At  $\phi = 180^\circ$   $E_V$  decreases constantly with decreasing  $d_{at}$ , with an amplitude of about -11 dB at  $d_{at} = 0.4$  m and of about -18 dB at  $d_{at} = 0.1$  m. At  $\phi = 0^\circ$   $E_V$  oscillates around 0 dB according to the results in section 7.3.1.: maxima occur at  $d_{at} \sim n \cdot \lambda / 4$ ,  $n = 1, 3, 5, \dots$  and minima at  $d_{at} \sim n \cdot \lambda / 2$ ,  $n = 0, 1, 2, \dots$ . The body acts like an efficient reflector if  $d_{at}$  amounts to  $n \cdot \lambda / 4$  and is a good absorber if  $d_{at} < 0.2$  m. As an example the forward/backward ratio is 17 dB at  $d_{at} = 0.2$  m / 350 MHz.

#### Radial E-field component $E_R$

- Below resonance: at 11 MHz  $E_R$  is very small at  $\phi = 0^\circ$  but increases with increasing frequency. Above 50 MHz both  $E_R$ 's increase with decreasing  $d_{at}$  and become larger than  $E_V$  at about  $d_{at} < 0.15$  m. Above 60 MHz both  $E_R$ 's are about symmetrical with about -2 dB at  $d_{at} = 0.1$  and -9 dB at  $d_{at} = 0.4$  m. At very small  $d_{at}$  the body acts like a director (11 MHz) and as a director/reflector (> 60 MHz).
- Above first resonance: from (60) to 200 MHz both  $E_R$ 's at  $\phi = 0$  and  $180^\circ$  are about symmetrical with high values at small  $d_{at}$ . Generally the  $E_R$ 's are larger than the  $E_V$ 's at  $d_{at} < 0.1$  m ( $< 0.3$  at  $\phi = 180^\circ$ ), and the body acts like a director/reflector for small  $d_{at}$ 's. Above 250 MHz  $E_R$  decreases first at  $\phi = 0^\circ$  and above 350 MHz also at  $\phi = 180^\circ$ . Above 450 MHz and  $d_{at} > 0.3$  m the  $E_R$ 's become very small, smaller than the  $E_V$ 's.

#### Resonance region 60 to 200 MHz

- Vertical  $E_V$  components: if  $d_{at} < \lambda / 4$ , the  $E_V$ 's decrease with decreasing  $d_{at}$  and are smallest at about 85 MHz at  $\phi = 180^\circ$  (-22 dB at  $d_{at} = 0.1$  m).
- Radial  $E_R$  components: Both  $E_R$ 's are larger (> -5 dB) at  $d_{at} < 0.15$  m.

#### 10.4.9. EFFECT OF DIFFERENT BODY SHAPES ON THE FIELDS IN THE SHADOW ZONE

The former computations with the simple body model FZYL revealed the systematic relations between antenna location and field quantities. The most important results are summarized in FIGURE 80 for  $\phi = 180^\circ$ :

- $E_V/f$  diagram: sharp anti-resonance at about 75-105 MHz, recovery of  $E_V$  at frequencies above 125 MHz and oscillation around - 16 dB ( $d_{at} = 0.1$  m)
- $E_R/f$  diagram: two peaks, one around 70 MHz (+0.5 dB) and a second of similar amplitude around 150 MHz (+0 dB) at  $d_{at} = 0.1$  m.
- $E_V - E_R/f$  diagram at  $d_{at} = 0.1$  m:  $E_R$  is up to 16 dB larger than  $E_V$  at frequencies below 550 MHz
- $E_V - E_R/f$  diagram at  $d_{at} = 0.4$  m:  $E_R$  is usually smaller than  $E_V$

The corresponding data has been computed for the man-models in FIGURE 79:

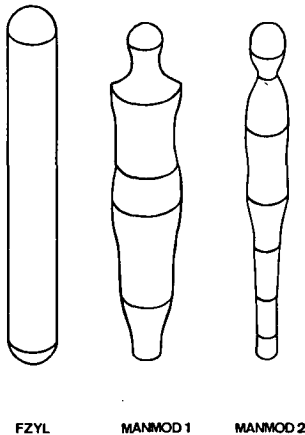


FIGURE 79 Computational body models

- FZYL : finite rotational symmetric cylinder with round end caps  
 $L_B = 1.8$  m ,  $D_B = 0.25$  m .
  - MANMOD 1 : rotational symmetric human body, front view = contour curve  
 $L_B = 1.68$  m ,  $D_B = 0.296$  m at  $d_{at} = 1.0$  m.
  - MANMOD 2 : rotational symmetric human body, side view = contour curve  
 $L_B = 1.68$  m ,  $D_B = 0.196$  m at  $d_{at} = 1.0$  m.
- (dimensions listed in Appendix 16.2.4.)

Comparing FIGURE 81 (MANMOD 1) with FIGURE 80 (FZYL) we find:

- $E_V/f$  diagram: there is still an anti-resonance at about 80-125 MHz but less sharp and without recovery.  $E_V$  drops with increasing frequency.
- $E_R/f$  diagram: only the first peak is well developed, amounts to +3 dB at  $d_{at} = 0.1$  m and occurs at 75 MHz.
- $E_R - E_V$  diagram at  $d_{at} = 0.1$  m:  $E_R > E_V$  (max. 16 dB) above 600 MHz

Comparing FIGURE 82 (MANMOD 2) with FIGURE 80 (FZYL) we find:

- $E_V/f$  diagram: very similar to FZYL (but shifted in frequency)
- $E_R/f$  diagram: very similar to FZYL but larger amplitude variations.  
First peak around 80 MHz (+4 dB) and second peak around 160 MHz (+2.5 dB).

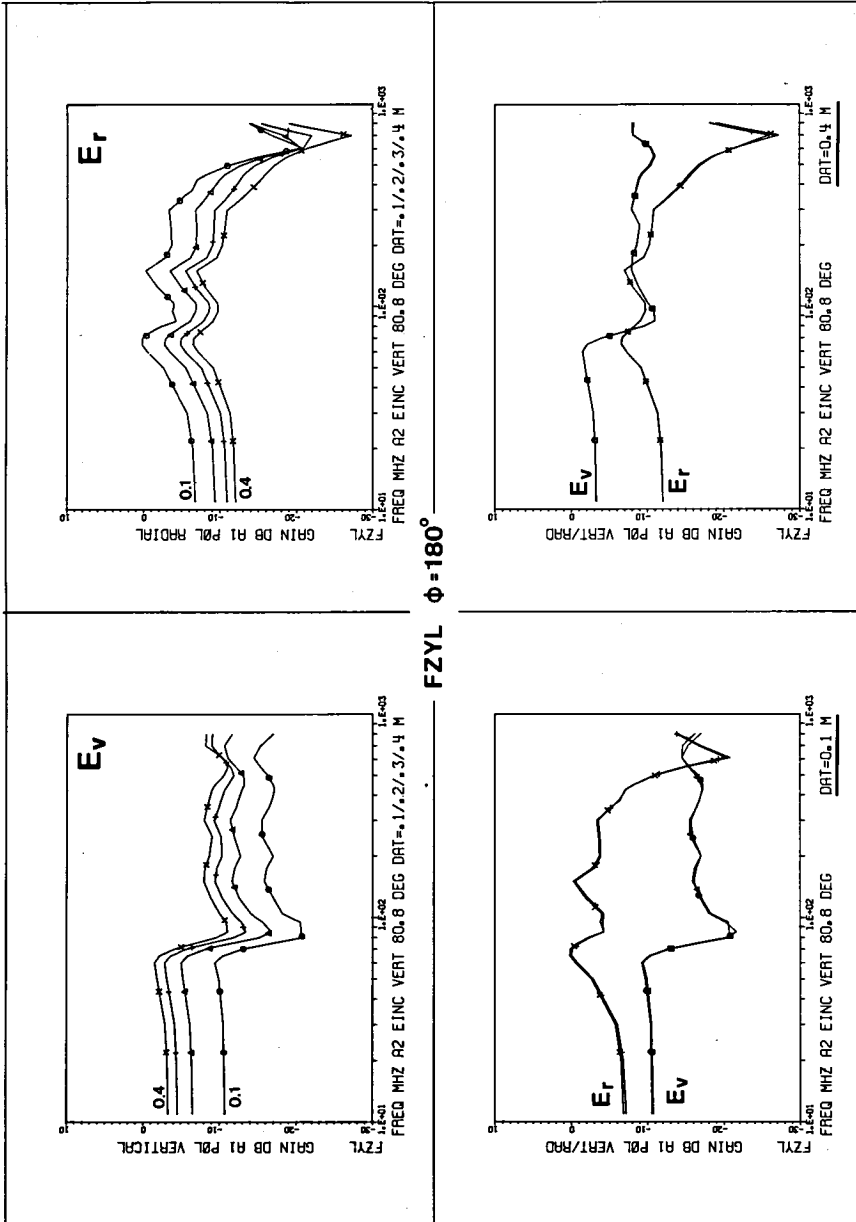


FIGURE 80 Summarized computational results from body model FZYL

$E_v$  versus  $f$ , parameter  $dat$

$E_r$  versus  $f$ , parameter  $dat$

$E_v$  and  $E_r$  at  $dat = 0.1$  m

$E_v$  and  $E_r$  at  $dat = 0.4$  m

Constant:  $\phi = 180^\circ$ ,  $p_2 = \text{vertical}$ ,  $\theta_i = 80.8^\circ$ ,  $h_b = 1.0$  m.



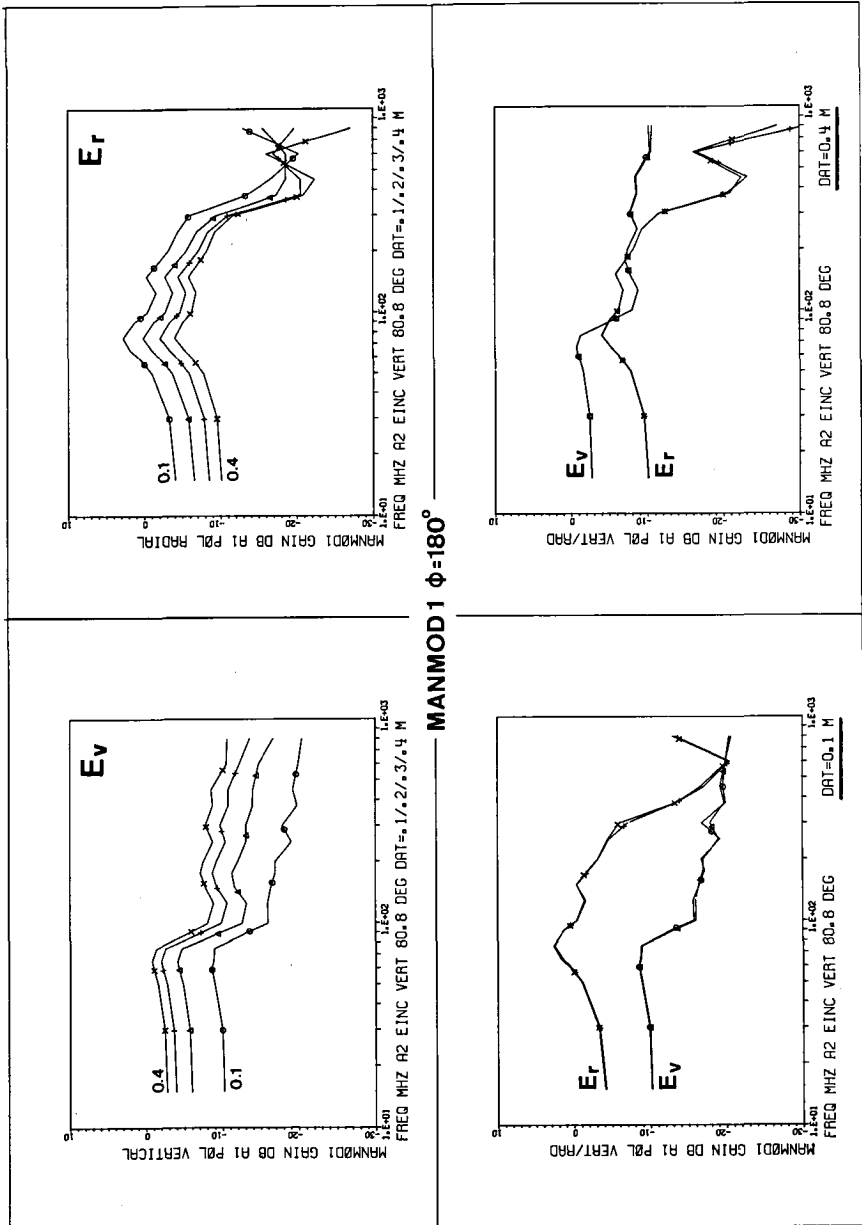


FIGURE 81 Summarized computational results from body model MANMOD 1

$E_v$  versus  $f$ , parameter  $d_{at}$

$E_r$  versus  $f$ , parameter  $d_{at}$

$E_v$  and  $E_r$  at  $d_{at} = 0.1$  m

$E_v$  and  $E_r$  at  $d_{at} = 0.4$  m

Constant:  $\phi = 180^\circ$ ,  $p_2 = \text{vertical}$ ,  $\theta_i = 80.8^\circ$ ,  $h_B = 1.0$  m.

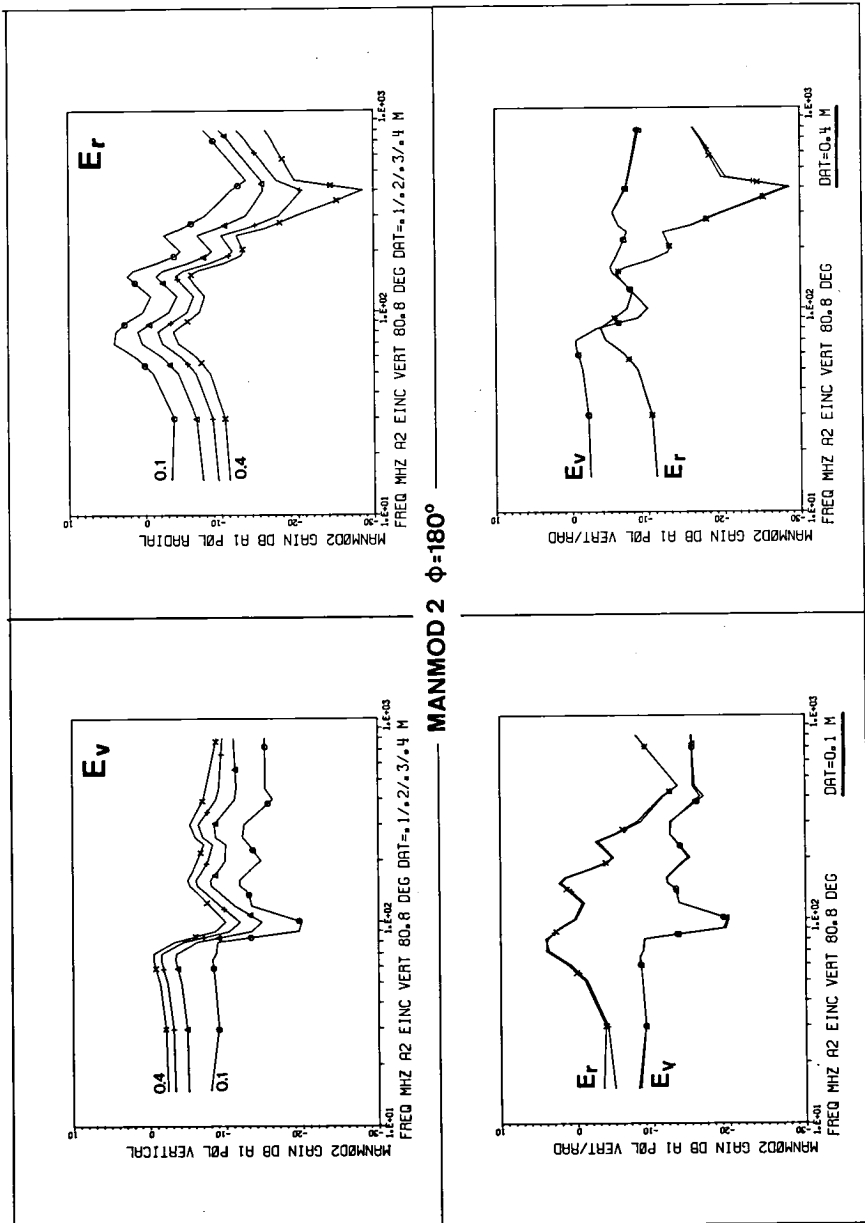


FIGURE 82 Summarized computational results from body model MANMOD2

$E_v$  versus  $f$ , parameter  $d_{at}$

$E_r$  versus  $f$ , parameter  $d_{at}$

$E_v$  and  $E_r$  at  $d_{at} = 0.1$  m

$E_v$  and  $E_r$  at  $d_{at} = 0.4$  m

Constant:  $\phi = 180^\circ$ ,  $p_2 = \text{vertical}$ ,  $\theta_i = 80.8^\circ$ ,  $h_B = 1.0$  m.

#### 10.4.10. EFFECT OF DIFFERENT BODY SHAPES ON AZIMUTHAL RADIATION PATTERNS

If we look at the azimuthal radiation patterns in 10.4.7., we notice the following frequency dependent changes of the field components:

- $E_v$  changes drastically between 60 and 100 MHz
- $E_r$  changes rapidly at about 50 MHz and above 250 MHz
- $E_h$  shows the same pattern up to 350 MHz

Changes of the field components occur only if the body dimensions are in a special relation to the wavelength. If the vertical circumference ( $\sim 2 L_B$ , see also FIGURE 18) is about  $\lambda$ , the  $E_v$  and  $E_r$  are affected. If the horizontal circumference  $D_B \cdot \pi$  is about  $\lambda$ ,  $E_h$  and  $E_r$  are affected.

Considering these facts it is easy to understand the changes in the azimuthal radiation patterns due to body shape alterations. Small changes of  $L_B$  and  $D_B$  provokes similar effects like small changes of the frequency.

Significant azimuthal radiation patterns are shown for the three bodies FZYL, MANMOD1 and MANMOD2 in FIGURES 83 a,b,c at 65 MHz and in FIGURES 84 a,b,c at 150 MHz. Additional samples for 11, 50, 75, 85, 200 and 800 MHz are presented in FIGURES 100 to 105 in Appendix 16.2.5..

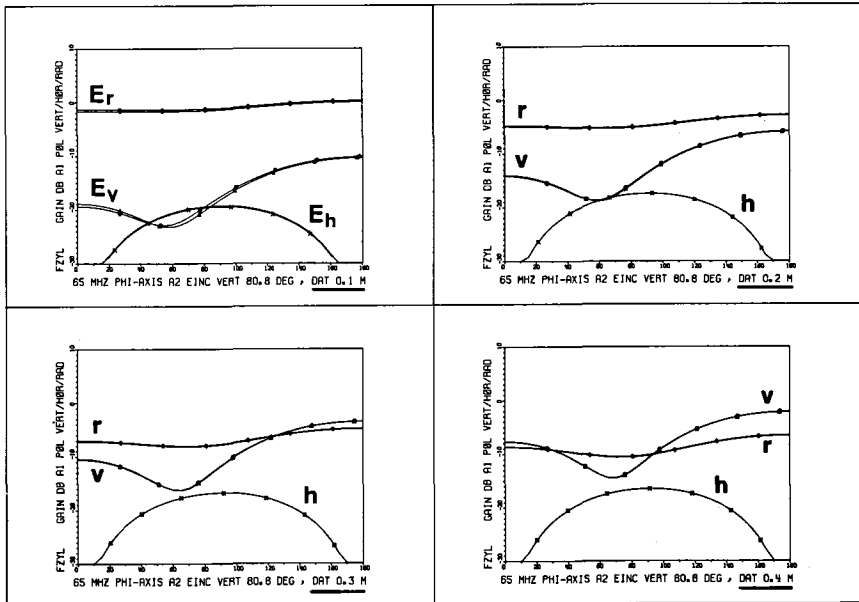


FIGURE 83a Azimuthal radiation patterns FZYL at 65 MHz.  $E_v$ ,  $E_r$  and  $E_h$  components at  $d_{at}=0.1, 0.2, 0.3$  and  $0.4$  m . See also FIGURE 75.

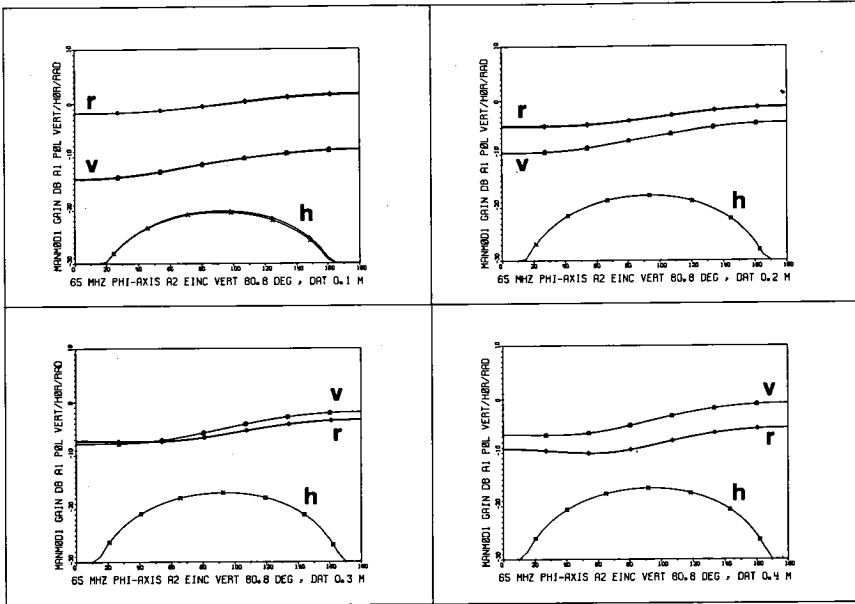


FIGURE 83b Azimuthal radiation patterns MANMOD1 at 65 MHz.

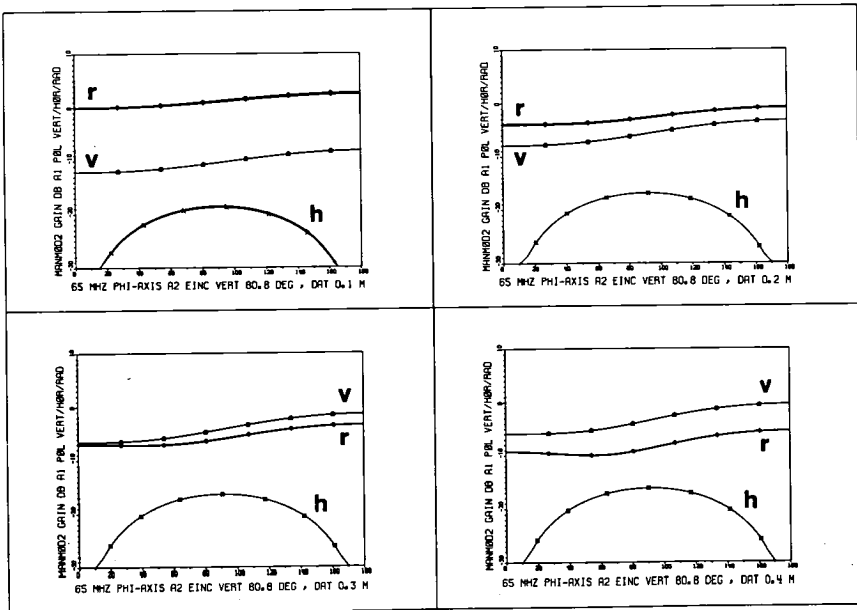


FIGURE 83c Azimuthal radiation patterns MANMOD2 at 65 MHz.

Comparing FIGURES 83a,b,c at 65 MHz we observe an  $L_B$ -effect:

- $E_v$  changes drastically from FZYL to MANMOD1 ( $L_B = 1.8$  and  $1.68$  m), but there are only small differences between MANMOD1 and 2 ( $L_B = 1.68$  m). As can be seen in Appendix 16.2.5., FIGURE 102, the MANMOD's resonate at about 75 MHz in contrast to FZYL at 65 MHz due to the 6.7% shorter  $L_B$ .
- $E_r$  varies only within 2 dB.
- $E_h$  varies only within 2 dB.

Comparing FIGURES 84a,b,c at 150 MHz we observe an  $L_B$  and  $D_B$ -effect:

- $E_v$  varies within 5 dB at  $\phi = 180^\circ$ . The second ( $\lambda$ ) resonance is best developed at MANMOD2 which has the largest  $L_B/D_B$ -ratio. The weakest  $\lambda$  resonance occurs at MANMOD1 with the smallest  $L_B/D_B$ -ratio.
- $E_r$  varies within 3 dB, and the values of FZYL are between those of MANMOD1 and 2, corresponding to the  $D_B$  ratio of the three bodies.
- $E_h$  varies within 3 dB. The theoretical horizontal resonant frequencies are 301 MHz (MANMOD1), 380 MHz (FZYL) and 487 MHz (MANMOD2). The asymmetry of  $E_h$  of MANMOD1 is caused by a subresonance, because 150 MHz is close to 301 MHz, the  $E_h$  of FZYL is already better and the  $E_h$  of MANMOD2 is very symmetrical because 150 MHz is well below 487 MHz.

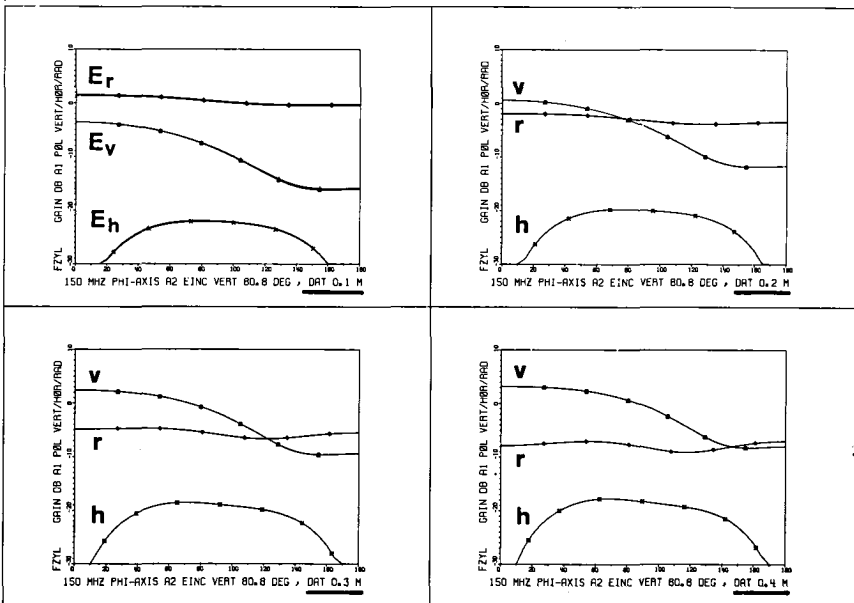


FIGURE 84a Azimuthal radiation patterns FZYL at 150 MHz.  $E_v$ ,  $E_r$  and  $E_h$  components at  $d_{at} = 0.1, 0.2, 0.3$  and  $0.4$  m. See also FIGURE 75.

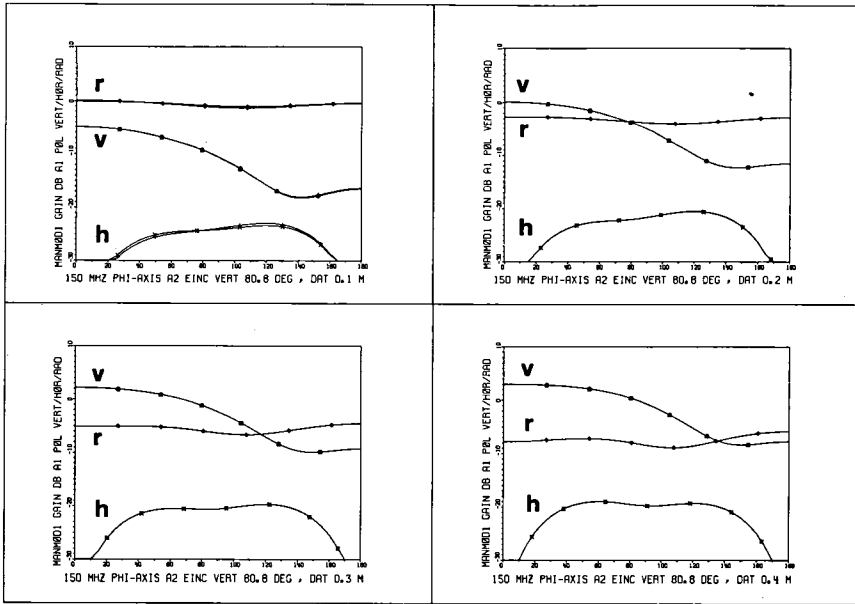


FIGURE 84b Azimuthal radiation patterns MANMOD1 at 150 MHz.

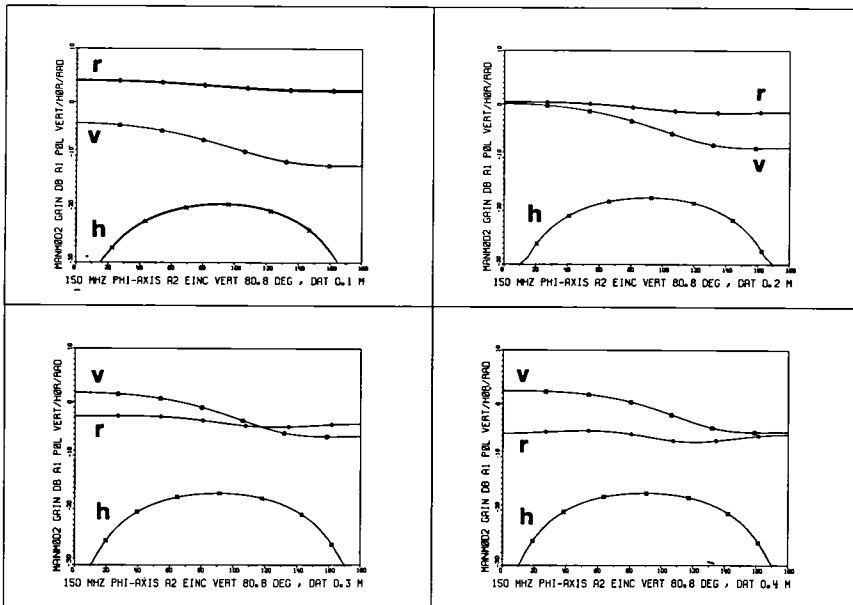


FIGURE 84c Azimuthal radiation patterns MANMOD2 at 150 MHz.

Leer - Vide - Empty

## 11. EXTENDED MEASURING METHOD FOR FIELD COMPONENTS SEPARATION

### 11.1. PURPOSE OF THE EXTENDED EXPERIMENTS

The experimental data in section 9. were obtained with the measuring method described in section 8. The computational data agreed with the experimental data within  $\pm 3$  dB for all three test bodies, but only at frequencies above 200 MHz and antenna-body distances above 0.1 m.

A poor agreement between experimental data and computation was noticed at frequencies below 200 MHz if  $d_{at}$  was smaller than 0.2 m. The reasons for this discrepancy can now be explained by the computational data found in section 10.:

- In the extreme proximity of the body the radial field exceeds the vertical polarized field, especially at  $\lambda/2$  resonance ( $\sim 65$  MHz) and at  $\lambda$  resonance ( $\sim 150$  MHz)
- Electrically small monopole antennas with insufficient counterpoise exhibit a considerable transverse sensitivity (receiving case) or radiate a not wholly pure vertical polarized field (transmitting case). The antenna tests in TABLE 51 tell us that the horizontal (or radial) sensitivity is only about 0-12 dB below the vertical sensitivity at 75 MHz, 19 dB at 125 MHz and 16-18 dB at 205 MHz. The antenna data at 101 MHz (25 dB) and 158 MHz (21 dB) are satisfactory, resulting in a better agreement as can be seen in FIGURES 56 and 57.
- Remotely fed test antennas disturb the fields in the proximity of the body, and especially at low signal levels a part of the signal is picked up by the feeding cable, even when surface waves are attenuated according to FIGURE 44.

Another problem was the fixed relative ( $h_B$ ) and absolute ( $h_1$ ) antenna height and the missing data concerning the field homogeneity.

The purpose of the extended experiments are therefore defined as:

- Separate measurement or generation of radial and vertical field components in the frequency region 50 to 200 MHz without disturbing the fields around the test body.
- Measurement of the  $h_1$  and  $h_B$ -dependence of the field components with and without test bodies for field homogeneity studies.



In section 9.1.5. the reciprocity theorem has been verified, so that the test antenna could be a receiving or a transmitting antenna for our extended experiments. Both methods have their advantages for special applications:

Probe receiving antenna  $A_1$  . A common probe antenna consists of a small dipole (whip, helical or conical for broadband) equipped with a rectifier attached to highly resistive, twisted cables. A remote precision DC amplifier measures the signal without range switching from about 1 mV to 1 V (see e.g. BELSHER [9]) almost linearly. The problem is the very low signal at  $A_1$  (e.g.  $E_v$  at 100 MHz and  $d_{at} < 0.1$  m) and the relative high field around the connecting cables. A better method would be to build the DC-amplifier and a fiber-optic transmitter close to  $A_1$ , but then problems have to be solved concerning power consumption (LED's!) and amplifier stability. This method would be best if broadband characteristic is urgently required and if the signal to be measured is much larger than the other RF-signals in the air. Selective built-in receivers cannot be recommended due to limited amplitude range, tuning problems and stability.

Probe transmitting antenna  $A_1$  . Free-oscillating miniature transmitters cannot be recommended due to amplitude and especially frequency stability problems, because the antenna load is not stable. Quartz-stabilized frequency synthesizers are not suited due to power consumption and space requirements. Thus separate, quartz-stabilized fixed-frequency transmitters offer the best solution concerning volume, power consumption, stability and costs. The main problem is the preset frequency, but on the other hand each probe transmitter can be matched properly to the suited antenna with best long-time stability. Such probe transmitters will be shown in section 11.3. and were used in the following experiments.

## 11.2. ANTENNA MANIPULATOR

A special antenna manipulator (FIGURE 85 and 86) has been developed with the following features:

- Translation of a complete transmitter along the vertical axis from  $0.1 < h_g < 1.7$  m. Continuous remote translation with permanent  $h_g$  recording (rubber band goniometry, accuracy better than 5 cm)
- Rotation of  $A_1$  around the antenna center for  $p_1$  vertical to radial
- Accurate and stable positioning of  $d_{at}$  at 0.1, 0.2, 0.3 and 0.4 m.

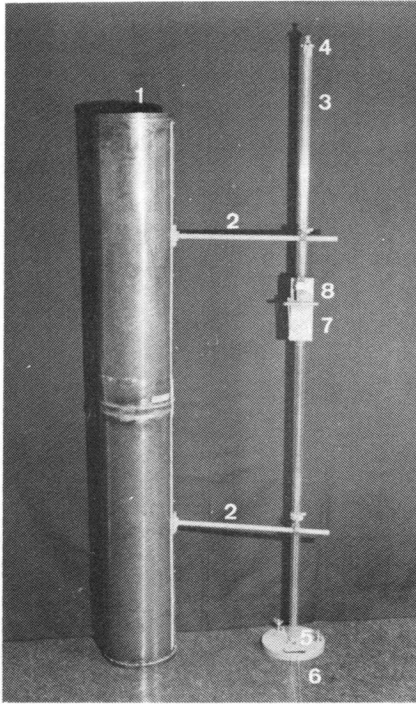


FIGURE 85 Antenna manipulator

- 1 : test body MET
- 2 : dat-spacers, 15 mm  $\varnothing$  PVC tubes screwed perpendicular to the surface of the test body
- 3 : vertical trackway, three 15 mm  $\varnothing$  plexiglass tubes
- 4 : anchoring strings and deflection pulley for strings (6)
- 5 : basement with deflection pulley (screwed on revolving stage)
- 6 : thin plastic strings for remote manual up/down pulling of the wagon carrying the antenna
- 7 : wagon, PVC plate with four PVC wheels shaped like cotton reels
- 8 : small revolving disk with lock for antenna rotation around the antenna center (details:FIG.86)

The main parts of the antenna manipulator are shown in FIGURE 85. In addition a rubber band goniometer (similar to FIGURE 45) in the horizontal plane on the basement (5) measures the antenna height. For outdoor experiments the top (4) of the trackway is fixed to the revolving stage by stretched strings to prevent mechanical oscillations.

For the experiments with standard body-earth spacing  $s$  ( $s=0.2\text{m}$ ) the test body is standing directly on the supporting revolving stage (FIGURE 45) for experiments with  $s=0.7\text{m}$  on wooden precision spacers.

### 11.3. ELECTRICALLY SMALL DIPOLE ANTENNAS WITH BUILT-IN OSCILLATORS

A test transmitter consists of an electrically small dipole antenna and of an autonomous RF-generator (FIGURE 86). The test transmitters have been developed in order to obtain very stable, independent and miniature field sources and are denoted as A01 (65 MHz), A02 (74 MHz), A03 (101 MHz) and A04 (164 MHz). The helical dipole antenna of  $2h<0.1\text{m}$  and  $D_h=11\text{mm}$  have been tuned to resonance (TABLE 88) and the RF-generators are mounted perpendicular to the center of the antennas in the neutral antenna plane.

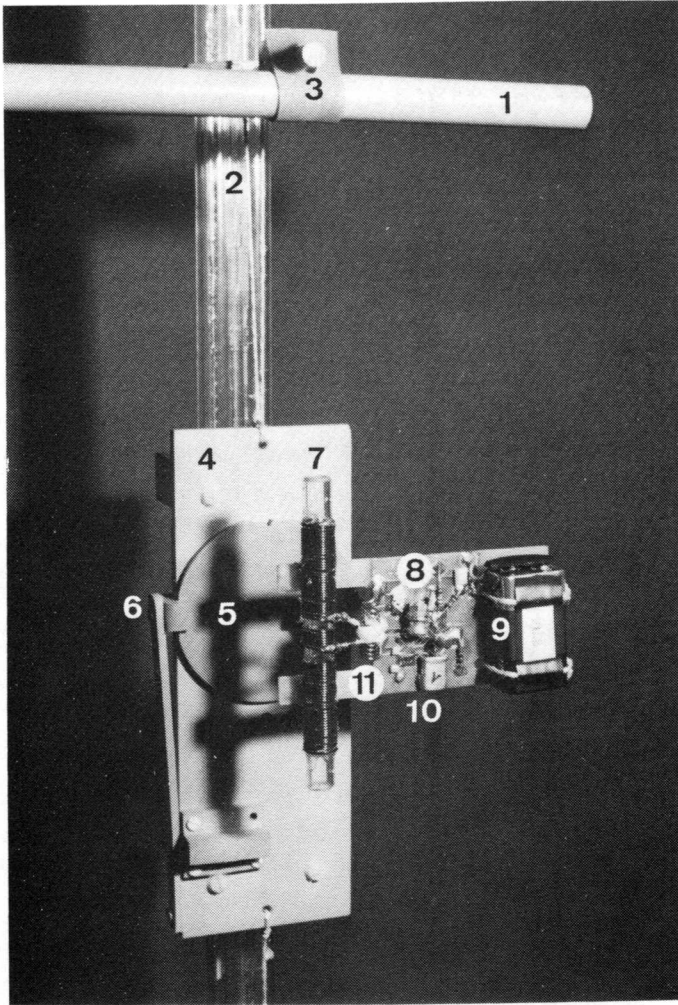


FIGURE 86 Test antenna  $A_1$  with built-in oscillator on antenna manipulator

- |   |   |
|---|---|
| 1 : $d_{at}$ -spacer (see also FIGURE 85) | 6 : lock of the revolving disk              |
| 2 : plexiglass vertical trackway          | 7 : helical dipole antenna $A_1$            |
| 3 : quick-fixing device for $d_{at}$      | 8 : RF-generator with:                      |
| 4 : antenna wagon with pulling strings    | 9 : 9V alkaline battery 540 mAh             |
| 5 : small revolving disk carrying $A_1$   | 10 : quartz (3 <sup>th</sup> harmonic mode) |
| for $p_1$ = vertical to radial            | 11 : RF-antenna coupler                     |

The construction of miniature, unshielded RF-generators of high amplitude stability is quite difficult at frequencies above 50 MHz. A solution was found in the modification of available high-standard RF-suboscillators of professional walkie-talkies (65,74 and 164 MHz) and in a special construction for 101 MHz. The main specifications of the final RF-oscillators are listed in TABLE 87, the output power amounts to 1-10 mW.

FREQ [MHz]	SUBOSCILLATOR manufacturer type	ADDITIONAL ELEMENTS (RF-coupling etc.)	INPUT CURR. [mA]	AMPLITUDE STABILITY (*) [dB]	DIMENSIONS without bat. [mm]
65	AUTOPHON (special)	ferrit 50 to 50 $\Omega$ balun, mod. TV balun	7	0.5	27 x 27 x 30
74	MOTOROLA KXN1067A	external 5 V reg., antenna center coil used as oscil. coil	8	0.1	19 x 9 x 28
101	WAFFEN FABRIK THUN (spec.)	inductive coupling 3 turns around osc.	6	1.0	50 x 40 x 10 (few elem.)
164	MOTOROLA KXN1041A 54.667 MHz	5 V reg., RF-amplif. freq. multiplier antenna center coil used as 164 MHz coil	40	0.5 (*): during 2 hours	19 x 9 x 28 + 25 x 17 x 15

TABLE 87 Specifications of the built-in quartz RF oscillators

The helical dipole antennas were computed according to Appendix 16.1. and tuned with the help of a network analyser. The application of lossy conductors (PVC insulation) increases the bandwidth (damping effect in a resonant RLC network) but decreases the (non important) efficiency. The data of the antennas are listed in TABLE 88.

FREQ [MHz]	TOTAL TURNS No.	CENTER TURNS No.	TOTAL LENGTH [mm]	CENTER LENGTH [mm]	CONDUCTOR MATERIAL DIAMETER, INSULAT. [mm]	-3 dB BANDWIDTH (analyser data) [MHz]
65	121	7	90	8	0.4 PVC center sec. 0.2 enamelled wire for 2x22 end turns	64 to 66
74	97	7	94	9	0.5 enamelled wire	72 to 75
101	72	6	82	9	0.8 enamelled wire	99 to 102
164	45	5	95	9	0.8 PVC	159 to 167

TABLE 88 Specifications of the helical dipole antennas A<sub>1</sub>

During the network analyser measurements the center turns of the dipole antenna were coupled to the  $50\Omega$  coaxial measuring cable with a miniature  $50$  to  $50\Omega$  ferrit balun (Appendix 16.1.1.). The obtained  $-3$  dB bandwidth may be different when coupled to the actual RF-oscillator and is generally larger at imperfect matching (reduced efficiency).

From the test transmitters A01 to A04 one cannot expect a totally omnidirectional radiation pattern with strict linear polarization. The transmitter's tests, however, revealed a very stable ( $0.5$  dB) azimuthal radiation pattern at  $p_1$  = vertical (see TABLE 90), and the actual experiments revealed that the transverse polarization (polarization perpendicular to the antenna axis) is about  $10$  to  $15$  dB smaller than the main polarization.

#### 11.4. TEST PROGRAM AND SOME EXPERIMENTAL RESULTS OBTAINED WITH A01 TO A04

1. PREPARATIONS				
1.1. Mounting of the $h_1$ -goniometer and calibrations				
1.2. Warming-up of the RF-equipment and recorder, initial calibrations				
1.3. Measuring of the FSL at $p_1$ = vertical and radial versus $\phi$ at $h_1 = 1.2$ m and $p_2$ = vertical. (see results in TABLE 90)				
1.4. Field homogeneity measurements at $0.7 < h_1 < 2.0$ m at $\phi = 0^\circ$				
1.5. Calibration of FSL to 0 dB at $p_1$ = vertical, $h_1 = 1.2$ m, $\phi = 0^\circ$				
2. TRANSMISSION EXPERIMENTS WITH VARIABLE ANTENNA HEIGHTS $h_1$				
2.1. MET at $\phi = 0^\circ$ , $dat = 0.1$ m, $s = 0.2$ m, $p_1$ = vertical/radial, $0.7 < h_1 < 1.5$				
2.2. " " $dat = 0.2$ m, " " " "				
2.3. " $\phi = 180^\circ$ , $dat = 0.1$ m, " " " "				
2.4. " " $dat = 0.2$ m, " " " "				
2.5. " $\phi = 0^\circ$ , $dat = 0.1$ m, $s = 0.7$ m, $p_1$ = vertical/radial, $1.2 < h_1 < 2.0$				
2.6. " " $dat = 0.2$ m, " " " "				
2.7. " $\phi = 180^\circ$ , $dat = 0.1$ m, " " " "				
2.8. " " $dat = 0.2$ m, " " " "				
3. TRANSMISSION EXPERIMENTS WITH VARIABLE AZIMUTHAL ANGLE $\phi$				
3.1. MET at $dat = 0.1$ m, $s = 0.2$ m, $h_1 = 1.2$ m, $p_1$ = vertical/radial, $0 < \phi < 360^\circ$				
3.2. " $dat = 0.2$ m, " " " "				
3.3. " $dat = 0.3$ m, " " " "				
3.4. " $dat = 0.4$ m, " " " "				
3.5. " $dat = 0.1$ m, $s = 0.7$ m, $h_1 = 1.7$ m, $p_1$ = vertical/radial, $0 < \phi < 360^\circ$				
3.6. " $dat = 0.2$ m, " " " "				
3.7. SUB at $dat = 0.1$ m, $s = 0.2$ m, $h_1 = 1.2$ m, $p_1$ = vertical/radial, $0 < \phi < 360^\circ$				
3.8. " $dat = 0.2$ m, " " " "				
3.9. " $dat = 0.1$ m, $s = 0.7$ m, $h_1 = 1.7$ m, $p_1$ = vertical/radial, $0 < \phi < 360^\circ$				
3.10. " $dat = 0.2$ m, " " " "				

TABLE 89 Summarized experiments with test transmitters A01, A02, A03, A04

The test set-up consists of a revolving stage, carrying the test body and the antenna manipulator, and the remote receiving antenna  $A_2$  at  $d = 31$  m and  $h_2 = 6.2$  m as shown in the similar test set-up in FIGURE 44. The performance of the LPD-antenna  $A_2$  is only specified for 100 - 1000 MHz. Below 100 MHz  $A_2$  is suited for relative field measurements of vertical polarized field components ( $p_2 = \text{vertical}$ ) but will also pick-up field components of other polarizations. The performance of the test transmitters A01 to A04 was measured by recording the azimuthal radiation pattern at  $p_1 = \text{vertical/radial}$  without TS. If both  $A_1$  and  $A_2$  would be strictly linear polarized, and if there would be no ground reflections, the following data had to be obtained: 1.)  $p_1 = \text{vertical}$  :  $E_0$  stable at 0 dB from  $0 < \phi < 360^\circ$ . 2.)  $p_1 = \text{radial}$  : A maximum of - 16 dB ( $E_0 \cos\theta_i$ ) should occur at  $\phi = 0, 180$  and  $360^\circ$ , and the signal should drop to  $-\infty$  dB at  $\phi = 90$  and  $270^\circ$ . The actual experimental data are listed in TABLE 90 :

FREQ. [MHz]	VERTICAL POL.	RADIAL POLARIZATION			
	Amplitude [dB]	Maximum Signal Amplitude [dB]	Angle $\phi$ [ $^\circ$ ]	Minimum Signal Amplitude [dB]	Angle $\phi$ [ $^\circ$ ]
65	$\pm 0.5$	-1, -3	80, 260	-9, -10	165, 350
74	$\pm 0.25$	-10, -7	45, 220	-15, -32	115, 320
101	$\pm 0.5$	-6, -9, -6	0, 185, 360	-16, -13	105, 260
164	$\pm 0.25$	-6, -8, -6	0, 190, 360	-14, -12	110, 270

TABLE 90 Experimental data of the performance of the test transmitters A01 to A04 at  $h_1 = 1.2$  m,  $p_2 = \text{vertical}$ ,  $\theta_i = 80.8^\circ$  in proximity to ground.

The test transmitters A03 and A04 perform best because the azimuthal radiation patterns are symmetrical and follow the predicted pattern. The test transmitters A01 (65 MHz) and A02 (74 MHz) have a disturbed azimuthal radiation pattern at  $p_1 = \text{radial}$ , caused primarily by ground reflections and by the elliptical polarization of the helical  $A_1$  antennas. However, measurements of the dominant field components in the proximity of the TS should be possible with a reduced accuracy.

The next test is concerned with the field homogeneity at  $p_1 = \text{vertical}$  and radial at variable antenna heights without TS. The results are shown in TABLE 91 for both polarizations at  $0.8 < h_1 < 1.8$  m.

VERTICALLY POLARIZED FIELD AMPLITUDE VARIATION AT VARIABLE ANTENNA HEIGHTS $h_1$						
FREQUENCY [MHz]	RELATIVE FREE-SPACE FIELD STRENGTH $E_0(h_1)$ IN DECIBELS AT HEIGHT					
	$h_1 = 0.8 \text{ m}$	$h_1 = 1.0 \text{ m}$	$h_1 = 1.2 \text{ m}$	$h_1 = 1.4 \text{ m}$	$h_1 = 1.6 \text{ m}$	$h_1 = 1.8 \text{ m}$
65	+ 0.5	+ 0.0	+ 0.0	- 0.0	- 0.5	- 0.5
74	+ 1.0	+ 0.5	+ 0.0	- 0.5	- 1.0	- 1.0
101	+ 1.5	+ 0.5	+ 0.0	+ 0.0	+ 0.0	+ 0.5
164	- 1.5	- 1.0	+ 0.0	+ 0.5	+ 1.5	+ 2.0

TOTAL FIELD AMPLITUDE AT $p_1$ = RADIAL / $p_2$ = VERTICAL AT VARIABLE ANTENNA HEIGHTS						
FREQUENCY [MHz]	RELATIVE FREE-SPACE FIELD STRENGTH RELATED TO $E_v$ AT $h_1 = 1.2 \text{ m}$ , $\phi = 0^\circ$					
	$h_1 = 0.8 \text{ m}$	$h_1 = 1.0 \text{ m}$	$h_1 = 1.2 \text{ m}$	$h_1 = 1.4 \text{ m}$	$h_1 = 1.6 \text{ m}$	$h_1 = 1.8 \text{ m}$
65	-10.5	-10.2	-10.0	- 9.5	- 9.0	- 8.2
74	-14.5	-13.5	-13.0	-12.5	-12.0	-11.0
101	- 7.0	- 6.6	- 6.0	- 5.0	- 4.5	- 4.5
164	- 6.0	- 5.5	- 6.0	- 7.0	- 8.0	- 9.0

TABLE 91 Field homogeneities of the field components at  $p_1$  = vertical (above) and  $p_1$  = radial (below), measured along the theoretical vertical axis of the TS (without TS) at  $\phi = 0^\circ$  and  $p_2$  = vertical. The reference field strength is the FSL (0 dB), measured with  $p_1$  = vertical at  $h_1 = 1.2 \text{ m}$ .

The upper data in TABLE 91 show that the field homogeneity at  $p_1 = p_2$  = vertical is within 1.5 dB at antenna heights  $h_1$  from 0.8 to 1.6 m.

The data below in TABLE 91 are a measure for the transversal Gain $_{\Gamma}$  of the antenna  $A_1$ , if  $A_2$  is assumed to be strictly linear polarized. The measured  $E_{\text{tot}}$  is the superposition of:

$$E_{\text{tot}} = E_0 \cos \theta_i + E_0 \sin \theta_i \cdot \cos \Delta\psi \cdot \text{Gain}_{\Gamma} \quad (245)$$

$\Delta\psi$  is the unknown argument of the transversal Gain $_{\Gamma}$ . With (245),  $E_{\text{tot}}$  and  $\Delta\psi = 0^\circ$  one obtains a Gain $_{\Gamma}^*$ , which is the minimum of the actual Gain $_{\Gamma}(\Delta\psi)$ :

Measured  $E_{\text{tot}}$  at  $p_1$  = radial,  $p_2$  = vert.      Minimum transversal Gain $_{\Gamma}$

< - 6.8 dB	> - 10.5 dB
< - 9.9 dB	> - 14.0 dB
< -11.8 dB	> - 20.0 dB

Thus, one may assume that the transverse polarization is about - 9 to -20 dB (mean values of TABLE 91, which are depending on the ground reflection)

## 12. COMPARISON OF IMPROVED EXPERIMENTAL DATA WITH THREE-DIMENSIONAL COMPUTATIONAL DATA

### 12.1. INVESTIGATED PARAMETERS

#### 12.1.1. EFFECT OF THE FREQUENCY ON THE FIELD COMPONENTS AT FZYL AND MET

Let us first compare the previous experimental data of section 9. with the new FZYL computational data of section 10.4.:

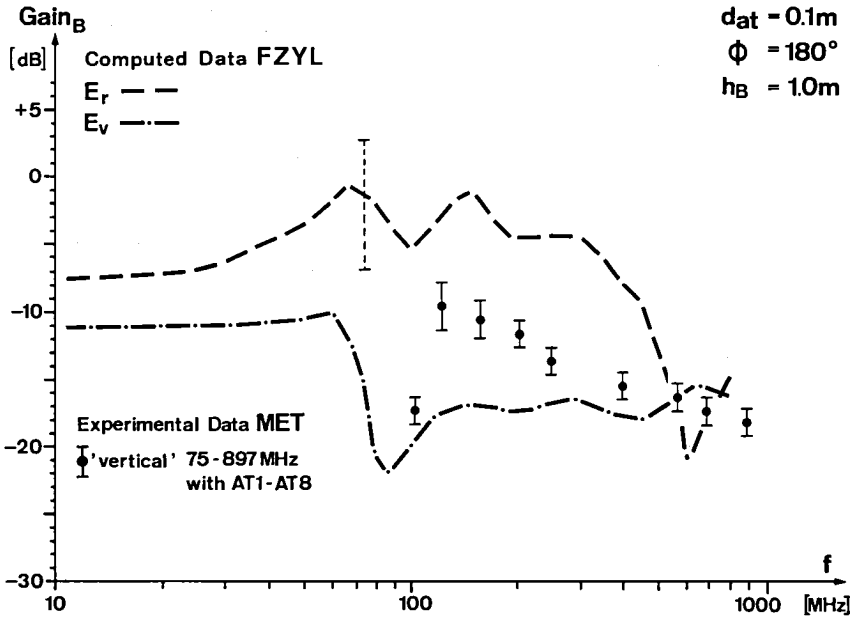


FIGURE 92  $\text{Gain}_B$  versus  $f$  at  $d_{at} = 0.1\text{m}$  and  $\phi = 180^\circ$ . Comparison between experimental MET data (9.1.1.) and computational FZYL data  $E_v$  and  $E_r$ .

FIGURE 92 shows the experimental MET data measured with the previous monopole antennas AT1 to AT8 (8.3.1.) at 74, 101, 125, 158, 205, 250, 400, 562, 700 and 897 MHz. Theoretically these measuring data should be close to the computed  $E_v$  curve. In fact, a good agreement is achieved at higher frequencies 250, 400, 562, 700 and 897 MHz. At lower frequencies, however, the agreement is poor; the experimental data are generally much higher than the computed  $E_v$ 's. It seems to be evident that the monopole antennas with their insufficient counterpoise do not only respond to the weak vertical field component but also to the very strong radial field component.



The experiments with the new test transmitters A01 to A04 prove the existence of the strong radial field components. The experiments are based on the verified reciprocity theorem (9.1.5.) and in order to quantify the effect of the proximity to the ground the experiments have been performed twice: first experiment with  $s = 0.2\text{ m}$ ,  $h_1 = 1.2\text{ m}$  ( $h_B = 1.0\text{ m}$ ) and second experiment with  $s = 0.7\text{ m}$ ,  $h_1 = 1.7\text{ m}$  ( $h_B = 1.0\text{ m}$ ). The results of the experiments are shown in FIGURE 93 :

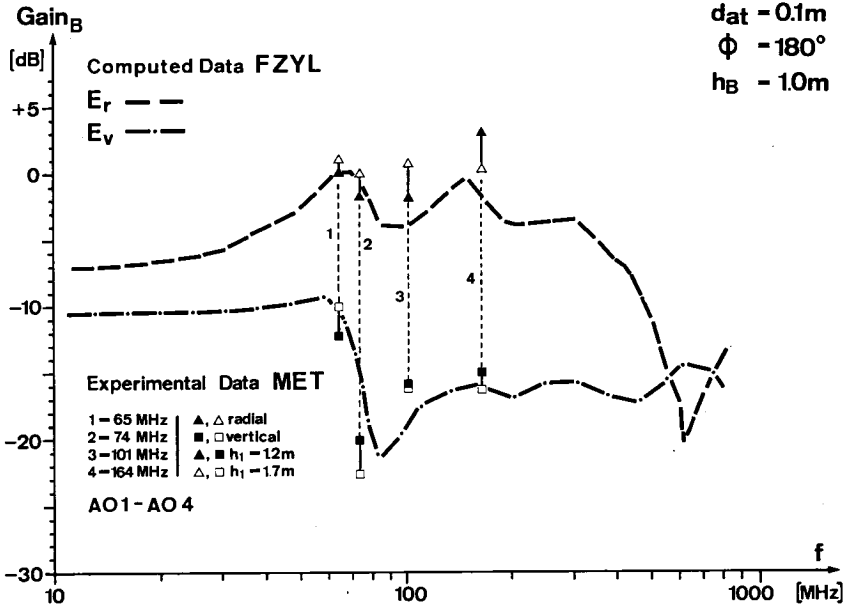


FIGURE 93 Gain<sub>B</sub> versus  $f$  at  $dat = 0.1\text{ m}$  and  $\phi = 180^\circ$ . Comparison between experimental MET data (obtained with the test transmitters A01 to A04) and computational FZYL data at vertical and radial polarizations. Standard experiments : full symbols,  $h_1 = 1.2\text{ m}$ ,  $h_B = 1.0\text{ m}$ ,  $s = 0.2\text{ m}$ . Experiments with reduced ground effects: empty symbols,  $h_1 = 1.7\text{ m}$ ,  $h_B = 1.0\text{ m}$ ,  $s = 0.7\text{ m}$ . (Test body separated by wooden spacers from the stage)

Vertical field components E<sub>v</sub> : The experimental data agree within 3 dB with the computational data, except at 75 MHz where the difference amounts to 5 dB. If one would shift the computed FZYL-data by 5 % to the left the agreement would be 2 dB. Thus, it could be that the actual resonant frequency is about 5 % lower than computed. The effect of the proximity to the ground is not very important, the differences are smaller than 3 dB.

Radial field components  $E_r$  : FIGURE 93 proves the existence of the theoretical predicted radial field components. The  $E_r$  are more than 10 dB larger than  $E_v$  at  $d_{at}=0.1$ . The experimental data agree within 2.5 dB with the computational data, except at 164 MHz where the difference amounts to 4 dB. Similar to the  $E_v$ -components, a better agreement could be achieved (but only for 65, 74 and 101 MHz) by shifting the FZYL-data by about 5 % to the left. The proximity to the ground results in a 2 dB difference at 65 and 74 MHz and a 4 dB difference at 101 and 164 MHz ( $s : 0.7/0.2$  m).

#### 12.1.2. EFFECT OF ANTENNA HEIGHT AND PROXIMITY TO THE GROUND

The computational data are valid for a body in free space, for a standard relative antenna height  $h_B=0.1$  m and for a standard irradiation angle  $\theta_i$  of  $80.8^\circ$ . The experimental data are obtained from a test body in proximity to the ground due to the reasons explained in section 5.3.1.. The antenna-body system is a resonant circuit as we can see from FIGURE 93. Any resonant system is very sensitive to external influences so that in our case the antenna-body system may change its function (e.g., resonant frequency) in proximity to the ground. In order to check if  $h_B$  is an exceptional relative antenna height (i.e., not a representative height) and in order to quantify the effect of the proximity to the ground both  $h_B$  (relative antenna height) and  $h_1$  (absolute antenna height) were varied and compared with the computational data in FIGURES 94 a,b,c,d.

Effect of the proximity to the ground : The FSL vary only by  $\Delta < 2$  dB from  $1.2 < h_1 < 1.7$  m. The computed data are calibrated to FSL ( $s=0.2$  m) and to 'FSL' ( $s=0.7$  m). A strong influence of the proximity of the ground is only noticed at  $E_v$  (65 MHz) and  $E_v$  (74 MHz) due to the different  $E_v(h_B)$  pattern. At a fixed  $h_B$  of 1.0 m the differences due to ground proximity are well below 3 dB for all  $E_v$  and  $E_r$ .

Effect of the relative antenna height : Generally, the  $E_r$  components increase with increasing  $h_B$  (except at 164 MHz, where  $E_r$  is almost constant) and vary up to  $\pm 5$  dB in the range  $0.8 < h_B < 1.2$  m. The  $E_v$  components are much lower than  $E_r$  and vary up to  $\pm 5$  dB in the same range. An  $h_B$  of 1.0 m is not an extraordinary antenna height: only at 74 MHz the  $E_v$  of the isolated body ( $s=0.7$  m) is close to a point of inflexion.

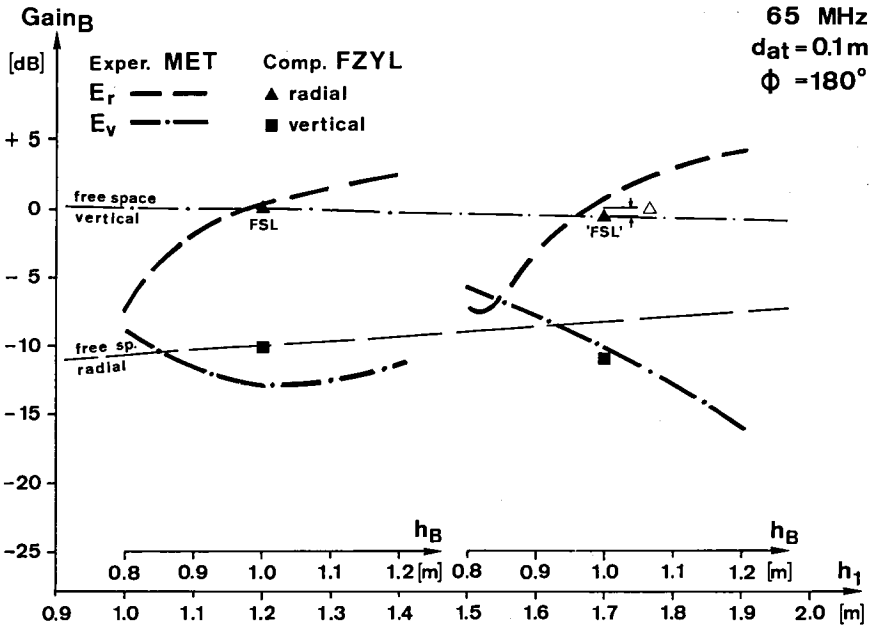


FIGURE 94a Effect of ground proximity and relative antenna height, 65 MHz

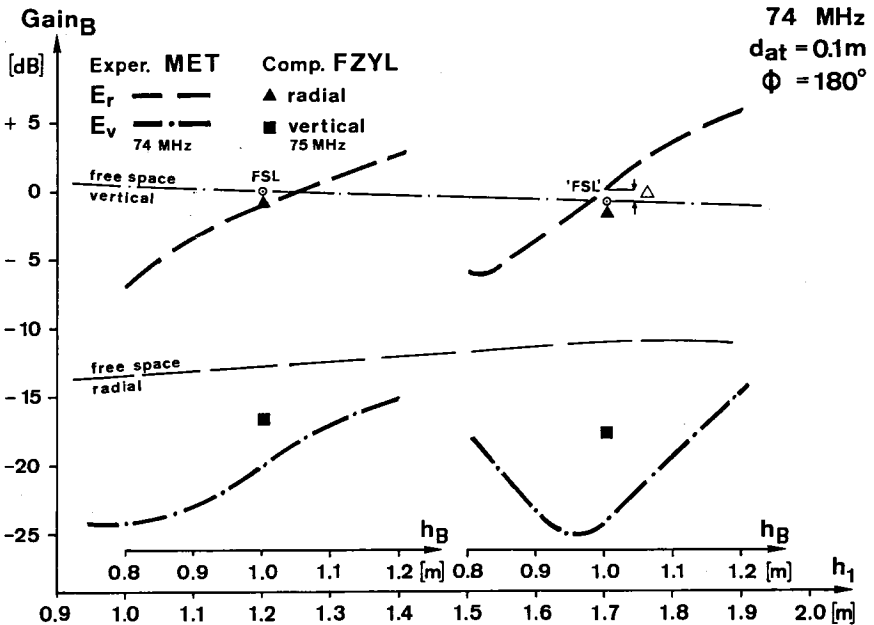


FIGURE 94b Effect of ground proximity and relative antenna height, 74 MHz

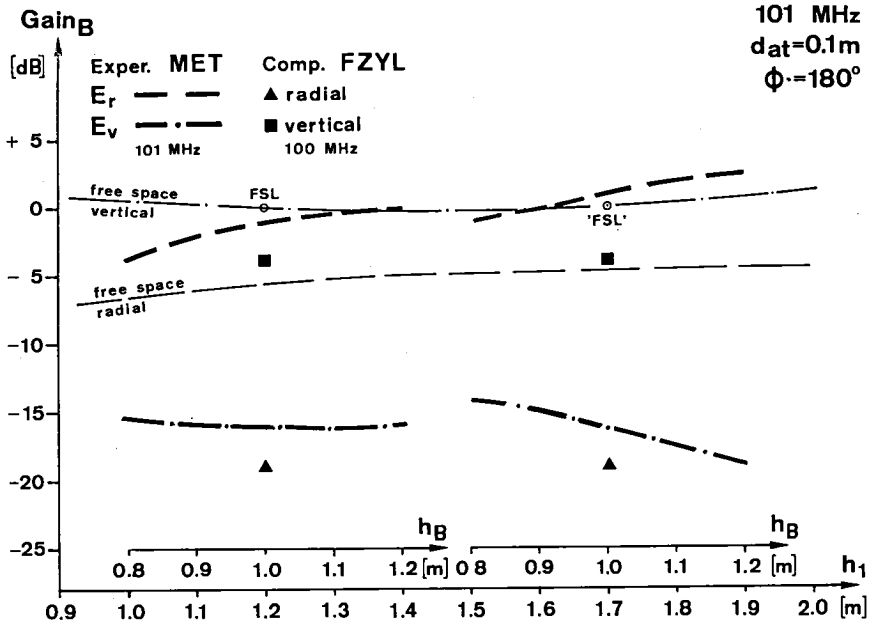


FIGURE 94 c Effect of ground proximity and relative antenna height, 101 MHz

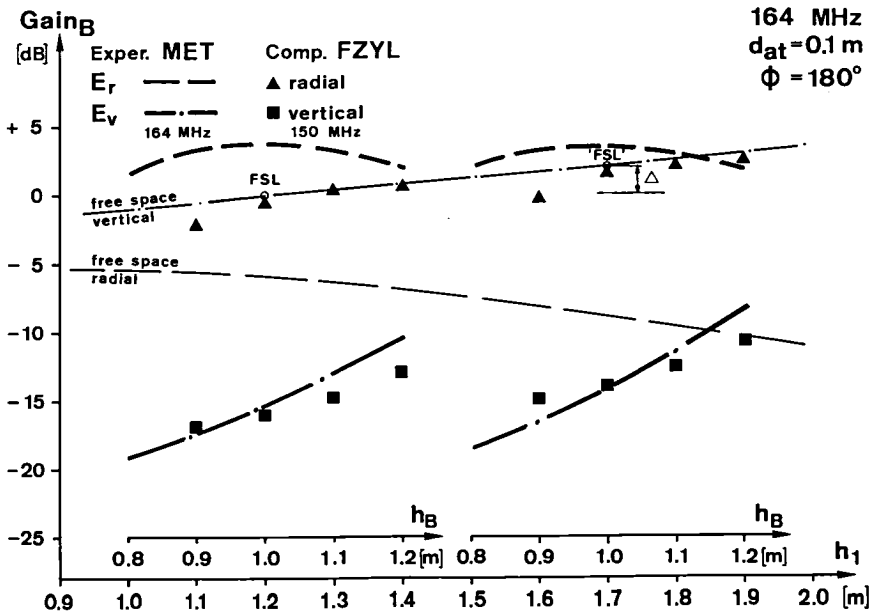


FIGURE 94 d Effect of ground proximity and relative antenna height, 164 MHz

### 12.1.3. EFFECT OF THE ANTENNA-BODY DISTANCE

FIGURE 92 and 93 revealed very low  $E_V$ 's above 100 MHz and large  $E_r$ 's at frequencies between 50 to 300 MHz at  $d_{at}=0.1$  m and  $\phi=180^\circ$ . FIGURES 95 a, b and c show the corresponding data for  $d_{at}=0.2, 0.3$ , and  $0.4$  m. Similar to FIGURE 92 the experimental  $E_V$  data above 250 MHz agree best with the computational data, the typical error is less than 2 dB. At lower frequencies the experimental  $E_r$  and  $E_V$  follow the computed patterns and the agreement between experiment and computations is generally better than 4 dB. The comparison of the experimental and computational pattern leads to the assumption that the MET body resonates about 5% lower than the FZYL. This effect could be explained by the larger circumference of MET (sharp cylinder ends) compared with FZYL (round end caps). FIGURES 95 a,b,c show clearly the increase of  $E_V$  with increasing  $d_{at}$  and the decrease of  $E_r$  with increasing  $d_{at}$ . FIGURE 95 c demonstrates the equilibrium of  $E_V$  and  $E_r$  at  $d_{at} = 0.4$  m in the frequency region 75 to 170 MHz experimentally and theoretically. At smaller  $d_{at}$  the radial component  $E_r$  is dominant and can be observed from minimum 40 MHz to maximum 500 MHz.

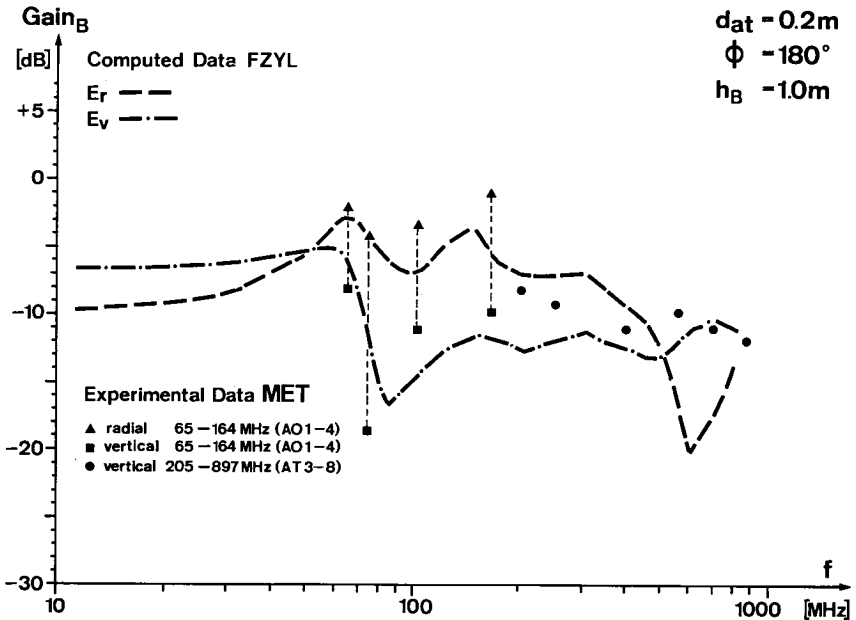


FIGURE 95 a  $Gain_B$  versus  $f$  at  $\phi=180^\circ$  and  $d_{at}=0.2$  m. Comparison between experimental MET data and computational FZYL data. Standard experiments with  $\theta_1 = 80.8^\circ$ ,  $h_1 = 1.2$  m,  $s = 0.2$  m,  $h_B = 1.0$  m with AO1-4 and AT3-8.

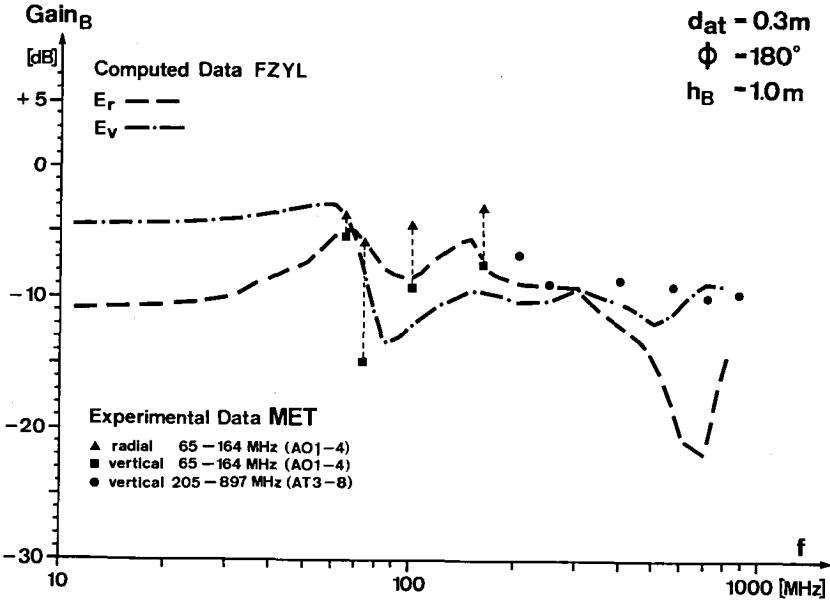


FIGURE 95 b Gain<sub>B</sub> versus f at φ = 180° and d<sub>at</sub> = 0.3m. Comparison like 95 a.

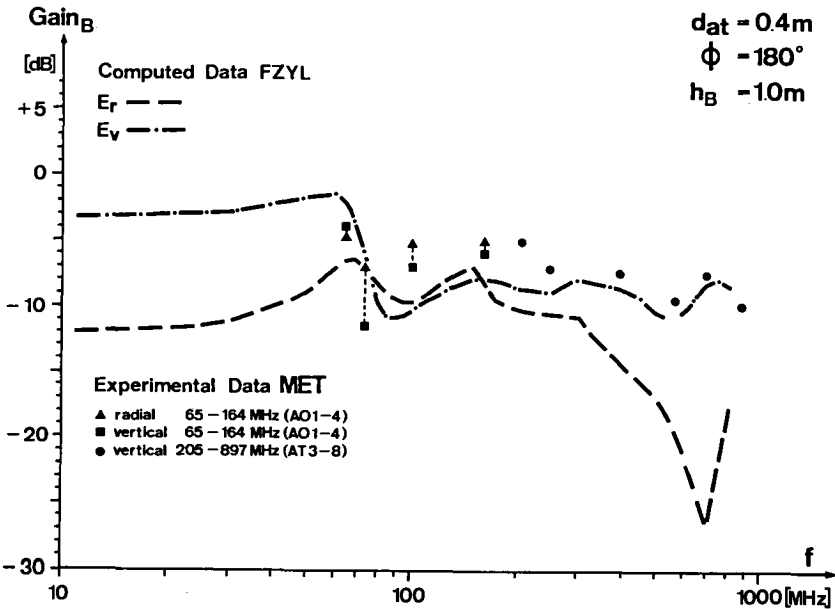


FIGURE 95 c Gain<sub>B</sub> versus f at φ = 180° and d<sub>at</sub> = 0.4m. Comparison like 95 a.

#### 12.1.4. EFFECT OF THE FREQUENCY ON THE FIELD COMPONENTS AT A HUMAN BODY

The experimental data in section 9.1.2. revealed only small differences between the test bodies MET, PHA and SUB at larger  $d_{at}$ 's. Thus, the experimental SUB data and the two computational data MANMOD1 and 2 are presented in FIGURE 96 for the most critical antenna-body distance  $d_{at}=0.1$  in the shadow zone  $\phi = 180^\circ$ :

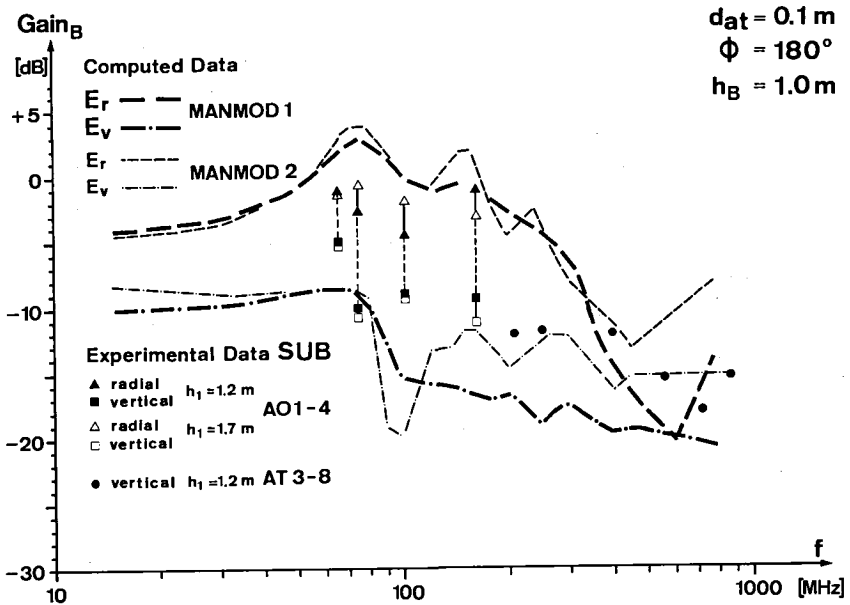


FIGURE 96 Gain<sub>B</sub> versus  $f$  at  $d_{at}=0.1$  and  $\phi = 180^\circ$ . Comparison between experimental SUB data and computational MANMOD1 & 2 data for  $E_r$  and  $E_v$  at two different absolute antenna heights. Full symbols :  $h_1 = 1.2$  m,  $h_B = 1.0$  m,  $s = 0.2$  m ; empty symbols :  $h_1 = 1.7$  m,  $h_B = 1.0$  m,  $s = 0.7$  m.

Vertical field components  $E_v$ : 9 of the 11 experimental data agree with the the MANMOD 1 or 2 - data within 3 dB. The experimental 400 MHz  $E_v$  is 4.5 dB higher than computed and the experimental 101 MHz  $E_v$  is 6.5 dB larger.

Radial field components  $E_r$ : All investigated frequencies prove the existence of the very large radial field components. The maximum difference between experiment and theory amounts to 3 dB ( $s = 0.7$ ) and 5 dB ( $s = 0.2$  m). The radial field component at a human body is up to 10 dB larger than the vertical component. Much higher radial fields were recorded with decreased  $d_{at}$ , but are not presented here due to insufficient accuracy.

#### 12.1.5. AZIMUTHAL RADIATION PATTERNS OF MET, SUB, FZYL AND MANMOD 1 & 2

The azimuthal radiation patterns at frequencies above 200 MHz (above resonance) have been treated in section 9.1.2. (TABLE 60) and 9.1.3. (FIGURE 59) since they could be explained with the simple two-dimensional computations on the IZYL model.

The following FIGURES 97a,b,c,d show the experimental and the computational azimuthal radiation patterns at 65, 74, 101 and 164 MHz at  $d_{at} = 0.1m$  of MET and FZYL, and FIGURES 98a,b,c,d that of SUB and MANMOD 1 & 2. The experimental data have been recorded with the test transmitters A01 to A04 (11.3.) in proximity to the ground ( $s = 0.2m$ ,  $h_1 = 1.2m$ ) and represent realistic azimuthal radiation patterns for practical applications. Because complete 0-180-360° revolutions have always been recorded, two 0-180° recordings may appear for the vertical component  $E_v$  and the radial component  $E_r$  due to the asymmetry of the test set-up (antenna manipulator, radial antenna not perfectly adjusted in the horizontal plane). For the following discussion of the comparison between experimental data (MET and SUB) and computational data (FZYL and MANMOD 1 & 2) the mean value of the experimental data at the distinct angle  $\phi$  will be regarded.

65 MHz : The MET  $E_v$  agree with FZYL  $E_v$  at  $\phi > 100^\circ$  within 3 dB, but at  $0^\circ$  the MET  $E_v$  are up to 14.5 dB higher than computed. Comparing MET with the FZYL data at 50 and 60 MHz one may assume that the discrepancy is caused by a lower resonant frequency of MET. The MET  $E_r$  agree, however, with FZYL  $E_r$  for all  $\phi$ 's within 3 dB.

The SUB  $E_v$  agree with MANMOD 1 & 2 at  $\phi > 90^\circ$  within 4 dB, but at  $0^\circ$  the SUB  $E_v$  are up to 10 dB higher than computed. The SUB  $E_r$  agree, however, with MANMOD 1  $E_r$  for all  $\phi$ 's within 3 dB.

The minimum radial component is always stronger than the maximum vertical component. Using the radial component for omnidirectional transmission an improvement of 7 to 13 dB (MET) and of 0 to 4 dB (SUB) can be achieved in realistic conditions.

74 MHz : The MET  $E_v$  agree with FZYL  $E_v$  at  $\phi > 140^\circ$  within 3 dB, but do not show the extreme loss at  $110^\circ$ , caused perhaps by a cross talk of the horizontal component of the elliptical polarized  $A_1$  antenna. The SUB  $E_r$  agree with the FZYL  $E_r$  for all  $\phi$ 's within 4.5 dB.





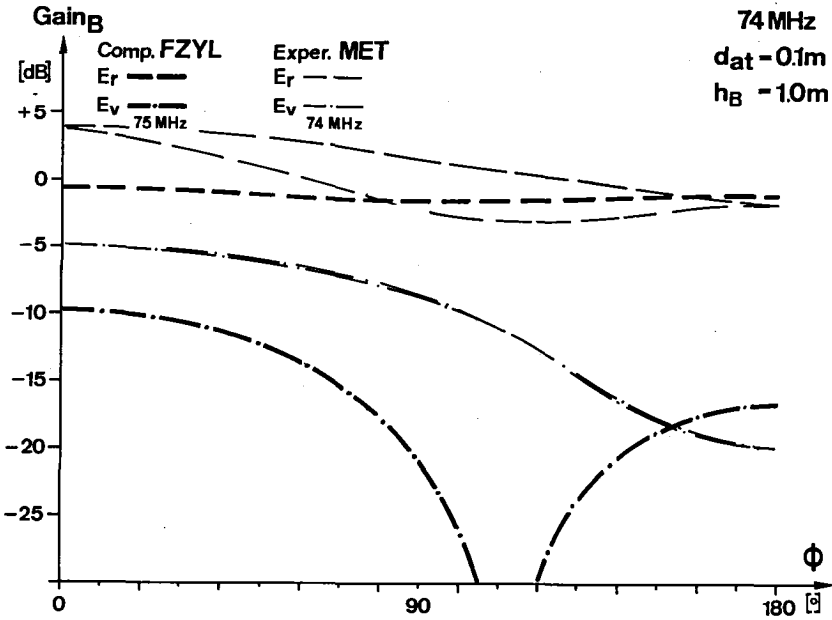


FIGURE 97 b Azimuthal radiation pattern MET and FZYL at  $d_{at} = 0.1m$ , 74 MHz.

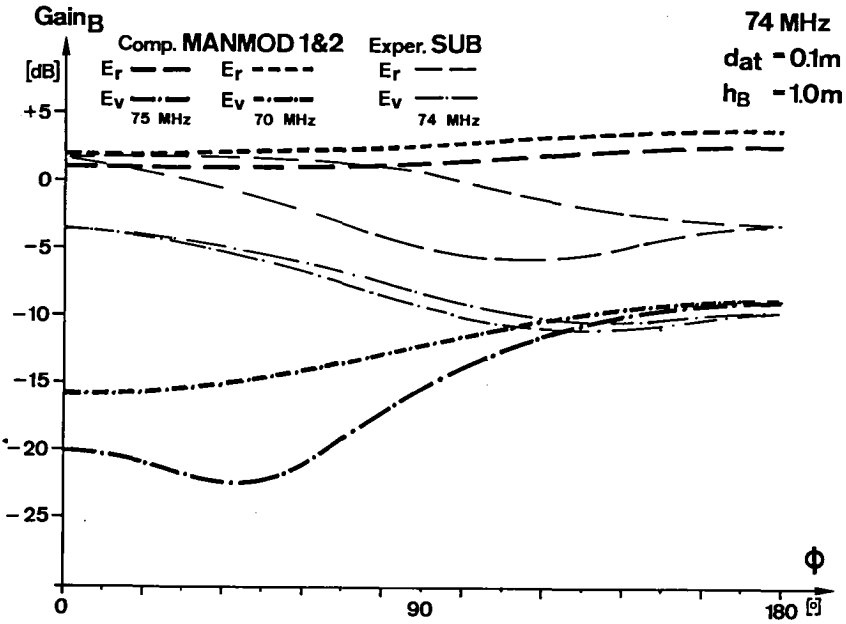


FIGURE 98 b Azimuthal radiation pattern SUB and MANMOD1 & 2, same  $d_{at}$  and  $f$ .

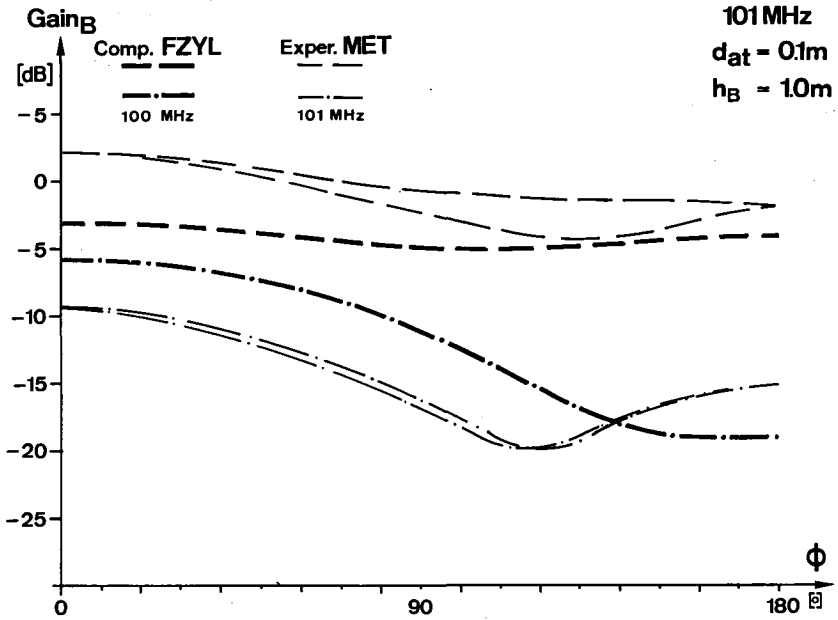


FIGURE 97 c Azimuthal radiation pattern MET and FZYL at  $d_{at} = 1.0m$ , 101 MHz.

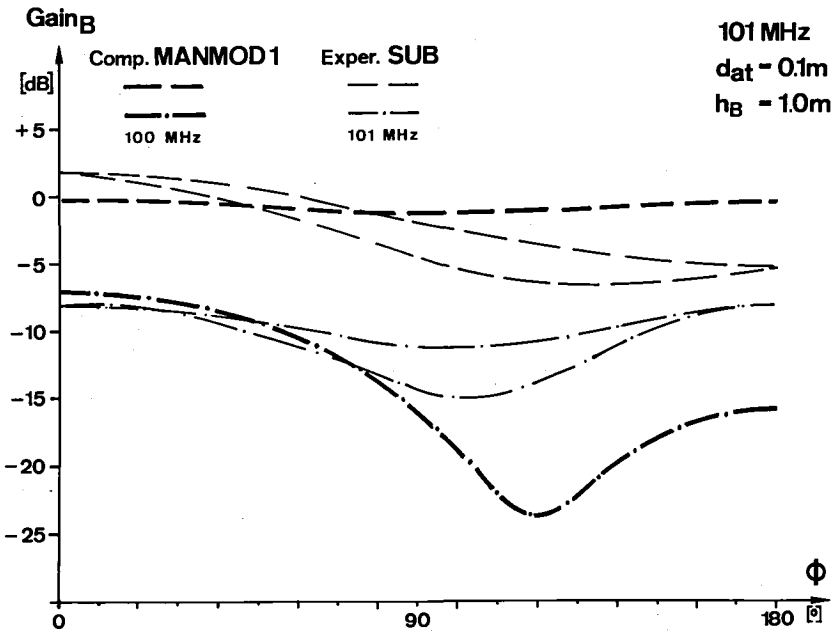


FIGURE 98 c Azimuthal radiation pattern SUB and MANMOD1 , same  $d_{at}$  and  $f$ .

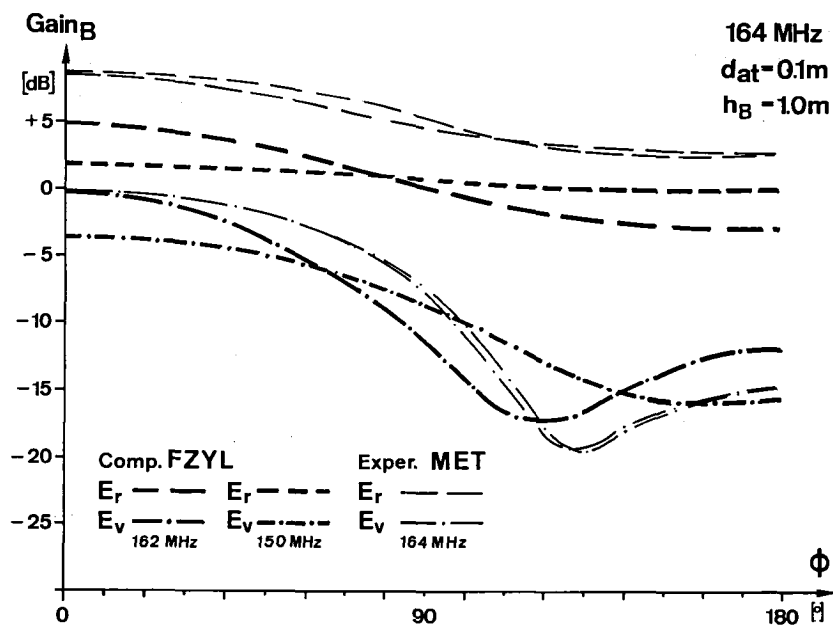


FIGURE 97 d Azimuthal radiation pattern MET and FZYL at  $d_{at} = 0.1 m$ , 164 MHz.

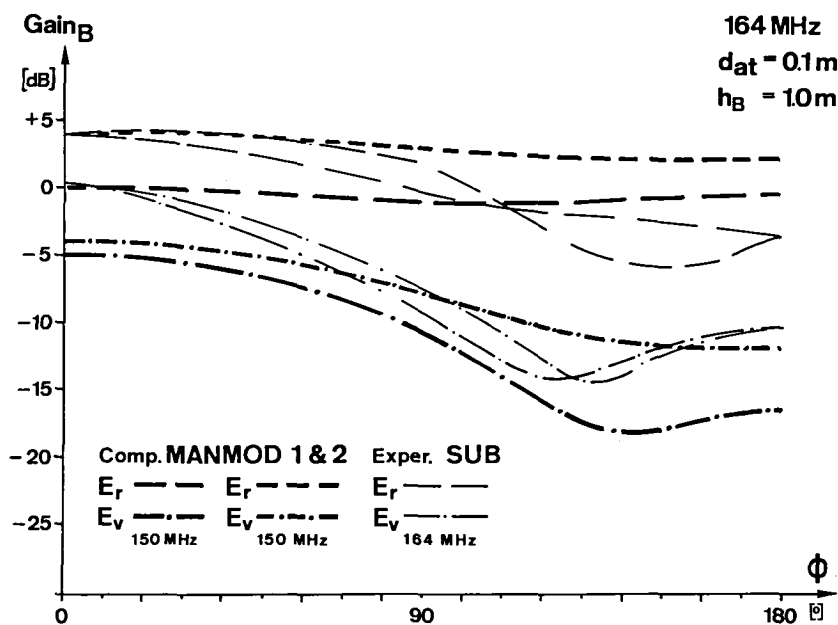


FIGURE 98 d Azimuthal radiation pattern SUB and MANMOD 1 & 2, same  $d_{at}$  and f.

74 MHz : (continued) The SUB  $E_v$  agree with MANMOD 2  $E_v$  at  $\phi > 90^\circ$  within 3 dB, but at  $0-90^\circ$  the SUB  $E_v$  are up to 13 dB higher than computed. The SUB  $E_r$  agree with MANMOD 1  $E_r$  for all  $\phi$ 's within 6 dB.

Generally the minimum radial component is always stronger than the maximum vertical component (except SUB:  $\phi = 0^\circ$ ). Using the radial component, the omnidirectional transmission can be improved by 12 to 14 dB (MET) and 5.5 to 8 dB (SUB) in realistic conditions.

101 MHz : The MET  $E_v$  agree with FZYL  $E_v$  at all  $\phi$ 's within 5 dB. A much better agreement could be achieved by comparing MET  $E_v$  with FZYL  $E_v$  at 85 to 95 MHz (see FIGURE 77 c). One may assume that MET resonates 10 % lower than computed (MET: sharp cylinder ends, FZYL: round end caps). The MET  $E_v$  agree with FZYL  $E_r$  at all  $\phi$ 's within 5 dB, compared with FZYL  $E_r$  at 95 MHz within 3 dB.

The SUB  $E_v$  agree with MANMOD 1  $E_v$  at  $\phi < 90^\circ$  within 3 dB, but at  $90$  to  $180^\circ$  the SUB  $E_v$  are up to 8 dB higher than computed. The SUB  $E_r$  agree with MANMOD 1  $E_r$  at all  $\phi$ 's within 5 dB.

The minimum radial component is always stronger than the maximum vertical component. Using the radial component, the omnidirectional transmission can be improved by 15 to 17 dB (MET) and 5 to 8 dB (SUB) in realistic conditions.

164 MHz : The MET  $E_v$  agree with FZYL  $E_v$  (150 MHz) at all  $\phi$ 's within 5 dB, and with FZYL  $E_v$  (162 MHz) within 3 dB. The MET  $E_r$  agree with FZYL  $E_r$  (162 MHz) at all  $\phi$ 's within 5 dB.

The SUB  $E_v$  agree with MANMOD 2  $E_v$  at all  $\phi$ 's within 4 dB. The SUB  $E_r$  agree with MANMOD 1  $E_r$  at all  $\phi$ 's within 3.5 dB. (Only MANMOD 1 & 2 data at 150 MHz are available)

Generally the minimum radial component is always stronger than the maximum vertical component (except SUB:  $\phi = 0^\circ$ ). Using the radial component, the omnidirectional transmission can be improved by 14 to 21 dB (MET) and 9 to 11 dB (SUB) in realistic conditions.

## 12.2. DISCUSSION OF THE LIMITATIONS OF EXPERIMENT AND COMPUTATION

Generally, the experimental data agree with the computational data within  $\pm 3$  dB at all frequencies and antenna-body-distances as small as 0.1 m.

Some experimental data in the resonance region differ more than 3 dB from the computational data, especially  $E_v$  at  $\phi = 0^\circ$  in proximity to the ground is larger than computed. However, the important data from the shadow zone and the big difference between  $E_v$  and  $E_r$  are of satisfactory agreement. Taking into account the large signal range from -24 to +6 dB the agreement between experiment and theory is satisfactory. A difference of  $\pm 3$  dB corresponds to a power variation of only 1% F.S., related to 0 dB = FSL = 100 %.

The experimental errors are caused mainly by five reasons:

- Capacitive coupling of the body with the ground. The resonant frequency depends on the proximity to the ground, as demonstrated by GANDHI et al. [24] in FIGURES 4 and 6. In our experiments with  $s = 0.2$  and  $0.7$  m the difference amounts to maximum 3 dB at  $\phi = 180^\circ$ .
- Transverse polarization of the test antenna  $A_1$ . The applied helical monopole and dipole antennas are elliptically polarized, so that theoretical signals below -10 dB can be superimposed by stronger transversally polarized field components which determine the recorded data.
- Transverse polarization of the remote antenna  $A_2$ . The LPD antenna is only specified for the 100-1000 MHz range. A cross-talk of transversally polarized field components (see TABLE 91) is very probable.
- Symmetry of fields in the proximity of the test body. The antenna-manipulator contains no metallic parts, but the dielectric material may cause field disturbances. The test transmitters are not infinitesimally small and the orientation of the antenna  $A_1$  may vary from the ideal value by about  $5^\circ$ , causing phase errors and thus amplitude errors.
- Position and shape of the test bodies. The metallic cylinder with its sharp ends (vessel without top and bottom plates) does not correspond completely to the computational cylinder FZYL with its round end caps. The human test subject is not rotationally symmetric and during the measurements a change of the position (vertical axis inclined by a few degrees) and a change of the shape (breathing, etc.) cannot be excluded. The shape of the human body is a very important factor in the resonance region, and the computational differences between MANMOD 1 and MANMOD 2 are in the same order of magnitude as the difference between the experimental SUB and computational MANMOD data.

The limitations and the accuracy of the computational model have been discussed in section 10.3.4.. Principally, the accurate computation is limited to frequencies below 500 MHz with the standard parameter set and each computational result needs to be carefully checked. The computation of a test point is not accurate a priori: only if the frequency, the position of the test point and the test segment length have been varied, without large changes of the result, are the computational data reliable.

The computational errors are caused mainly by three reasons:

- At small  $d_{at}$  one can only compute the averaged field components in the environment of the selected test point.
- The computational field data depend very much on the shape of the body. If the body model is of complicated shape (MANMOD1 & 2) the standard number of contour points is at the lower limit and the field data vary greatly at small variations of  $d_{at}$ ,  $h_b$  and  $f$ . The experiments in 9.1.1. have lead to the conclusion that the body material is of little significance at  $d_{at}$  above 0.05 m and  $f$  above 200 MHz. Thus, the computational model for a human body should be first adapted to the asymmetric body shape and for frequencies below 200 MHz later on to the body material. However, an improvement of the body model is of secondary significance with respect to the practical applications of the obtained data, because the agreement between experimental and computational data is already satisfactory for the fields outside the human body.
- Computational effort. The present state of art allows the computation of 4 test points with a computational time of about 700 seconds on a CDC 6500 computer. More accurate computations are only possible with considerably improved computers with higher speed and more storage capacity.

## 13. CONCLUSIONS AND PERSPECTIVES

### 13.1. IMPORTANT INVESTIGATED PARAMETERS OF THE ANTENNA-BODY SYSTEM

#### 13.1.1. OVERVIEW OF THE INVESTIGATED ANTENNA-BODY SYSTEM

The purpose of the antenna-body study has been defined in section 2.. A standard test situation according to FIGURE 11 has been selected which represents the actual operational conditions on one hand and which could be computed on the other hand. Different antenna-body models have been computed and the results have been compared with corresponding experimental data obtained with representative body models. A relatively simple, analytically treatable, computational model was found which explains the effects of the human body on the EM field at frequencies above 200 MHz. A more complicated, numerically treatable, computational model was found which explains the effects in the entire investigated frequency range from 10 to 1000 MHz. Reliable experiments could be performed in the frequency range from 65 to 900 MHz. The agreement between theory and experiment was generally better than 3 dB (corresponding to a 1 % F.S. accuracy at power levels ranging from -25 to + 6 dB) with some few exceptions at extremely small antenna-body distances (see section 9. and 12.).

Interesting systematic computable correlations were found among frequency, body geometry, relative position of the antenna and transmission loss. The main question concerned the worst-case transmission loss in the azimuthal radiation pattern  $0 < \phi < 180^\circ$ . The parameters determining the performance may be listed in the order of their importance as follows:

- frequency ( $f$ ) and size (length) of the test subject ( $L_B$ )
- antenna-body distance ( $d_{at}$ )
- polarization of the body-mounted antenna ( $p_1$ )
- relative antenna height of the body-mounted antenna ( $h_B$ )
- lateral and sagittal diameter of the test subject ( $D_B$ )
- body material

The most interesting feature of the human body is the field polarization transformation effect which will lead to a new class of electrically small antennas for extremely close mounting on the human body. As found by computations and experiments, omnidirectional transmissions with less than 6 dB transmission loss are practically possible with antennas of less



6 x 6 x 6 cm dimensions mounted directly on the surface of the body. These antennas can be used for transmitters and receivers in the frequency range from about 60 to 160 MHz if the remote antenna  $A_2$  is vertical polarized, without biological problems at power levels up to about 2 W.

### 13.1.2. THE EFFECT OF THE FREQUENCY ON THE FIELD DISTRIBUTION

In the following discussions we regard only the  $p_2$  = vertical polarization at  $p_1$  = vertical, radial and horizontal. The  $p_2$  = horizontal polarization is of little practical interest with respect on omnidirectional transmission, as can be seen from the data in section 10.3.5..

At  $p_2$  = vertical the wavelength of frequencies between 10 and 1000 MHz are of comparable magnitude like the circumference (from head to feet) of the human body. Thus one distinguishes three principal frequency regions:

- below 50 MHz : Rayleigh region (below first resonance)
- 50 to 200 MHz : Mie- or resonance region (including first resonance at about 65 MHz, second resonance at about 140 MHz, and first anti-resonance at about 100 MHz)
- above 200 MHz : Optical region (above second resonance)

Vertical polarized E-field components ( $p_1$  = vertical) : Considering FIGURE 77 one notices the largest transmission  $Loss_B$  above 85 MHz at  $\phi \sim 180^\circ$ . Comparing the  $d_{at}$  dependences in FIGURE 78 one notices the largest  $Loss_B$  at minimum  $d_{at}$ . Thus, we have to look at only the  $Gain_B$  versus  $f$  diagrams at  $\phi = 180^\circ$  at  $d_{at} = 0.1$  m for maximum  $Loss_B$  considerations, e.g., FIGURES 92, 93 and 96. At a given (small)  $d_{at}$  the  $Loss_B$  is relatively small (10 dB) and almost constant from 10 to 50 MHz. Below the first resonance a body is not transparent for EM-waves as could be assumed from the well-known radar cross section (RCS) pattern in FIGURE 17, if we regard small  $d_{at}$ 's. From 50 to 65 MHz  $Loss_B$  decreases a few, but less than could be assumed by the RCS pattern. At 65 to 120 MHz  $Loss_B$  increases drastically (especially at  $\phi \sim 90^\circ$ , see FIGURE 77c), amounting to 15-20 dB at  $d_{at} = 0.1$  m. From about 150 to 1000 MHz  $Loss_B$  remains large as demonstrated best by FIGURE 72. The best agreement between theory and experiment is obtained at frequencies above 200 MHz, due to the small radial  $E_r$ 's above 200 MHz.

Radial polarized E-field components ( $p_1$  = radial) : The radial  $Loss_B$  versus  $f$  pattern is completely different from the vertical  $Loss_B$  pattern.

The radial field is maximum at minimum  $d_{at}$  and is almost independent of  $\phi$  in the frequency range from 60 to 250 MHz. At frequencies below 30 MHz the radial component is small and the minimum is located at  $\phi = 0^\circ$  (FIGURE 77). The radial component becomes interesting above 50 MHz, and its properties are best demonstrated in the  $\text{Gain}_B$  versus  $f$  diagrams at  $\phi = 180^\circ$  (FIGURES 92, 93 and 96).  $\text{Loss}_B$  decreases considerably from 50 to 65 MHz and at  $d_{at} = 0.1\text{m}$  an actual gain of some dB can be observed. A first  $\text{Loss}_B$  maximum of about 5 dB occurs at about 100 MHz, but not so accentuated in the vertical polarization. A second  $\text{Loss}_B$  minimum is at about 150 MHz with about 1 to 3 dB. With increasing frequency  $\text{Loss}_B$  increases, too. At frequencies above 250 MHz  $\text{Loss}_B$  is higher than 6 dB ( $\phi = 0^\circ$ , FIGURE 77b) and above 350 MHz the maximum radial  $\text{Loss}_B$  is larger than the maximum vertical  $\text{Loss}_B$ . However, at  $\phi = 180^\circ$  the radial  $\text{Loss}_B$  remains small up to about 400 MHz (FIGURES 93 and 96).

The experimental and computational azimuthal radiation patterns in FIGURES 97 and 98 reveal excellent omnidirectional characteristics with up to 11 dB (human test subject) and 21 dB (metallic cylinder) better performance than compared with the vertical component. For practical applications the radial component is limited to frequencies between first and second resonance, that is about 50 to 200 MHz.

Horizontal polarized E-field components ( $p_1 = \text{horizontal}$ ): The transmission  $\text{Loss}_B$  at horizontal polarization is of little practical significance as demonstrated with FIGURE 77. At  $\phi = 0$  and  $180^\circ$   $\text{Loss}_B$  is very high, only at  $\phi = 90^\circ$  a  $\text{Loss}_B$  of less than 20 dB is noticed. Small losses, but only for  $\phi$  around 0 and  $180^\circ$ , are only obtained at  $p_2 = \text{horizontal}$  which we do not discuss here. Some data for that case are to be found in TABLES 69 and 70 and in the Appendix 16.2.4. for the frequencies 65 to 425 MHz.

### 13.1.3. THE EFFECT OF THE ANTENNA-BODY DISTANCE

In the following discussion we regard again only the  $p_2 = \text{vertical}$  polarization. From the practical point of view the small  $d_{at}$ 's are of main interest, but only the knowledge of the  $\text{Gain}_B$ - $d_{at}$  dependence lead to an understanding of the shape of the azimuthal radiation patterns.

Vertical polarized E-field components ( $p_1 = \text{vertical}$ ): As long as  $d_{at}$  is smaller than  $\lambda/4$  the transmission  $\text{Loss}_B$  increases with decreasing  $d_{at}$ . At larger  $d_{at}$ 's standing waves with highly varying  $\text{Loss}_B$  are observed.

The human body consists of a material which reflects an EM wave similar to a perfect conductor (see details in section 5.2.4.). The reflection factor for the E-component is thus -1, so that the superimposed signal from scattered and incident field is maximum at  $d_{at} \sim \lambda/4$  at  $\phi = 0$  (see FIGURES 56,57 and 68). A similar situation occurs at  $\phi = 90^\circ$ , where the maximum is at  $d_{at} \sim \lambda/2$ . At such extraordinary  $d_{at}/\phi$  conditions the transmission  $Loss_B$  is very low or even a gain of some dB can be measured, so that the human body can be regarded as a reflector similar to the reflector of a Yagi antenna. A quasi-parabolic antenna can be arranged with 3 persons (FIGURE 54), effecting a directive gain of more than 4 dB. Considering the fact that + 3 dB is the double power, this result is quite interesting. This  $\lambda/4$  to  $\lambda/2$ -effect (depending on  $\phi$ ) is also observed in daily life, if one approaches a mobile receiver (e.g. FM, 80 to 120 MHz) which is tuned to a weak radio station : at some distances the signal is very clear and varying some centimeters distortions can be heard. Thus, for frequencies above 300 MHz practical antenna-body distances may be larger than  $\lambda/4$ , effecting large  $Loss_B$  variations in the azimuthal radiation patterns (see e.g. FIGURE 59), which can now be understood and well predicted.

Radial polarized E-field components ( $p_1$  = radial): The radial field effect occurs only in the proximity to the body, as can be seen in FIGURE 78. At very small  $d_{at}$  and frequencies between 50 to 250 MHz the  $Loss_B$  is very low or even a gain can be observed, independent on  $\phi$ . In this frequency range  $Loss_B$  decreases considerably with decreasing  $d_{at}$ , e.g. from 11 dB/ $d_{at} = 1.0m$  to -2 dB/ $d_{at} = 0.05m$  at  $f = 150$  MHz and  $\phi = 180^\circ$ . At about  $d_{at} = 0.3m$  the amplitude of the radial components are as large as the amplitude of the vertical components, and above 250 MHz a similar, but inverted pattern like the  $d_{at}/Gain_B$  versus  $\lambda$  in the vertical component can be noticed.

Horizontal polarized E-field components ( $p_1$  = horizontal): The horizontal components depend little on  $d_{at}$ , because they are essentially only the residual, little disturbed horizontal components of the incident field (see effect of the irradiation angle in FIGURE 76).

#### 13.1.4. THE DOMINANT RULE OF THE RADIAL E-FIELD COMPONENT

At frequencies from about 50 to 200 MHz (first to second resonance of the human body) the human body acts like a very efficient polarization con-

verter. The only conditions are :  $d_{at}$  below 0.3m and  $p_2$  = vertical. At  $d_{at} = 0.1$ m the transmission loss amounts to  $\pm 5$  dB which is much better than the widely varying transmission Loss<sub>B</sub> of -4 dB to -20 dB obtained with a vertical polarized antenna. The mechanism of the polarization transformation effect can be briefly summarized as follows:

- Receiving case: We assume a standing human test subject, irradiated by a plane, mostly vertical polarized wave by a remote antenna with an incident angle of 70 to 90°. At frequencies from about 50 to 200 MHz the relative and the specific absorption cross section (FIGURES 3 and 4) is high. Thus, the body collects not only RF-energy corresponding to its shadow area, but also from outer regions similar to a good receiving antenna with a large effective area. The RF- currents are flowing mainly in the outer layers of the body and surface charges are generated. Both currents and charges produce a scattered field around the body. Because the human body is now the new RF-source, it is not astonishing that a certain field component is largest very close to the surface, and because the vertical and the horizontal components are weak, the radial component must be large due to the total collected RF-energy (this explanation is logical for a metallic body, but only partially acceptable for biological bodies). The source of the tremendous radial field component must be the surface charges. The integral effect is completely described by the Maxwell equations and is proven by experiments. It explains the practically important transmission loss or gain, but a further study on the detailed mechanism may be interesting from the scientific point of view.
- Transmitting case: The reciprocity theorem (section 5.2.1.) says that the transmission loss from  $A_2$  to  $A_1$  is the same as from  $A_1$  to  $A_2$ . With this answer the explanation is given why a radial transmitting antenna performs best, because the receiving case is mathematically clear. However, the detailed mechanism is not clear at all, only in the integral sense is this explanation satisfactory if we speak only of the transmission loss, which was the purpose of this study. It might be that a radial antenna produces above all large surface charges which evoke axial currents. These currents are comparable to those in a thick mono- or dipole, producing a ver-

tical polarized far field. As we shall see in section 13.3.2., an applicable radial antenna will be equipped with a metallic plate on the surface of subject, so that biological problems can be excluded at reasonable RF-power (body shielded from the large reactive near-field of the antenna). However, a future study on the detailed coupling mechanism might be of scientific interest. In this context it should be mentioned that some unexplainable (parapsychological ?) effects occurred with the test transmitters described in section 11.3. : Some test subjects complained to feel an irritating sensation when the antenna was held radial to the head. Further, an irregular signal could be heard on the monitor receiver if the transmitter was positioned at two distinct points of the upper forehead and to the wrist of the hands. It should be mentioned that the transmitters were quartz stabilized (modulation only possible by selective RF-absorption) and that the CW power was much less than 10 mW.

- Practical significance : The polarization transformation effect is not only very important for specially designed radial antennas, but also for most of the generally applied electrically small antennas, such as the helical monopole antennas of walkie talkies : If self-resonant, electrically small antennas are developed, it is very difficult to obtain a strictly linear polarization. There is always a transverse polarization, e.g., in the case of helical antennas with its elliptical polarization (see Appendix 16.1.) the secondary polarization axis increases with  $\pi^2 D_h^2 / p \lambda$ , where  $p$  is the pitch and  $D_h$  is the helical diameter. Greatly simplified, the transverse polarization is relatively large compared with the desired axial polarization, if the helical antenna length  $h$  is small compared with  $\lambda/4$ . In addition, a helical monopole antenna would require a counterpoise of about  $\lambda/2$  diameter in order to operated properly. Transmitting devices are, however, generally much smaller than  $\lambda/4$  (maximum housing dimension), so that the electromagnetic counterpoise is not sufficient. As a consequence, the antenna does not radiate the computed elliptical polarized field, but also additional field components of arbitrary polarizations. For constant antenna and transmitter length the ratio of radial to vertical polarization increases with decreasing frequency. At frequencies of 100 MHz this ratio may amount to about -5 dB, at 200 MHz to about -10 dB and at 400 MHz to about -20 dB. Due to this

inevitable transverse sensitivity (receiving case) and transverse radiation (transmitting case) the transmission loss does not sharply increase above 75 MHz (FIGURE 96) but increases slowly up to about 300 MHz (FIGURE 92). Above 250 MHz not only the investigated radial effect is of smaller influence, but also the antenna and its counterpoise approaches an ideal, strictly linear polarized radiation system. In this case, the computed  $G_{\text{avg}}/f$  dependence for vertical polarization becomes accurate also for practically realizable mobile radio sets. Thus, the unexpected good performance of practical body-mounted antennas in the proximity of a human test subject at frequencies between 50 and 200 MHz can be now explained by the polarization transformation effect and the technically inevitable transverse polarization of electrically small antennas.

- Perspectives : The polarization transformation effect is of great practical significance and could be proven theoretically and experimentally. Only roughly has the dependence of the relative antenna height been studied (FIGURES 94 a,b,c,d) and little is known about this effect in extreme proximity to the human body. A future study of the parameters  $d_{\text{at}}$  (0 to 0.1 m),  $h_{\text{B}}$  (0.8 to 1.8 m),  $\theta_i$  (70 to 90°), body-geometry and body material would be of great interest. Because the computational cost would be very high (improved model of man with more than 200 contour points required, investigation of the significance of the body material, many  $d_{\text{at}}$  and  $h_{\text{B}}$  steps necessary), such a future study should start with experiments. Test transmitters similar to those described in section 11., but of reduced size, and an improved antenna manipulator would be required.

### 13.2. INTERESTING ADDITIONAL FEATURES OF THE ANTENNA-BODY SYSTEM

#### 13.2.1. THE BROAD-BAND CHARACTERISTICS OF THE HUMAN BODY

The presented study dealt with an antenna-body system where the antenna  $A_1$  was separated from the body. In an other study the active radiation of the human body was investigated (NEUKOMM [63]). Briefly summarized, the main results of that study are:

- A thick monopole antenna was mounted on a large counterpoise and fed properly by a continuously enlarge coaxial line according to HEILMANN

[42], page 110. The radiation pattern of metallic rotational cylinder of a diameter  $D_B = 0.25\text{ m}$  (diameter of a human body) and a monopole length  $1/2 L_B = 0.9\text{ m}$  (1/2 human size) was an omnidirectional pattern in the azimuthal plane, with a gain of more than -3 dB at frequencies between 60 to 200 MHz at an elevation angle of about 0 to  $10^\circ$ . At frequencies above 200 MHz a side lobe at an elevation angle of about  $45^\circ$  is developed, causing high losses at 0 to  $10^\circ$ . The results agreed partially with those of KRAUS [51].

- The same experiment was repeated with a phantom (comparable with PHA in section 5.4.1., but equipped with a similar feeding as mentioned above). The astonishing result was, that the phantom showed almost the same broad-band characteristics, with only little additional losses: from 60 to 180 MHz an omnidirectional radiation pattern was obtained with a gain of more than -5 dB (reference: isotropic antenna).
- Actual experiments with human test subject could not be performed, but there is no doubt that the human body would show a similar performance. If an RF-current is flowing along the vertical axis of the human body, it flows not only in the outer layers, but also in depths of some centimeters (TABLE 1). Thus, the current carrying area is relatively large, resulting in a small resistance  $R_{10SS}$ . Due to the shape of the human body ('thick cylinder') the radiation resistance is relatively large compared with the reactive impedance (general theory of thick monopoles and dipoles). This means that the human body is an efficient broad-band antenna for the frequency range 60 to 180 MHz, as proven with the phantom experiments.

Unfortunately, the practical feeding of the human body causes severe problems. Theoretical and experimental investigations by FISCHER and CASTELLI [23] revealed the impossibility of the RF-coupling by means of a toroid. This idea looks very promising at first sight: A toroid coil generates a circular H-field in the horizontal plane and is theoretically appropriated to induce an axial current in a body situated in the center of the toroid. However, in the regarded frequency range 60 to 200 MHz the circumference around the hip is larger than  $0.12 \lambda$ . Because of the helical construction of the toroid a phase difference of minimum  $90^\circ$  occurs because the signal velocity along the toroid is reduced by a factor of 2 to 5 (see Appendix 16.1.), so that the induced axial currents are not

in phase. Several improved feeding methods were suggested, including segmental toroids and capacitive coupling, but up to now a practically applicable solution is missing (FISCHER and CASTELLI [23]).

The broad-band characteristics of the human body has its main significance for personal radio sets with inefficient, poorly matched antennas, as for instance wireless microphones in the frequency range 30 to 150 MHz. Below 100 MHz the design of tuned, efficient and body-mounted antennas for vertical polarization is very difficult. The main problems are the detuning effect of the body proximity and the efficiency at small  $h/\lambda$  ratio. If a short monopole or dipole cable antenna is in the proximity of the human body, the body acts like a lengthening of the antenna, as can be noticed with any short-wave or ultra-short-wave receiver. If the original antenna is relatively bad (general situation), the human body is a considerable improvement. Since many transmitters operated with such cable antennas (e.g. biotelemetry in the 37 MHz band), an investigation of the active radiation pattern of the human body and a detailed study on the coupling mechanism would be sensible. Principally, there are two ways for a theoretical analysis:

- Integration of the near-field data of section 10.4. along a multi-dimensional antenna. By designing a special antenna with matched amplitude- and phase- correlations along the selected polarization axes the desired coupling might be obtained.
- Computing of aperture radiation according to HARRINGTON and MAUTZ [40]. In this case the RF-energy has to be coupled into the body by means of surface electrodes or capacitive plates. This method seems to be risky with respect to biological effects and encumbrance, but perhaps an acceptable solution is possible.

#### 13.2.2. BODY-MOUNTED ANTENNA ARRAYS

The presented study dealt essentially with body-mounted antennas of very small dimensions, after having proved the field homogeneity around the test points. The data computed in section 10.3.5. may be also used for larger antennas, antenna arrays and antennas with more than one polarization axes. Such antennas would be of interest, if quasi-isotropic transmission is required. For such applications the computer programs are already prepared to compute similar data for changing incident angles  $\theta_i$ .



### 13.3. PROPOSALS FOR EFFICIENT, BODY-MOUNTED ANTENNAS

#### 13.3.1. VERTICAL POLARIZED ANTENNAS

Most of the currently used antennas are vertical polarized. Constructional details can be found by GOUBAU and SCHWERING [32], KANDOIAN and SICHAK [47], LI and BEAM [54], NEUKOMM [62,63], OEHEN and BALZARINI [67], TONG [80] and WHEELER [85]. It is not possible to discuss these antennas here, but the main limitations should be mentioned:

- Transmission loss of the vertical polarized E-field component. As studied in this report, the transmission loss increases with increasing frequency and with decreasing antenna-body distance. Above 100 MHz and  $d_{at}$  below 0.1 m it is not possible to obtain a worst-case transmission loss of less than 10 dB. Usually the transmission loss is physically limited on 10 to 30 dB at higher frequencies and smaller  $d_{at}$ 's, and the largest loss occurs usually in the shadow zone.
- Bandwidth. If an electrically small antenna occupies only a small fraction of the radiansphere (WHEELER [85]), the bandwidth decreases with decreasing volume (at constant frequency), if no additional resistive elements are involved. If a body is near to the near-field zone of the antenna, severe detuning effects are most probable.
- Efficiency. Usually, the radiation resistance is small, decreasing with decreasing volume of the antenna (at constant frequency). Each additional loss (ohmic losses in the conductor, earth losses, matching losses, etc.) decreases the efficiency. At frequencies below 200 MHz an important loss is caused by the insufficient counterpoise of monopole antennas.

A comparison of some helical antennas is given in Appendix 16.1.2. A special group of non-resonant antennas are the cable antennas for frequencies below 100 MHz: in contrast to the resonant antenna they may perform better in proximity to the body as in free-space, but also here the overall loss, compared with an ideal dipole in free-space, is in the region of 5 to 20 dB.

#### 13.3.2. RADIAL POLARIZED ANTENNAS

These antennas are up to now little explored. The test transmitters of section 11.3. are not developed for optimal efficiency and are not intend-

ed for practical applications. FISCHER and CASTELLI [23] tried to design some radial polarized antennas for practical applications and performed some experiments with metallic and lossy body models (1/3 scale of MET and PHA, see also section 5.4.1.). In principle, these antennas are short helical monopoles with a top capacitor, mounted on a limited counterpoise and feed from a 50  $\Omega$  coaxial cable (FIGURE 99).

#### Top C-Helix mounted on Phantom

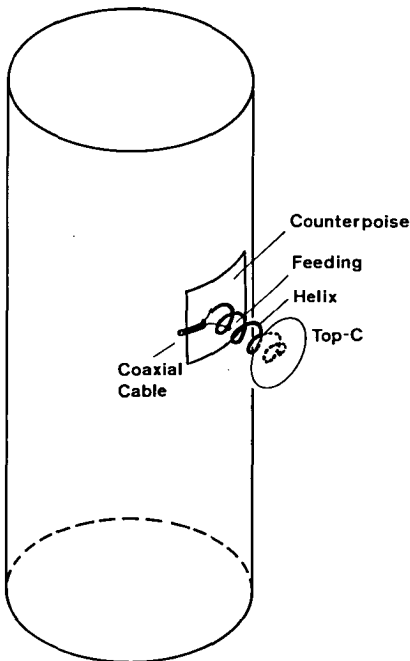


FIGURE 99

Radial polarized antenna (Top C-Helix) mounted on a Phantom.

Antenna dimensions:

$h$  : 34 mm (monopole length)

$D_h$  : 12 mm (helical diameter)

$n$  : 1/2 to feeding point

5  $\frac{1}{2}$  to top C

(number of turns)

$D_C$  : 47 mm (top C diameter)

$L_C$  : 100 x 100 mm (dimensions of the counterpoise)

Body dimensions: (1/3 scale PHA)

$L_B$  : 0.6 m (length)

$D_B$  : 0.084 m (diameter)

(Source: FISCHER and CASTELLI [23])

The experimental data are of limited accuracy, because the measurements have been performed in a very small anechoic chamber:

Bandwidth on metallic cylinder (1/3 MET) : 311 to 319 MHz

Bandwidth on model phantom (1/3) PHA : 313 to 321 MHz

Minimum/maximum azimuthal gain on 1/3 MET : -12 dB / -5 dB

Minimum/maximum azimuthal gain on 1/3 PHA : -16 dB / -9 dB

Bandwidth when mounted on a large c-poise : 309 to 317 MHz

Gain at vertical polarization " " : - 0.5 dB

All gain data are related to the ideal, isotropic radiator (0 dB), and not to the FSL as usually used in this study. The comparison of the data

with those studied in section 12. lead to the following conclusions:

- The experiments of FISCHER and CASTELLI [23] are comparable to the experiments in section 12. performed at 101 MHz (1/3 of the model size = 1/3 of the nominal frequency). At this frequency the radial  $G_{\text{avg}}$  is minimum and amounts to -5 dB. The new measured data are about 7 to 11 dB lower in the worst case.
- The efficiency of the presented radial antenna could be improved by a larger counterpoise. The increase of the center frequency from 313 to 315 to 317 MHz from mounting on a large counterpoise to 1/3 MET to 1/3 PHA points to a too small counterpoise and efficiency loss.

The presented radial antenna is a promising solution, albeit the predicted high gain could not be achieved completely. However, comparing the radial antenna with a standard vertical polarized antenna of similar volume and mounting, the radial antenna prototype is already better in many respects:

- High absolute gain when mounted very close to the body, little variation of the field amplitude from  $0 < \phi < 360^\circ$
- Human body well shielded from the near-fields of the antenna (Safety)
- Simple mounting, small volume and little encumbrance
- little or no detuning of the resonant frequency when counterpoise is sufficiently large
- Constant VSWR, direct matching to a  $50 \Omega$  coaxial line
- Little difference in gain when separated from the body (however, axis of the antenna must be vertical when separated from the body).

The physically given disadvantage of all electrically small antennas, the limited bandwidth, is of minor importance, because there are only very small detuning effects from the body. The reduced efficiency (in context with the extremely small length/ $\lambda$  ratio) is balanced by a better matching but is still a subject for improvement.

The improvement of the radial antenna and the optimization of  $h_g$  and  $d_{\text{at}}$  for frequencies between 50 and 200 MHz would be an interesting field of research. The literature on electrically small antennas and the experimental and theoretical data in this study may lead to practical body-mounted antenna with better performance and less biological risks.

### 13.4. THE OPTIMAL FREQUENCY RANGE FOR BODY-MOUNTED ANTENNAS

#### 13.4.1. CONCLUSIONS FROM THE OBTAINED DATA

As a result of this study the optimal frequency range for omni-directional transmission with body-mounted antennas can be defined as follows:

OPTIMAL FREQUENCY RANGE : 35 TO 180 MHz
---

Some remarks are needed with respect to the practical use of personal radio sets. The antenna type, the antenna efficiency, the dimension of the radio set, the matching of the antenna to the RF-terminal and some other factors may lead to a slightly different choice. Thus, we may define four categories of optimal frequencies:

- 35 to 65 MHz : Strictly vertical polarized, well-matched, efficient, electrically small antennas (very theoretical, exist very seldom in practice). The transmission loss is minimum at 65 MHz and increases slightly with decreasing frequency. The lower the frequency, the more difficulties occur with bandwidth, detuning and efficiency.
- 50 to 200 MHz : Strictly radial polarized antennas. Good (experimentally proved) and excellent (predicted theoretically) performance can be obtained at small antenna-body distances in this range.
- 60 to 150 MHz : Technically realizable antennas with dominant vertical polarization but additional transverse (radial) polarization, such as helical monopoles on small transmitting and receiving devices, especially small walkie-talkies. The unexpectedly good performance in moderate proximity to the human body is mainly caused by a cross-talk of the radial component. Usually the transverse polarization was considered as an unavoidable lack of electrically small antennas. Above 150 MHz the design of more vertically polarized antennas becomes possible. As a consequence, the performance becomes better in free space, but worse in the proximity to the body, because both transverse polarization and radial component decreases with increasing frequency.
- 20 to 100 MHz : Cable antennas, inefficient, usually not matched antennas of less than  $\lambda/4$  length (wireless microphones, biotelemetry transmitters in the 37 MHz band). The human becomes a part of the antenna due to different effects with resulting better performance.

#### 13.4.2. FUTURE FREQUENCIES FOR BIOTELEMETRY

As a member of the working group TC 62 of the IEC the author took part in the preparation of the IEC document 62(Secretariat) 38 . This document recommends new biotelemetry frequencies to be proposed at the ITU world conference of frequency allocation. The official proposal concludes with:

- 8.1. A frequency band, ranging from 36.7 to 37.9 MHz, power 50 mW ERP, should be reserved and allocated for biotelemetry.
- 8.2. Two frequency bands between 70 to 200 MHz, each of 1 MHz width and with a power of 50 mW ERP, should be reserved and allocated for biotelemetry.

The IEC document explains the special needs of biotelemetry, especially the urgently requested international standardization of frequencies which allow omnidirectional transmission with body-mounted antennas. It points to the potential risks of frequencies above 300 MHz at power densities above  $10 \mu\text{W}/\text{cm}^2$  and recommends therefore lower frequencies with only 50 mW effective radiated power (ERP). If the IEC recommendations became accepted at the ITU conference, at least 110 small band channels (37 MHz) 40 medium band channels (70 - 200 MHz) and 9 broad band channels (37, 70-200 MHz) would be internationally usable during the next 20 years.

## 14. SUMMARIES

### 14. SUMMARY

The influence of the human body on the radiation pattern of body-mounted antennas has been investigated in the frequency range 10 to 1000 MHz (below, up to above main resonances of the human body). An analytically formulated, computable antenna-body-model has been developed which explains the correlations between the electrical field (amplitude and phase) and antenna location (antenna-body distance  $d_{at}$  and azimuthal rotation angle  $\phi$ ) at frequencies above 200 MHz (above resonance region) at vertical polarization (E-field parallel to the largest axis of the body). With the method of moments a computational antenna-body model has been investigated which explains the correlations among electrical field, antenna location ( $d_{at}, \phi$ , and relative antenna height  $h_B$ ) and irradiation angle  $\theta_i$ , at all polarization axes and frequencies, especially within the resonance region. Experimental data with human test subjects and body models have been collected with special measuring antennas and field generators at frequencies between 25 to 900 MHz, whereby  $d_{at}, \phi$  and  $h_B$  have been varied continuously (or in small steps) within large limits. The agreement between the theoretical and experimental data amounted to 3 dB, except at extreme conditions (measuring range: -20 to +5 dB). The main conclusions from the complete study are: 1. There is a mathematical correlation between transmission loss (from a body-mounted to a remote antenna) and frequency, antenna location, body geometry, and polarization. 2. Within 50 to 200 MHz (just below first, up to just above second resonance) the human body (and other, in material and geometry comparable bodies) acts like an efficient polarization transformer. At  $d_{at}$  below 0.3m a radial polarized, small antenna allows omnidirectional (i.e. little depending on  $\phi$ ) transmission, where the transmission loss decreases with decreasing  $d_{at}$ . Even a gain compared with an ideal isotropic radiator in free space can be achieved. 3. The antenna-body distance  $d_{at}$  is the parameter of greatest influence in antennas close to a body. Especially at frequencies above 200 MHz and vertical polarization the  $d_{at}$  determines the different reflections of the E-field at the body and determines the azimuthal radiation pattern of the antenna-body system. 4. The shape of a (lossy) body is much more important than the (biological) material. 5. The reciprocity theorem is applicable on body-mounted antennas, as experimentally proven at low power,

at frequencies between 65 and 900 MHz, and at  $d_{at}$  ranging from 0.05 - 4 m. 6. The optimal frequency range for omnidirectional transmission with body-mounted, electrically small antennas is between 35 to 180 MHz, as resulting from both theoretical and experimental data.

The order of magnitude of electric and magnetic field strengths of the near-fields of electrically small antennas have been approximatively determined and compared with the maximum permissible limits of international safety standards. At higher transmitter power (above approximately 100 mW, very much depending on antenna type and location) these limits may be exceeded, especially by walkie-talkies with vertical polarized helical antennas. Based on the recent results on the biological significance of non-ionizing radiation, RF-induced biological effects are possible, above all at frequencies above the first resonance. These effects may lead to artifacts (Biotelemetry transmitter) and perhaps to health hazards (transmitters of walkie-talkies). Comparing a standard antenna (e.g. vertical polarized helical antenna) with a radial antenna at the same extreme antenna-body distance (below 0.1 m) and at the same input power, the radial antenna does not only decrease the risk, but also offers a smaller transmission loss.

## 14.2. ZUSAMMENFASSUNG

Der Einfluss des menschlichen Körpers auf das Strahlungsmuster von körpernahen Antennen wurde im Frequenzbereich 10 bis 1000 MHz (unterhalb bis oberhalb der Hauptresonanzen des menschlichen Körpers) untersucht. Es wurde ein analytisch beschreibbares, berechenbares Antennen-Körper-Modell entwickelt, das die Zusammenhänge zwischen elektrischem Feld (Amplitude und Phase) und Antennenposition (Antennen-Körperabstand  $d_{at}$  und azimuthalem Drehwinkel  $\phi$ ) bei Frequenzen oberhalb der Hauptresonanz ab 200 MHz bei vertikaler Polarisierung (E-Feld parallel zu Körperlängsachse) erklärt. Mit der 'Method of Moments' wurde ein numerisch berechenbares Antennen-Körper-Modell untersucht, das die wichtigen Zusammenhänge zwischen elektrischem Feld, Antennenposition ( $d_{at}$ ,  $\phi$  und relativer Antennenhöhe  $h_g$ ) und Einstrahlungswinkel  $\theta_i$  bei allen Polarisationsrichtungen und Frequenzen, insbesondere im Resonanzbereich, erklärt. Experimentelle Daten mit Versuchspersonen und Körpermodellen wurden im Frequenzbereich 25 bis 900 MHz mit Hilfe von speziell entwickelten Messantennen und Feldgeneratoren gesammelt, wobei  $d_{at}$ ,  $\phi$  und  $h_g$  kontinuierlich (oder in feinen Abstufungen) in weiten Grenzen variiert wurden. Mit Ausnahme bei extremen Bedingungen wurde eine Übereinstimmung von 3 dB (Messbereich -20 bis +5 dB) zwischen den experimentellen und berechneten Daten erzielt. Die wichtigsten Folgerungen aus der gesamten Untersuchung lauten: 1. Es besteht ein mathematischer Zusammenhang zwischen Übertragungsverlust (von körpernaher Antenne zu entfernter Antenne), der Frequenz, der Antennenposition, der Körpergeometrie und den Polarisationsrichtungen. 2. Innerhalb 50 bis 200 MHz (knapp unterhalb erster bis knapp oberhalb zweiter Resonanz) wirkt der menschliche Körper (und andere, geometrisch und materiell vergleichbare Körper) als effizienter Polarisations-Transformator: Bei  $d_{at}$  unterhalb 0.3 m erlaubt eine radial polarisierte (d.h. E-Feld radial zur Körper-Längsachse) kleine Antenne eine omnidirektionale (d.h. wenig von  $\phi$  abhängige) Übertragung, wobei der Übertragungsverlust mit abnehmendem  $d_{at}$  abnimmt und sogar ein Gewinn gegenüber einer idealen, isotropen Antenne im freien Raum möglich ist. 3. Der Antennen-Körperabstand  $d_{at}$  ist der wichtigste Parameter bei körpernahen Antennen. Speziell bei Frequenzen oberhalb 200 MHz und vertikaler Polarisierung bestimmt  $d_{at}$  die unterschiedlichen Reflexionen des E-Feldes am Körper und damit die Azimutal-Strahlungsdiagramme des Antennen-Körper-Systems. 4. Die Form des (verlustbehafteten) Körpers ist von weitaus grösserer Bedeutung als das (biologische) Körpermaterial.



5. Experimente im Frequenzbereich 65 bis 900 MHz bei kleinen Leistungen (1 - 10 mW) und  $d_{at}$  von 0.05 bis 4 m haben gezeigt, dass das Reziprozitätsgesetz auch für elektrisch kleine, körpernahe Antennen gilt. 6. Aus Theorie und Experiment geht hervor, dass der optimale Frequenzbereich für omnidirektionale Übertragung mit kleinen, körpernahen Antennen zwischen 35 und 180 MHz liegt.

Die Größenordnung der elektrischen und magnetischen Feldstärken im Nahfeld elektrisch kleiner Antennen wurde abgeschätzt und mit den entsprechenden zulässigen Grenzwerten internationaler Sicherheitsvorschriften verglichen. Bei höherer Sendeleistung (ab ca. 100 mW, Grenze sehr stark von Antennentyp und Position zu Körper abhängig) werden diese Grenzwerte überschritten, besonders von Funksprechgeräten mit vertikal polarisierten Helix-Antennen. Auf Grund der neuesten Erkenntnisse sind, vor allem bei Frequenzen oberhalb der ersten Resonanz, HF-induzierte biologische Effekte möglich, die zu Artefakten (Biotelemetrie-Sender) und Gesundheitsschäden (Funksprech-Sender) führen können. Vergleicht man eine Standardantenne (z.B. vertikal polarisierte Helix-Antenne) mit einer Radial-Antenne bei extrem kleinen Antennen-Körperabständen ( $d_{at}$  kleiner als 0.1 m) so kann mit der Radial-Antenne bei gleicher Eingangsleistung nicht nur das Sicherheitsrisiko, sondern auch der Übertragungsverlust verringert werden.

## 15. REFERENCES

- [1] ANDREASEN M.G. Scattering from Bodies of Revolution. IEEE Trans., Vol. AP-15, No.2, March 1965, pp. 303-310.
- [2] ANSI American National Standards Institute: Safety Level of Electromagnetic Radiation with Respect to Personnel. ANSI C95.1-1974, IEEE, New York, 1974.
- [3] ARRL The ARRL Antenna Book. American Radio Relay League, Newington, Conn., 1974.
- [4] BACH S.A. Effects of Radiofrequency Energy on Human Gamma Globulin. In: Biological Effects of Microwave Radiation, (Ed. M.F. Peyton), Plenum, New York, 1961.  
LUZZIO A.J.  
BROWNELL A.S.
- [5] BAGGENSTOS H. Vorlesung Elektromagnetische Felder, ETH 1977, Kapitel 4: Rasch veränderliche Felder. Electr. Dept., Swiss Federal Institute of Technology, Zurich, 1977.
- [6] BARANSKI S. Biological Effects of Microwaves. Dowden, Hutchinson & Ross, Inc., Stroudsburg, Pa., 1976.  
CZERSKI P.
- [7] BECKER K.D. Ausbreitung Elektromagnetischer Wellen. Springer Verlag, Berlin, 1974.
- [8] BELDING H.A. Index for Evaluating Heat Stress in Terms of Resulting Physiological Strains. Heating, Piping, Air Conditioning, Aug. 1955, pp.129-136.  
HATCH T.R.
- [9] BELSHER D.R. Development of Near-Field Electric Energy Density Meter Model EDM-2. HEW Publ. No. (NIOSH) 75-140, 1975.
- [10] BEVENSEE R.M. The Syracuse Computer Code for Radiation and Scattering from Bodies of Revolution, Extended for Near-Field Computations. Report UCRL-51622, TID-4500, UC-32, Lawrence Livermore Laboratory, 1974.
- [11] BRONSTEIN I. Taschenbuch der Mathematik, Verlag Harri Deutsch, Zürich, 1975.  
SEMENDJAJEW K.
- [12] BUCHANAN H. Human Body Effect on Signal Patterns of Personal Telemetry Transmitters. Report SAM-TR-70-4, USAF School of Aerospace Medicine, Aerospace Medical Division (AFSC), Brooks Air Force Base, Texas, Jan. 1970.  
MOORE W.F.  
RICHTER C.R.
- [13] CHANG D.C. The Electromagnetic Field Very Near to a Monopole. IEEE Trans., Vol. EMC-17, No.2, May 1975, pp.97-105.  
HALBGEWACHS R.D.  
HARRISON C.W.
- [14] CHEN K.M. Internal EM Field and Absorbed Power Density in Human Torsos Induced by 1-500-MHz EM Waves. IEEE Trans., Vol. MTT-25, No. 9, Sept. 1977, pp. 746-756.  
GURU B.S.
- [15] CHEN K.M. Induced EM Fields Inside Human Bodies Irradiated by EM waves of up to 500 MHz. Internal Report by the Department of El.Eng. and Syst. Sci., Michigan State Univ., 1977.  
GURU B.S.

- [16] CHOU C.K.  
GUY A.W.      The Effect of the Electromagnetic Fields on the Nervous System. Scientific Report No.6, Aug. 1975, Bioelectromagnetic Res. Lab., Univ. of Washington School of Medicine, Seattle, Wash.98195.
- [17] CONSUMER  
REPORTS      Microwave Ovens: We can tell you how well they performed - but no one really knows how safe they are. Consumer Reports, (USA), June 1976, pp. 314-321.
- [18] DDR-STANDARD      Arbeitshygiene: Elektrische, Magnetische und Elektromagnetische Felder und Wellen. TGL 32602/01. Staatsverlag DDR, Berlin, 1975. Zusätze: ASAO 5: MfGe Nr.1/1977, Gesetzesblatt 109, 17. März 1978, Teil 1, Nr.8.
- [19] DODGE C.H.  
GLASER Z.R.      Trends in Nonionizing Electromagnetic Radiation Bioeffects. Research and Related Occupational Health Aspects. J. of Microwave Power, Vol. 12(4), Dec. 1977, pp. 319-334.
- [20] DUMANSKI J.D.  
SANDALA M.G.      The Biologic Action and Hygienic Significance of Electromagnetic Fields of Superhigh and Ultrahigh Frequencies in Densely Populated Areas. In: ref. [69], pp. 289-293.
- [21] EGGERT S.  
GOLTZ S.  
KUPFER J.      Results at the Development of One Near-Field Strength Meter at the Measurement of the Electrical Component of the Electromagnetic RF Field in the GDR. Proc. of the 1977 USNC/URSI Meeting, Arlie, Va. (in press). See also: Nahfeldstärke-Messgerät NFM-1, Zentralinst.f.Arbeitsmed.der DDR,Berlin,1976.
- [22] EMERY A.F.  
SHORT R.E.  
GUY A.W.  
KRANING K.K.  
LIN J.C.      The Numerical Thermal Simulation of the Human Body When Absorbing Non-ionizing Microwave Irradiation - With Emphasis on the Effect of Different Sweat Models. In: Biological Effects of Electromagnetic Waves, Vol.II, Selected Papers of the 1975-USNC/URSI Annual Meeting, Boulder, Colo.1976,pp. 96-118.
- [23] FISCHER T.  
CASTELLI J.      Aktivierung des menschlichen Körpers als Sendean-tenne. Study work at the Electronics Inst. and Bio-mechanics Lab., ETH Zurich, 1979.
- [24] GANDHI O.P.  
HAGMANN M.J.  
D'ANDREA J.A.      Some Recent Results on Deposition of Electro-magnetic Energy in Animals and in Models of Man. In: Abstracts of Scientific Papers, International USNC/URSI Symposium on the Biological Effects of Electromagnetic Waves, Arlie, Va., 1977.
- [25] GANDHI O.P.  
SEDIGH K.  
BECK G.S.  
HUNT E.L.      Distribution of Electromagnetic Energy Deposition in Models of Man with Frequencies Near Resonance. In: Biological Effects of Electromagnetic Waves, selected papers of the 1975-USNC/URSI Annual Meet-ing, Boulder, Colo.,(HEW publ. (FDA) 77-8011), pp.44-67.
- [26] GANDHI O.P.  
HUNT E.L.  
D'ANDREA J.A.      Deposition of Electromagnetic Energy in Animals and in Models of Man With and Without Grounding and Re-flector Effects. Radio Science Vol. 12, No. 6 (S), 1977, pp. 39-47.

- [27] GANDHI O.P. Recent Results on Deposition of Electromagnetic Energy in Animals and in Models of Man. Lecture presented at the ETH, Aug.17, 1978.
- [28] GLASER Z.R. Biomedical Aspects of Radio Frequency and Microwave Radiation: A Review of Selected Soviet, East European, and Western References. In: Biological Effects of Electromagnetic Waves. Selected papers of the 1975-USNC/URSI meeting, Boulder, Colo. Vol.1, Dec.1976 (HEW publ. (FDA) 77-8011), pp. 2-34.
- [29] GLASER Z.R. Bibliography of Reported Biological Phenomena ('Effects') and Clinical Manifestations Attributed to Microwave and Radio-Frequency Radiation. Ninth Supplement, Nov.1977. DHEW (NIOSH) Publ. No. 78-126. First bibliog.: Res.Rep.No.2, NMRI, Bethesda, Md.1971. Available from NTIS, Springfield, Va. 22151.
- [30] GORDON Z.V. Main Directions and Results of Research Conducted in the USSR on the Biologic Effects of Microwaves. In: ref. [69], pp. 22-35.
- [31] GORDON Z.V. Biological Effect of Microwaves in Occupational Hygiene. Izdatel'stvo Meditsina, Leningrad, 1966. US-Translation TT 70-50087, NASA TT F-633, 1970.
- [32] GOUBAU G. Proceedings of the ECOM-ARO Workshop on Electrically Small Antennas. U.S. Army Electronics Command, Fort Monmouth, May 1976.
- [33] GREEN F.M. Development of Magnetic Near-Field Probes. HEW Publ. No. (NIOSH) 75-127, 1975.
- [34] GREEN F.M. Development of an RF Near-Field Exposure Synthesizer (10 to 40 MHz). Interagency Agreement NIOSH-IA-75-16. Available from NIOSH, Cincinnati, Ohio 45226.
- [35] GUY A.W. Quantitation of Induced Electromagnetic Field Patterns in Tissue and Associated Biological Effects. In: ref.[69], pp. 203-217.
- [36] GUY A.W. Determination of Power Absorption in Man Exposed to High Frequency Electromagnetic Fields by Thermographic Measurements on Scale Models. IEEE Trans., Vol. BME-23, No.5, Sept. 1976, pp.361-371.
- [37] GUY A.W. Microwave-Induced Acoustic Effects in Mammalian Auditory Systems and Physical Materials. Ann. of the N.Y. Acad. of Sciences, Vol. 242, Febr. 1975, pp. 194-218.
- [38] GUY A.W. Phantom Models for Muscle, Brain, Fat, and Bone at MW Frequencies, Private communication, 1976.
- [39] HANKIN N.N. High Power Radiofrequency and Microwave Radiation Sources: A Study of Relative Environmental Significance. Operational Health Physics, Proc. Ninth Midyear Topical Symp. of the Health Physics Society. (Compiled by P.L. Carson et al.), Febr. 1976.

- [40] HARRINGTON R.F.    Radiation and Scattering from Bodies of Revolution.  
MAUTZ J.R.            Rep. AFCRL-69-0305, 1969, and : Generalized Network  
                         Parameters for Bodies of Revolution. Rep. TR-68-7,  
                         1968, Syracuse Univ., El. Eng.Dept. Syracuse, N.Y.
- [41] HARRINGTON R.F.    Field Computation by Moment Methods, Macmillian Co.,  
                         N.Y., 1968 (Second printing: write to the author).
- [42] HEILMANN A.        Antennen I. BI Hochschultaschenbücher 140/140a,  
                         Mannheim, 1970.
- [43] HELLER J.H.        The Effect of Electromagnetic Fields on Unicellar  
                         Organisms. In: IRE,AIEE,ISA Conf.Electrical Tech-  
                         nology in Medicine and Biology, Vol.7, 1959.
- [44] HIRSCH F.G.        Bilateral Lenticular Opacities Occurring in a Tech-  
PARKER J.T.            nician Operating a Microwave Generator. AMA Arch.  
                         Ind.Hyg.Occup. Med.6:1952, pp. 512-517.
- [45] JOHNSON C.C.        Nonionizing Electromagnetic Wave Effects in Bio-  
GUY A.W.              logical Materials and Systems. Proc. IEEE, Vol.60,  
                         No.6, 1972, pp. 692-718.
- [46] KALADA T.V.        Biologic Effects of Radiation in the 30-300 MHz  
FUKOLOVA P.P.        Range. In: ref.[69], pp. 52-57.  
GONCAROVA N.N.
- [47] KANDOIAN A.G.      Wide-Frequency-Range Tuned Helical Antennas and  
SICHAK W.            Circuits. IRE Nat. Conv. Rec. Part 2, Antennas and  
                         Components, 1953, pp. 42-47.
- [48] KING H.E.        Characteristics of Body-Mounted Antennas for Per-  
                         sonal Radio Sets. IEEE Trans.,Vol.AP-23, 1975,  
                         pp. 242-244.
- [49] KING H.E.        Effects of a Human Body on a Dipole Antenna at 450  
WONG J.L.            and 900 MHz. IEEE Trans.,Vol.AP-25,1977,pp.376-379.
- [50] KING R.W.P.        The Scattering and Diffraction of Waves. Harvard  
WU T.T.              Univ. Press, Cambridge, Mass., 1959, Chapter 2.
- [51] KRAUS J.D.        Antennas. McGraw Hill, 1950, Chapter 9.
- [52] KRITIKOS H.N.      The Distribution of Heating Potential Inside Lossy  
SCHWAN H.P.        Spheres., IEEE Trans., Vol.BME-22, No.6, Nov. 1975,  
                         pp. 457-463.
- [53] KRUPKA Z.        The Effect of the Human Body on the Radiation Pro-  
                         perties of Small-Sized Communication Systems. IEEE  
                         Trans., Vol. AP-16, 1968, pp. 154-163.
- [54] LI T.            Helical Folded Dipoles and Unipoles. Proc. Nat.  
BEAM R.E.            Electr. 13: 1957, pp. 89-105.
- [55] LIVESHITS N.N.    Conditioned Reflex Activity in Dogs under Local In-  
                         fluence of a VHF Field upon Certain Zones of the  
                         Cerebral Cortex. Biophys. J., Vol.2,1957, p. 198.
- [56] LIU L.M.        The Relation of Teratogenesis in Tenebrio Molitor to  
ROSENBAUM H.J.      the Incidence of Low-Level Microwaves. IEEE Trans.,  
PICKARD W.F.        Vol. MTT-23, Nov. 1975, pp. 929-931.

- [57] MICHAELSON S.M. Effect of Exposure to Microwaves: Problems and Perspectives. Environmental Health Persp. Vol.8, 1974, pp. 133-156.
- [58] MICHAELSON S.M. The Tri-Service Program - A Tribute to George M. Knauf, USAF (MC). IEEE Trans., Vol. MTT-19, No. 2, Febr. 1971, pp. 131-146.
- [59] MILROY W.C. Microwave Cataractogenesis: A Critical Review of the Literature. Aerospace Medicine, Vol. 43, No.1, 1972, pp. 67-75.
- [60] MOOR F.B. Microwave Diathermy. In: Therapeutic Heat and Cold, (Ed.:Licht S.), New Haven, Conn, 1965, Sec. 12, pp. 310-320.
- [61] MUTH E. Appearance of Pearl-Chain Formation of Particles in Emulsions Caused by Alternating Fields. Kolloid-Z., Vol. 41, 1927, p. 97.
- [62] NEUKOMM P.A. Body-Mounted Transmitting Antennas: Radiation Patterns and Design of Helical Dipole Antennas. In : Biotelemetry III (Eds.:Fryer T.B., H.A. Miller and H.Sandler), Acad. Press, Inc., N.Y., 1976, pp. 345-348.
- [63] NEUKOMM P.A. Biotelemetry Antennas: The Problem of Small Body-Mounted Antennas. Proc.int.conf. BIOSIGMA 78, Vol. 2, Paris 1978, pp. 99-106.
- [64] NEUKOMM P.A. Artifacts from RF and MW Telemetry: Estimation of Safety Aspects and Review on Biological Effects. In: Biotelemetry IV (Eds.: Klewe H.J. and H.P.Kimmich), Döring-Druck, Druckerei und Verlag, Braunschweig, 1979.
- [65] NEUKOMM P.A. The Rubber Band Goniometry. J.Biotelemetry 1, 1974, pp. 12-20.
- [66] NYQUIST D.P. Coupling Between Small Thin-Wire Antennas and a Biological Body. IEEE Trans., Vol.AP-25, No.6, Nov. 1977, pp. 863-866.
- [67] OEHEN W. Helix Biotelemetrie Antennen. Study work at the Lab. BALZARINI N. Microwave Tech. and Biomechanics Lab., ETH Zurich, 1975.
- [68] OLSEN R.G. Microwave-Induced Chronotropic Effects in the Isolated Rat Heart. Ann. of Biomed. Engineering 5, 1977, pp. 396-409.
- [69] PROCEEDINGS Biologic Effects and Health Hazards of Microwave WARSAW Radiation. Proc. Int.Symposium Warsaw, 15-18 Oct., 1973, Polish Medical Publishers, Warsaw, 1974.
- [70] ROMERO-SIERRA C. Effect of an Electromagnetic Field on the Sciatic Nerve of the Rat. In: The Nervous System and Electric Currents, (Ed.:Wulfsch N.L.), Vol.2, Plenum, N.Y., 1971, pp. 81-85.
- [71] ROTHAMMEL K. Antennenbuch. Telekosmos-Verlag, Franckh'sche Verlagshandlung, Stuttgart, 1976.

- [72] SCHWAN H.P.      Microwave Radiation: Biophysical Considerations and Standards Criteria. IEEE Trans., Vol. BME-19, No. 4, July 1972, pp. 304-312.
- [73] SCHWAN H.P.      Biophysics of Diathermy. In: Therapeutic Heat and Cold, (Ed.: Licht S.), New Haven, Conn., 1965, Sec. 3, pp. 63-125.
- [74] SCHWAN H.P.  
PIERSOL G.M.      The Absorption of Electromagnetic Energy in Body Tissues. Int. Review of Physical Medicine and Rehabilitation, Vol. 33, 1954, pp. 371-404.
- [75] SCHWAN H.P.  
LI.K.      Capacity and Conductivity of Body Tissues at Ultra-high Frequencies. Proc. IRE, Vol. 41, Dec. 1953, pp. 1735-1740.
- [76] TELL R.A.      Microwave Energy Absorption in Tissue. Report by the Environ. Protection Agency, Twinbrook Res. Lab., 12709 Twinbrook Parkway, Rockville, Md. 20852. Feb. 1972.
- [77] TELL R.A.      An Analysis of Radiofrequency and Microwave Absorption Data with Consideration of Thermal Safety Standards. (Draft). U.S. Environ. Protection Agency, Las Vegas, Nev. 89114, P.O. Box 15027, Dec. 1977.
- [78] TELL R.A.  
O'BRIEN P.J.      Radiation Intensities Due to Mobile Communication Systems. U.S. Environ. Protection Agency, Office of Radiation Program, Silver Spring, Md 20910, 1976.
- [79] TOLER J.  
SEALS J.      RF Dielectric Properties Measurement System: Human and Animal Data. DHEW (NIOSH) Publ. No. 77-176, 1977.
- [80] TONG D.A.      The Normal Mode Helical Aerial. Radio Communication, July 1974, pp. 432-437.
- [81] VAN BLADEL J.      Electromagnetic Fields. McGraw-Hill, 1964, Chapt. 12.
- [82] VREELAND R.W.  
SHEPHERD M.D.  
HUTCHINSON J.C.      The Effects of FM and TV Broadcast Stations upon Cardiac Pacemakers. IEEE Symp. Record (Publ. No. IEEE 74CH0803-7 EMC), 1974.
- [83] WHEELER H.A.      Fundamental Limitations of Small Antennas. Proc. IRE, Dec. 1947, pp. 1479-1484.
- [84] WHEELER H.A.      The Radiansphere Around a Small Antenna. Proc. IRE, Aug. 1959, pp. 1325-1331.
- [85] WHEELER H.A.      Small Antennas. IEEE Trans., Vol. AP-23, No. 4, July 1975, pp. 462-469.

## 16. APPENDIX

### CONTENTS

	page
16.1. Helical Antennas	237
16.1.1. Properties, Design, Efficiency Measurement and Matching	237
16.1.2. Comparison of some Antenna Types	243
16.2. Computer Programs and Additional Results	245
16.2.1. Program PANA and IZYL Results	245
16.2.2. Program HARRA and Output Sample	253
16.2.3. Program PANB and Output Sample	262
16.2.4. Program PANC, Data Cards for Test Bodies FZYL, MANMOD 1 and MANMOD 2, Field Homogeneity Results with FZYL	281
16.2.5. Additional Results from Field Computations with FZYL, MANMOD 1 and MANMOD 2	280



Leer - Vide - Empty

## 16.1. HELICAL ANTENNAS

### 16.1.1. PROPERTIES, DESIGN, EFFICIENCY MEASUREMENT AND MATCHING

A helical antenna is a typical electrically small antenna. Its maximum dimension is a small fraction of the wavelength. The "normal mode" helical antenna (FIGURE 106) consists of a helical conductor in the shape of a long cylinder with the diameter  $D_h$  ( $D_h \ll \lambda$ ) and with the axial (monopole) length  $h$  ( $h < \lambda/4$ ). The polarization of the radiated E-field is elliptical, with a dominant axis parallel to the helical cylinder axis (see FIGURE 106, bottom). The radiation pattern is very similar to that of an ordinary whip antenna. i.e. maximum radiation radial to the helical axis.

#### Helical Normal Mode Antenna

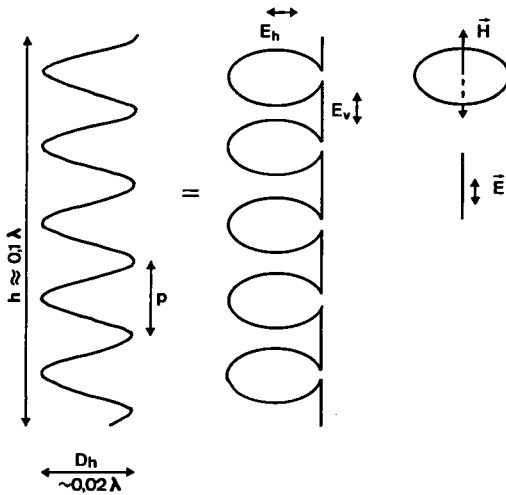


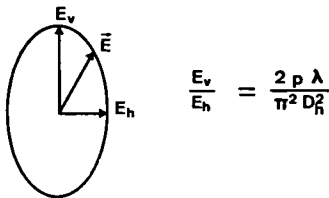
FIGURE 106

#### Helical Normal Mode Antenna

Vertical  $E_v$  far-field generated from the vertical flowing antenna currents,  
Horizontal  $E_h$  far-field generated from the horizontal flowing antenna currents.

$$p = \text{pitch}$$

#### Elliptical Polarization



The helix is a slow-wave structure. When used as a waveguide, the axial phase velocity of the wave guided by the helix is less than the velocity of light in free space. Accordingly, the resonant length of a helix is

shorter than the corresponding resonant length of a linear wire antenna. Thus, one may reduce the axial length  $h$  by a factor of 3 to 8 without adding external tuning elements. Compared with the short (non-resonant) whip antenna one obtains a better current distribution (see FIGURE 107), resulting in a higher radiation resistance:

Current Distribution on the Helix

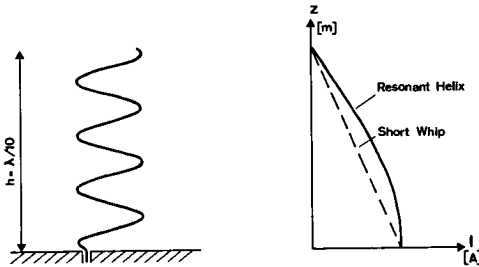


FIGURE 106

Current distribution  
on the helical antenna  
 $z$ : vertical antenna  
axis  
 $I$ : current in the  
conductor

The radiation resistance of a half-wave helical dipole can be evaluated by integrating the far-field Poynting vector over a large spherical surface. For a thin half-wave helical dipole of length  $2h$ , an approximate expression for the radiation resistance is : (LI and BEAM [54])

$$R_{\text{rad Helix}} = 1280 (h/\lambda)^2 \text{ [Ohm]} \quad (246)$$

As a comparison, the radiation resistance of a small linear dipole of the length  $2h$  and with linear (triangular) current distribution is

$$R_{\text{rad Whip}} = 790 (h/\lambda)^2 \text{ [Ohm]} \quad (247)$$

Hence the radiation resistance of a small-diameter half-wave helical dipole is approximately 62 percent greater than that of a small linear dipole of the same length. If the antennas are operated above a perfect ground, the radiation resistances are reduced by a factor of 2 and one obtains the values of KANDOIAN and SICHAK [47]

$$R_{\text{rad Helix above ground}} = (25.3 h/\lambda)^2 \text{ [Ohm]} \quad (248)$$

$$R_{\text{rad Whip above ground}} = (20 h/\lambda)^2 \text{ [Ohm]} \quad (249)$$

Principally, there are four methods to design a helical antenna:

1. Computation with the method of moments: OEHEN and BALZARINI [67] adapted an existing antenna modelling program (BURKE and SELDEN, Microfiches AD - 767 420, 1973) to the helical dipole problem. This method is very

accurate, if the number of subsegments is large enough ( $\sim 200$ ) and offers many results : impedance, gain, bandwidth, effect of near-by conducting surfaces, etc. The ROUND HELICAL DIPOLE (RHD) in FIGURE 107 has been computed with this method, and the experimental data (16.1.2.) agree quite well with the computed data. However, this method is very expensive and should only be applied for antenna optimization.

2. Analytical approach. LI and BEAM [54] investigated the characteristic equation for helical waveguide and presented the results in nomograms. This method offers an insight in the complicated correlations between antenna geometry, bandwidth and general performance.
3. Approximative computation. KANDOIAN and SICHAKE [47] evaluated approximative computational methods, which were adapted by TONG [80] for computation on pocket calculators. For a given antenna length ( $h$ ), diameter ( $D_h$ ) and wavelength ( $\lambda$ ) the number of turns ( $N_h$ ) respectively the number  $n_h = N_h/h$  can be approximatively computed for long helices:

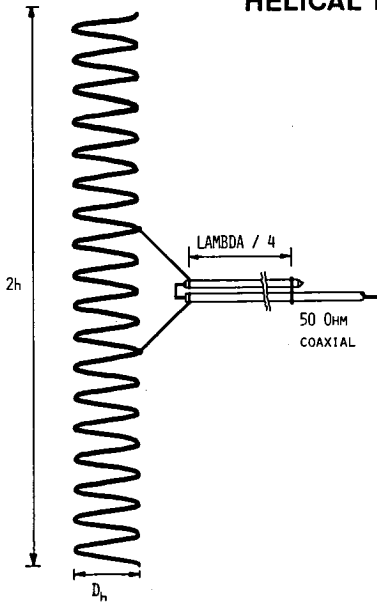
$$\log n_h = 0.4 \left( \log \left( \frac{\lambda}{h} - 4 \right) + \log \left( \frac{\lambda}{h} + 4 \right) + 0.5 \log \lambda - 3 \log D_h \right) - 1 \quad (250)$$

This method offers data for design with an accuracy of about 20 %, if  $h/\lambda$  is not smaller than 1/10 and if  $D_h$  is smaller than 0.3  $h$ .

4. Experimental approach. If a network analyser and a small anechoic chamber is available, a well performing helical antenna can be designed as follows: For a monopole helical antenna a wire of a length of  $\lambda/2$  is wrapped in a shape of a helix with the desired  $D_h$  and  $h$ . The 'hot end' is contacted on a large counterpoise, and the feeding coaxial cable (inner conductor) is contacted at the  $m^{\text{th}}$  turn ( $m \approx N/10$ ) from the now grounded 'hot end'. The Smith Chart (see FIGURE 109) shows the resonance frequency, the bandwidth and the input impedance (transformed  $R_{\text{rad}} + R_{\text{loss}}$  at  $f_{\text{res}}$ ). Varying the feeding point (changing  $m$ ) one obtains a match to 50 Ohm (with a resulting relative bandwidth) and by cutting the upper antenna ends one obtains the wanted resonance frequency, because the initial  $f_{\text{res}}$  is usually  $\sim 30\%$  too small.

The problems of all helical antennas are : 1.) small bandwidth , 2.) reduced efficiency, 3.) low radiation resistance, 4.) sensitivity to detuning effects from proximity to obstacles, 5.) transverse polarization. Because the helical is an electrically small antenna the fundamental laws

# HELICAL DIPOLE ANTENNA RHD



## Specifications:

### GEOMETRY :

LENGTH	$2h$ :	22 cm
DIAMETER	$D_h$ :	2 cm
WIRE DIAMETER	$D_w$ :	2 mm
NUMBER OF TURNS	$2N_h$ :	18

### COMPUTER DATA :

EFFICIENCY	$\text{EFF}$ :	94 %
GAIN VERT. POLARIZATION	$G_{\text{VERT}}$ :	+1.4 dB
GAIN HOR. POLARIZATION	$G_{\text{HOR}}$ :	-17 dB
RADIATION RESISTANCE	$R_R$ :	9.2 Ohm

### NETWORK ANALYSER DATA :

RESONANT FREQUENCY	$F_{\text{RES}}$ :	236 MHz
BANDWIDTH (-3 dB)	$BW$ :	17 MHz
INPUT RESISTANCE	$R_I$ :	24 Ohm

## Azimuthal Radiation Pattern of the Helical RHD Dipole Antenna

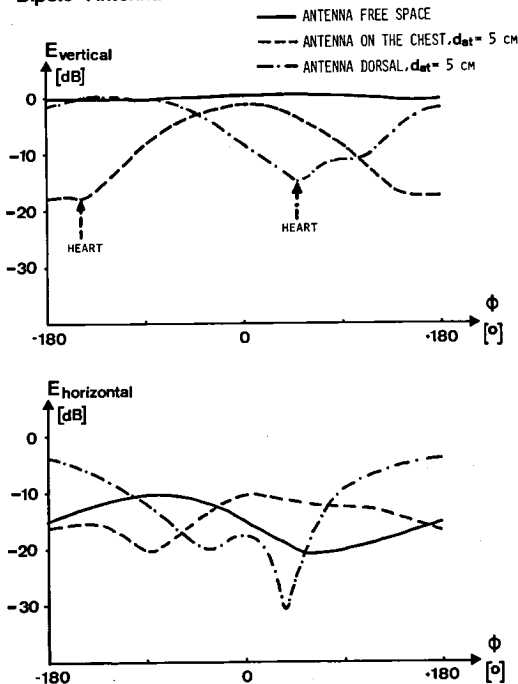


FIGURE 107 (above)

FIGURE 108 (left)

Round helical dipole (RHD)

mechanical details,  
computer predictions  
(antenna modelling pro-  
gram, see [67])  
network analyser data  
and (left)  
performance of the  
antenna mounted on  
the human test subject  
(0 dB : isotropic ra-  
diator)

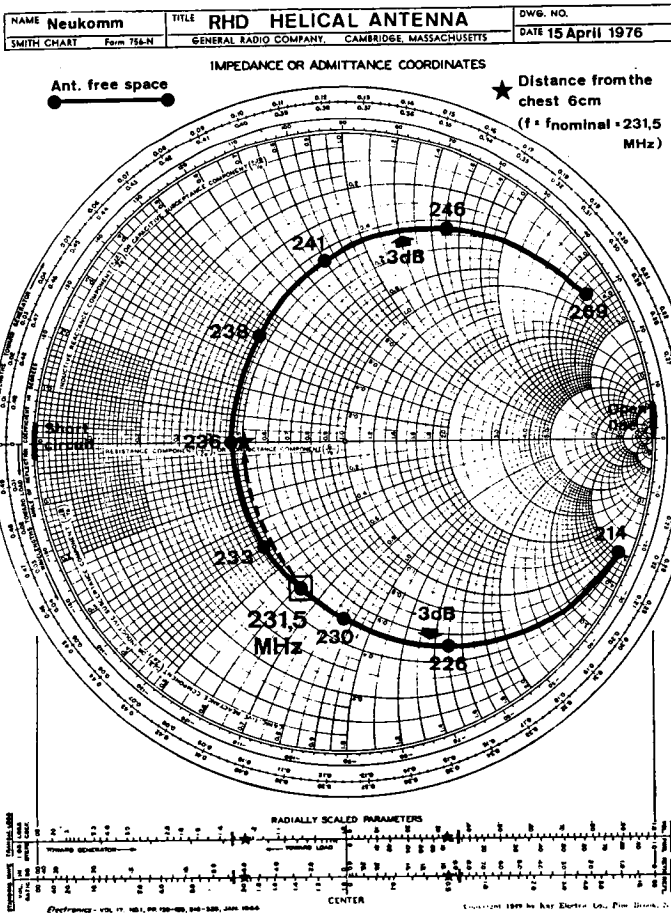


FIGURE 109 Smith Chart of the round helical dipole antenna RHD. Solid line : antenna in free space (anechoic chamber), dashed line : antenna mounted on human test subject at  $d_{at} = 6$  cm . Due to the losses effected by the body the resistance increases with decreasing  $d_{at}$  and the resonant frequency lowers with decreasing  $d_{at}$ .

found by WHEELER [83,85] must be considered. The bandwidth is determined by the  $h/\lambda$  ratio (see equations 9 to 13 in section 4.5) but can be controlled within small limits with matching (good match = smaller bandwidth and perhaps a better efficiency) and increasing the radiation resistance (higher radiation resistance = smaller bandwidth). The efficiency is main-

ly determined by ground losses, by losses in the matching network and, in complicated helical structures (double helix, etc.), by resistive losses in the antenna conductor. An example may illustrate the importance of the ground losses:

The standard helical monopole antenna of 173 MHz walkie-talkie (MOTOROLA HT 220) is specified as:

$h_t$	= 114 mm	(total length)
$h$	= 106 mm	(length of the helix)
$N_h$	= 42	(total number of turns)
$D_w$	= 1.2 mm	(wire diameter)
$D_h$	= 9.6-6.7 mm	(tapered helical diameter)

The computation according to equation 250 and 246 result in an  $N_h$  of  $\sim 40$  and a radiation resistance of 5.5 Ohm. The housing of the walkie talkie is maximum 180 mm  $\approx \lambda/10$ . The VSWR of the complete antenna-transmitter system is close to 1:1, so that the ground losses amount to about 44.5 dB. The efficiency in radiation is thus  $5.5 / 44.5 + 5.5 = 11\%$ , so that the complete system radiates about -9.5 dB less than an ideal dipole. A helical dipole according to FIGURE 107 has an efficiency of about 94 (theoretical) and 89 % (measured) and a gain of - 0.75 dB (theoretical ) and - 2 dB (measured) compared with an ideal full-length dipole.

The low radiation resistance is a potential source of bad efficiency, if the match to the feeding line is poor, if there are losses in the antenna conductor or in the matching network and if (in the case of monopole antennas) the counterpoise is not large enough. According to LI and BEAM [54] special helical antennas with multi-conductors were designed. As can be seen in the comparison FIGURE 110, 16.1.2., a higher gain can be obtained, but paying the price of a very small bandwidth. Thus, a maximum radiation resistance or a perfect matching is not very sensible with respect to detuning sensitivity: the more the antenna is "improved" for free-space operation, the more delicate it responds to external influences. One further problem could be the transverse polarization. If the height is about 0.9 times the diameter, the antenna becomes circular polarized. However, as discussed in section 13.1.4., a transverse polarization at frequencies between 50 to 200 MHz may be even an advantage at small antenna-body distances, also when the radiation is reduced at

axial polarization. The transverse polarization could be computed by the formulas indicated in FIGURE 106,[54] and [74], but the agreement with the experimental data is so poor, that one should trust only the actually measured data. The same situation happens with the actual bandwidth: it is better not to cite the formulas here. If the bandwidth becomes really very important, one should use the accurate method of moments or one should perform representative experiments.

An important point is the matching of a dipole antenna on a 50  $\Omega$  coaxial cable and the determination of the efficiency. Below 1 Watt power and below 300 MHz a ferrit 1:1 balun (manufactured from a 0.5 cm<sup>3</sup> standard 1:4 balun for TV-application) leads to very good results. The additional loss is below 10 %, the volume of the network is very small and is not critical with respect to bandwidth. The parallel  $\lambda/4$  bazooka in FIGURE 106 is only a few percent better, but cumbersome and of limited bandwidth. However, an investigation by the author has shown, that the total bandwidth of dipole antenna plus bazooka is slightly larger than that of the antenna alone, because the reactance of the antenna is partially compensated by the reactance of the bazooka at changing input frequencies. The best method to determine the efficiency follows from the application of the equations by WHEELER [85]: The Smith Chart of the antenna in free-space is recorded, and one reads the real part of the impedance R at resonant frequency  $f_{res}$ . The antenna is then located in a conducting vessel with the dimension of the radiansphere (see section 4.5.). The Smith Chart is again recorded, and the highest ohmic resistance near  $f_{res}$  represents the total loss resistance  $R_{loss}$ . The efficiency Eff can be calculated with

$$\text{Efficiency} = \frac{R - R_{loss}}{R} \quad (251)$$

The absolute accuracy is in the region of 25 %, but the relative accuracy is much better than 5 %, e.g., if only the feeding point of an antenna is varied. If one combines the efficiency measurement with transmission tests (network analyser, second input channel), the actual performance of a helical antenna can be reliably quantified.

#### 16.1.2. COMPARISON OF SOME ANTENNA TYPES

Five antennas have been selected for a discussion of the performance: The GROUNDPLANE ANTENNA GA is a vertical  $\lambda/4$  whip on 4 ground rods, each  $\lambda/4$



of length and at an angle of  $135^\circ$  to the radiating whip. The HELMET ANTENNA HGA is a vertical  $\lambda/4$  whip (32.6 cm) on a plastic helmet, coated with a copper mesh. The ROUND HELICAL DIPOLE RHD is the antenna shown in FIGURE 107. The FLAT HELICAL DIPOLE FHD is a flat helix with  $2N_h = 10.5$  turns,  $2h = 20$  cm,  $D_{h1} = 0.5$  cm,  $D_{h2} = 5.3$  cm. In the center section the antenna conductor is parallel to the antenna axis at a total length of 6 cm, representing the feed antenna segment ( $\Delta$ -match with bazooka, similar to the feeding in FIGURE 107). The FLAT FOLDED HELICAL DIPOLE FFHD consists of a  $240\Omega$  parallel line with the shape of a helix, with single conductors at the antenna ends (see LI and BEAM [54]). The size of the FFHD is the same as that of the FHD, but  $2N_h$  is 13.5.

COMPARISON OF SOME BODY-MOUNTED ANTENNNAS USED IN BIOTELEMETRY									
ANT. TYPE	ANTENNA DATA IN FREE SPACE WITHOUT TEST SUBJECT					VERTICAL ANTENNA MOUNTED DORSALLY ON THE TEST SUBJECT WITH $d_{at} = 57$ mm, $h_B = 1.4$ m, $\phi = 180^\circ/0^\circ$			
	RES. FREQ.	BAND- WIDTH	GAIN	EFFI- CIEN- CY	VSWR	RES. FREQ.	BAND- WIDTH	GAIN at $\phi = 180^\circ$	FREQ. SHIFT
	[MHz]	[MHz]	[dB]	[%]	[1]	[MHz]	[MHz]	[dB]	[MHz]
GA	220	65	2.15	-	1:1.4	-	-	-	-
HGA	237	47	+0.5	-	1:1.3	-	-	-	-
RHD	236.3	18	+0.2	89	1:2.5	229.2	23	-20	-7.7
FHD	237.5	25	+0.8	79	1:4.0	231.8	24	-21	-6.1
FFHD	242.1	8.8	+1.0	78	1:1.3	236.8	9.6	-20	-4.0

TABLE 110 Comparison of some body-mounted antennas.

TABLE 110 shows the performance of these antennas. The helical antennas were mounted on the phantom PHA, the antenna center was spaced 57 mm from the surface of the phantom. These results hold true within 2 dB when mounted dorsally on a human test subject SUB. The performance of the GA was measured at an absolute antenna height of 1.4 m, and the helmet antenna HGA was mounted at the head of the SUB, with the head at the same absolute antenna height. This comparison shows clearly that a good antenna in free space may perform poorly in extreme proximity to a body. The interesting FFHD with its high gain and its excellent VSWR cannot be applied in practice, because varying antenna-body distances may detune the antenna in excess of its bandwidth. A good compromise seems to be the flat helical dipole FHD.

## 16.2. COMPUTER PROGRAMS AND ADDITIONAL RESULTS

### General remarks

In the following sections the listings of the used computer programs are presented with all necessary comments. The source programs are those of HARRINGTON and MAUTZ [40] (program A is essentially the here presented program HARRA) and of BEVENSEE [10] (program HARRDF is a part of the here presented program PANB). Program PANA and PANC are new programs.

The programs are written in FORTRAN IV for a CDC computer. Card decks are available from HARRINGTON, BEVENSEE or from the author. Depending on your computer system, some of the characters need to be changed or the punched characters do not agree with the listing obtained from the punched cards. Please check above all the following characters:

- C : for comment
- = : might be printed (and read) as a >
- \* : might be printed (and read) as a †
- + : might be printed (and read) as a {

If you notice some differences between your listing (from the card deck) and the presented listing, use a subroutine DECODE for character replacement. Such subroutines should be available at your computer center.

Depending on your computer system, the organisation of the main programs and the subroutines may be different. Problems may occur with the COMMON statements. Check the listings and ask the specialists of the computer center. Before actual computing the punched cards beginning with a C,R or E must be replaced by the corresponding control cards :

- C : This card is only a comment card and has no influence on the computation
- R : Replace that card by an appropriate control card
- E : Take this punched card out of the program

Except program PANA, the execution of the programs is quite expensive. The minimum computational time on a CDC 6500 for a series of 4 test points at one single frequency is in the order of 1000 seconds.

### 16.2.1. PROGRAM PANA AND IZYL RESULTS



[illegible]

1	AN(T)=JN(I)/CHPLX(JN(I),-YN(I))	PANA 157
	CALL BSSYN(LRK,HPI,JN,YN)	PANA 158
2	DO 2 I=1,NPI(JN(I),-YN(I))	PANA 159
	HNKR(I)=CHPLX(JN(I),-YN(I))	PANA 160
	ELSC=HN(I)*HNKR(I)	PANA 161
	ELI=HN(I)	PANA 162
	DO 3 N=1,M	PANA 163
	NU=NI+1	PANA 164
	BN=-CHPLX(I0,N*3,1415926/2.)	PANA 165
	BN=2.*CCS(N*PI)*CEXP(BN)	PANA 166
3	EZ1=EZ1+BN*(NU)	PANA 167
	ELSC=EZSC+BN*HNKR(NU)*AN(NU)	PANA 168
	V=CABS(1.-EZSC/EZ1)	PANA 169
	G=(ALOG10(V)*20.)	PANA 170
	RETURN \$ END	PANA 171
C	*****	PANA 172
R	HERE END OF RECORD CARD	PANA 173
E	DATA CARDS	PANA 174
	0.05 0.25 05 12	PANA 175
	0.05 1.00 20 25	PANA 176
	0.125	PANA 177
	150 MHZ	PANA 178
	205 MHZ	PANA 179
	250 MHZ	PANA 180
	HERE END OF INFORMATION CARD	

AZIMUTHAL RADIATION PATTERN FREQUENCY 125 MHZ										DIRECTIVE RADIATION PATTERN FREQUENCY 125 MHZ									
TWO-DIMENSIONAL ANTENNA-BODY SYSTEM										TWO-DIMENSIONAL ANTENNA-BODY SYSTEM									
TESTBODY: INFINITE ROT. SYM. CYLINDER										TESTBODY: INFINITE ROT. SYM. CYLINDER									
DAT(1) : DIAMETER: .25 M										DIAMETER: .25 M									
PHI : HORIZONTAL ROTATION ANGLE IN DEGREES										POLARISATION: VERTICAL/VERTICAL									
DAT(1) DAT(2) DAT(3) DAT(4) DAT(5)										DAT(1) GAI(1) PHI									
.000 .100 .150 .200 .250										M DB DEG									
PHI GAI(1) GAI(2) GAI(3) GAI(4) GAI(5)																			
0	-9.3	-4.4	-1.8	-1	1.0					1.00	-2.07	0							
5	-9.3	-4.4	-1.8	-1	1.0					.95	-1.34	0							
10	-9.4	-4.4	-1.8	-2	1.0					.90	-.83	0							
15	-9.4	-4.5	-1.9	-2	.9					.85	-.16	0							
20	-9.5	-4.6	-2.0	-3	.8					.80	1.16	0							
25	-9.7	-4.7	-2.1	-3	.8					.75	1.78	0							
30	-9.8	-4.9	-2.3	-6	.6					.70	2.29	0							
35	-10.0	-5.1	-2.6	-7	.3					.65	2.68	0							
40	-10.2	-5.3	-2.9	-9	.1					.60	2.96	0							
45	-10.5	-5.5	-3.1	-1.4	.2					.55	3.16	0							
50	-10.7	-5.8	-3.4	-1.4	.2					.50	3.07	0							
55	-11.0	-6.1	-3.8	-1.7	.7					.45	2.84	0							
60	-11.4	-6.4	-3.8	-2.9	.9					.40	2.84	0							
65	-11.7	-6.8	-4.5	-2.3	-1.4					.35	2.85	0							
70	-12.1	-7.2	-4.5	-2.7	-1.4					.30	1.86	0							
75	-12.6	-7.6	-4.9	-3.1	-1.8					.25	1.04	0							
80	-13.0	-8.0	-5.4	-3.6	-2.3					.20	-.12	0							
85	-13.5	-8.5	-5.8	-4.1	-2.7					.15	-1.79	0							
90	-14.0	-9.0	-6.4	-4.6	-3.2					.10	-4.39	0							
95	-14.5	-9.6	-6.9	-5.1	-3.8					.05	-9.30	0							
100	-15.1	-10.1	-7.5	-5.7	-4.4					0.00	-19.60	180							
105	-15.6	-10.7	-8.0	-6.3	-5.0					.10	-14.61	180							
110	-16.2	-11.3	-8.6	-6.9	-5.6					.15	-12.34	180							
115	-16.8	-11.9	-9.2	-7.5	-6.2					.20	-10.75	180							
120	-17.3	-12.4	-9.8	-8.1	-6.8					.25	-9.62	180							
125	-17.8	-12.9	-10.3	-8.6	-7.4					.30	-8.77	180							
130	-18.2	-13.4	-10.8	-9.1	-7.9					.35	-8.09	180							
135	-18.6	-13.8	-11.3	-9.6	-8.4					.40	-7.54	180							
140	-18.9	-14.1	-11.6	-10.0	-8.8					.45	-7.08	180							
145	-19.2	-14.4	-11.9	-10.3	-9.1					.50	-6.69	180							
150	-19.4	-14.6	-12.1	-10.5	-9.3					.55	-6.06	180							
155	-19.5	-14.7	-12.2	-10.6	-9.5					.60	-5.80	180							
160	-19.6	-14.8	-12.3	-10.7	-9.6					.65	-5.57	180							
165	-19.6	-14.8	-12.3	-10.7	-9.6					.70	-5.37	180							
170	-19.6	-14.8	-12.3	-10.7	-9.6					.75	-5.18	180							
175	-19.6	-14.8	-12.3	-10.7	-9.6					.80	-5.01	180							
180	-19.6	-14.8	-12.3	-10.7	-9.6					.85	-4.85	180							
										.90	-4.71	180							
										.95	-4.58	180							
										1.00	-4.58	180							

IZYL 125 MHZ

AZIMUTHAL RADIATION PATTERN FREQUENCY 300 MHZ										DIRECTIVE RADIATION PATTERN FREQUENCY 300 MHZ									
TWO-DIMENSIONAL ANTENNA-BODY SYSTEM										TWO-DIMENSIONAL ANTENNA-BODY SYSTEM									
TESTBODY: INFINITE ROT. SYM. CYLINDER										TESTBODY: INFINITE ROT. SYM. CYLINDER									
DIAETER: .25 M										DIAETER: .25 M									
NUMBER OF MODI: 12										NUMBER OF MODI: 25									
POLARISATION: VERTICAL/VERTICAL										POLARISATION: VERTICAL/VERTICAL									
DAT(1) : ANTENNA-BODY DISTANCE IN METERS										DAT(1) : GAI(1) DB									
PHI : HORIZONTAL ROTATION ANGLE IN DEGREES										PHI DEG									
DAT(1) DAT(2) DAT(3) DAT(4) DAT(5)										-20 DB -15 DB -10 DB -5 DB +0 DB +5 DB									
.050 .100 .150 .200 .250																			
PHI GAI(1) GAI(2) GAI(3) GAI(4) GAI(5)																			
0	-3.8	-8	2.8	3.6	3.5	1	1	2 35	1	1.00	-2.71	0	0	0	0	0	0	0	0
5	-3.8	-8	2.8	3.6	3.6	1	1	2 35	1	1.00	-2.49	0	0	0	0	0	0	0	0
10	-3.9	-7	2.8	3.5	3.6	1	1	2 35	1	1.00	-1.00	0	0	0	0	0	0	0	0
15	-4.0	-7	2.7	3.5	3.6	1	1	2 35	1	1.00	1.78	0	0	0	0	0	0	0	0
20	-4.1	-5	2.6	3.5	3.6	1	1	2 35	1	1.00	2.31	0	0	0	0	0	0	0	0
25	-4.2	-4	2.5	3.4	3.6	1	1	2 35	1	1.00	1.60	0	0	0	0	0	0	0	0
30	-4.4	-2	2.4	3.4	3.6	1	1	2 35	1	1.00	1.18	0	0	0	0	0	0	0	0
35	-4.7	-2	2.2	3.3	3.5	1	1	2 35	1	1.00	1.00	0	0	0	0	0	0	0	0
40	-4.9	-2	2.0	3.1	3.5	1	1	2 35	1	1.00	1.00	0	0	0	0	0	0	0	0
45	-5.2	-5	1.8	3.0	3.4	1	1	2 35	1	1.00	1.00	0	0	0	0	0	0	0	0
50	-5.5	-7	1.6	2.8	3.2	1	1	2 35	1	1.00	1.00	0	0	0	0	0	0	0	0
55	-5.9	-11	1.3	2.6	3.1	1	1	2 35	1	1.00	1.00	0	0	0	0	0	0	0	0
60	-6.3	-14	1.0	2.4	3.1	1	1	2 35	1	1.00	1.00	0	0	0	0	0	0	0	0
65	-6.7	-19	.6	2.1	2.9	1	1	2 35	1	1.00	1.00	0	0	0	0	0	0	0	0
70	-7.2	-23	.2	1.7	2.6	1	1	2 35	1	1.00	1.00	0	0	0	0	0	0	0	0
75	-7.7	-28	-.2	1.4	2.4	1	1	2 35	1	1.00	1.00	0	0	0	0	0	0	0	0
80	-8.3	-33	-.7	.9	2.0	1	1	2 35	1	1.00	1.00	0	0	0	0	0	0	0	0
85	-8.9	-39	-1.2	.5	1.6	1	1	2 35	1	1.00	1.00	0	0	0	0	0	0	0	0
90	-9.5	-45	-1.8	-.1	1.1	1	1	2 35	1	1.00	1.00	0	0	0	0	0	0	0	0
95	-10.2	-52	-2.4	-.6	.6	1	1	2 35	1	1.00	1.00	0	0	0	0	0	0	0	0
100	-10.9	-59	-3.1	-1.3	.0	1	1	2 35	1	1.00	1.00	0	0	0	0	0	0	0	0
105	-11.7	-67	-3.9	-2.0	-.7	1	1	2 35	1	1.00	1.00	0	0	0	0	0	0	0	0
110	-12.6	-75	-4.7	-2.8	-1.5	1	1	2 35	1	1.00	1.00	0	0	0	0	0	0	0	0
115	-13.5	-84	-5.6	-3.7	-2.3	1	1	2 35	1	1.00	1.00	0	0	0	0	0	0	0	0
120	-14.5	-94	-6.6	-4.7	-3.2	1	1	2 35	1	1.00	1.00	0	0	0	0	0	0	0	0
125	-15.5	-104	-7.6	-5.7	-4.2	1	1	2 35	1	1.00	1.00	0	0	0	0	0	0	0	0
130	-16.5	-115	-8.7	-6.8	-5.4	1	1	2 35	1	1.00	1.00	0	0	0	0	0	0	0	0
135	-17.5	-125	-9.7	-7.9	-6.5	1	1	2 35	1	1.00	1.00	0	0	0	0	0	0	0	0
140	-18.5	-135	-10.7	-8.9	-7.6	1	1	2 35	1	1.00	1.00	0	0	0	0	0	0	0	0
145	-19.5	-145	-11.6	-9.8	-8.5	1	1	2 35	1	1.00	1.00	0	0	0	0	0	0	0	0
150	-19.8	-152	-12.3	-10.5	-9.3	1	1	2 35	1	1.00	1.00	0	0	0	0	0	0	0	0
155	-20.1	-159	-12.6	-11.0	-9.8	1	1	2 35	1	1.00	1.00	0	0	0	0	0	0	0	0
160	-20.2	-163	-12.8	-11.2	-10.0	1	1	2 35	1	1.00	1.00	0	0	0	0	0	0	0	0
165	-20.1	-163	-12.8	-11.2	-10.0	1	1	2 35	1	1.00	1.00	0	0	0	0	0	0	0	0
170	-20.1	-163	-12.8	-11.2	-10.0	1	1	2 35	1	1.00	1.00	0	0	0	0	0	0	0	0
175	-20.0	-162	-12.6	-11.1	-9.9	1	1	2 35	1	1.00	1.00	0	0	0	0	0	0	0	0
180	-20.0	-162	-12.6	-11.0	-9.8	1	1	2 35	1	1.00	1.00	0	0	0	0	0	0	0	0

IZYL 300 MHZ

AZIMUTHAL RADIATION PATTERN FREQUENCY 400 MHZ										DIRECTIVE RADIATION PATTERN FREQUENCY 400 MHZ									
TWO-DIMENSIONAL ANTENNA-BODY SYSTEM										TWO-DIMENSIONAL ANTENNA-BODY SYSTEM									
TESTBODY: INFINITE ROT. SYM. CYLINDER										TESTBODY: INFINITE ROT. SYM. CYLINDER									
DIAMETER: .25 M										DIAMETER: .25 M									
NUMBER OF MODI: 12										NUMBER OF MODI: 25									
POLARISATION: VERTICAL/VERTICAL										POLARISATION: VERTICAL/VERTICAL									
DAT(1) : ANTENNA-BODY DISTANCE IN METERS										ROT. ANGLE PHI : 0 ABOVE, 180 BELOW									
GAI(1) : GAIN, FIELD STRENGTH AT THE ANTENNA A1 IN DB, 0 DB = FREE SPACE										NUMBER OF MODI: 25									
PHI : HORIZONTAL ROTATION ANGLE IN DEGREES										POLARISATION: VERTICAL/VERTICAL									
DAT(1) DAT(2) DAT(3) DAT(4) DAT(5)										DAT(1) GAI(1) PHI DEG									
.050 .100 .150 .200 .250										-20 DB -10 DB -5 DB +0 DB +5 DB									
PHI GAI(1) GAI(2) GAI(3) GAI(4) GAI(5)																			
0 -1.9 2.4 3.8 3.6 2.1										1.00 .98 0									
5 -1.9 2.4 3.8 3.6 2.1										.95 2.00 0									
10 -1.9 2.3 3.8 3.6 2.2										.90 2.01 0									
15 -2.0 2.3 3.7 3.7 2.3										.85 -1.95 0									
20 -2.2 2.2 3.7 3.7 2.4										.80 -3.11 0									
25 -2.3 2.0 3.6 3.7 2.6										.75 -2.22 0									
30 -2.5 1.9 3.5 3.7 2.7										.70 -2.27 0									
35 -2.8 1.7 3.4 3.7 2.9										.65 2.60 0									
40 -3.1 1.4 3.3 3.7 3.1										.60 2.63 0									
45 -3.4 1.2 3.1 3.7 3.2										.55 2.66 0									
50 -3.7 .9 2.9 3.6 3.3										.50 2.68 0									
55 -4.1 .5 2.6 3.5 3.4										.45 .12 0									
60 -4.6 .2 2.3 3.3 3.4										.40 -3.15 0									
65 -5.1 -.3 2.0 3.1 3.4										.35 -4.53 0									
70 -5.6 -.7 1.6 2.8 3.3										.30 -2.98 0									
75 -6.1 -1.2 1.2 2.5 3.2										.25 2.07 0									
80 -6.7 -1.8 -.7 2.2 2.9										.20 3.63 0									
85 -7.4 -2.4 -.4 1.7 2.6										.15 3.80 0									
90 -8.0 -3.0 -.4 1.3 2.3										.10 2.40 0									
95 -8.8 -3.7 -1.0 .7 1.8										.05 -1.86 0									
100 -9.5 -4.4 -.1 2.3 4.5										.05 -20.35 180									
105 -10.3 -5.2 -1.7 1.3										.15 -15.47 180									
110 -11.2 -6.1 -3.3 -1.4										.20 -12.91 180									
115 -12.2 -7.0 -4.2 -2.3										.25 -10.09 180									
120 -13.2 -8.1 -5.2 -3.2										.30 -9.20 180									
125 -14.4 -9.2 -6.3 -4.3										.35 -8.50 180									
130 -15.5 -10.4 -7.5 -5.5										.40 -7.92 180									
135 -16.8 -11.6 -8.8 -6.8										.45 -7.44 180									
140 -18.0 -12.9 -10.1 -8.1										.50 -7.04 180									
145 -19.2 -14.1 -11.3 -9.4										.55 -6.69 180									
150 -20.1 -15.1 -12.3 -10.5										.60 -6.36 180									
155 -20.6 -15.6 -13.0 -11.3										.65 -6.11 180									
160 -20.8 -15.9 -13.3 -11.6										.70 -5.87 180									
165 -20.7 -15.8 -13.3 -11.6										.75 -5.65 180									
170 -20.6 -15.7 -13.1 -11.5										.80 -5.46 180									
175 -20.4 -15.5 -13.0 -11.3										.85 -5.28 180									
180 -20.4 -15.5 -12.9 -11.3										.90 -5.12 180									
										.95 -4.97 180									
										1.00 -4.83 180									

IZYL 400 MHZ

AZIMUTHAL RADIATION PATTERN FREQUENCY 700 MHZ										DIRECTIVE RADIATION PATTERN FREQUENCY 700 MHZ									
TWO-DIMENSIONAL ANTENNA-BODY SYSTEM										TWO-DIMENSIONAL ANTENNA-BODY SYSTEM									
TESTBODY: INFINITE ROT.SYM.CYLINDER										TESTBODY: INFINITE ROT.SYM.CYLINDER									
DIA(1) : ANTENNA-BODY DISTANCE IN METERS										DIA(1) : ANTENNA-BODY DISTANCE IN METERS									
GAI(1) : GAIN, FIELD STRENGTH AT THE ANTENNA A1 IN DB, 0 DB = FREE SPACE										GAI(1) : GAIN, FIELD STRENGTH AT THE ANTENNA A1 IN DB, 0 DB = FREE SPACE									
PHI : HORIZONTAL ROTATION ANGLE IN DEGREES										PHI : HORIZONTAL ROTATION ANGLE IN DEGREES									
DAT(1) DAT(2) DAT(3) DAT(4) DAT(5)										DAT(1) GAI(1) PHI DEG									
.050 .100 .150 .200 .250										-20 DB -15 DB -10 DB -5 DB +0 DB +5 DB									
PHI GAI(1) GAI(2) GAI(3) GAI(4) GAI(5)																			
0	1.8	4.3	2.0	-5.4	-7					1.01	1.95	0							
5	1.8	4.3	2.0	-5.4	-7					.95	1.95	0							
10	1.8	4.3	2.1	-5.1	-1.0					.85	-2.77	0							
15	1.7	4.3	2.2	-4.8	-1.4					.80	2.21	0							
20	1.5	4.3	2.4	-4.2	-2.0					.75	2.21	0							
25	1.4	4.2	2.6	-3.5	-2.7					.65	-2.93	0							
30	1.2	4.2	2.9	-2.7	-3.6					.55	2.27	0							
35	.9	4.1	3.1	-1.8	-4.5					.50	1.89	0							
40	.6	3.9	3.3	-1.1	-5.3					.45	-2.24	0							
45	.3	3.8	3.5	.1	-5.2					.40	-2.46	0							
50	.1	3.6	3.7	.9	-4.5					.35	2.15	0							
55	-.6	3.3	3.8	1.7	-3.2					.30	2.90	0							
60	-1.1	3.0	3.8	2.8	-1.7					.25	-5.42	0							
65	-1.6	2.7	3.6	2.8	-3					.20	1.97	0							
70	-2.2	2.2	3.4	3.4	1.9					.15	1.34	0							
75	-2.9	1.8	3.1	3.4	1.9					.10	1.34	0							
80	-3.6	1.2	2.7	3.4	2.5					.05	1.84	0							
85	-4.3	.6	2.1	3.4	3.0					0.00	-21.58	180							
90	-5.2	-.2	1.6	2.8	3.2					.10	-16.53	180							
95	-6.0	-.9	1.2	2.3	3.0					.15	-13.85	180							
100	-7.0	-1.8	.9	1.7	2.6					.20	-12.11	180							
105	-7.9	-2.7	.1	1.7	2.1					.25	-10.86	180							
110	-8.9	-3.6	-.8	1.0	2.1					.30	-9.91	180							
115	-10.0	-4.6	-1.7	.2	1.4					.35	-8.16	180							
120	-11.0	-5.7	-2.7	-.7	.6					.40	-6.55	180							
125	-12.2	-6.8	-3.8	-1.8	-.3					.45	-5.04	180							
130	-13.4	-8.0	-5.0	-2.9	-1.4					.50	-3.60	180							
135	-14.8	-9.4	-6.3	-4.2	-2.7					.55	-2.22	180							
140	-16.4	-11.0	-7.9	-5.8	-4.2					.60	-1.01	180							
145	-18.2	-12.8	-9.7	-7.6	-5.9					.65	-.61	180							
150	-20.1	-14.7	-11.6	-9.5	-7.9					.70	-.35	180							
155	-21.7	-16.4	-13.5	-11.4	-9.9					.75	-.10	180							
160	-22.7	-17.5	-14.7	-12.8	-11.4					.80	-.00	180							
165	-22.7	-17.5	-14.9	-13.1	-11.8					.85	-.50	180							
170	-22.2	-17.2	-14.5	-12.7	-11.5					.90	-.51	180							
175	-21.8	-16.7	-14.0	-12.3	-11.0					.95	-.53	180							
180	-21.6	-16.5	-13.9	-12.1	-10.9					1.00	-.53	180							

IIZYL 700 MHZ



AZIMUTHAL RADIATION PATTERN FREQUENCY 897 MHZ										DIRECTIVE RADIATION PATTERN FREQUENCY 897 MHZ									
TWO-DIMENSIONAL ANTENNA-BODY SYSTEM										TWO-DIMENSIONAL ANTENNA-BODY SYSTEM									
TESTBODY: INFINITE ROT. SYM. CYLINDER										TESTBODY: INFINITE ROT. SYM. CYLINDER									
DIA(1) : ANTENNA-BODY DISTANCE IN METERS										DIA(1) : ANTENNA-BODY DISTANCE IN METERS									
GAI(1) : GAIN, FIELD STRENGTH AT THE ANTENNA A1 IN DB, 0 DB = FREE SPACE										GAI(1) : GAIN, FIELD STRENGTH AT THE ANTENNA A1 IN DB, 0 DB = FREE SPACE									
PHI : HORIZONTAL ROTATION ANGLE IN DEGREES										PHI : HORIZONTAL ROTATION ANGLE IN DEGREES									
DAT(1) DAT(2) DAT(3) DAT(4) DAT(5)										DAT(1) GAI(1) PHI									
.050 .100 .150 .200 .250										DB DEG									
PHI GAI(1) GAI(2) GAI(3) GAI(4) GAI(5)										DB DEG									
0	3.3	3.8	-4.4	-0	3.3					1.00	-2.53	0							
5	3.3	3.8	-4.0	-0.3	3.3					.95	-1.91	0							
10	3.2	3.9	-4.0	-0.3	3.3					.90	-1.74	0							
15	3.1	3.9	-3.5	-0.7	3.3					.85	-1.67	0							
20	3.0	4.0	-2.9	-1.3	3.2					.80	-1.45	0							
25	2.9	4.1	-2.1	-2.0	3.1					.75	2.20	0							
30	2.7	4.1	-1.3	-3.1	2.8					.65	-2.30	0							
35	2.4	4.2	-1.4	-4.3	2.4					.60	2.06	0							
40	2.1	4.2	-1.2	-5.4	1.8					.55	-1.28	0							
45	1.8	4.2	-1.2	-5.9	.9					.50	-1.22	0							
50	1.4	4.1	1.9	-5.2	-4					.45	2.52	0							
55	1.0	4.0	2.5	-3.7	-2.0					.35	-2.70	0							
60	.5	3.9	3.0	-1.9	-3.8					.25	3.31	0							
65	-.1	3.6	3.4	-4	-5.0					.15	-4.37	0							
70	-.7	3.3	3.7	2.0	-4.3					.10	3.81	0							
75	-1.3	2.9	3.6	2.7	-5					.05	3.28	0							
80	-2.1	2.4	3.6	3.4	1.1					0.00									
85	-2.9	1.8	3.4	3.4	2.1														
90	-3.8	1.1	3.1	3.4	1.1														
95	-4.7	.4	2.6	3.3	2.8														
100	-5.7	-.5	2.0	3.1	3.1														
105	-6.8	-1.5	1.2	2.6	3.1														
110	-8.0	-2.5	-.3	1.9	2.8														
115	-9.1	-3.7	-.7	1.1	2.2														
120	-10.3	-4.8	-1.8	.2	1.5														
125	-11.5	-6.0	-2.9	-.9	.6														
130	-12.8	-7.2	-4.1	-2.0	-.5														
135	-14.1	-8.6	-5.4	-3.2	-1.7														
140	-15.7	-10.1	-6.9	-4.7	-3.1														
145	-17.4	-11.9	-8.7	-6.5	-4.8														
150	-19.5	-14.0	-10.8	-8.6	-6.8														
155	-21.8	-16.3	-13.1	-10.9	-9.3														
160	-23.6	-18.2	-15.2	-13.1	-11.5														
165	-24.0	-18.8	-15.9	-14.0	-12.6														
170	-23.4	-18.2	-15.4	-13.6	-12.3														
175	-22.6	-17.5	-14.7	-12.9	-11.6														
180	-22.4	-17.2	-14.4	-12.6	-11.4														

IZYL 897 MHZ

16.2.2. PROGRAM HARRA AND OUTPUT SAMPLE



```

118 FORMAT(1X/' T,J')
WRITE(3,6) (TJ(I),I=1,N)
DO 2 J=1,NPHI
ANG(J)=(J-.5)*DP
AC(J)=COS(ANG(J))
2 CONTINUE
N3=0
DO 10 M=45,M6
M1=M-3
M2=M3-NPHI
DO 11 K=1,NPHI
K1=M2-K
CSH(K1)=DP*COS(M1*ANG(K))
11 CONTINUE
M3=M3+1
10 CONTINUE
DO 16 J=1,KG
DEL=5*DH(J)
DEL1=5*DH(J)*BK
AA=DP*R(J)*DEL*FK
DO 17 I=1,KG
Z3=Z5(J)-Z5(I)
RR1=SV(J)*R(J)+CV(J)*Z3
RR2=SV(J)*R(I)
RR3=R(J)*R(J)+R(I)*R(I)+Z3*Z3
RR4=-2.*R(J)*R(I)
X1=ABS(R(J)-R(I))+ABS(Z3)
DO 5 K=1,NPHI
IF(K.NE.1.OR.X1.NE.0.) GO TO 7
X=R(J)*DP
XX=SQRT(DEL*DEL-X*XX)
W1=X*ALOG((DEL-XX)/DEL-XX)/X+DEL*ALOG((X-XX)/DEL)/AA
W2=-1.
CS(I)=W1+W2
GO TO 5
7 T=ABS(RR1+AC(K)*RR2)
RD=RR3+RR4*AC(K)
RK=BK*SQRT(RD)
D2=RD-Y*Y
Y1=Y-DEL
Y2=Y+DEL
R1=SQRT(Y1*Y1+D2)
R2=SQRT(Y2*Y2+D2)
IF(Y1) 72,73,73
72 TIN=ALOG((Y2-R2)/(Y1+R1))*(Y2+R2)/D2
GO TO 25
73 TIN=ALOG((Y2-R2)/(Y1+R1))
25 SN=SIN(RK)
CS(K)=CS-COS(RK)
GS(K)=(CS-U*SN)*(TIN-U*(BK*DH(J)-RK*TIN))/DEL1
5 CONTINUE
N3=(J-1)*KG+1

```

HARRA104  
HARRA105  
HARRA106  
HARRA107  
HARRA108  
HARRA109  
HARRA110  
HARRA111  
HARRA112  
HARRA113  
HARRA114  
HARRA115  
HARRA116  
HARRA117  
HARRA118  
HARRA119  
HARRA120  
HARRA121  
HARRA122  
HARRA123  
HARRA124  
HARRA125  
HARRA126  
HARRA127  
HARRA128  
HARRA129  
HARRA130  
HARRA131  
HARRA132  
HARRA133  
HARRA134  
HARRA135  
HARRA136  
HARRA137  
HARRA138  
HARRA139  
HARRA140  
HARRA141  
HARRA142  
HARRA143  
HARRA144  
HARRA145  
HARRA146  
HARRA147  
HARRA148  
HARRA149  
HARRA150  
HARRA151  
HARRA152  
HARRA153  
HARRA154  
HARRA155

```

DO 68 M=1,3
M1=M-1
M4=M1*NPHI
M2=M1*NC+M3
G(M2)=0.
DO 13 K=1,NPHI
K2=K-M1
G(M2)+G(M2)+GS(K)*CSH(K2)
13 CONTINUE
68 CONTINUE
17 CONTINUE
16 CONTINUE
DO 74 J=1,NM
J2=2*(J-1)+1
J3=J2+1
J4=J3+1
J5=J4+1
J6=J5*(J-1)+1
J7=J6+1
J8=J7+1
J9=J8+1
DEL1=5H(J2)+DH(J3)
DEL2=5H(J4)+DH(J5)
TP(J6)=5H(J2)/DEL1
TP(J7)=5H(J3)/DEL1
TP(J8)=5H(J4)/DEL2
TP(J9)=5H(J5)/DEL2
T(J6)=5H(J2)*DH(J2)/2./DEL1
T(J7)=5H(J3)*DH(J2)+DH(J3)/2./DEL1
T(J8)=5H(J4)*DH(J4)/2./DEL2
T(J9)=5H(J5)*DH(J5)/2./DEL2
74 CONTINUE
DO 75 J=1,NM4
TR(J)=T(J)
75 CONTINUE
115 IF((ZH(1)-ZH(NP-2)).EQ.0..AND.(RH(1)-RH(NP-2)).EQ.0.) GO TO 78
IF(RH(1)) 77,23,77
77 DEL1=5H(1)+DH(2)
TR(1)=5H(1)*1.+5H(2)+DH(1)/2./DEL1
TR(2)=5H(2)*1.+5H(2)/2./DEL1
23 IF(RH(NP)) 79,78,79
79 J1=(N-2)*K+3
J2=J1+1
DEL2=5H(NP-2)+DH(KG)
TR(J1)=5H(NP-2)*1.+5H(NP-2)/2./DEL2
TR(J2)=5H(KG)*1.+5H(NP-2)+DH(KG)/2./DEL2
116 TR(J2)=5H(KG)*1.+5H(NP-2)+DH(KG)/2./DEL2
78 DO 30 J=1,NM
JL=(J-1)*NM2
J3=(J-1)*M
J1=2*(J-1)
DO 31 I=1,NM
L1=JL+I

```

HARRA156  
HARRA157  
HARRA158  
HARRA159  
HARRA160  
HARRA161  
HARRA162  
HARRA163  
HARRA164  
HARRA165  
HARRA166  
HARRA167  
HARRA168  
HARRA169  
HARRA170  
HARRA171  
HARRA172  
HARRA173  
HARRA174  
HARRA175  
HARRA176  
HARRA177  
HARRA178  
HARRA179  
HARRA180  
HARRA181  
HARRA182  
HARRA183  
HARRA184  
HARRA185  
HARRA186  
HARRA187  
HARRA188  
HARRA189  
HARRA190  
HARRA191  
HARRA192  
HARRA193  
HARRA194  
HARRA195  
HARRA196  
HARRA197  
HARRA198  
HARRA199  
HARRA200  
HARRA201  
HARRA202  
HARRA203  
HARRA204  
HARRA205  
HARRA206  
HARRA207





NN= 0 NP= 41 NPHI= 20 UK= .343400E+10 FREQUENCY = 16.40 MHZ									
RESULTS FROM HARRA									
ONLY MODE NN = 0 SHOWN HERE									
RH	0.0000	.5000	.5150	.5150	.5000	.5150	.5150	.5250	.5250
	.5750	.6200	.6500	.7100	.7800	.8250	1.0300	1.0300	1.0300
	.9800	.9900	1.0200	1.0350	1.1000	1.0700	1.0400	.9300	.8500
	.6300	.4800	.4900	.6200	.7600	.8900	.8200	.7000	.5500
ZH	0.0000	0.0000	.3500	.7600	1.2700	1.7400	2.1800	2.5900	3.1200
	4.0400	5.5000	5.9600	6.5100	7.0600	7.6300	8.2400	8.7000	9.2000
	9.7400	10.7700	11.3400	11.8200	12.2700	12.5500	12.8200	13.1900	13.5100
	13.8200	14.3100	14.5500	14.7000	15.0000	15.4000	15.7000	16.0500	16.4200
	16.8000								
TJ	.8503	1.7705	2.6804	3.6209	4.7650	6.0041	7.0177	8.1602	9.2429
	11.3174	12.3713	13.1039	13.7534	14.5485	15.2066	15.7362	16.4463	17.1894
Y1	.2244E-04	.1244E-03	.44878E-04	.2618E-04	.6413E-04	.1155E-04	.7421E-04	.3309E-05	.7637E-04
	.6853E-04	.4244E-04	.5337E-04	.4761E-04	.3018E-04	.4682E-04	.5559E-05	.3697E-04	.3335E-04
	.5927E-04	.4061E-04	.7195E-04	.5896E-05	.7854E-04	.1634E-04	.7567E-04	.2295E-04	.2648E-04
	.7241E-04	.2606E-04	.6710E-04	.2621E-04	.4755E-04	.2154E-04	.1620E-04	.6630E-05	.7610E-04
	.4801E-04	.2954E-04	.1048E-03	.1614E-03	.1342E-03	.3021E-04	.1603E-03	.7142E-05	.1673E-03
	.1501E-03	.8221E-04	.1139E-03	.9502E-04	.6887E-04	.9597E-04	.7184E-05	.7882E-05	.5013E-04
	.1127E-02	.2801E-04	.1512E-03	.6994E-05	.1662E-03	.2632E-04	.1692E-03	.4015E-04	.4673E-04
	.1364E-03	.6901E-04	.1411E-03	.6824E-02	.1101E-03	.4045E-04	.3493E-04	.1647E-04	.1620E-03
	.6320E-04	.1245E-04	.1395E-03	.7032E-04	.1832E-03	.1445E-03	.2138E-03	.3560E-06	.2233E-03
	.2018E-03	.8729E-04	.1631E-03	.1103E-03	.9390E-04	.1209E-03	.4160E-05	.1031E-03	.8369E-04
	.1430E-03	.5711E-04	.1951E-03	.1103E-03	.2135E-03	.4665E-04	.4598E-04	.1936E-04	.8241E-04
	.7920E-03	.5848E-04	.1809E-03	.5446E-04	.2135E-03	.1438E-06	.2496E-03	.1096E-03	.2625E-03
	.2392E-03	.3467E-04	.1946E-03	.1219E-03	.1181E-03	.1191E-03	.2597E-05	.1180E-03	.4571E-04
	.1600E-03	.4240E-04	.12240E-03	.1399E-04	.4258E-03	.1551E-04	.2520E-03	.3552E-04	.7508E-04
	.2943E-03	.5636E-04	.2150E-03	.5116E-04	.1535E-03	.4376E-04	.5393E-04	.1936E-04	.8368E-04
	.7898E-04	.1666E-03	.5031E-04	.5031E-04	.2233E-03	.5114E-04	.2623E-03	.4609E-04	.2778E-03
	.2557E-03	.7835E-04	.2166E-03	.1015E-03	.1831E-03	.1229E-03	.1433E-04	.1189E-03	.8114E-04
	.1546E-03	.8745E-04	.2133E-03	.1070E-04	.2469E-03	.1274E-05	.2544E-03	.1706E-04	.2457E-03
	.2787E-03	.3745E-04	.1433E-03	.3564E-04	.1565E-03	.3636E-04	.5431E-04	.1558E-04	.3077E-04
	.6764E-04	.4168E-04	.1507E-03	.8221E-04	.2021E-03	.9706E-04	.2396E-03	.9433E-04	.2561E-03
	.2400E-03	.8610E-04	.2031E-03	.5870E-04	.1351E-03	.8296E-04	.3089E-04	.9659E-04	.5371E-04
	.1198E-03	.7660E-04	.1735E-03	.4911E-04	.2056E-03	.2142E-04	.1413E-03	.1207E-04	.9244E-04
	.2024E-03	.3678E-05	.1854E-03	.7637E-05	.1450E-03	.1502E-04	.4791E-04	.7624E-05	.2088E-03
	.5311E-04	.4709E-03	.1136E-03	.9935E-04	.1620E-03	.1162E-03	.1937E-03	.2221E-03	.2105E-03
	.2014E-03	.5635E-04	.1291E-03	.1291E-03	.1290E-03	.4212E-04	.4551E-04	.6394E-04	.1031E-03
	.7214E-04	.1209E-03	.6174E-04	.1415E-03	.1415E-03	.4946E-04	.1524E-03	.1989E-04	.7528E-04
	.1463E-03	.2505E-04	.1333E-03	.1938E-04	.9862E-04	.8723E-05	.1687E-04	.3850E-04	.1504E-03
	.2960E-04	.4622E-04	.6888E-04	.9617E-04	.9573E-04	.1210E-03	.1319E-03	.7550E-06	.1329E-03
	.1349E-03	.8255E-04	.1248E-03	.4353E-04	.1016E-03	.1561E-03	.6191E-04	.1790E-04	.2758E-04
	.1764E-05	.5906E-04	.3179E-04	.6851E-04	.4773E-04	.6327E-04	.5614E-04	.6629E-04	.5832E-04







.1974E-05	.1213E-05	.2040E-05	-.8330E-05	.2312E-05	.2024E-04	.3+02E-05	-.4407E-04	.4604E-05	.1162E-03
.6066E-05	-.2819E-03	.6811E-05	-.8332E-03	.1073E-05	-.2617E-02	.1600E-04	-.6041E-02	.9559E-05	-.1180E-01
.1337E-05	.6393E-02	.1443E-04	.3144E-04	.8212E-04	-.1673E-02	.1113E-04	-.5671E-03	.4452E-05	.2391E-03
.1572E-05	-.1077E-03	.7516E-05	.5110E-04	.9062E-05	-.1113E-04	.4652E-05	.5176E-05	.4803E-05	-.4646E-04
.1693E-05	-.3003E-05	.1376E-05	.2470E-04	.8265E-05	-.5296E-05	.3482E-05	.2104E-04	.1357E-04	.6380E-02
.6693E-05	-.1204E-01	.7931E-05	-.4357E-04	.1246E-04	.9040E-03	.1691E-04	-.2427E-02	.9788E-03	-.5816E-02
.1330E-05	-.1820E-01	.1301E-04	.8197E-02	.1451E-04	-.3916E-02	.142E-04	.1522E-02	.4376E-03	.2433E-04
.6021E-05	-.2804E-05	.9900E-05	.9754E-04	.1227E-04	.4931E-04	.6506E-05	-.8695E-05	.4376E-03	.2433E-04
.7918E-06	-.1740E-03	.1331E-05	.3237E-05	.6157E-04	.2771E-05	.2922E-05	-.1168E-04	.1438E-04	.3121E-02
.1883E-05	-.6554E-04	.7311E-05	.1858E-03	.1319E-04	-.4095E-03	.1956E-04	.1325E-02	.8051E-05	.1607E-02
.6486E-05	.8452E-02	.2162E-04	-.1608E-01	.2045E-04	.1102E-01	.1894E-04	-.3826E-02	.4376E-03	.2433E-04
.2731E-05	.1729E-01	.1376E-04	.3347E-03	.1774E-04	-.7940E-04	.9915E-05	.3867E-04	.8051E-05	.1607E-02
.8733E-07	-.2195E-05	.7034E-06	.6003E-06	.1304E-05	-.3736E-05	.1963E-05	.3868E-05	.3127E-03	-.1282E-04
.4968E-05	.3093E-04	.5653E-05	-.8578E-04	.1064E-04	.2400E-03	.1603E-04	.5981E-03	.1264E-04	.1583E-02
.1507E-04	-.3835E-02	.2115E-04	.1037E-01	.1673E-04	-.2249E-01	.1798E-04	.1228E-01	.7257E-05	-.4659E-02
.2644E-05	-.2237E-02	.1232E-04	.8147E-03	.1720E-04	.3609E-03	.9924E-05	-.7506E-04	.2219E-03	.3061E-05
-.3749E-06	-.1470E-05	.2373E-06	.4612E-05	.6735E-06	-.7701E-06	.1252E-05	.3345E-05	.1119E-04	-.5550E-03
.3794E-05	.1184E-04	.4534E-05	.3333E-04	.8942E-05	-.8426E-05	.1356E-04	.2441E-03	.7956E-05	.1098E-01
.1433E-04	.1493E-02	.1913E-04	.3770E-02	.1743E-04	.1232E-01	.1641E-04	.2337E-01	.6307E-05	.2451E-05
.3202E-05	-.5075E-02	.1323E-04	.2211E-02	.1763E-04	-.6703E-03	.1047E-04	.2305E-03	.4376E-03	.2534E-03
-.2993E-06	.5813E-06	.4998E-07	.3607E-06	.7805E-07	.9323E-06	.2926E-06	.1476E-05	.2584E-05	.1727E-01
.1224E-05	.4004E-05	.1531E-05	.1333E-04	.3147E-05	.3506E-04	.5233E-05	.8958E-04	.3776E-05	.5354E-03
.5579E-05	-.5737E-03	.8013E-05	.1570E-02	.7215E-05	-.4931E-02	.7898E-05	.1400E-01	.2584E-05	.1727E-01
.1686E-05	.1054E-01	.5039E-05	.3764E-02	.7503E-05	.1538E-02	.4518E-05	.3569E-03	.2776E-06	.5047E-06
-.1330E-06	-.2102E-06	.2935E-07	.2707E-06	.1365E-07	.1534E-06	.1270E-06	-.6549E-06	.1905E-05	-.4027E-03
.5395E-06	-.2238E-05	.6773E-06	.5834E-05	.1390E-05	-.1594E-04	.2298E-05	.4350E-04	.1755E-05	.4025E-01
.2491E-07	-.1972E-01	.3956E-05	.7016E-03	.3026E-05	.5194E-02	.2949E-05	-.4925E-02	.9120E-03	-.1572E-05
-.1691E-07	-.1972E-01	.3956E-05	.7016E-03	.3026E-05	.5194E-02	.2949E-05	-.4925E-02	.7307E-05	.4979E-04
-.1931E-05	-.2447E-06	.1911E-06	.7718E-06	.7266E-08	-.1102E-05	.3641E-06	-.9457E-06	.5490E-05	-.3718E-02
.5942E-05	-.9547E-04	.1339E-04	.3282E-03	.5117E-05	.6669E-05	.8628E-05	-.1332E-04	.9306E-05	-.4027E-03
.2507E-05	.1365E-01	.9275E-03	.2104E-01	.1217E-04	-.8136E-03	.1256E-04	.2174E-02	.5386E-06	-.1698E-05
-.1104E-05	-.7011E-06	-.5788E-06	.8846E-06	.4471E-06	-.1214E-05	-.4064E-07	.1480E-05	.9226E-05	-.1064E-04
.1747E-05	-.2291E-05	.2446E-05	.8563E-06	.5651E-05	-.3900E-05	.1032E-04	.7368E-05	.8303E-05	.1538E-02
.1266E-05	.4846E-04	.1918E-04	.7690E-04	.1699E-04	-.3014E-03	.1733E-04	.6628E-03	.7924E-07	-.1029E-06
.2682E-05	-.3778E-02	.1326E-04	.4092E-01	.2062E-04	.1725E-01	.1379E-04	.6656E-02	.4694E-05	.5011E-05
-.7087E-06	-.1379E-06	.4615E-06	.3257E-06	.4686E-06	-.5461E-06	-.2993E-06	-.6876E-06	.4961E-05	.5011E-05
.4649E-06	-.1192E-05	.4601E-06	.4504E-05	.2169E-05	-.1395E-05	.4878E-05	.2480E-05	.4961E-05	.5011E-05
.6456E-05	-.8423E-05	.1011E-04	.3806E-04	.9733E-05	-.7740E-04	.1050E-04	.2258E-03	.4961E-05	.5011E-05
.1770E-05	.1055E-02	.8941E-05	-.2894E-02	.1374E-04	.6639E-02	.6414E-05	-.9563E-02		

NN = 1 NP = 41 NPHI = 20 B<= .3434903E+00 FREQUENCY = 16.40 MHZ

PROGRAM DELIVERS THE GENERALIZED ADMITTANCE MATRICES FOR ALL MODI UP TO NN = 7 (Y2.Y3 ≠ 0)

6.2.3. PROGRAM PANB AND OUTPUT SAMPLE



```

PAMB 156
PAMB 157
PAMB 158
PAMB 159
PAMB 160
PAMB 161
PAMB 162
PAMB 163
PAMB 164
PAMB 165
PAMB 166
PAMB 167
PAMB 168
PAMB 169
PAMB 170
PAMB 171
PAMB 172
PAMB 173
PAMB 174
PAMB 175
PAMB 176
PAMB 177
PAMB 178
PAMB 179
PAMB 180
PAMB 181
PAMB 182
PAMB 183
PAMB 184
PAMB 185
PAMB 186
PAMB 187
PAMB 188
PAMB 189
PAMB 190
PAMB 191
PAMB 192
PAMB 193
PAMB 194
PAMB 195
PAMB 196
PAMB 197
PAMB 198
PAMB 199
PAMB 200
PAMB 201
PAMB 202
PAMB 203
PAMB 204
PAMB 205
PAMB 206
PAMB 207

DO 7 I=1,NM
  I1=2*(I-1)+1
  I2=I1+1
  SS=SS+DH(I1)+DH(I2)
  TJ(I)=SS
7 CONTINUE
  DEL=TJ(NM)
  IF(KL.NE.0) DEL=DEL+DH(NP-2)+DH(NP-1)
  DEL=DEL/10.
  DO 8 J=1,NM
    TJ(J)=TJ(J)/DEL
8 CONTINUE
  DO 42 J=1,NT
    E1(J)=0.
    E2(J)=0.
42 CONTINUE
  IF(NTEST.EQ.0XGO TO 707
  READ(1,49)(RTEST(J),ZTEST(J),DTEST(J),J=1,NTEST)
49 FORMAT(3F8.4)
  DO 708 J=1,NTEST
    RRT=SQRT(RTEST(J))*2-ZTEST(J)**2
    -START(J)=RTEST(J)/RRT $COST(J)=ZTEST(J)/RRT
708 CONTINUE
707 DP=PI/NPHI
  CA=BK*FK*ETA $CQ=ETA
  DO 709 J=1,NPHI
    ANG(J)=(J-.5)*DP
    AC(J)=COS(ANG(J))
    DPT=PI/(NPHI-1)
    DO 500 J=1,NPHI
      PHI(J)=DPT*(J-1) $ PHIJ(J)=PHI(J)*PPR
      NN=N-1
      COSHI(M,J)= COS(NN*PHI(J))
      SIRHI(M,J)= U*STN(NN*PHI(J))
501 CONTINUE
500 CONTINUE
  DO 502 I=1,NTEST
    ARSTA=SQRT(ZTEST(I))*RTEST(I)+RTEST(I)*RTEST(I)
    STIN(I) = RTEST(I)/ARSTA $ COTN(I) = ZTEST(I)/ARSTA
502 CONTINUE
  DO 40 M=1,KK
    NN=N-1
    CALL PLANE(VVR,THR,NP,NT,1,R,25,SV,CV,T,TR)
    CALL PROG8
127 READ(6)(Y(I),I=1,NZ)
  WHITE(3,112)NN
112 FORMAT('112',0*,6X,$SIG 00*,6X,$SIG 00*,6X,
  1$MAG 500*,10X,$MODE NN=*,12)
  WHITE(3,113)

```

```

PAMB 104
PAMB 105
PAMB 106
PAMB 107
PAMB 108
PAMB 109
PAMB 110
PAMB 111
PAMB 112
PAMB 113
PAMB 114
PAMB 115
PAMB 116
PAMB 117
PAMB 118
PAMB 119
PAMB 120
PAMB 121
PAMB 122
PAMB 123
PAMB 124
PAMB 125
PAMB 126
PAMB 127
PAMB 128
PAMB 129
PAMB 130
PAMB 131
PAMB 132
PAMB 133
PAMB 134
PAMB 135
PAMB 136
PAMB 137
PAMB 138
PAMB 139
PAMB 140
PAMB 141
PAMB 142
PAMB 143
PAMB 144
PAMB 145
PAMB 146
PAMB 147
PAMB 148
PAMB 149
PAMB 150
PAMB 151
PAMB 152
PAMB 153
PAMB 154
PAMB 155

DH(I2)=SQRT(RR1*RR1+RR2*RR2)
ZS(I2)=.5*(ZH(I)+ZH(I2))
SV(I2)=.5*(RH(I)+RH(I2))
CV(I2)=RR1/DH(I2)
CV(I2)=RR2/DH(I2)
57 CONTINUE
C BEBESTELLUNG DES EINFALLS- UND REFLEKTIONSWINKELS
DT=0.394
DO 1 J=1,NT
  THR(J)=DT*(J-1) + 1.410
  IF(RUN.EQ.2) THR(J)=DT*J + 1.410
1 CONTINUE
  BK2=BK*FK
  P1=SQRT(BK2*BK2*ETA*ETA/4./PT**3)
  RM=(NP-3)/2
  RM4=RM**4
  NM2=NM**2
  NM4=NM**4
  KG=NP-1
  DO 70 J=1,NM
    J2=2*(J-1)+1
    J3=J2+1
    J4=J3+1
    J5=J4+1
    J6=4*(J-1)+1
    J7=J6+1
    J8=J7+1
    J9=J8+1
    DEL1=DH(J2)+DH(J3)
    DEL2=DH(J4)+DH(J5)
    TP(J6)= DH(J2)/DEL1 $TP(J7)= DH(J3)/DEL1
    TP(J8)= -DH(J4)/DEL2 $TP(J9)= -DH(J5)/DEL2
    T(G6)=DH(J2)*DH(J2)/2./DEL1
    T(G7)=DH(J3)*DH(J2)+DH(J3)/2./DEL1
    T(G8)=DH(J4)*DH(J5)+DH(J4)/2./DEL2
    T(G9)=DH(J5)*DH(J5)/2./DEL2
74 CONTINUE
  DO 75 J=1,NM4
    TR(I)=T(G)
75 CONTINUE
115 IF(KL.EQ.0) GO TO 78
  IF(DH(I1)) 77,73,77
77 DEL1=DH(I1)+DH(I2)
  TR(I)=DH(I1)*(1.+DH(I2)+DH(I1)/2.)/DEL1
  TR(I2)=DH(I2)*(1.+DH(I2)/2./DEL1)
23 IF(OH(NP)) 79,78,79
79 J1=(NM-1)*4+3
  J2=J1+1
  DEL2=DH(NP-2)+DH(NP-1)
  TR(I1)=DH(NP-2)*(1.+DH(NP-2)/2./DEL2)
  TR(I2)=DH(NP-1)*(1.+DH(NP-2)+DH(NP-1)/2.)/DEL2
78 SS=0.

```

```

113 FORMAT(*, -$, 10X, $--, 11X, $--, 10X, $//, 11X, $//*)
DO 41 L=1, IIT
L2=(L-1)*NM4
DO 2 J=1, NM2
E3(L, J)=0.
E4(L, J)=0.
DO 3 I=1, NM1
J1=J*(I-1)*NM2
J2=J1+NM1*NM2
I1=I+L2
I2=I+LNM4
I3=I+LNM2
I4=I+LNM2
3 CONTINUE
DO 43 J=1, NM2
J1=J+L2
E1(L)=E1(L)+E3(L, J)*VVR(1, J1)
E2(L)=E2(L)+E4(L, J)*VVR(1, J2)
43 CONTINUE
IF (NM) 44, 45, 44
45 E1(L)=.5*E1(L)
E2(L)=.5*E2(L)
44 X1=THR(L)*PR
X3=P1*CADS(E1(L))
X2=X3*X3
X5=P1*CADS(E2(L))
Y4=X5*W5
WRITE(3, 111) X1, X2, X3, X4, X5
111 FORMAT(1X, F6.2, 4E12.4)
41 CONTINUE
IF (NTEST.EQ.0) GO TO 40
DO 7100 ITEX=1, NTEST
WRITE(3, 712) NTEST(ITE), ZTEST(ITE), DTEST(ITE)
712 FORMAT(////, 4X, *NTEST=*, F8.4, 4X, *ZTEST=*, F8.4, 4X, *DTEST=*, F8.4,
1 //)
DR(1)=DTEST(ITE)*SINT(ITE) $DZ(1)=DTEST(ITE)*COST(ITE)
DR(2)=DZ(1) $DZ(2)=-DR(1)
FTEST=0.5/(P1*DTEST(ITE))
IF (NM.EQ.0) FTEST=0.5*FTEST
DO 706 IT=1, 2
CALL NEARZ(RTEST(ITE), ZTEST(ITE), DTEST(ITE), IT)
706 CALL PLANE(VWR, THR, 5, MT, IT, RT, ZST, SVT, CVT, TT, TRT)
DO 7101 L=1, NT
X1=THR(L)*PR
DO 702 IT=1, 2
ESC(1, 1)=CHPLX(0., 0.) $ESC(1, 2)=CHPLX(0., 0.)
ESC(1, 3)=CHPLX(0., 0.) $ESC(1, 4)=CHPLX(0., 0.)
DO 703 I=1, NM

```

```

PAND 260
PAND 261
PAND 262
PAND 263
PAND 264
PAND 265
PAND 266
PAND 267
PAND 268
PAND 269
PAND 270
PAND 271
PAND 272
PAND 273
PAND 274
PAND 275
PAND 276
PAND 277
PAND 278
PAND 279
PAND 280
PAND 281
PAND 282
PAND 283
PAND 284
PAND 285
PAND 286
PAND 287
PAND 288
PAND 289
PAND 290
PAND 291
PAND 292
PAND 293
PAND 294
PAND 295
PAND 296
PAND 297
PAND 298
PAND 299
PAND 300
PAND 301
PAND 302
PAND 303
PAND 304
PAND 305
PAND 306
PAND 307
PAND 308
PAND 309
PAND 310
PAND 311

J1=I
J2=I+NM2
I1=I
I2=I+NM
ESC(1, 1)=ESC(1, 1)-ZK(1, J1)*E3(L, 1)-ZK(1, J2)*E3(L, 1, 2)
ESC(1, 2)=ESC(1, 2)-ZK(1, J1)*E3(L, 1)-ZK(1, J2)*E3(L, 1, 2)
ESC(1, 3)=ESC(1, 3)-ZK(1, J1)*E4(L, 1)-ZK(1, J2)*E4(L, 1, 2)
ESC(1, 4)=ESC(1, 4)-ZK(1, J1)*E4(L, 1)-ZK(1, J2)*E4(L, 1, 2)
703 CONTINUE
702 CONTINUE
J1=(L-1)*4
I1=J1+1 $I2=I1+1 $I3=I2+1 $I4=I3+1
ERR=FTEST*REAL(VWR(1, I1)) $ERI=FTEST*ADMAG(VWR(1, I1))
ETHR=FTEST*REAL(VWR(2, I1)) $ETHI=FTEST*ADMAG(VWR(2, I1))
EPH1R=FTEST*REAL(VWR(1, I2)) $EPH1I=FTEST*ADMAG(VWR(1, I2))
EPH2R=FTEST*REAL(VWR(2, I2)) $EPH2I=FTEST*ADMAG(VWR(2, I2))
ETHR=ERR $ETRI=ERI $ETHR=ETHR $ETHI=ETHI
ETP1R=EPH1R $ETP1I=EPH1I $ETP2R=EPH2R $ETP2I=EPH2I
WRITE(3, 704) X1
704 FORMAT(10X, *FENC, *, IX5.1, 4X, *ETHETA INC*/)
WRITE(3, 705) ERR, ERI, EPH1R, EPH1I, ETHR, ETHI, EPH2R, EPH2I
705 FORMAT(1X, *FEND=*, 2E12.4, 1X, *EPH1=*, 2E12.4, 2X, *ETH=*, 2E12.4, 1X,
1*EPH1=*, 2E12.4)
ERR=REAL(ESC(1, 1))*FTEST $ERI=ADMAG(ESC(1, 1))*FTEST
ETHR=REAL(ESC(2, 1))*FTEST $ETHI=ADMAG(ESC(2, 1))*FTEST
EPH1R=REAL(ESC(1, 2))*FTEST $EPH1I=ADMAG(ESC(1, 2))*FTEST
EPH2R=REAL(ESC(2, 2))*FTEST $EPH2I=ADMAG(ESC(2, 2))*FTEST
WRITE(3, 710) X1
710 FORMAT(9X, *ESCAT, *, IX5.1, 4X, *ETHETA INC*/)
WRITE(3, 705) ENR, ERI, EPH1R, EPH1I, ETHR, ETHI, EPH2R, EPH2I
ETHR=ETHR+ERR $ETRI=ETRI+ERI $ETHR=ETHR+ETHR
ETHI=ETHI+ETHI $ETP1R=ETP1R+EPH1R $ETP1I=ETP1I+EPH1I
ETP2R=ETP2R+EPH2R $ETP2I=ETP2I+EPH2I
ETH(N, ITE, L)=CMPLX(ETHR, ETHI)
ETP(N, ITE, L)=CMPLX(ETP2R, ETP2I)
EPI=(ETP1R+ETP2R)/2 $EPI=(ETP1I+ETP2I)/2
ETP(N, ITE, L)=CMPLX(ETP, EPI)
WRITE(3, 711) X1
711 FORMAT(10X, *ETOT, *, IX5.1, 4X, *ETHETA INC*/)
WRITE(3, 705) ETOT, ETRI, ETP1R, ETP1I, ETHR, ETHI, ETP2R, ETP2I
ERR=FTEST*REAL(VWR(1, 13)) $ERI=FTEST*ADMAG(VWR(1, 13))
ETHR=FTEST*REAL(VWR(2, 13)) $ETHI=FTEST*ADMAG(VWR(2, 13))
EPH1R=FTEST*REAL(VWR(1, 14)) $EPH1I=FTEST*ADMAG(VWR(1, 14))
EPH2R=FTEST*REAL(VWR(2, 14)) $EPH2I=FTEST*ADMAG(VWR(2, 14))
ETHR=ERR $ETRI=ERI $ETHR=ETHR $ETHI=ETHI $ETP1R=EPH1R
ETP1I=EPH1I $ETP2R=EPH2R $ETP2I=EPH2I
WRITE(3, 714) X1
714 FORMAT(10X, *FENC, *, IX5.1, 4X, *EPH1 INC*/)
WRITE(3, 705) ERR, ERI, EPH1R, EPH1I, ETHR, ETHI, EPH2R, EPH2I
ERR=REAL(ESC(1, 3))*FTEST $ERI=ADMAG(ESC(1, 3))*FTEST
ETHR=REAL(ESC(2, 3))*FTEST $ETHI=ADMAG(ESC(2, 3))*FTEST
EPH1R=REAL(ESC(1, 4))*FTEST $EPH1I=ADMAG(ESC(1, 4))*FTEST
EPH2R=REAL(ESC(2, 4))*FTEST $EPH2I=ADMAG(ESC(2, 4))*FTEST

```

```

PAMB 312 ETTOT = ETTOT + ETT(M,ITE,L) * COPHI(M,J)
PAMB 313 EPTOT = EPTOT + ETP(M,ITE,L) * SIPHI(M,J)
PAMB 314 IF(J.EQ.1,OR(J.EQ.37) WRITE(3,545) NH,ETOT,EPTOT,EPTOT
PAMB 315 IF(J.EQ.19) WRITE(3,545) NH,ETOT,EPTOT,EPTOT
PAMB 316
PAMB 317 506 CONTINUE
PAMB 318 GO TO 913
PAMB 319 DO 911 M=1,NK
PAMB 320 NH=M-1
PAMB 321 ERTOT = ERTOT + FTR(M,ITE,L) * SIPHI(M,J)
PAMB 322 EPTOT = EPTOT + FTT(M,ITE,L) * SIPHI(M,J)
PAMB 323 EPTOT = EPTOT + FTF(M,ITE,L) * COPHI(M,J)
PAMB 324 IF(J.EQ.1,OR(J.EQ.37) WRITE(3,545) NH,ETOT,EPTOT,EPTOT
PAMB 325 IF(J.EQ.19) WRITE(3,545) NH,ETOT,EPTOT,EPTOT
PAMB 326 911 CONTINUE
PAMB 327 913 CONTINUE
PAMB 328 JDI=JDI+1
PAMB 329 ERTOT = ERTOT * COTN(ITE) - ETTOT * SITH(ITE)
PAMB 330 SVJ(JDI) = ERTOT
PAMB 331 EPTOT = EPTOT
PAMB 332 SVH(JDI) = ERTOT
PAMB 333 ESTOT = ERTOT * SITH(ITE) + ETTOT * COTN(ITE)
PAMB 334 SYS(JDI) = ESTOT
PAMB 335 IF(CABS(EVOT)) LT QQ) EVOT = PP
PAMB 336 IF(CABS(EVOT)) LT QQ) EVOT = PP
PAMB 337 IF(CABS(EVOT)) LT QQ) EVOT = PP
PAMB 338 GTOIT(ITE,L,J) = 20.*ALOG10(CABS(EVOT))
PAMB 339 GSTOT(ITE,L,J) = 20.*ALOG10(CABS(EVOT))
PAMB 340 PVOT(ITE,L,J) = ATAN2(REAL(EVOT),AIMAG(EVOT))
PAMB 341 PHOT(ITE,L,J) = ATAN2(REAL(EVOT),AIMAG(EVOT))
PAMB 342 PSTOT(ITE,L,J) = ATAN2(REAL(EVOT),AIMAG(EVOT))
PAMB 343 505 CONTINUE
PAMB 344 504 CONTINUE
PAMB 345 WRITE(7)(SW(1),I=1,NST)
PAMB 346 WRITE(7)(SW(1),I=1,NST)
PAMB 347 WRITE(7)(SW(1),I=1,NST)
PAMB 348 DO 918 I=1,3
PAMB 349 J = (I*18)-17
PAMB 350 WRITE(3,509) F,X1,DU,HO,TEXT(POL),DA,TEXT(JA),TEXT(JR),
PAMB 351 TEXT(JC)
PAMB 352 509 FORMAT(1H1,11X,
PAMB 353 1*AZIMUTHAL STRAHLUNGS DIAGRAM*,
PAMB 354 1 11X,FREQUENZ = *F6.1*,MHZ*/1HO,KOEPPER : VERTPAMB 406
PAMB 355 2KALER ROT.SYM.MENSCHOD - MESSANTENNE : PUNKTANTENNE AUF
PAMB 356 3INSTRALUNG : WINKEL THETA = *F5.1* GRAD*/1H 10X *DURCHMESSER PAMB 408
PAMB 357 A = *F5.2* METER*/21X,FH.2, *METER *HOEHE = *20X *POLARISATION = * PAMB 409
PAMB 358 5,R10*/1H, 10X *ACHSENLENGE = *F5.2* METER*/21X,PHI UND DIST VAPAMB 410
PAMB 359 6R.* 5X,MESSANTENNE : POLARISATION = *R10*/1HO,3R10,/
PAMB 360 WRITE(3,553) PHO(J)
PAMB 361 553 FORMAT(1H0,"ROTATIONSWINKEL PHI = *F6.2* GRAD*/)
PAMB 362 552 FORMAT(1H1,"DIST : ABSTAND DER MESSANTENNE VON DER KOERPEROBERPAMB 415
PAMB 363

```

```

1 LAECHE IN METER */1H. *PHI : HORIZONTALER ROTATIONSWINKEL INPAND 416
2 GRAD: 180 GRAD = SCHWIERIG */1H *GAIN : FELDSTARKE BEI DER MPAND 417
3 ZESAMMENFUEHRUNG IN GRAD: 0 DB = MAX.FREESPACE*/1H *PHASE : PHASE DES PAND 418
4 WINKELPUNKTES IN GRAD: 22X, *WINKELPUNKT*/1H, *PHASE DES PAND 419
5 DER FELDSTARKE IN HESSPUNKT*, 35X, *PHASENLAGE DER FELDSTARKE PAND 420
6 HESSPUNKT*/1H
7
562 FORMAT(1H10, *DIST GAIN PHASE -25 DB -20 DB -15 DB
110 DB -5 DB +5 DB*.7X,-180 -90 0
2 +90 +180*/1H)
563 FORMAT(1H1, F4.0, 2F8.2)
567 FORMAT(1H*, 23X, 7(1H., 9X), 2X, 4(1H., 8X), 11H.)
568 FORMAT(1H*, 25X, 61(R1))
569 FORMAT(1H*, 97X, 37(R1))
DO 512 IFE=1, NTEST
WRITE(3, 513) DI(ITE), GWTOT(ITE, L, J), PVTOT(ITE, L, J)
513 FORMAT(1H1, F4.2, 2F8.2)
DO 514 NA = 1, 61
514 D(NA)=1H
Q=GWTOT(ITE, L, J)
IF(Q.GT.5.0E-04.LT.-25.) GO TO 515 $ Q = Q*2.
KV=IFIX(Q*50.5)
D(KV)=18A
515 DO 526 NRI=1, 37
526 E(NRI)=1H
B=PVTOT(ITE, L, J)/10.
KVP=IFIX(B*19.0)
E(KVP)=18B
WRITE(3, 516)
516 FORMAT(1H*, 24X, 7(1H., 9X), 2X, 4(1H., 8X), 11H.)
517 FORMAT(1H*, 25X, 61(R1))
531 WRITE(3, 531)(ENPP), NPP=1, 37)
528 FORMAT(1H1, F4.2, 20X, 7(1H., 9X), 2X, 4(1H., 8X), 11H.)
IF(ITE.EQ.3)WRITE(3, 528) 0.20
IF(ITE.EQ.4)WRITE(3, 528) 0.30
IF(ITE.EQ.5)WRITE(3, 528) 0.40
IF(ITE.EQ.6)WRITE(3, 528) 0.45
IF(ITE.EQ.7)WRITE(3, 528) 0.55
IF(ITE.EQ.8)WRITE(3, 528) 0.60
IF(ITE.EQ.9)WRITE(3, 528) 0.70
IF(ITE.EQ.10)WRITE(3, 528) 0.75
IF(ITE.EQ.11)WRITE(3, 528) 0.85
IF(ITE.EQ.12)WRITE(3, 528) 0.90
IF(ITE.EQ.13)WRITE(3, 528) 0.95
512 CONTINUE
518 CONTINUE
519 CONTINUE
520 CONTINUE
521 CONTINUE
522 STOP
END

```

```

C *****
E SUBROUTINE
SUBROUTINE PLANE(VPR, THR, HP, MT, IT, R, ZS, SV, CV, T, TR)
COMPLEX VPR(2, 1), A5, A6, U
COMMON/BLK/IN
DIMENSION BK(120), THR(1), FK(20), R(041), ZS(041), SV(041), CV(041),
11(076), TR(076)
U=CMPLX(0., 1.)
KG=HP-1
NH=KG/2-1
N2=NH-2
A5=2.*3.141593/PI*(NH+1)
NV=NH*4
FK(1)=1.
DO 153 J=1, N2
J1=J+1
FK(J1)=FK(J)*J
153 CONTINUE
DO 156 L=1, NT
L1=(L-1)*PIV
CS=COS(THR(L))
SN=SIN(THR(L))
RCS=BK*CS
RCS=BN*SN
X=R(J)*BK*SN
J1=J
J1=NH
IF(J1) 303, 304, 303
304 I1=I+1
J1=J+1*KG
303 DO 305 JJ=I1, N2
1 IF(J1-E-5) 1, 1, 2
1 IF(JJ-I) 3, 3, 4
3 BJ(J1)=1.
GO TO 306
4 BJ(J1)=0.
GO TO 306
2 RH2=RH*PI
RH3=RH*PI*(JJ-1)
SS=BJ(J1)
8 SST=SS*1.E-7
DO 155 K=1, 20
BJ(J1)=BJ(J1)+SS
SS=SS*RH2/K/(K+JJ-1)
155 CONTINUE
WRITE(3, 1000)
1000 FORMAT(1HSTOP AT 155)
RETURN

```

PAND 468  
PAND 469  
PAND 470  
PAND 471  
PAND 472  
PAND 473  
PAND 474  
PAND 475  
PAND 476  
PAND 477  
PAND 478  
PAND 479  
PAND 480  
PAND 481  
PAND 482  
PAND 483  
PAND 484  
PAND 485  
PAND 486  
PAND 487  
PAND 488  
PAND 489  
PAND 490  
PAND 491  
PAND 492  
PAND 493  
PAND 494  
PAND 495  
PAND 496  
PAND 497  
PAND 498  
PAND 499  
PAND 500  
PAND 501  
PAND 502  
PAND 503  
PAND 504  
PAND 505  
PAND 506  
PAND 507  
PAND 508  
PAND 509  
PAND 510  
PAND 511  
PAND 512  
PAND 513  
PAND 514  
PAND 515  
PAND 516  
PAND 517  
PAND 518  
PAND 519





```

1SV(OH1),CV(OH1),ANG(20),CSH(GO)
COMPLEX VWR(2,760),Y(1444),ZM(2,DT6),GT(4764)
COMMON      VWR,Y,ZM,GT
DP=3,141593/NPHI
NH=KG/2-1 $NH2=NH*2
DO 2 I=1,5
  X1=I-3
  RHT(I)=X1*DR(IT) *RTST
  2 ZUT(I)=X1*PZ(IT) *ZTEST
DO 57 I=2,5
  R1=I-1
  R2=I-2
  R3=I-3
  R4=I-4
  R5=I-5
  R6=I-6
  R7=I-7
  R8=I-8
  R9=I-9
  R10=I-10
  R11=I-11
  R12=I-12
  R13=I-13
  R14=I-14
  R15=I-15
  R16=I-16
  R17=I-17
  R18=I-18
  R19=I-19
  R20=I-20
  R21=I-21
  R22=I-22
  R23=I-23
  R24=I-24
  R25=I-25
  R26=I-26
  R27=I-27
  R28=I-28
  R29=I-29
  R30=I-30
  R31=I-31
  R32=I-32
  R33=I-33
  R34=I-34
  R35=I-35
  R36=I-36
  R37=I-37
  R38=I-38
  R39=I-39
  R40=I-40
  R41=I-41
  R42=I-42
  R43=I-43
  R44=I-44
  R45=I-45
  R46=I-46
  R47=I-47
  R48=I-48
  R49=I-49
  R50=I-50
  R51=I-51
  R52=I-52
  R53=I-53
  R54=I-54
  R55=I-55
  R56=I-56
  R57=I-57
  R58=I-58
  R59=I-59
  R60=I-60
  R61=I-61
  R62=I-62
  R63=I-63
  R64=I-64
  R65=I-65
  R66=I-66
  R67=I-67
  R68=I-68
  R69=I-69
  R70=I-70
  R71=I-71
  R72=I-72
  R73=I-73
  R74=I-74
  R75=I-75
  R76=I-76
  R77=I-77
  R78=I-78
  R79=I-79
  R80=I-80
  R81=I-81
  R82=I-82
  R83=I-83
  R84=I-84
  R85=I-85
  R86=I-86
  R87=I-87
  R88=I-88
  R89=I-89
  R90=I-90
  R91=I-91
  R92=I-92
  R93=I-93
  R94=I-94
  R95=I-95
  R96=I-96
  R97=I-97
  R98=I-98
  R99=I-99
  R100=I-100
  R101=I-101
  R102=I-102
  R103=I-103
  R104=I-104
  R105=I-105
  R106=I-106
  R107=I-107
  R108=I-108
  R109=I-109
  R110=I-110
  R111=I-111
  R112=I-112
  R113=I-113
  R114=I-114
  R115=I-115
  R116=I-116
  R117=I-117
  R118=I-118
  R119=I-119
  R120=I-120
  R121=I-121
  R122=I-122
  R123=I-123
  R124=I-124
  R125=I-125
  R126=I-126
  R127=I-127
  R128=I-128
  R129=I-129
  R130=I-130
  R131=I-131
  R132=I-132
  R133=I-133
  R134=I-134
  R135=I-135
  R136=I-136
  R137=I-137
  R138=I-138
  R139=I-139
  R140=I-140
  R141=I-141
  R142=I-142
  R143=I-143
  R144=I-144
  R145=I-145
  R146=I-146
  R147=I-147
  R148=I-148
  R149=I-149
  R150=I-150
  R151=I-151
  R152=I-152
  R153=I-153
  R154=I-154
  R155=I-155
  R156=I-156
  R157=I-157
  R158=I-158
  R159=I-159
  R160=I-160
  R161=I-161
  R162=I-162
  R163=I-163
  R164=I-164
  R165=I-165
  R166=I-166
  R167=I-167
  R168=I-168
  R169=I-169
  R170=I-170
  R171=I-171
  R172=I-172
  R173=I-173
  R174=I-174
  R175=I-175
  R176=I-176
  R177=I-177
  R178=I-178
  R179=I-179
  R180=I-180
  R181=I-181
  R182=I-182
  R183=I-183
  R184=I-184
  R185=I-185
  R186=I-186
  R187=I-187
  R188=I-188
  R189=I-189
  R190=I-190
  R191=I-191
  R192=I-192
  R193=I-193
  R194=I-194
  R195=I-195
  R196=I-196
  R197=I-197
  R198=I-198
  R199=I-199
  R200=I-200
  R201=I-201
  R202=I-202
  R203=I-203
  R204=I-204
  R205=I-205
  R206=I-206
  R207=I-207
  R208=I-208
  R209=I-209
  R210=I-210
  R211=I-211
  R212=I-212
  R213=I-213
  R214=I-214
  R215=I-215
  R216=I-216
  R217=I-217
  R218=I-218
  R219=I-219
  R220=I-220
  R221=I-221
  R222=I-222
  R223=I-223
  R224=I-224
  R225=I-225
  R226=I-226
  R227=I-227
  R228=I-228
  R229=I-229
  R230=I-230
  R231=I-231
  R232=I-232
  R233=I-233
  R234=I-234
  R235=I-235
  R236=I-236
  R237=I-237
  R238=I-238
  R239=I-239
  R240=I-240
  R241=I-241
  R242=I-242
  R243=I-243
  R244=I-244
  R245=I-245
  R246=I-246
  R247=I-247
  R248=I-248
  R249=I-249
  R250=I-250
  R251=I-251
  R252=I-252
  R253=I-253
  R254=I-254
  R255=I-255
  R256=I-256
  R257=I-257
  R258=I-258
  R259=I-259
  R260=I-260
  R261=I-261
  R262=I-262
  R263=I-263
  R264=I-264
  R265=I-265
  R266=I-266
  R267=I-267
  R268=I-268
  R269=I-269
  R270=I-270
  R271=I-271
  R272=I-272
  R273=I-273
  R274=I-274
  R275=I-275
  R276=I-276
  R277=I-277
  R278=I-278
  R279=I-279
  R280=I-280
  R281=I-281
  R282=I-282
  R283=I-283
  R284=I-284
  R285=I-285
  R286=I-286
  R287=I-287
  R288=I-288
  R289=I-289
  R290=I-290
  R291=I-291
  R292=I-292
  R293=I-293
  R294=I-294
  R295=I-295
  R296=I-296
  R297=I-297
  R298=I-298
  R299=I-299
  R300=I-300
  R301=I-301
  R302=I-302
  R303=I-303
  R304=I-304
  R305=I-305
  R306=I-306
  R307=I-307
  R308=I-308
  R309=I-309
  R310=I-310
  R311=I-311
  R312=I-312
  R313=I-313
  R314=I-314
  R315=I-315
  R316=I-316
  R317=I-317
  R318=I-318
  R319=I-319
  R320=I-320
  R321=I-321
  R322=I-322
  R323=I-323
  R324=I-324
  R325=I-325
  R326=I-326
  R327=I-327
  R328=I-328
  R329=I-329
  R330=I-330
  R331=I-331
  R332=I-332
  R333=I-333
  R334=I-334
  R335=I-335
  R336=I-336
  R337=I-337
  R338=I-338
  R339=I-339
  R340=I-340
  R341=I-341
  R342=I-342
  R343=I-343
  R344=I-344
  R345=I-345
  R346=I-346
  R347=I-347
  R348=I-348
  R349=I-349
  R350=I-350
  R351=I-351
  R352=I-352
  R353=I-353
  R354=I-354
  R355=I-355
  R356=I-356
  R357=I-357
  R358=I-358
  R359=I-359
  R360=I-360
  R361=I-361
  R362=I-362
  R363=I-363
  R364=I-364
  R365=I-365
  R366=I-366
  R367=I-367
  R368=I-368
  R369=I-369
  R370=I-370
  R371=I-371
  R372=I-372
  R373=I-373
  R374=I-374
  R375=I-375
  R376=I-376
  R377=I-377
  R378=I-378
  R379=I-379
  R380=I-380
  R381=I-381
  R382=I-382
  R383=I-383
  R384=I-384
  R385=I-385
  R386=I-386
  R387=I-387
  R388=I-388
  R389=I-389
  R390=I-390
  R391=I-391
  R392=I-392
  R393=I-393
  R394=I-394
  R395=I-395
  R396=I-396
  R397=I-397
  R398=I-398
  R399=I-399
  R400=I-400
  R401=I-401
  R402=I-402
  R403=I-403
  R404=I-404
  R405=I-405
  R406=I-406
  R407=I-407
  R408=I-408
  R409=I-409
  R410=I-410
  R411=I-411
  R412=I-412
  R413=I-413
  R414=I-414
  R415=I-415
  R416=I-416
  R417=I-417
  R418=I-418
  R419=I-419
  R420=I-420
  R421=I-421
  R422=I-422
  R423=I-423
  R424=I-424
  R425=I-425
  R426=I-426
  R427=I-427
  R428=I-428
  R429=I-429
  R430=I-430
  R431=I-431
  R432=I-432
  R433=I-433
  R434=I-434
  R435=I-435
  R436=I-436
  R437=I-437
  R438=I-438
  R439=I-439
  R440=I-440
  R441=I-441
  R442=I-442
  R443=I-443
  R444=I-444
  R445=I-445
  R446=I-446
  R447=I-447
  R448=I-448
  R449=I-449
  R450=I-450
  R451=I-451
  R452=I-452
  R453=I-453
  R454=I-454
  R455=I-455
  R456=I-456
  R457=I-457
  R458=I-458
  R459=I-459
  R460=I-460
  R461=I-461
  R462=I-462
  R463=I-463
  R464=I-464
  R465=I-465
  R466=I-466
  R467=I-467
  R468=I-468
  R469=I-469
  R470=I-470
  R471=I-471
  R472=I-472
  R473=I-473
  R474=I-474
  R475=I-475
  R476=I-476
  R477=I-477
  R478=I-478
  R479=I-479
  R480=I-480
  R481=I-481
  R482=I-482
  R483=I-483
  R484=I-484
  R485=I-485
  R486=I-486
  R487=I-487
  R488=I-488
  R489=I-489
  R490=I-490
  R491=I-491
  R492=I-492
  R493=I-493
  R494=I-494
  R495=I-495
  R496=I-496
  R497=I-497
  R498=I-498
  R499=I-499
  R500=I-500
  R501=I-501
  R502=I-502
  R503=I-503
  R504=I-504
  R505=I-505
  R506=I-506
  R507=I-507
  R508=I-508
  R509=I-509
  R510=I-510
  R511=I-511
  R512=I-512
  R513=I-513
  R514=I-514
  R515=I-515
  R516=I-516
  R517=I-517
  R518=I-518
  R519=I-519
  R520=I-520
  R521=I-521
  R522=I-522
  R523=I-523
  R524=I-524
  R525=I-525
  R526=I-526
  R527=I-527
  R528=I-528
  R529=I-529
  R530=I-530
  R531=I-531
  R532=I-532
  R533=I-533
  R534=I-534
  R535=I-535
  R536=I-536
  R537=I-537
  R538=I-538
  R539=I-539
  R540=I-540
  R541=I-541
  R542=I-542
  R543=I-543
  R544=I-544
  R545=I-545
  R546=I-546
  R547=I-547
  R548=I-548
  R549=I-549
  R550=I-550
  R551=I-551
  R552=I-552
  R553=I-553
  R554=I-554
  R555=I-555
  R556=I-556
  R557=I-557
  R558=I-558
  R559=I-559
  R560=I-560
  R561=I-561
  R562=I-562
  R563=I-563
  R564=I-564
  R565=I-565
  R566=I-566
  R567=I-567
  R568=I-568
  R569=I-569
  R570=I-570
  R571=I-571
  R572=I-572
  R573=I-573
  R574=I-574
  R575=I-575
  R576=I-576
  R577=I-577
  R578=I-578
  R579=I-579
  R580=I-580
  R581=I-581
  R582=I-582
  R583=I-583
  R584=I-584
  R585=I-585
  R586=I-586
  R587=I-587
  R588=I-588
  R589=I-589
  R590=I-590
  R591=I-591
  R592=I-592
  R593=I-593
  R594=I-594
  R595=I-595
  R596=I-596
  R597=I-597
  R598=I-598
  R599=I-599
  R600=I-600
  R601=I-601
  R602=I-602
  R603=I-603
  R604=I-604
  R605=I-605
  R606=I-606
  R607=I-607
  R608=I-608
  R609=I-609
  R610=I-610
  R611=I-611
  R612=I-612
  R613=I-613
  R614=I-614
  R615=I-615
  R616=I-616
  R617=I-617
  R618=I-618
  R619=I-619
  R620=I-620
  R621=I-621
  R622=I-622
  R623=I-623
  R624=I-624
  R625=I-625
  R626=I-626
  R627=I-627
  R628=I-628
  R629=I-629
  R630=I-630
  R631=I-631
  R632=I-632
  R633=I-633
  R634=I-634
  R635=I-635
  R636=I-636
  R637=I-637
  R638=I-638
  R639=I-639
  R640=I-640
  R641=I-641
  R642=I-642
  R643=I-643
  R644=I-644
  R645=I-645
  R646=I-646
  R647=I-647
  R648=I-648
  R649=I-649
  R650=I-650
  R651=I-651
  R652=I-652
  R653=I-653
  R654=I-654
  R655=I-655
  R656=I-656
  R657=I-657
  R658=I-658
  R659=I-659
  R660=I-660
  R661=I-661
  R662=I-662
  R663=I-663
  R664=I-664
  R665=I-665
  R666=I-666
  R667=I-667
  R668=I-668
  R669=I-669
  R670=I-670
  R671=I-671
  R672=I-672
  R673=I-673
  R674=I-674
  R675=I-675
  R676=I-676
  R677=I-677
  R678=I-678
  R679=I-679
  R680=I-680
  R681=I-681
  R682=I-682
  R683=I-683
  R684=I-684
  R685=I-685
  R686=I-686
  R687=I-687
  R688=I-688
  R689=I-689
  R690=I-690
  R691=I-691
  R692=I-692
  R693=I-693
  R694=I-694
  R695=I-695
  R696=I-696
  R697=I-697
  R698=I-698
  R699=I-699
  R700=I-700
  R701=I-701
  R702=I-702
  R703=I-703
  R704=I-704
  R705=I-705
  R706=I-706
  R707=I-707
  R708=I-708
  R709=I-709
  R710=I-710
  R711=I-711
  R712=I-712
  R713=I-713
  R714=I-714
  R715=I-715
  R716=I-716
  R717=I-717
  R718=I-718
  R719=I-719
  R720=I-720
  R721=I-721
  R722=I-722
  R723=I-723
  R724=I-724
  R725=I-725
  R726=I-726
  R727=I-727
  R728=I-728
  R729=I-729
  R730=I-730
  R731=I-731
  R732=I-732
  R733=I-733
  R734=I-734
  R735=I-735
  R736=I-736
  R737=I-737
  R738=I-738
  R739=I-739
  R740=I-740
  R741=I-741
  R742=I-742
  R743=I-743
  R744=I-744
  R745=I-745
  R746=I-746
  R747=I-747
  R748=I-748
  R749=I-749
  R750=I-750
  R751=I-751
  R752=I-752
  R753=I-753
  R754=I-754
  R755=I-755
  R756=I-756
  R757=I-757
  R758=I-758
  R759=I-759
  R760=I-760
  R761=I-761
  R762=I-762
  R763=I-763
  R764=I-764
  R765=I-765
  R766=I-766
  R767=I-767
  R768=I-768
  R769=I-769
  R770=I-770
  R771=I-771
  R772=I-772
  R773=I-773
  R774=I-774
  R775=I-775
  R776=I-776
  R777=I-777
  R778=I-778
  R779=I-779
  R780=I-780
  R781=I-781
  R782=I-782
  R783=I-783
  R784=I-784
  R785=I-785
  R786=I-786
  R787=I-787
  R788=I-788
  R789=I-789
  R790=I-790
  R791=I-791
  R792=I-792
  R793=I-793
  R794=I-794
  R795=I-795
  R796=I-796
  R797=I-797
  R798=I-798
  R799=I-799
  R800=I-800
  R801=I-801
  R802=I-802
  R803=I-803
  R804=I-804
  R805=I-805
  R806=I-806
  R807=I-807
  R808=I-808
  R809=I-809
  R810=I-810
  R811=I-811
  R812=I-812
  R813=I-813
  R814=I-814
  R815=I-815
  R816=I-816
  R817=I-817
  R818=I-818
  R819=I-819
  R820=I-820
  R821=I-821
  R822=I-822
  R823=I-823
  R824=I-824
  R825=I-825
  R826=I-826
  R827=I-827
  R828=I-828
  R829=I-829
  R830=I-830
  R831=I-831
  R832=I-832
  R833=I-833
  R834=I-834
  R835=I-835
  R836=I-836
  R837=I-837
  R838=I-838
  R839=I-839
  R840=I-840
  R841=I-841
  R842=I-842
  R843=I-843
  R844=I-844
  R845=I-845
  R846=I-846
  R847=I-847
  R848=I-848
  R849=I-849
  R850=I-850
  R851=I-851
  R852=I-852
  R853=I-853
  R854=I-854
  R855=I-855
  R856=I-856
  R857=I-857
  R858=I-858
  R859=I-859
  R860=I-860
  R861=I-861
  R862=I-862
  R863=I-863
  R864=I-864
  R865=I-865
  R866=I-866
  R867=I-867
  R868=I-868
  R869=I-869
  R870=I-870
  R871=I-871
  R872=I-872
  R873=I-873
  R874=I-874
  R875=I-875
  R876=I-876
  R877=I-877
  R878=I-878
  R879=I-879
  R880=I-880
  R881=I-881
  R882=I-882
  R883=I-883
  R884=I-884
  R885=I-885
  R886=I-886
  R887=I-887
  R888=I-888
  R889=I-889
  R890=I-890
  R891=I-891
  R892=I-892
  R893=I-893
  R894=I-894
  R895=I-895
  R896=I-896
  R897=I-897
  R898=I-898
  R899=I-899
  R900=I-900
  R901=I-901
  R902=I-902
  R903=I-903
  R904=I-904
  R905=I-905
  R906=I-906
  R907=I-907
  R908=I-908
  R909=I-909
  R910=I-910
  R911=I-911
  R912=I-912
  R913=I-913
  R914=I-914
  R915=I-915
  R916=I-916
  R917=I-917
  R918=I-918
  R919=I-919
  R920=I-920
  R921=I-921
  R922=I-922
  R923=I-923
  R924=I-924
  R925=I-925
  R926=I-926
  R927=I-927
  R928=I-928
  R929=I-929
  R930=I-930
  R931=I-931
  R932=I-932
  R933=I-933
  R934=I-934
  R935=I-935
  R936=I-936
  R937=I-937
  R938=I-938
  R939=I-939
  R940=I-940
  R941=I-941
  R942=I-942
  R943=I-943
  R944=I-944
  R945=I-945
  R946=I-946
  R947=I-947
  R948=I-948
  R949=I-949
  R950=I-950
  R951=I-951
  R952=I-952
  R953=I-953
  R954=I-954
  R955=I-955
  R956=I-956
  R957=I-957
  R958=I-958
  R959=I-959
  R960=I-960
  R961=I-961
  R962=I-962
  R963=I-963
  R964=I-964
  R965=I-965
  R966=I-966
  R967=I-967
  R968=I-968
  R969=I-969
  R970=I-970
  R971=I-971
  R972=I-972
  R973=I-973
  R974=I-974
  R975=I-975
  R976=I-976
  R977=I-977
  R978=I-978
  R979=I-979
  R980=I-980
  R981=I-981
  R982=I-982
  R983=I-983
  R984=I-984
  R985=I-985
  R986=I-986
  R987=I-987
  R988=I-988
  R989=I-989
  R990=I-990
  R991=I-991
  R992=I-992
  R993=I-993
  R994=I-994
  R995=I-995
  R996=I-996
  R997=I-997
  R998=I-998
  R999=I-999
  R1000=I-1000
  R1001=I-1001
  R1002=I-1002
  R1003=I-1003
  R1004=I-1004
  R1005=I-1005
  R1006=I-1006
  R1007=I-1007
  R1008=I-1008
  R1009=I-1009
  R1010=I-1010
  R1011=I-1011
  R1012=I-1012
  R1013=I-1013
  R1014=I-1014
  R1015=I-1015
  R1016=I-1016
  R1017=I-1017
  R1018=I-1018
  R1019=I-1019
  R1020=I-1020
  R1021=I-1021
  R1022=I-1022
  R1023=I-1023
  R1024=I-1024
  R1025=I-1025
  R1026=I-1026
  R1027=I
```

```

IF (N1.EQ.O)GO TO 706
704 ZH(IT,L2)=ZH(IT,L2)+CA*SV(J2)*TT(IT)*T(J7)*A4 -FM*CO*GT(J5)*TT(IT)PAMB 728
1*TP(J7)/TT(I2)PAMB 729
705 ZH(IT,L3)=ZH(IT,L3)-CA*SV(I2)*TT(IT)*T(J7)*A4PAMB 730
ZH(IT,L3)=ZH(IT,L3)+FM*CO*GT(J5)*TT(IT)*T(J7)/R(J2)PAMB 731
706 ZH(IT,L4)=ZH(IT,L4)+CA*A3-FM*CO/TT(I2)/R(J2)*GT(J5))*TT(IT)*PAMB 732
1TR(J7)*UPAMB 733
71 CONTINUEPAMB 734
70 CONTINUEPAMB 735
30 CONTINUEPAMB 736
RETURNPAMB 737
ENDPAMB 738
PAMB 739
PAMB 740
PAMB 741
PAMB 742
PAMB 743
PAMB 744
PAMB 746
PAMB 745

C *****
R HERE END OF RECORD CARD
E DATA CARDS
E PARAMETER DESCRIPTION
COORH1020001000037 0.343808E+00 01 16.4 MIHZ
E BODY DESCRIPTION
0.000 0.500 0.515 0.515 0.500 0.500 0.515 0.515 0.515 0.525 0.525
0.575 0.600 0.625 0.660 0.710 0.780 0.925 1.050 1.050 1.000
0.980 0.980 1.020 1.085 1.100 1.070 1.040 1.000 0.930 0.850
0.630 0.480 0.490 0.620 0.760 0.850 0.870 0.820 0.700 0.500
0.000
0.000 0.000 0.350 0.760 1.270 1.740 2.180 2.580 3.120 3.680
4.260 4.880 5.500 5.960 6.510 7.060 7.630 8.240 8.700 9.200
9.740 10.270 10.770 11.340 11.820 12.270 12.550 12.820 13.190 13.510
13.920 14.310 14.550 14.700 15.000 15.400 15.700 16.050 16.420 16.680
16.800
E TEST POINT DESCRIPTION
1.75 10.0 0.2
2.25 10.0 0.2
2.75 10.0 0.2
3.75 10.0 0.2
4.75 10.0 0.2
6.25 10.0 0.2
7.75 10.0 0.2
9.25 10.0 0.2
11.25 10.0 0.2
R HERE END OF RECORD CARD
ADD,S164D9, RESULT,NO.
LIST
R HERE END OF INFORMATION CARD
PAMB 767
PAMB 768
PAMB 769
PAMB 770
PAMB 771

```

RESULTS FROM PROGRAM \* P A N B \* (ONLY MODE NN = 1 SHOW HERE)

KK= 8 NP= 41 NPHI= 20 NT= 1 NTEST= 9 NNPHI= 37 BK= .343480E+00 DIREKTE EINSTRALUNG

RM  
0.0000 .5000 .5150 .5150 .5000 .5000 .5150 .5150 .5250 .5250  
.5750 .6000 .6250 .6500 .7150 .7800 .9250 1.0500 1.0500 1.0000  
.9900 .9800 1.0200 1.0850 1.1000 1.0700 1.0400 1.0000 .9300 .8500  
.6300 .4800 .4900 .6200 .7600 .8500 .8700 .8200 .7000 .5000  
0.0000

ZH  
0.0000 0.0000 .3500 .7600 1.2700 1.7400 2.1800 2.5800 3.1200 3.6800  
4.2600 4.8400 5.5000 5.9600 6.5100 7.0500 7.6300 8.2400 8.7000 9.2000  
9.7400 10.2700 10.7700 11.3300 11.8200 12.2700 12.5500 12.8200 13.4900 13.5100  
13.9200 14.3100 14.5500 14.7000 15.0000 15.4000 15.7000 16.0500 16.4200 16.6800  
16.8000

0 SIG 00 MAG S00 SIG MA MAG S00 MODE NN= 1  
80.79 .2021E+00 .4495E+00 .2109E-01 .1703E+00

RIEST= 1.7500 ZTEST= 10.0000 ZTEST= .2000

	EINC, 80.8	ETHETA INC									
ERAD=	.3090E+00	-.44579E+00	EPH=	-.8004E-01	.1336E+00	ETH=	.6659E-01	.1540E+00	EPH=	-.8002E-01	.1305E+00
	ESCAT, 80.8	ETHETA INC									
ERAU=	-.8361E-01	.2103E+00	EPH=	.0599E-02	-.4437E-01	ETH=	.6505E-01	.5339E-01	EPH=	.7253E-02	-.4374E-01
	ETOT, 80.8	ETHETA INC									
ERAD=	.2254E+00	-.2476E+00	EPH=	-.7704E-01	.8621E-01	ETH=	.1324E+00	.2074E+00	EPH=	-.7276E-01	.8679E-01
	EINC, 80.8	EPHI INC									
ERAD=	.8618E-01	-.1406E+00	EPH=	.7427E+00	.4532E+00	ETH=	.4923E+00	-.8031E+00	EPH=	.7418E+00	.4548E+00
	ESCAT, 80.8	EPHI INC									
ERAD=	.1430E-01	-.5590E-01	EPH=	-.2277E+00	-.2110E+00	ETH=	.1088E+00	-.4296E+00	EPH=	-.2358E+00	-.2149E+00
	ETOT, 80.8	EPHI INC									
ERAU=	.1005E+00	-.1965E+00	EPH=	.5150E+00	.2442E+00	ETH=	.6011E+00	-.1233E+01	EPH=	.5360E+00	.2398E+00

<u>RTEST= 2.2500</u> ZTEST= 10.0000 DTTEST= .2000				
EINC, 80.8 ETHETA INC				
ERAD=	.3804E+00	-.5672E+00	EPH=	-.7773E-01
			ETH=	.1268E+00
			EPH=	.1952E+00
			ETH=	-.7771E-01
			EPH=	.1268E+00
ESCAT, 80.8 ETHETA INC				
ERAD=	-.6107E-01	.1547E+00	EPH=	.1077E-01
			ETH=	-.3246E-01
			EPH=	.8401E-02
			ETH=	.1021E-01
			EPH=	-.3246E-01
ETOT, 80.8 ETHETA INC				
ERAD=	.3193E+00	-.4126E+00	EPH=	-.6696E-01
			ETH=	.9334E-01
			EPH=	.6858E-01
			ETH=	-.6750E-01
			EPH=	.9429E-01
EINC, 80.8 EPHI INC				
ERAD=	.1066E+00	-.1739E+00	EPH=	.6739E+00
			ETH=	.4130E+00
			EPH=	.4735E+00
			ETH=	-.7724E+00
			EPH=	.6731E+00
			ETH=	.4127E+00
ESCAT, 80.8 EPHI INC				
ERAD=	.7722E-02	-.5367E-01	EPH=	-.1253E+00
			ETH=	-.1573E+00
			EPH=	.4680E-01
			ETH=	-.3026E+00
			EPH=	-.1282E+00
			ETH=	-.1588E+00
ETOT, 80.8 EPHI INC				
ERAD=	.1143E+00	-.2275E+00	EPH=	.5486E+00
			ETH=	.2557E+00
			EPH=	.5203E+00
			ETH=	-.1075E+01
			EPH=	.5449E+00
			ETH=	.2539E+00
<u>RTEST= 2.7500</u> ZTEST= 10.0000 DTTEST= .2000				
EINC, 80.8 ETHETA INC				
ERAD=	.4403E+00	-.6618E+00	EPH=	-.7490E-01
			ETH=	.1222E+00
			EPH=	.2419E+00
			ETH=	-.7488E-01
			EPH=	.1221E+00
ESCAT, 80.8 ETHETA INC				
ERAD=	-.3916E-01	.1310E+00	EPH=	.1054E-01
			ETH=	-.2561E-01
			EPH=	.2847E-01
			ETH=	-.1487E-01
			EPH=	.1039E-01
			ETH=	-.2565E-01
ETOT, 80.8 ETHETA INC				
ERAD=	.4011E+00	-.5378E+00	EPH=	-.6436E-01
			ETH=	.9657E-01
			EPH=	.5570E-02
			ETH=	.2271E+00
			EPH=	-.6450E-01
			ETH=	.9649E-01
EINC, 80.8 EPHI INC				
ERAD=	.1240E+00	-.2029E+00	EPH=	.5910E+00
			ETH=	.3622E+00
			EPH=	.4510E+00
			ETH=	-.7356E+00
			EPH=	.5903E+00
			ETH=	.3619E+00
ESCAT, 80.8 EPHI INC				
ERAD=	.2830E-02	-.5085E-01	EPH=	-.8025E-01
			ETH=	-.1235E+00
			EPH=	.1183E-01
			ETH=	-.2254E+00
			EPH=	-.8149E-01
			ETH=	-.1301E+00
ETOT, 80.8 EPHI INC				
ERAD=	.1269E+00	-.2532E+00	EPH=	.5107E+00
			ETH=	.6327E+00
			EPH=	.4628E+00
			ETH=	-.9610E+00
			EPH=	.5088E+00
			ETH=	.2318E+00

<u>RTEST= 3.7500</u>				<u>ZTEST= 10.0000</u>				<u>QTEST= .2000</u>			
EINC, 80.8 ETHETA INC											
ERAD=	.5201E+00	-.7989E+00	EPH=	-.6786E-01	.1107E+00	ETH=	-.1280E+00	.3403E+00	EPH=	-.6785E-01	.1107E+00
ESCAT, 80.8 ETHETA INC											
ERAD=	-.7614E-02	.1009E+00	EPH=	.0189E-02	-.1848E-01	ETH=	.1096E-01	-.3195E-01	EPH=	.0230E-02	-.1849E-01
ETOT, 80.8 ETHETA INC											
ERAD=	.5125E+00	-.6980E+00	EPH=	-.5967E-01	.9223E-01	ETH=	-.1171E+00	.3084E+00	EPH=	-.5962E-01	.9219E-01
EINC, 80.8 EPHI INC											
ERAD=	.1488E+00	-.2428E+00	EPH=	.3711E+00	.2396E+00	ETH=	.3968E+00	-.6473E+00	EPH=	.3906E+00	.2396E+00
ESCAT, 80.8 EPHI INC											
ERAD=	-.6382E-02	-.4475E-01	EPH=	-.5228E-01	-.9951E-01	ETH=	-.2376E-01	-.1340E+00	EPH=	-.5255E-01	-.9966E-01
ETOT, 80.8 EPHI INC											
ERAD=	.1424E+00	-.2875E+00	EPH=	.3788E+00	.1401E+00	ETH=	.3731E+00	-.7813E+00	EPH=	.3781E+00	.1400E+00
<u>RTEST= 4.7500</u>											
<u>ZTEST= 10.0000</u>											
<u>QTEST= .2000</u>											
EINC, 80.8 ETHETA INC											
ERAD=	.5431E+00	-.8603E+00	EPH=	-.5731E-01	.9677E-01	ETH=	-.2291E+00	.4262E+00	EPH=	-.5932E-01	.9675E-01
ESCAT, 80.8 ETHETA INC											
ERAD=	.1356E-01	.7835E-01	EPH=	.5486E-02	-.1519E-01	ETH=	-.1875E-02	-.3572E-01	EPH=	.5552E-02	-.1520E-01
ETOT, 80.8 ETHETA INC											
ERAD=	.5566E+00	-.7825E+00	EPH=	-.5782E-01	.8153E-01	ETH=	-.2310E+00	.3905E+00	EPH=	-.5377E-01	.6155E-01
EINC, 80.8 EPHI INC											
ERAD=	.1589E+00	-.2593E+00	EPH=	.1619E+00	.9905E-01	ETH=	.3347E+00	-.5458E+00	EPH=	.1517E+00	.9931E-01
ESCAT, 80.8 EPHI INC											
ERAD=	-.1447E-01	-.3737E-01	EPH=	-.5175E-01	-.7912E-01	ETH=	-.3769E-01	-.8122E-01	EPH=	-.5179E-01	-.7916E-01
ETOT, 80.8 EPHI INC											
ERAD=	.1445E+00	-.2367E+00	EPH=	.1102E+00	.4393E-01	ETH=	.2970E+00	-.6271E+00	EPH=	.1099E+00	.2015E-01

<u>RTEST= 6.2500</u>				<u>ZTEST= 10.0000</u>	<u>OTEST= .2000</u>
EINC, 80.8 ETHETA INC					
ERAU=	.4791E+00	-.9178E+00	CPH=	-.44470E-01	.7295E-01 ETH= -.3352E+00 EPH= -.4473E-01 .7294E-01
ESCAT, 80.8 ETHETA INC					
ERAU=	.3226E-01	.4930E-01	EPH=	.1649E-02	-.1266E-01 ETH= -.1819E-01 .3144E-01 EPH= .1709E-02 -.1269E-01
ETOT, 80.8 ETHETA INC					
ERAU=	.5114E+00	-.7685E+00	EPH=	-.4305E-01	.6027E-01 ETH= -.3534E+00 .4575E+00 EPH= -.4302E-01 .6025E-01
EINC, 80.8 EPHI INC					
ERAU=	.1480E+00	-.2415E+00	EPH=	-.1398E+00	-.1166E+00 ETH= .2369E+00 -.3863E+00 EPH= -.1398E+00 -.1161E+00
ESCAT, 80.8 EPHI INC					
ERAU=	-.2269E-01	-.2444E-01	EPH=	-.6023E-01	-.5811E-01 ETH= -.4030E-01 .3449E-01 EPH= -.6020E-01 -.5012E-01
ETOT, 80.8 EPHI INC					
ERAU=	.1253E+00	-.2659E+00	EPH=	-.2500E+00	-.1667E+00 ETH= .1966E+00 -.4205E+00 EPH= -.2500E+00 -.1663E+00
<u>RTEST= 7.7500</u>					
<u>ZTEST= 10.0000</u>					
<u>OTEST= .2000</u>					
EINC, 80.8 ETHETA INC					
ERAU=	.3296E+00	-.6451E+00	CPH=	-.2949E-01	.4312E-01 ETH= -.3542E+00 .4393E+00 EPH= -.2951E-01 .4810E-01
ESCAT, 80.8 ETHETA INC					
ERAU=	.3873E-01	.2400E-01	EPH=	-.1955E-02	-.1562E-01 ETH= -.2957E-01 .1973E-01 EPH= -.1309E-02 -.1064E-01
ETOT, 80.8 ETHETA INC					
ERAU=	.3683E+00	-.6211E+00	EPH=	-.3133E-01	.3749E-01 ETH= -.3837E+00 .4195E+00 EPH= -.3132E-01 .3746E-01
EINC, 80.8 EPHI INC					
ERAU=	.1128E+00	-.1841E+00	EPH=	-.4972E+00	-.2388E+00 ETH= .1457E+00 -.2375E+00 EPH= -.4971E+00 -.2384E+00
ESCAT, 80.8 EPHI INC					
ERAU=	-.2544E-01	-.1122E-01	EPH=	-.0401E-01	-.2155E-01 ETH= -.3289E-01 .7642E-02 EPH= -.6398E-01 -.2056E-01
ETOT, 80.8 EPHI INC					
ERAU=	.8730E-01	-.1953E+00	EPH=	-.5512E+00	-.3194E+00 ETH= .1126E+00 -.2445E+00 EPH= -.5511E+00 -.3190E+00

<u>RTESI= 9.2500</u>				ZTEST= 10.0000	OTEST= .2000	
EINC, 80.8				ETHETA INC		
ERAD=	.1440E+00	-.1390E+00	EPH=	-.1530E-01	.2498E-01	ETH= -.2799E+00 .2791E+00 EPH= -.1532E-01 .2497E-01
ESCAT, 80.8				ETHETA INC		
ERAD=	.3604E-01	.3607E-02	EPH=	-.4735E-02	-.8093E-02	ETH= -.3385E-01 -.4286E-02 EPH= -.4706E-02 -.8120E-02
ETOT, 80.8				ETHETA INC		
ERAD=	.1800E+00	-.3954E+00	EPH=	-.2003E-01	.1699E-01	ETH= -.3137E+00 .2748E+00 EPH= -.2303E-01 .1689E-01
EINC, 80.8				EPHI INC		
ERAD=	.6487E-01	-.1099E+00	EPH=	-.6715E+00	-.4417E+00	ETH= .7025E-01 -.1145E+00 EPH= -.6715E+00 -.4116E+00
ESCAT, 80.8				EPHI INC		
ERAD=	-.2319E-01	.2557E-03	EPH=	-.5847E-01	.6708E-02	ETH= -.2193E-01 .6349E-02 EPH= -.5845E-01 .6702E-02
ETOT, 80.8				EPHI INC		
ERAD=	.4168E-01	-.1057E+00	EPH=	-.7300E+00	-.4050E+00	ETH= .4632E-01 -.1081E+00 EPH= -.7300E+00 -.4049E+00
<u>RTESI= 11.2500</u>				ZTEST= 10.0000	OTEST= .2000	
EINC, 80.8				ETHETA INC		
ERAD=	-.7773E-01	-.5859E-01	EPH=	-.3132E-03	.5290E-03	ETH= -.7894E-01 -.3611E-01 EPH= -.3266E-03 .5146E-03
ESCAT, 80.8				ETHETA INC		
ERAD=	.2379E-01	-.1381E-01	EPH=	-.6370E-02	-.3909E-02	ETH= -.2787E-01 .1530E-01 EPH= -.6963E-02 -.3937E-02
ETOT, 80.8				ETHETA INC		
ERAD=	-.5394E-01	-.7240E-01	EPH=	-.7283E-02	-.3380E-02	ETH= -.1068E+00 -.2081E-01 EPH= -.7289E-02 -.3422E-02
EINC, 80.8				EPHI INC		
ERAD=	.1462E-02	-.2470E-02	EPH=	-.6893E+00	-.4225E+00	ETH= .1355E-02 -.2135E-02 EPH= -.6893E+00 -.4226E+00
ESCAT, 80.8				EPHI INC		
ERAD=	-.1515E-01	.1044E-01	EPH=	-.3801E-01	.3337E-01	ETH= -.7785E-02 .1231E-01 EPH= -.3900E-01 .3306E-01
ETOT, 80.8				EPHI INC		
ERAD=	-.1368E-01	.7972E-02	EPH=	-.7273E+00	-.3994E+00	ETH= -.6430E-02 .1018E-01 EPH= -.7273E+00 -.3895E+00



# EINFLUSS DER ANZAHL BERUECKSICHTIGTEN MOOI AUF E TOT

FREQUENZ = 164.0 MHZ EINSTRALHUNG : WINKEL THETA = 80.8 GRAD POLARISATION : VERTIKAL  
ANTENNENHOEHE = 1.00 METER

## DIREKTE EINSTRALHUNG

TESTSEGMENT NR	1	ABSTAND DIST = .09 METER	ROT.WINKEL PHI = 0. GRAD			
MODE 0 BIS 0	1	ERTOT = .1792E+00	EPLOT = 0.	0.	ERTOT = .1321E+01	.4990E+00
MODE 0 BIS 1	2	ERTOT = .4045E+00	EPLOT = 0.	0.	ERTOT = .1454E+01	.7064E+00
MODE 0 BIS 2	3	ERTOT = .4643E+00	EPLOT = 0.	0.	ERTOT = .1418E+01	.7434E+00
MODE 0 BIS 3	4	ERTOT = .4591E+00	EPLOT = 0.	0.	ERTOT = .1412E+01	.7385E+00
MODE 0 BIS 4	5	ERTOT = .4587E+00	EPLOT = 0.	0.	ERTOT = .1413E+01	.7380E+00
MODE 0 BIS 5	6	ERTOT = .4587E+00	EPLOT = 0.	0.	ERTOT = .1413E+01	.7380E+00
MODE 0 BIS 6	7	ERTOT = .4587E+00	EPLOT = 0.	0.	ERTOT = .1413E+01	.7380E+00
MODE 0 BIS 7	8	ERTOT = .4587E+00	EPLOT = 0.	0.	ERTOT = .1413E+01	.7380E+00
TESTSEGMENT NR	1	ABSTAND DIST = .09 METER	ROT.WINKEL PHI = 90. GRAD			
MODE 0 BIS 0	1	ERTOT = .1792E+00	EPLOT = 0.	0.	ERTOT = .1321E+01	.4990E+00
MODE 0 BIS 1	2	ERTOT = .1792E+00	EPLOT = 0.	0.	ERTOT = .1321E+01	.4990E+00
MODE 0 BIS 2	3	ERTOT = .1194E+00	EPLOT = -.8650E-01	-.7160E-01	ERTOT = .1357E+01	.4620E+00
MODE 0 BIS 3	4	ERTOT = .1194E+00	EPLOT = -.9212E-01	-.7513E-01	ERTOT = .1357E+01	.4615E+00
MODE 0 BIS 4	5	ERTOT = .1189E+00	EPLOT = -.9212E-01	-.7513E-01	ERTOT = .1357E+01	.4615E+00
MODE 0 BIS 5	6	ERTOT = .1189E+00	EPLOT = -.9212E-01	-.7513E-01	ERTOT = .1357E+01	.4615E+00
MODE 0 BIS 6	7	ERTOT = .1189E+00	EPLOT = -.9212E-01	-.7513E-01	ERTOT = .1357E+01	.4615E+00
MODE 0 BIS 7	8	ERTOT = .1189E+00	EPLOT = -.9212E-01	-.7513E-01	ERTOT = .1357E+01	.4615E+00
TESTSEGMENT NR	1	ABSTAND DIST = .09 METER	ROT.WINKEL PHI = 180. GRAD			
MODE 0 BIS 0	1	ERTOT = .1792E+00	EPLOT = 0.	0.	ERTOT = .1321E+01	.4990E+00
MODE 0 BIS 1	2	ERTOT = .4623E+00	EPLOT = .2996E-07	.2480E-07	ERTOT = .1189E+01	.2517E+00
MODE 0 BIS 2	3	ERTOT = .1355E+00	EPLOT = .4450E-07	.1170E-09	ERTOT = .1156E+01	.3267E+00
MODE 0 BIS 3	4	ERTOT = .1876E+00	EPLOT = .3846E-07	-.3554E-08	ERTOT = .1156E+01	.3306E+00
MODE 0 BIS 4	5	ERTOT = .1830E+00	EPLOT = .3846E-07	-.2753E-08	ERTOT = .1156E+01	.3306E+00
MODE 0 BIS 5	6	ERTOT = .1827E+00	EPLOT = .3823E-07	-.2706E-08	ERTOT = .1156E+01	.3306E+00
MODE 0 BIS 6	7	ERTOT = .1827E+00	EPLOT = .3824E-07	-.2712E-08	ERTOT = .1156E+01	.3306E+00
MODE 0 BIS 7	8	ERTOT = .1827E+00	EPLOT = .3824E-07	-.2712E-08	ERTOT = .1156E+01	.3306E+00

FOR THE TESTSEGMENTS NR. 2 TO 9 ONLY THE VALUES FOR PHI = 1800 ARE SHOWN HERE



TESTSEGMENT NR 6 ABSTAND DIST = .57 METER ROT.WINKEL PHI = 180. GRAD

MODE	0	BIS	0	1	ERTOT	EPLOT	0.	1.	ERTOT	EPLOT
MODE 0 BIS 0	1	ERTOT	=	-1811E+00	-1547E+00	EPLOT	=	0.	1.	ERTOT
MODE 0 BIS 1	1	ERTOT	=	-1330E+00	-4138E+00	EPLOT	=	-2087E-07	1.	1491E-07
MODE 0 BIS 2	1	ERTOT	=	-1904E+00	-7752E+00	EPLOT	=	-6228E-07	0.	-5259E-07
MODE 0 BIS 3	1	ERTOT	=	-3447E+00	-7782E+00	EPLOT	=	-2654E-08	-0.914E-07	EPLOT
MODE 0 BIS 4	1	ERTOT	=	-2913E+00	-5315E+00	EPLOT	=	-1544E-07	-0.933E-07	EPLOT
MODE 0 BIS 5	1	ERTOT	=	-2803E+00	-5429E+00	EPLOT	=	-5331E-08	-0.529E-07	EPLOT
MODE 0 BIS 6	1	ERTOT	=	-2823E+00	-5450E+00	EPLOT	=	-3700E-08	-0.556E-07	EPLOT
MODE 0 BIS 7	1	ERTOT	=	-2826E+00	-5447E+00	EPLOT	=	-4267E-08	-0.560E-07	EPLOT
MODE 0 BIS 0	1	ERTOT	=	-1811E+00	-1547E+00	EPLOT	=	0.	1.	ERTOT
MODE 0 BIS 1	1	ERTOT	=	-1330E+00	-4138E+00	EPLOT	=	-2087E-07	1.	1491E-07
MODE 0 BIS 2	1	ERTOT	=	-1904E+00	-7752E+00	EPLOT	=	-6228E-07	0.	-5259E-07
MODE 0 BIS 3	1	ERTOT	=	-3447E+00	-7782E+00	EPLOT	=	-2654E-08	-0.914E-07	EPLOT
MODE 0 BIS 4	1	ERTOT	=	-2913E+00	-5315E+00	EPLOT	=	-1544E-07	-0.933E-07	EPLOT
MODE 0 BIS 5	1	ERTOT	=	-2803E+00	-5429E+00	EPLOT	=	-5331E-08	-0.529E-07	EPLOT
MODE 0 BIS 6	1	ERTOT	=	-2823E+00	-5450E+00	EPLOT	=	-3700E-08	-0.556E-07	EPLOT
MODE 0 BIS 7	1	ERTOT	=	-2826E+00	-5447E+00	EPLOT	=	-4267E-08	-0.560E-07	EPLOT

TESTSEGMENT NR 7 ABSTAND DIST = .58 METER ROT.WINKEL PHI = 180. GRAD

MODE	0	BIS	0	1	ERTOT	EPLOT	0.	1.	ERTOT	EPLOT
MODE 0 BIS 0	1	ERTOT	=	-1741E+00	-2525E+00	EPLOT	=	0.	0.	ERTOT
MODE 0 BIS 1	1	ERTOT	=	-1194E+00	-3687E+00	EPLOT	=	-1298E-07	1.	1085E-07
MODE 0 BIS 2	1	ERTOT	=	-532E+00	-7642E+00	EPLOT	=	-5374E-07	0.	-556E-07
MODE 0 BIS 3	1	ERTOT	=	-5357E+00	-4636E+00	EPLOT	=	-2443E-07	-0.103E-06	EPLOT
MODE 0 BIS 4	1	ERTOT	=	-5311E+00	-4745E+00	EPLOT	=	-5483E-07	-0.512E-07	EPLOT
MODE 0 BIS 5	1	ERTOT	=	-5044E+00	-4827E+00	EPLOT	=	-3294E-07	-0.398E-07	EPLOT
MODE 0 BIS 6	1	ERTOT	=	-5106E+00	-4092E+00	EPLOT	=	-1285E-07	-0.470E-07	EPLOT
MODE 0 BIS 7	1	ERTOT	=	-5119E+00	-4080E+00	EPLOT	=	-3042E-07	-0.462E-07	EPLOT
MODE 0 BIS 0	1	ERTOT	=	-1741E+00	-2525E+00	EPLOT	=	0.	0.	ERTOT
MODE 0 BIS 1	1	ERTOT	=	-1194E+00	-3687E+00	EPLOT	=	-1298E-07	1.	1085E-07
MODE 0 BIS 2	1	ERTOT	=	-532E+00	-7642E+00	EPLOT	=	-5374E-07	0.	-556E-07
MODE 0 BIS 3	1	ERTOT	=	-5357E+00	-4636E+00	EPLOT	=	-2443E-07	-0.103E-06	EPLOT
MODE 0 BIS 4	1	ERTOT	=	-5311E+00	-4745E+00	EPLOT	=	-5483E-07	-0.512E-07	EPLOT
MODE 0 BIS 5	1	ERTOT	=	-5044E+00	-4827E+00	EPLOT	=	-3294E-07	-0.398E-07	EPLOT
MODE 0 BIS 6	1	ERTOT	=	-5106E+00	-4092E+00	EPLOT	=	-1285E-07	-0.470E-07	EPLOT
MODE 0 BIS 7	1	ERTOT	=	-5119E+00	-4080E+00	EPLOT	=	-3042E-07	-0.462E-07	EPLOT

TESTSEGMENT NR 8 ABSTAND DIST = .87 METER ROT.WINKEL PHI = 180. GRAD

MODE	0	BIS	0	1	ERTOT	EPLOT	0.	1.	ERTOT	EPLOT
MODE 0 BIS 0	1	ERTOT	=	-1434E+00	-1429E+00	EPLOT	=	0.	0.	ERTOT
MODE 0 BIS 1	1	ERTOT	=	-3460E+00	-2525E+00	EPLOT	=	-5842E-08	0.	-693E-08
MODE 0 BIS 2	1	ERTOT	=	-3702E+00	-6162E+00	EPLOT	=	-4172E-07	-0.515E-07	EPLOT
MODE 0 BIS 3	1	ERTOT	=	-3531E+00	-8244E+00	EPLOT	=	-4850E-07	-0.106E-06	EPLOT
MODE 0 BIS 4	1	ERTOT	=	-3626E+00	-3421E+00	EPLOT	=	-9305E-07	-0.240E-07	EPLOT
MODE 0 BIS 5	1	ERTOT	=	-5309E+00	-1405E+00	EPLOT	=	-5401E-07	-0.1027E-07	EPLOT
MODE 0 BIS 6	1	ERTOT	=	-5460E+00	-1559E+00	EPLOT	=	-4441E-07	-0.259E-07	EPLOT
MODE 0 BIS 7	1	ERTOT	=	-5499E+00	-1525E+00	EPLOT	=	-4494E-07	-0.290E-07	EPLOT
MODE 0 BIS 0	1	ERTOT	=	-1434E+00	-1429E+00	EPLOT	=	0.	0.	ERTOT
MODE 0 BIS 1	1	ERTOT	=	-3460E+00	-2525E+00	EPLOT	=	-5842E-08	0.	-693E-08
MODE 0 BIS 2	1	ERTOT	=	-3702E+00	-6162E+00	EPLOT	=	-4172E-07	-0.515E-07	EPLOT
MODE 0 BIS 3	1	ERTOT	=	-3531E+00	-8244E+00	EPLOT	=	-4850E-07	-0.106E-06	EPLOT
MODE 0 BIS 4	1	ERTOT	=	-3626E+00	-3421E+00	EPLOT	=	-9305E-07	-0.240E-07	EPLOT
MODE 0 BIS 5	1	ERTOT	=	-5309E+00	-1405E+00	EPLOT	=	-5401E-07	-0.1027E-07	EPLOT
MODE 0 BIS 6	1	ERTOT	=	-5460E+00	-1559E+00	EPLOT	=	-4441E-07	-0.259E-07	EPLOT
MODE 0 BIS 7	1	ERTOT	=	-5499E+00	-1525E+00	EPLOT	=	-4494E-07	-0.290E-07	EPLOT

TESTSEGMENT NR 9 ABSTAND DIST = 1.07 METER ROT.WINKEL PHI = 180. GRAD

MODE	0	BIS	0	1	ERTOT	EPLOT	0.	1.	ERTOT	EPLOT
MODE 0 BIS 0	1	ERTOT	=	-3968E+00	-2788E+00	EPLOT	=	0.	0.	ERTOT
MODE 0 BIS 1	1	ERTOT	=	-1436E+00	-4460E+00	EPLOT	=	-1178E-08	0.	-252E-08
MODE 0 BIS 2	1	ERTOT	=	-6234E+00	-2813E+00	EPLOT	=	-2352E-07	-0.377E-07	EPLOT
MODE 0 BIS 3	1	ERTOT	=	-3262E+00	-1776E+00	EPLOT	=	-1697E-07	-0.950E-07	EPLOT
MODE 0 BIS 4	1	ERTOT	=	-5637E+00	-7824E+00	EPLOT	=	-1335E-06	-5.26E-08	EPLOT
MODE 0 BIS 5	1	ERTOT	=	-5645E+00	-2712E+00	EPLOT	=	-6244E-07	-0.475E-07	EPLOT
MODE 0 BIS 6	1	ERTOT	=	-5419E+00	-2342E+00	EPLOT	=	-4137E-07	-0.127E-07	EPLOT
MODE 0 BIS 7	1	ERTOT	=	-5134E+00	-2347E+00	EPLOT	=	-5496E-07	-0.421E-08	EPLOT
MODE 0 BIS 0	1	ERTOT	=	-3968E+00	-2788E+00	EPLOT	=	0.	0.	ERTOT
MODE 0 BIS 1	1	ERTOT	=	-1436E+00	-4460E+00	EPLOT	=	-1178E-08	0.	-252E-08
MODE 0 BIS 2	1	ERTOT	=	-6234E+00	-2813E+00	EPLOT	=	-2352E-07	-0.377E-07	EPLOT
MODE 0 BIS 3	1	ERTOT	=	-3262E+00	-1776E+00	EPLOT	=	-1697E-07	-0.950E-07	EPLOT
MODE 0 BIS 4	1	ERTOT	=	-5637E+00	-7824E+00	EPLOT	=	-1335E-06	-5.26E-08	EPLOT
MODE 0 BIS 5	1	ERTOT	=	-5645E+00	-2712E+00	EPLOT	=	-6244E-07	-0.475E-07	EPLOT
MODE 0 BIS 6	1	ERTOT	=	-5419E+00	-2342E+00	EPLOT	=	-4137E-07	-0.127E-07	EPLOT
MODE 0 BIS 7	1	ERTOT	=	-5134E+00	-2347E+00	EPLOT	=	-5496E-07	-0.421E-08	EPLOT

# A Z I M U T A L   S T R A H L U N G S   D I A G R A M M

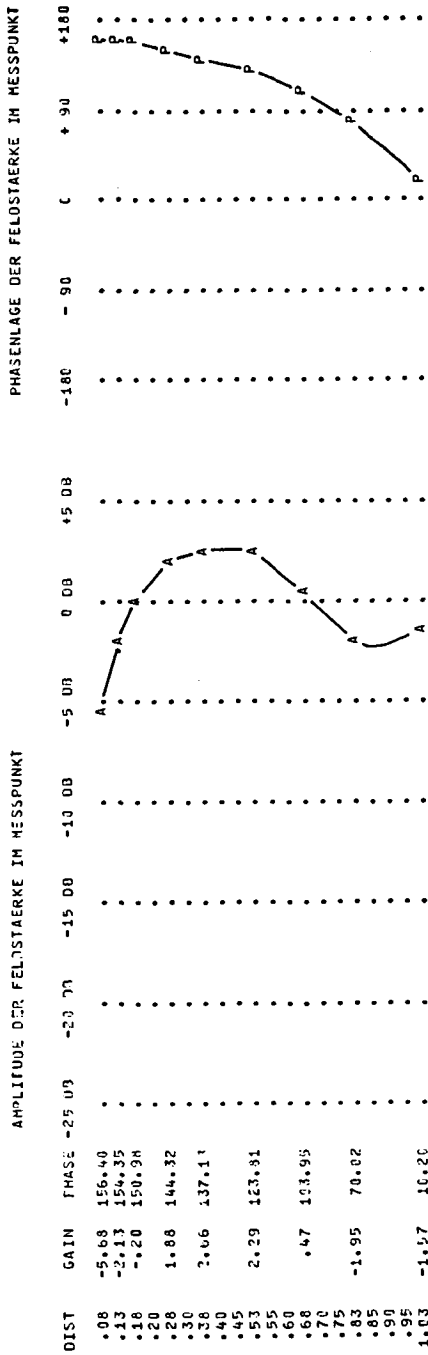
F R E Q U E N Z = 164.0 M H Z  
E I N S T R A H L U N G : W I N K E L   T H E T A = 80.8 G R A D  
P O L A R I S A T I O N = V E R T I K A L  
M E S S A N T E N N E : P O L A R I S A T I O N = V E R T I K A L

K O E R P E R : V E R T I K A L E R   P O T . S Y N . H E N S C H I M M O D .   M E S S A N T E N N E : P U N K T A N T E N N E   A U F  
D U R C H M E S S E R = .20 M E T E R  
A C H S E N L A E N G E = 1.65 M E T E R  
P H I   U N D   D I S T   V A R .

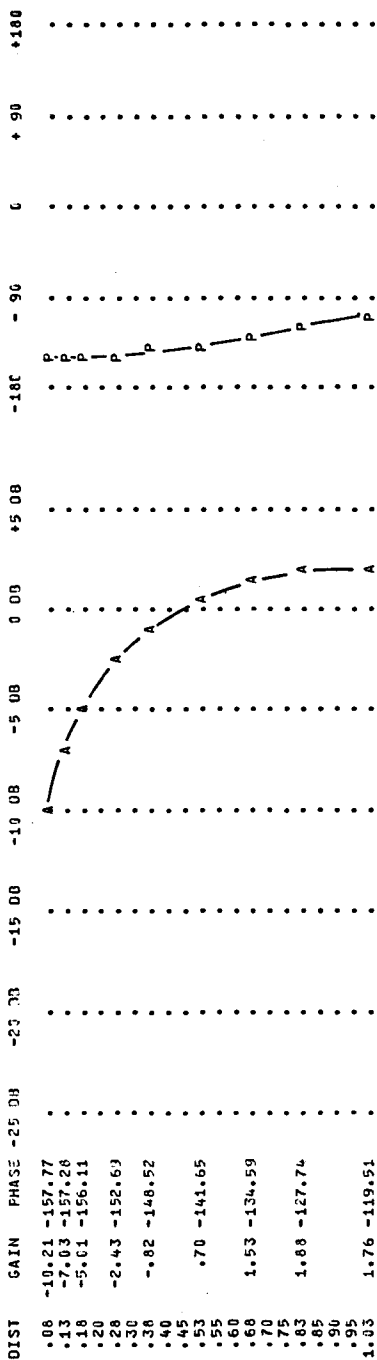
## D I R E K T E   E I N S T R A H L U N G

R O T A T I O N S W I N K E L   P H I = 0.00 G R A D

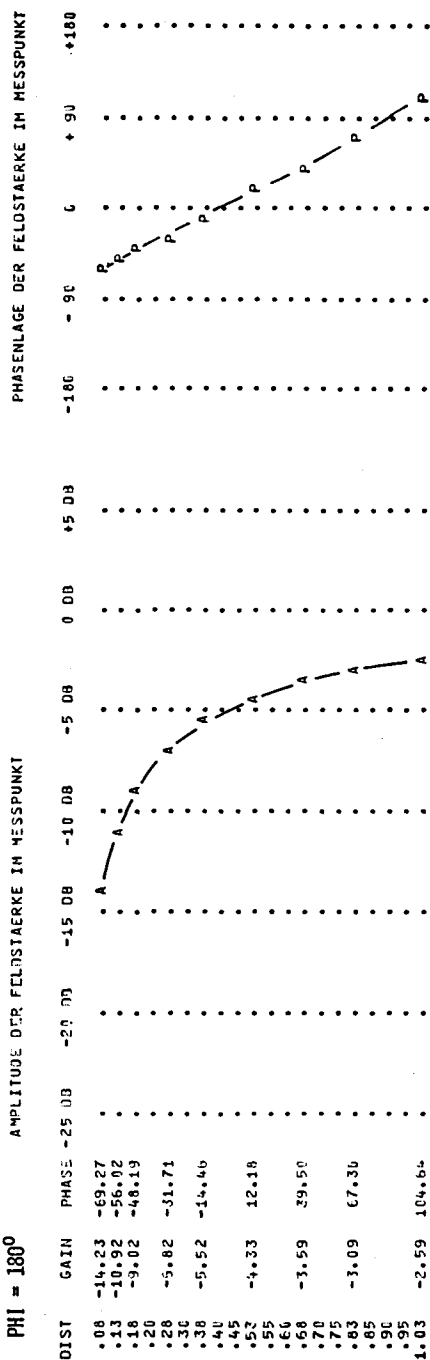
D I S T : A B S T A N D   D E R   M E S S A N T E N N E   V O N   D E R   K O R P E R O B E R F L A E C H E   I N   M E T E R  
P H I : H O R I Z O N T A L E R   R O T A T I O N S W I N K E L   I N   G R A D ; 180 G R A D = S C H A T T E N  
G A I N : F E L D S T A E R K E   B E I   D E R   M E S S A N T E N N E   I N   D B ; 0.00 = M A X . F R E E S P A C E  
P H A S E : P H A S E   D E S   M E S S P U N K T E S   I N   D B



I N   T H I S   P R O G R A M   T H E   V A L U E S   A R E   A V A I L A B L E   F O R   P H I = 5.10.15.....180° (A1 POLARISATION VERT/HOR/RAD)  
F O R   A N   I N C I D E N T   W A V E   W I T H   T H E T A (=V E R T I C A L)   A N D   P H I (=H O R I Z O N T A L)   P O L A R I S A T I O N  
S H O W N   A R E   H E R E   O N L Y   A1   V E R T I C A L / A2   V E R T I C A L   F O R   P H I = 0°   A N D   90°,   R E S P .   180°   (N E X T   P A G E)



PHI = 180°



16.2.4. PROGRAM PANC, DATA CARDS FOR TEST BODIES FZYL, MANMOD 1 AND  
MANMOD 2, FIELD HOMOGENEITY RESULTS WITH FZYL

---

```

E PROGRAM *PANC*, COMPUTATION OF THE HOMOGENEITY OF THE FIELDS
E *****
E CONTROL CARDS
PAN, 3571, CM70000, CTS.
FTN.
ATTACH HOMOG.
CALL, F10005, F=HOMOG,B=DISK.
LFO.
B HERE END OF RECORD CARD
C *****
C PROGRAM PANC (INPUT, OUTPUT, DISK, TAPE1=INPUT, TAPE3=OUTPUT,
C *****
C *****
C THIS PROGRAM IS AN EXTENSION TO PROGRAM PANC AND COMPUTES THE FIELD
C HOMOGENEITY ALONG A DIPOLE ANTENNA (2H=0.1M) ORIENTED (P1) VERTICALLY, PANC
C HORIZONTALLY OR RADIIALLY SPACED (DNT=0,M) FROM THE BODY SURFACE
C AND FOR BOTH INCIDENT FIELD POLARIZATIONS (P2).
C THE OUTPUT IS A TABLE WITH FOLLOWING INFORMATIONS:
C P1: HORIZONTAL ROTATION ANGLE (AZIMUTHAL ANGLE)
C P2: HORIZONTAL ROTATION ANGLE (AZIMUTHAL ANGLE)
C PHASE CENTER: FIELD COMPONENT AT THE CENTER POINT OF THE ANTENNA
C PHASE CENTER: PHASE OF THE FIELD COMPONENT AT THE CENTER POINT
C MEAN ERROR: LOGARITHMIC DIFFERENCE (DELTA U) BETWEEN THE INDICED
C VOLTAGE (CENTER E * 2H) AND THE ACTUAL INDUCED VOLTAGE ( INTEGRAL E
C FROM -H TO +H)
C MAXIMUM GAINVAR: LOGARITHMIC DIFFERENCE (SMALL DELTA E) BETWEEN THE
C FIELDS AT THE ENDS OF THE DIPOLE ANTENNA.
C MAXIMUM PHASEVAR: DIFFERENCE (SMALL DELTA PHI) BETWEEN THE PHASES
C OF THE FIELDS AT THE ENDS OF THE DIPOLE ANTENNA.
C PRIOR TO THE RUN OF THIS PROGRAM PANC THE FOLLOWING COMPUTATIONS
C ARE NEEDED:
C Y-MATRICES WITH PROGRAM HARRA (FZYL DATA SET, MODEL FREQUENCY 10 MHZ,
C MODI 0 TO 7)
C FIELD POINTS WITH PROGRAM PANC (FZYL DATA SET, MODEL FREQUENCY 10 MHZ,
C KX=8, RUN=1, NTEST=5, TESTSEQUENTS 2.25 10.0 0.2 / 1.75 10.0 0.2 /
C 2.75 10.0 0.2 / 2.25 9.5 0.2 / 2.25 10.5 0.2)
C THE RESULTS OF PANC SHOULD BE STORED IN THE FILE F10005 IN THE COLLECTPANC
C FILE HOMOG.
C *****
C *****
COMPLEX STV(185),SVH(185),SYS(185)
REAL F,DA,DU,H0,X1
INTEGER TEXT(2),ROL,NPHI
COMPLEX PP
DIMENSION DI(5)
READ(1,10) F
10 FORMAT(2X,F5.1)
DA=1.8 * DI(1)/0.1 * DU=0.25 * H0=1.0 * X1=80.8
NPHI=37 * NST=185
PI=57.141593
CS= (DU/2.-DI(1))/PI/(NPHI-1)
FAC=DI(1)/(4.*CS)

```

```

PP= CMPLX(1.0E-32,1.0E-32)
QQ=1.0E-32 * Q=10000.
PR=180./PI
TEXT(1)=10HORIZONTAL
TEXT(2)=10HORIZONTAL
REWIND 6
DO 701 POL=1,2
READ(6)(SVH(I),I=1,NST)
READ(6)(SVH(I),I=1,NST)
READ(6)(SVH(I),I=1,NST)
READ(6)(SVH(I),I=1,NST)
520 FORMAT(1H1,X,
1 1F A Z I M U T H A L R A D I A T I O N P A T T E R N F R E Q U E
PANC 52 PANC 53 PANC 54 PANC 55 PANC 56 PANC 57 PANC 58 PANC 59 PANC 60 PANC 61 PANC 62 PANC 63 PANC 64 PANC 65 PANC 66 PANC 67 PANC 68 PANC 69 PANC 70 PANC 71 PANC 72 PANC 73 PANC 74 PANC 75 PANC 76 PANC 77 PANC 78 PANC 79 PANC 80 PANC 81 PANC 82 PANC 83 PANC 84 PANC 85 PANC 86 PANC 87 PANC 88 PANC 89 PANC 90 PANC 91 PANC 92 PANC 93 PANC 94 PANC 95 PANC 96 PANC 97 PANC 98 PANC 99 PANC 100 PANC 101 PANC 102
2N C Y4,I4,* M H Z4,/H0,1X,HOMOGENEITY CHECK OF THE FIELD ALONG APANC
3 0.1 METER DIPOLE ANTENNA*/H0,1X,*TESTBODY: ROT.SYM.CYLINDER* 8X,
4FIELD POINT* 7X,*INCIDENT WAVE*/H, 11X,
5AXIAL LENGTH =,F5.2,* M DAT =,F4.2,* M* 7X,*POLAR. =,R10/HIPANC
6,11X,*DIAMETER =,F5.2,* M HB =,F4.2,* M* 7X,*THETA =,
7F5.1 * DEG*/)
521 FORMAT(1H0,1X,5X,
1VERTICAL POLARIZED ANTENNA*,13X,*RADIAL POLARIZED ANTENNA*/H0,1XPANC
2,*PHI GAIN PHASE MEAN MAXIMUM MAXIMUM* 4X,
3,*PHI GAIN PHASE MEAN MAXIMUM MAXIMUM*/H, 1X,5X,
4,*CENTER CENTER ERROR GAINVAR PHASEVAR* 3X,
5,*CENTER CENTER ERROR GAINVAR PHASEVAR*)
522 FORMAT(1H0,1X,5X,
1HORIZONTAL POLARIZED ANTENNA*,11X,*RADIAL POLARIZED ANTENNA*/H0,1XPANC
21X,*PHI GAIN PHASE MEAN MAXIMUM MAXIMUM* 4X,
3,*PHI GAIN PHASE MEAN MAXIMUM MAXIMUM*/H, 1X,5X,
4,*CENTER CENTER ERROR GAINVAR PHASEVAR* 3X,
5,*CENTER CENTER ERROR GAINVAR PHASEVAR*)
522 FORMAT(1H, 1X,
1DEG 10B DEG DB DB DEG* 8X,
2 40B DEG DB DB DEG* 8X,
3 40B DEG DB DB DEG* 8X,
4 40B DEG DB DB DEG* 8X,
5 40B DEG DB DB DEG* 8X,
523 FORMAT(1H, 1X,13,2X,F5.1,1X,F6.1,2X,F5.2,1X,F5.1,1X,F6.1,1X,
F5.1,1X,F6.1,2X,F5.2,1X,F5.1,1X,F6.1)
1 WRITE(3,520) IFIX(F),DA,DI(1),TEXT(POL),DU,H0,X1
IF (POL.EQ.2) GOTO 1
WRITE(3,521) * GOTO 2
1 WRITE(3,524) * GOTO 2
2 CONTINUE
WRITE(3,522)
DO 700 J=1,NPHI
IH1=J-2 * IH2=J+2 * NC=NPHI-1
IF (J.EQ.1) IH1=J+2 * IF (J.EQ.2) IH1=J
IF (J.EQ.NC) IH2=J * IF (J.EQ.NPHI) IH2=J-2
ITE1 = J
ITE2 = J+NPHI
ITE3 = J+NPHI*2
ITE4 = J+NPHI*3
ITE5 = J+NPHI*4
JJJ = (J*5)-5

```





AZIMUTHAL RADIATION PATTERN FREQUENCY 65 MHZ											
HOMOGENEITY CHECK OF THE FIELD ALONG A 0.1 METER DIPOLE ANTENNA											
TESTBODY: ROT. SYM. CYLINDER AXIAL LENGTH = 1.80 M DIAMETER = .25 M						FIELD POINT DAT = 10 M HB = 1.00 M					
INCIDENT WAVE POLAR. = VERTICAL THETA = 80.8 DEG						INCIDENT WAVE POLAR. = HORIZONTAL THETA = 80.8 DEG					
VERTICAL POLARIZED ANTENNA						RADIAL POLARIZED ANTENNA					
PHI DEG	GAIN DB	PHASE CENTER DEG	MEAN ERROR DB	MAXIMUM GAINVAR DB	MAXIMUM PHASEVAR DEG	PHI DEG	GAIN DB	PHASE CENTER DEG	MEAN ERROR DB	MAXIMUM GAINVAR DB	MAXIMUM PHASEVAR DEG
0	-19.4	-167.8	.01	1.0	6.5	-1.7	-27.3	-32	4.3	4.1	4.1
5	-19.4	-167.5	.01	1.0	6.6	-1.7	-27.3	-32	4.3	4.0	4.1
10	-19.6	-166.6	.01	9.9	6.7	-1.7	-27.5	-31	4.3	4.0	6.6
15	-19.8	-165.0	.00	9.9	7.0	-1.7	-27.7	-31	4.4	3.9	6.5
20	-20.1	-162.6	.00	9.9	7.5	-1.7	-28.1	-31	4.4	3.9	6.3
25	-20.5	-159.4	.01	8.8	8.0	-1.7	-28.6	-31	4.4	3.9	6.1
30	-21.0	-155.2	.02	7.7	8.7	-1.7	-29.2	-31	4.4	3.6	5.8
35	-21.5	-149.7	.03	5.9	9.4	-1.7	-29.9	-31	4.4	3.4	5.4
40	-22.0	-142.8	.05	3.3	10.0	-1.7	-30.6	-30	4.4	3.2	5.1
45	-22.5	-134.4	.07	0.3	10.3	-1.7	-31.5	-30	4.4	3.0	4.6
50	-22.8	-124.3	.09	3.0	10.0	-1.7	-32.5	-30	4.4	2.6	4.2
55	-22.9	-112.8	.08	8.8	9.9	-1.7	-33.5	-29	4.5	2.3	3.7
60	-22.7	-100.9	.11	1.0	9.9	-1.7	-34.5	-29	4.5	1.9	3.2
65	-22.2	-89.3	.11	1.0	4.5	-1.7	-35.7	-28	4.4	1.5	2.7
70	-21.4	-78.8	.11	1.0	2.4	-1.7	-36.8	-28	4.4	1.2	2.1
75	-20.5	-69.8	.10	9.9	.6	-1.6	-37.9	-27	4.4	.4	1.5
80	-19.5	-62.2	.09	8.6	1.5	-1.5	-40.2	-25	4.3	.1	.9
85	-18.5	-55.8	.08	6.6	1.5	-1.4	-41.3	-25	4.3	.3	.3
90	-17.5	-50.5	.07	5.2	2.3	-1.3	-42.4	-24	4.2	.5	.3
95	-16.7	-46.0	.06	4.6	2.6	-1.2	-43.3	-23	4.1	.7	.9
100	-15.8	-42.2	.06	3.2	2.6	-1.1	-44.3	-22	4.0	1.0	1.5
105	-15.1	-38.9	.05	2.2	2.6	-1.1	-45.1	-21	3.9	1.1	2.1
110	-14.4	-36.0	.05	1.1	2.6	-1.0	-45.9	-20	3.8	1.1	2.7
115	-13.8	-33.4	.04	0.0	2.6	-1.0	-46.6	-20	3.8	1.1	3.2
120	-13.2	-31.2	.04	0.0	2.6	-1.0	-47.2	-19	3.7	1.1	3.8
125	-12.7	-29.2	.04	0.0	2.5	-1.0	-47.7	-19	3.7	1.1	4.4
130	-12.3	-27.5	.03	1.1	2.4	-1.0	-48.2	-18	3.6	1.0	5.2
135	-11.9	-25.9	.03	1.1	2.3	-1.0	-48.6	-18	3.6	.9	6.0
140	-11.5	-24.6	.03	1.1	2.3	-1.0	-49.2	-17	3.5	.9	6.3
145	-11.2	-23.4	.03	2.2	2.2	-1.1	-49.4	-17	3.5	.8	6.8
150	-10.9	-22.4	.03	2.2	2.1	-1.1	-49.6	-16	3.4	.7	7.0
155	-10.7	-21.5	.03	2.2	2.1	-1.0	-49.8	-16	3.4	.6	7.1
160	-10.5	-20.3	.03	2.2	2.1	-1.0	-49.9	-16	3.4	.6	7.2
165	-10.3	-19.7	.02	2.2	2.0	-1.0	-49.9	-16	3.4	.6	7.2
170	-10.2	-19.7	.02	2.2	2.0	-1.0	-49.9	-16	3.4	.6	7.2
180	-10.2	-19.7	.02	2.2	2.0	-1.0	-49.9	-16	3.4	.6	7.2

AZIMUTHAL RADIATION PATTERN FREQUENCY 75 MHZ									
HOMOGENEITY CHECK OF THE FIELD ALONG A 0.1 METER DIPOLE ANTENNA									
TESTBODY: ROT-SM. CYLINDER AXIAL LENGTH = 1.80 M DIA = .10 M DIA = .25 M									
INCIDENT WAVE POLAR. = HORIZONTAL THETA = 80.8 DEG									
FIELD POINT DAT = 1.00 M HB = 1.00 M									
HORIZONTAL POLARIZED ANTENNA									
PHI DEG	GAIN DB	PHASE CENTER DEG	MEAN ERROR DB	MAXIMUM GAIN DB	MAXIMUM PHASEVAR DEG	MAXIMUM GAIN DB	MEAN ERROR DB	MAXIMUM GAIN DB	MAXIMUM PHASEVAR DEG
0	-10.0	157.3	.02	5	1.7	-9	2.5	-31	4.1
5	-10.0	157.3	.02	5	1.7	-9	2.5	-31	4.1
10	-10.0	157.3	.02	5	1.6	-9	2.4	-31	4.1
15	-10.2	157.7	.02	5	1.6	-9	2.4	-31	4.1
20	-10.4	158.1	.02	5	1.5	-9	2.0	-30	4.1
25	-10.6	158.6	.02	5	1.5	-1.0	1.7	-30	4.1
30	-10.9	159.2	.02	5	1.4	-1.1	1.3	-30	4.2
35	-11.2	159.9	.03	5	1.3	-1.1	.8	-30	4.2
40	-11.6	160.7	.03	5	1.2	-1.2	.3	-30	4.2
45	-12.1	161.6	.03	4	1.1	-1.3	-.4	-29	4.2
50	-12.6	162.6	.03	4	1.0	-1.4	-1.1	-29	4.2
55	-13.2	163.7	.03	4	.8	-1.4	-1.9	-28	4.3
60	-14.0	164.8	.04	4	.7	-1.5	-2.8	-28	4.3
65	-14.8	166.1	.04	4	.5	-1.6	-3.8	-27	4.3
70	-15.7	167.6	.05	4	.2	-1.7	-4.9	-27	4.3
75	-16.8	169.1	.05	4	.1	-1.7	-6.0	-26	4.3
80	-18.1	170.8	.07	3	.9	-1.8	-7.2	-26	4.3
85	-19.6	172.8	.09	2	1.3	-1.8	-8.5	-25	4.3
90	-21.4	175.3	.09	2	1.5	-1.9	-9.7	-24	4.2
95	-23.8	178.5	.11	2	2.0	-1.9	-11.0	-24	4.2
100	-27.0	176.5	.15	3	3.6	-1.9	-12.3	-23	4.2
105	-31.7	165.8	.23	1.2	5.3	-1.8	-13.5	-22	4.1
110	-39.3	122.3	.06	3.8	18.0	-1.8	-14.7	-22	4.1
115	-35.3	40.6	.46	7	12.0	-1.8	-15.9	-21	4.0
120	-29.5	21.7	.23	1.0	9.5	-1.7	-17.0	-20	3.9
125	-26.0	15.1	.15	1.0	6.4	-1.7	-18.0	-20	3.9
130	-23.6	11.4	.11	.9	4.0	-1.6	-18.9	-19	3.8
135	-21.8	9.0	.09	.9	4.0	-1.5	-19.7	-18	3.7
140	-20.5	7.2	.07	.8	3.0	-1.5	-20.4	-18	3.7
145	-19.4	5.8	.06	.8	3.4	-1.4	-21.1	-17	3.6
150	-18.6	4.7	.05	.8	2.5	-1.4	-21.6	-17	3.6
155	-17.9	3.8	.05	.8	2.7	-1.3	-22.0	-17	3.5
160	-17.4	3.1	.05	.8	2.2	-1.3	-22.4	-16	3.5
165	-17.0	2.6	.05	.8	2.2	-1.2	-22.7	-16	3.4
170	-16.8	2.2	.04	.7	2.1	-1.2	-22.9	-16	3.4
175	-16.6	2.0	.04	.7	2.1	-1.2	-23.0	-16	3.4
180	-16.6	1.9	.04	.7	2.0	-1.2	-23.0	-16	3.4

FZYL 75 MHz

AZIMUTHAL RADIATION PATTERN FREQUENCY 100 MHZ									
HOMOGENEITY CHECK OF THE FIELD ALONG A 0.1 METER DIPOLE ANTENNA									
TESTBODY: ROT. SIM. CYLINDER AXIAL LENGTH = 1.80 M DIAMETER = .25 M					FIELD POINT DAT = .10 M HB = 1.00 M				
INCIDENT WAVE POLAR. = VERTICAL THETA = 80.8 DEG					INCIDENT WAVE POLAR. = HORIZONTAL THETA = 80.8 DEG				
VERTICAL POLARIZED ANTENNA					RADIAL POLARIZED ANTENNA				
RHI DEG	GAIN DB	PHASE CENTER DEG	MEAN ERROR DB	MAXIMUM GAINVAR DB	RHI DEG	GAIN DB	PHASE CENTER DEG	MEAN ERROR DB	MAXIMUM GAINVAR DB
0	-5.8	167.3	-0.0	3	0	-3.5	43.7	.09	0.0
5	-5.8	167.4	-0.0	3	5	-3.5	43.8	.09	0.4
10	-5.8	167.7	-0.0	3	10	-3.6	44.3	.09	.7
15	-5.9	168.2	-0.0	3	15	-3.8	45.1	.08	1.1
20	-6.0	168.9	-0.0	3	20	-4.0	46.1	.08	1.5
25	-6.1	169.7	-0.0	3	25	-4.3	47.5	.08	1.9
30	-6.3	170.8	-0.0	3	30	-4.7	49.2	.08	2.3
35	-6.5	172.0	-0.0	3	35	-5.2	51.1	.08	2.8
40	-6.8	173.4	-0.0	3	40	-5.8	53.4	.08	3.3
45	-7.0	175.0	-0.0	2	45	-6.5	56.0	.08	4.0
50	-7.3	176.8	-0.1	2	50	-7.3	58.9	.08	4.7
55	-7.7	178.8	-0.1	2	55	-8.3	62.3	.08	5.7
60	-8.1	179.1	-0.1	2	60	-9.5	66.1	.07	7.0
65	-8.5	176.7	-0.1	2	65	-10.9	70.5	.06	8.7
70	-8.9	174.2	-0.1	2	70	-12.7	75.9	.04	11.4
75	-9.4	171.5	-0.1	2	75	-14.9	83.0	-0.7	15.7
80	-10.0	168.6	-0.1	2	80	-17.9	93.9	-1.7	21.3
85	-10.5	165.4	-0.1	2	85	-22.1	115.5	-3.0	29.9
90	-11.2	162.0	-0.1	1	90	-25.2	166.5	-5.3	41.4
95	-11.8	158.2	-0.1	1	95	-21.7	144.7	-2.8	29.9
100	-12.6	154.2	-0.1	1	100	-17.6	124.4	-0.6	18.1
105	-13.3	149.8	-0.1	1	105	-14.6	114.0	-1.0	15.7
110	-14.1	144.9	-0.1	1	110	-12.3	101.9	.04	11.5
115	-14.9	139.6	-0.1	1	115	-10.5	101.9	.04	8.9
120	-15.6	133.7	-0.1	2	120	-9.1	97.6	.07	7.1
125	-16.4	127.3	-0.1	3	125	-7.9	94.0	.07	5.9
130	-17.1	120.3	-0.0	4	130	-6.8	90.8	.07	4.9
135	-17.7	113.0	-0.0	5	135	-6.0	88.0	.08	4.1
140	-18.3	105.4	-0.1	7	140	-5.3	85.5	.08	3.5
145	-18.6	98.0	-0.1	8	145	-4.7	83.4	.08	2.9
150	-18.9	91.0	-0.1	9	150	-4.1	81.5	.08	2.4
155	-19.0	84.8	-0.2	1.1	155	-3.7	79.9	.09	1.9
160	-19.1	79.5	-0.2	1.1	160	-3.4	78.7	.09	1.5
165	-19.1	75.3	-0.2	1.2	165	-3.1	77.7	.09	1.1
170	-19.0	72.3	-0.2	1.2	170	-3.0	77.0	.09	.7
175	-19.0	70.5	-0.2	1.3	175	-2.8	76.5	.09	.4
180	-19.0	69.9	-0.2	1.3	180	-2.8	76.4	.09	0.0

FZYL 100 MHZ

\*\*\*\*\*  
-18.6 53.3 -17 2.3 11.1  
-12.7 53.5 -17 2.3 10.9  
-9.2 53.9 -17 2.3 10.4  
-6.8 54.5 -17 2.2 10.1  
-4.9 55.2 -17 2.2 9.6  
-3.4 56.1 -17 2.2 9.1  
-2.2 57.1 -17 2.2 8.6  
-1.2 58.2 -17 2.2 8.1  
-.4 59.5 -17 2.2 7.9  
1.0 60.9 -17 2.2 7.2  
1.5 63.9 -17 2.1 6.5  
1.9 65.6 -17 2.1 5.7  
2.2 67.3 -17 2.1 4.8  
2.5 69.1 -17 2.1 4.0  
2.7 70.9 -17 2.1 3.1  
2.8 72.7 -17 2.1 2.2  
2.9 74.5 -17 2.1 1.3  
2.8 76.4 -17 2.1 .4  
2.8 78.2 -17 2.1 .5  
2.6 80.0 -17 2.1 1.4  
2.4 81.7 -17 2.1 2.3  
1.7 85.0 -17 2.1 4.0  
1.2 88.6 -17 2.1 5.5  
.6 89.0 -17 2.1 6.3  
-.1 88.4 -17 2.1 6.9  
-1.1 90.6 -17 2.1 7.5  
-1.9 91.7 -17 2.1 8.1  
-3.1 92.7 -17 2.1 8.6  
-4.5 93.5 -17 2.1 9.0  
-6.4 94.2 -17 2.1 9.3  
-8.8 94.8 -17 2.1 9.6  
-12.2 95.1 -17 2.1 9.8  
-18.2 95.4 -17 2.1 9.9  
\*\*\*\*\*

[illegible]

AZIMUTHAL RADIATION PATTERN FREQUENCY 300 MHZ									
HOMOGENEITY CHECK OF THE FIELD ALONG A 0.1 METER DIPOLE ANTENNA									
TESTBODY: ROT. SYM. CYLINDER AXIAL LENGTH = 1.80 M DIAMETER = .25 M									
INCIDENT WAVE POLAR. = VERTICAL THETA = 80.8 DEG									
FIELD POINT DAT = .10 M HB = 1.00 M									
FZYL 300 MHZ									
HORIZONTAL POLARIZED ANTENNA									
RHI DEG	GAIN DB	PHASE CENTER DEG	MEAN ERROR DB	MAXIMUM GAINVAR DB	MAXIMUM PHASEVAR DEG	RHI DEG	GAIN DB	PHASE CENTER DEG	MEAN ERROR DB
0	-1.7	-84.4	.16	0.0	0.0	0	-1.7	-84.4	.16
5	-1.8	-84.2	.16	0.0	0.0	5	-1.8	-84.2	.16
10	-2.0	-83.4	.16	1.4	4.9	10	-2.0	-83.4	.16
15	-2.0	-82.2	.16	2.9	9.8	15	-2.0	-82.2	.16
20	-2.8	-80.5	.15	3.7	12.3	20	-2.8	-80.5	.15
25	-3.4	-78.4	.14	4.8	14.8	25	-3.4	-78.4	.14
30	-4.2	-75.7	.13	6.0	17.3	30	-4.2	-75.7	.13
35	-5.2	-72.6	.11	7.6	20.0	35	-5.2	-72.6	.11
40	-6.4	-69.0	.07	9.8	23.1	40	-6.4	-69.0	.07
45	-8.0	-64.8	.02	13.3	27.2	45	-8.0	-64.8	.02
50	-10.0	-60.0	.02	13.3	35.4	50	-10.0	-60.0	.02
55	-12.5	-54.5	-.07	21.5	105.0	55	-12.5	-54.5	-.07
60	-16.1	-47.6	-.37	14.3	222.2	60	-16.1	-47.6	-.37
65	-21.9	-37.0	-.74	14.3	222.2	65	-21.9	-37.0	-.74
70	-35.9	22.4	2.7	213.3	4.4	70	-35.9	22.4	2.7
75	-24.5	131.0	1.4	6.9	214.4	75	-24.5	131.0	1.4
80	-18.8	144.9	.14	18.2	180.2	80	-18.8	144.9	.14
85	-15.8	154.6	.65	17.9	54.4	85	-15.8	154.6	.65
90	-14.0	164.0	.51	9.1	50.2	90	-14.0	164.0	.51
95	-12.9	173.7	.38	5.6	56.8	95	-12.9	173.7	.38
100	-12.1	175.7	.35	3.6	61.7	100	-12.1	175.7	.35
105	-11.6	164.1	.11	2.2	66.2	105	-11.6	164.1	.11
110	-11.2	151.4	-.03	2.2	66.2	110	-11.2	151.4	-.03
115	-10.9	137.8	-.16	2.4	69.3	115	-10.9	137.8	-.16
120	-10.4	123.7	-.24	3.0	66.4	120	-10.4	123.7	-.24
125	-9.7	109.9	-.25	3.6	66.4	125	-9.7	109.9	-.25
130	-8.9	97.0	-.20	4.1	61.0	130	-8.9	97.0	-.20
135	-8.0	85.6	-.13	4.4	53.8	135	-8.0	85.6	-.13
140	-7.1	75.8	-.06	4.4	45.9	140	-7.1	75.8	-.06
145	-6.2	67.6	.01	4.1	38.3	145	-6.2	67.6	.01
150	-5.5	60.9	.06	3.7	31.2	150	-5.5	60.9	.06
155	-4.8	55.5	.09	3.1	24.9	155	-4.8	55.5	.09
160	-4.2	51.3	.12	2.5	19.2	160	-4.2	51.3	.12
165	-3.8	48.9	.14	1.9	14.0	165	-3.8	48.9	.14
170	-3.5	46.1	.15	1.3	9.1	170	-3.5	46.1	.15
175	-3.3	44.5	.15	.6	4.5	175	-3.3	44.5	.15
180	-3.2	44.1	.16	0.0	0.0	180	-3.2	44.1	.16
VERTICAL POLARIZED ANTENNA									
RHI DEG	GAIN DB	PHASE CENTER DEG	MEAN ERROR DB	MAXIMUM GAINVAR DB	MAXIMUM PHASEVAR DEG	RHI DEG	GAIN DB	PHASE CENTER DEG	MEAN ERROR DB
0	6	93.6	-.00	1	7.3	0	6	93.6	-.00
5	6	94.6	-.00	1	7.3	5	6	94.6	-.00
10	6	94.6	-.00	1	7.3	10	6	94.6	-.00
15	6	95.9	-.00	1	7.3	15	6	95.9	-.00
20	4	97.7	-.00	1	7.4	20	4	97.7	-.00
25	3	102.7	-.00	1	7.4	25	3	102.7	-.00
30	3	107.0	-.00	1	7.5	30	3	107.0	-.00
35	3	109.7	-.00	1	7.5	35	3	109.7	-.00
40	3	113.9	-.00	1	7.6	40	3	113.9	-.00
45	9	118.4	-.00	0	7.6	45	9	118.4	-.00
50	12	123.4	-.00	0	7.7	50	12	123.4	-.00
55	12	128.8	-.00	0	7.7	55	12	128.8	-.00
60	9	134.5	-.00	0	7.8	60	9	134.5	-.00
65	6	140.2	-.00	0	7.9	65	6	140.2	-.00
70	5	146.8	-.00	1	8.0	70	5	146.8	-.00
75	3	153.4	-.00	1	8.1	75	3	153.4	-.00
80	4	160.2	-.00	2	8.2	80	4	160.2	-.00
85	4	167.4	-.00	2	8.2	85	4	167.4	-.00
90	5	174.4	-.00	2	8.3	90	5	174.4	-.00
95	6	181.2	-.00	3	8.4	95	6	181.2	-.00
100	6	188.6	-.00	3	8.4	100	6	188.6	-.00
105	7	196.1	-.01	5	8.5	105	7	196.1	-.01
110	8	203.7	-.01	6	8.6	110	8	203.7	-.01
115	9	211.4	-.01	8	8.7	115	9	211.4	-.01
120	10	219.1	-.01	9	8.8	120	10	219.1	-.01
125	11	226.8	-.01	1.2	2.8	125	11	226.8	-.01
130	12	234.5	-.01	1.2	2.8	130	12	234.5	-.01
135	13	242.2	-.01	1.2	2.8	135	13	242.2	-.01
140	14	250.0	-.01	1.2	2.8	140	14	250.0	-.01
145	15	257.8	-.01	1.2	2.8	145	15	257.8	-.01
150	16	265.6	-.01	1.2	2.8	150	16	265.6	-.01
155	17	273.4	-.01	1.2	2.8	155	17	273.4	-.01
160	18	281.2	-.01	1.2	2.8	160	18	281.2	-.01
165	19	289.0	-.01	1.2	2.8	165	19	289.0	-.01
170	20	296.8	-.01	1.2	2.8	170	20	296.8	-.01
175	21	304.6	-.01	1.2	2.8	175	21	304.6	-.01
180	22	312.4	-.01	1.2	2.8	180	22	312.4	-.01

AZIMUTHAL RADIATION PATTERN FREQUENCY 425 MHZ									
HOMOGENEITY CHECK OF THE FIELD ALONG A 0.1 METER DIPOLE ANTENNA									
TESTBODY: ROT. SW. CYLINDER		FIELD POINT		INCIDENT WAVE					
AXIAL LENGTH = 1.80 M		DAT = .10 M		POLAR. = VERTICAL					
DIAMETER = .25 M		HB = 1.00 M		THETA = 80.8 DEG					
PHI DEG	VERTICAL POLARIZED ANTENNA				RADIAL POLARIZED ANTENNA				FZYL 425 MHz
	GAIN DB	PHASE CENTER DEG	MEAN ERROR DB	MAXIMUM GAINVAR DB	GAIN DB	PHASE CENTER DEG	MEAN ERROR DB	MAXIMUM GAINVAR DB	
0	2.6	47.1	.00	8.0	-15.6	-97.4	-97	5.9	65.4
5	2.5	47.5	.00	8.0	-15.6	-97.0	-96	5.9	65.0
10	2.5	48.5	.00	8.0	-15.7	-95.9	-93	5.9	63.9
15	2.4	50.2	.00	8.0	-15.8	-94.2	-88	5.9	62.1
20	2.3	52.6	.00	7.9	-15.9	-91.8	-82	5.9	59.5
25	2.2	55.7	.00	7.9	-16.0	-88.8	-75	5.8	56.3
30	2.1	59.4	.00	7.8	-16.2	-85.5	-66	5.8	52.5
35	1.9	63.8	.00	7.8	-16.5	-81.9	-57	5.7	48.3
40	1.6	68.8	.00	7.7	-16.9	-78.2	-49	5.5	43.8
45	1.4	74.4	.00	7.7	-17.3	-74.7	-40	5.3	39.3
50	1.1	80.5	.00	7.7	-17.9	-71.7	-33	5.1	34.8
55	.7	87.3	.00	7.7	-18.6	-69.7	-26	4.9	30.8
60	.4	94.5	.00	7.8	-19.5	-69.3	-21	4.7	27.4
65	-.1	102.3	.00	7.9	-20.5	-71.5	-17	4.6	25.2
70	-.5	110.4	.00	8.0	-21.5	-77.8	-16	4.3	24.7
75	-.9	119.0	.00	8.2	-22.2	-88.9	-16	3.8	25.4
80	-1.5	128.0	.00	8.5	-21.9	-103.0	-17	2.9	24.9
85	-2.1	137.2	.00	8.7	-20.6	-115.4	-17	2.0	21.5
90	-2.7	146.7	.00	9.0	-18.8	-123.3	-15	1.4	16.7
95	-3.4	156.3	.00	9.4	-17.0	-127.0	-14	1.1	12.1
100	-4.1	166.0	.00	9.7	-15.3	-128.0	-13	1.0	8.2
105	-4.9	175.8	.00	10.1	-13.8	-127.3	-13	1.0	4.8
110	-5.7	174.4	.01	10.6	-12.6	-125.5	-13	1.1	1.9
115	-6.6	164.7	.01	11.1	-11.5	-123.2	-14	1.2	.6
120	-7.6	154.9	.01	11.6	-10.6	-120.6	-14	1.4	2.8
125	-8.7	145.0	.01	12.2	-9.8	-117.9	-15	1.5	4.7
130	-9.9	134.9	.01	13.0	-9.2	-115.2	-16	1.8	6.4
135	-11.2	124.2	.00	14.1	-8.7	-112.7	-17	2.0	7.9
140	-12.7	112.8	.00	15.3	-8.3	-110.3	-18	2.2	9.1
145	-14.1	100.0	.01	16.8	-8.0	-108.2	-19	2.5	10.1
150	-15.5	85.7	.03	18.2	-7.7	-106.3	-20	2.7	10.9
155	-16.6	70.2	.06	19.0	-7.5	-104.7	-21	2.9	11.5
160	-17.2	54.8	.08	18.6	-7.4	-103.4	-22	3.1	12.0
165	-17.4	41.6	.08	17.4	-7.3	-102.4	-22	3.3	12.3
170	-17.4	31.6	.08	16.6	-7.2	-101.6	-23	3.4	12.5
175	-17.3	25.7	.08	15.0	-7.2	-101.2	-23	3.5	12.6
180	-17.2	23.7	.08	1.7	-7.1	-101.1	-23	3.5	12.7

16.2.5. ADDITIONAL RESULTS FROM FIELD COMPUTATIONS WITH FZYL, MANMOD 1  
AND MANMOD 2

---

EFFECT OF THE FREQUENCY ON THE DIRECTIVE RADIATION PATTERN (EXTENSION)

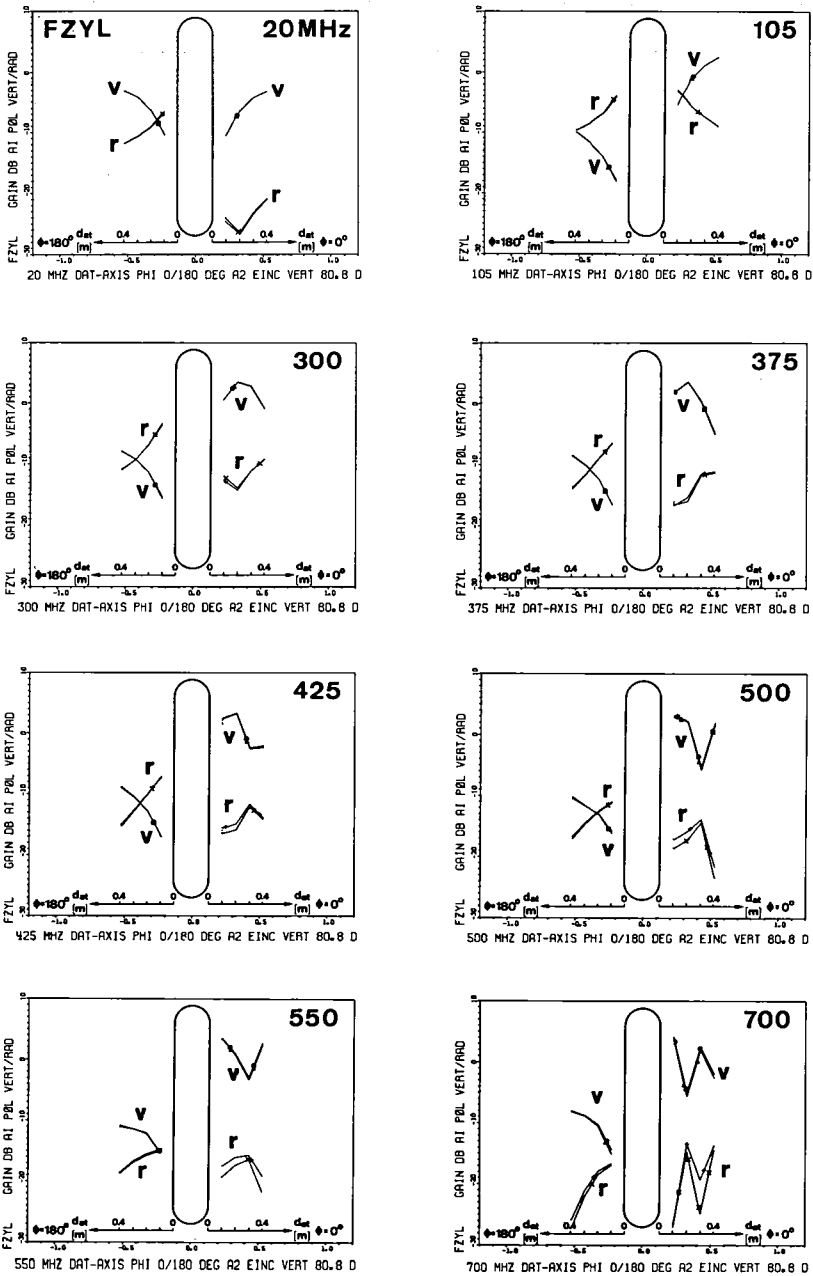


FIGURE 78d Field components  $E_V$  and  $E_R$  versus  $d_{at}$  at  $\phi = 0$  and  $180^\circ$ , with the parameter  $f$  20 to 700 MHz. Constant:  $p_2 = \text{vertical}$ ,  $\theta_i = 80.8^\circ$ ,  $h_B = 1.0 \text{ m}$ .



EFFECT OF THE FREQUENCY ON THE AZIMUTHAL RADIATION PATTERNS (EXTENSION)

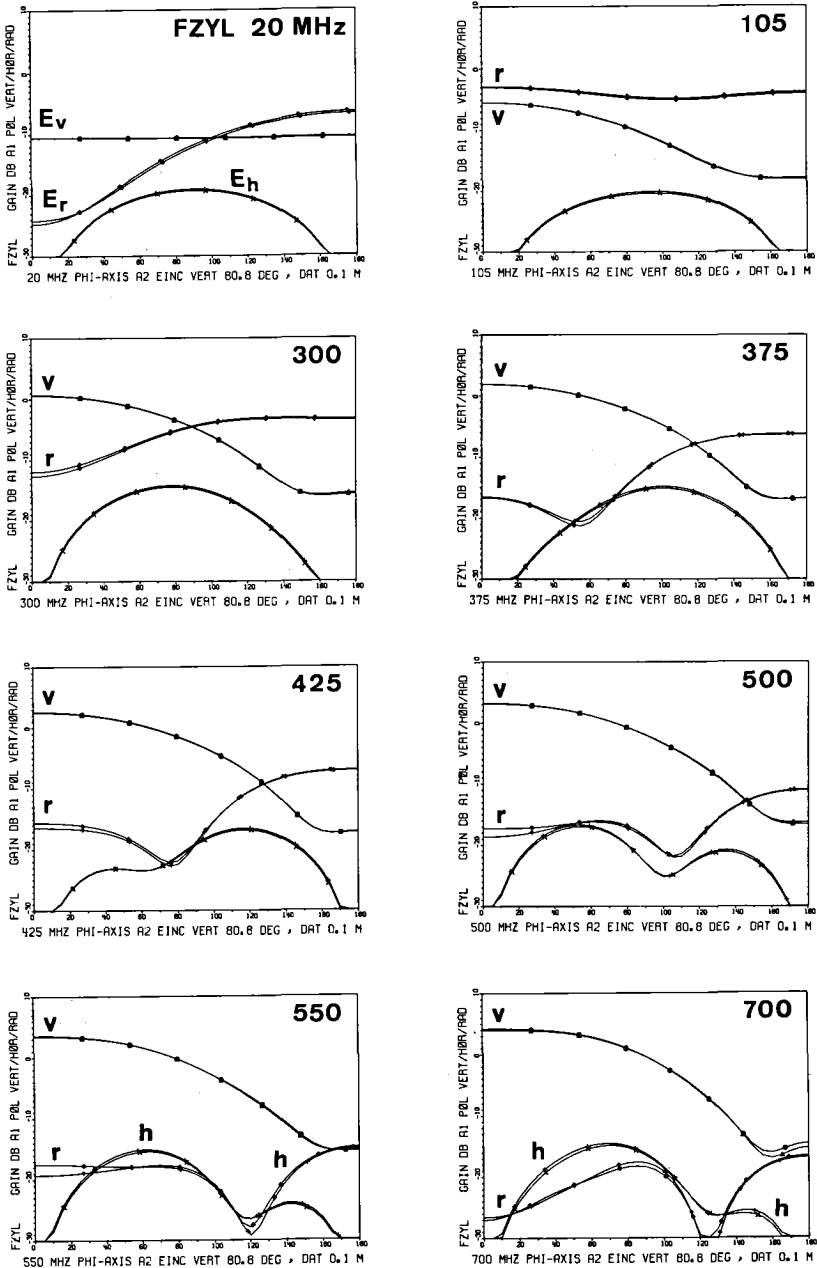


FIGURE 77d Field components  $E_v$ ,  $E_r$  and  $E_h$  versus  $\phi$  with the parameter  $f$  20 to 700 MHz. Constant:  $d_{at} = 0.1$  m,  $p_2$  = vertical,  $\theta_i = 80.8^\circ$ ,  $h_g = 1.0$  m.

Leer - Vide - Empty

# AZIMUTHAL RADIATION PATTERNS IN THE 11 MHz RANGE

- FZYL : 11 MHz
- MANMOD 1 : 15 MHz
- MANMOD 2 : 15 MHz

The three figures show the azimuthal radiation patterns of the field components  $E_v$ ,  $E_r$  and  $E_h$  at  $d_{at} = 0.1, 0.2, 0.3$  and  $0.4$  m.

Effect of the body shape:

- $E_v$  varies only within 2 dB
- $E_r$  varies extremely, especially at small  $d_{at}$
- $E_h$  varies only within 2 dB

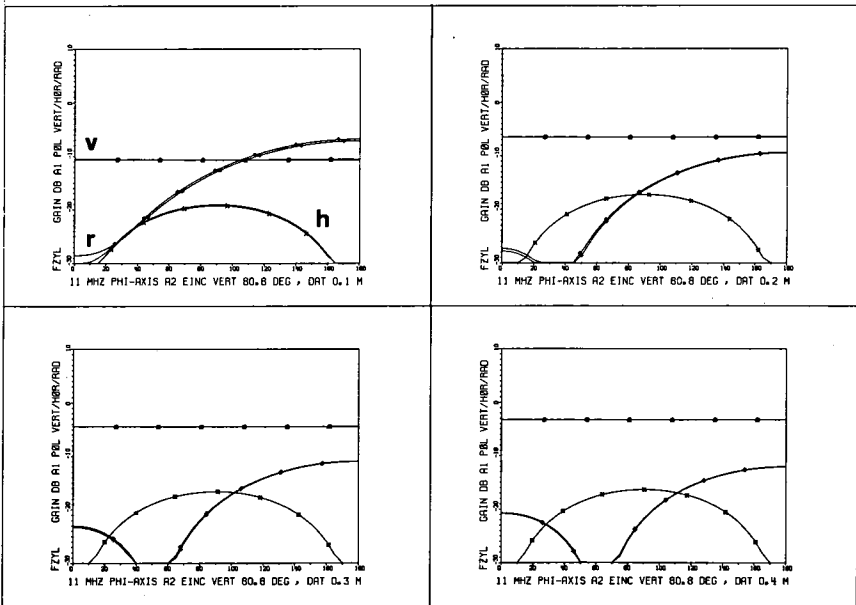


FIGURE 100a Azimuthal radiation pattern FZYL at 11 MHz.

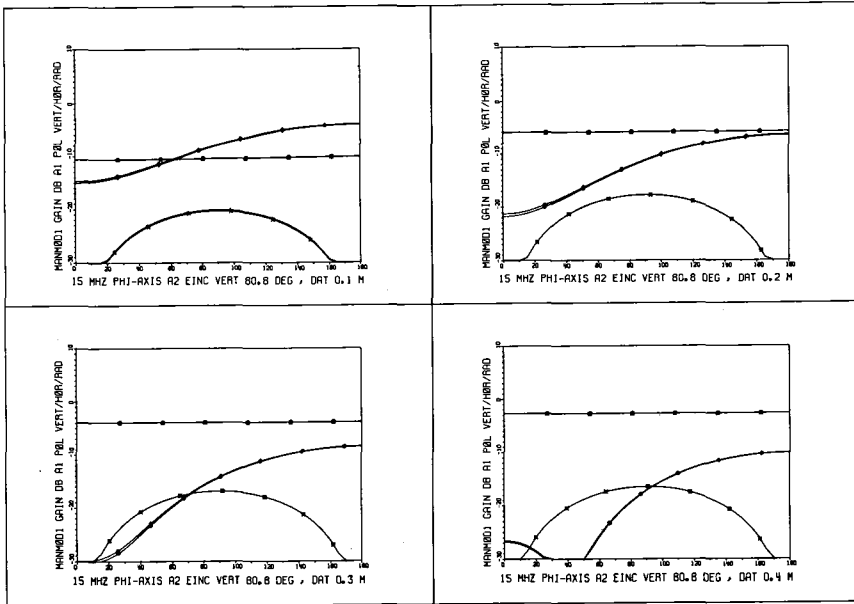


FIGURE 100b Azimuthal radiation pattern MANMOD1 at 15 MHz.

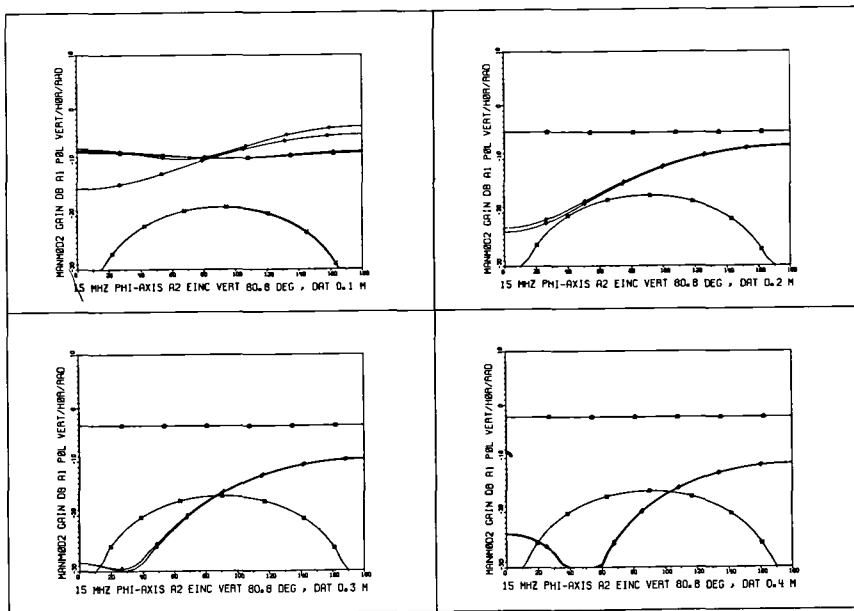


FIGURE 100c Azimuthal radiation pattern MANMOD2 at 15 MHz.

# AZIMUTHAL RADIATION PATTERNS IN THE 50 MHz RANGE

- FZYL : 50 MHz
- MANMOD 1 : 50 MHz
- MANMOD 2 : 50 MHz

The three figures show the azimuthal radiation patterns of the field components  $E_v$ ,  $E_r$  and  $E_h$  at  $d_{at} = 0.1, 0.2, 0.3$  and  $0.4$  m.

Effect of the body shape:

- $E_v$  varies only within 2.5 dB
- $E_r$  varies only within 2.5 dB
- $E_h$  varies only within 2.0 dB

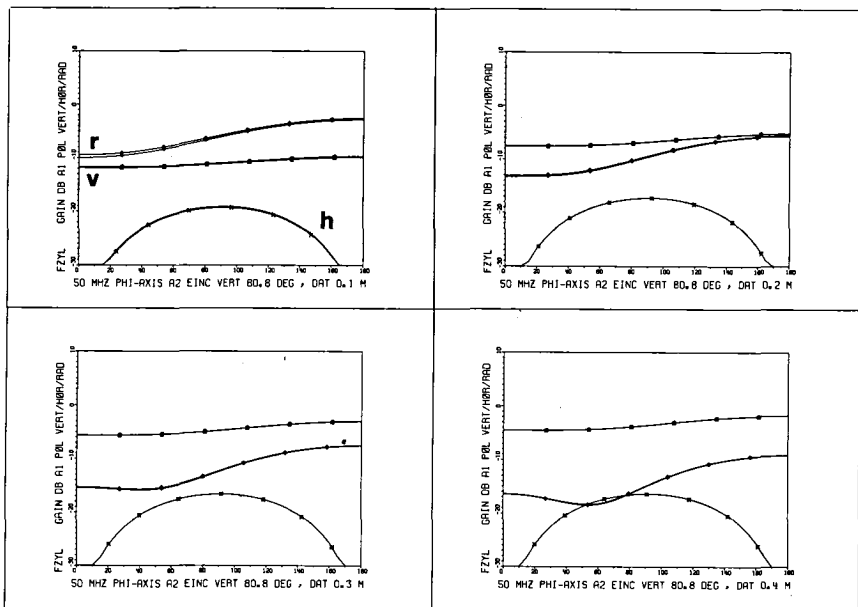


FIGURE 101a Azimuthal radiation patterns FZYL at 50 MHz.

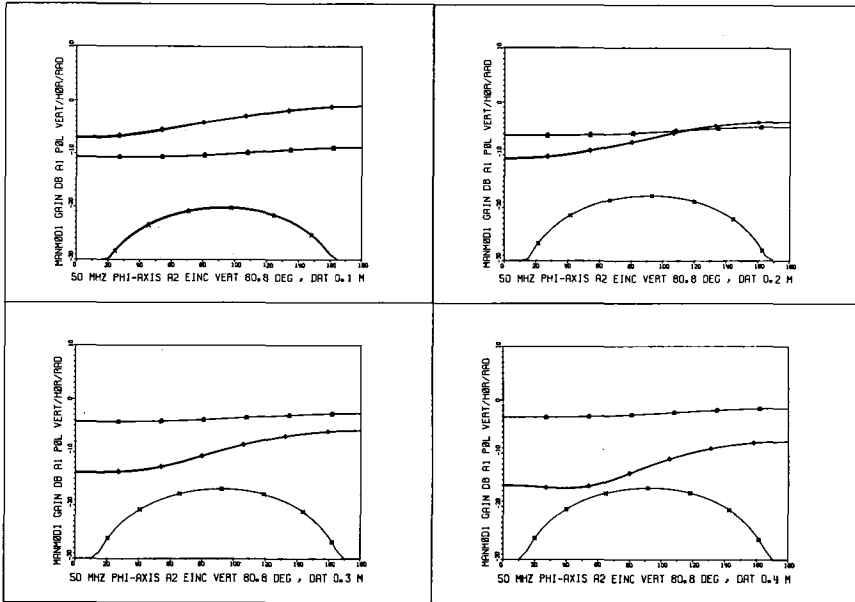


FIGURE 101b Azimuthal radiation patterns MANMOD1 at 50 MHz.

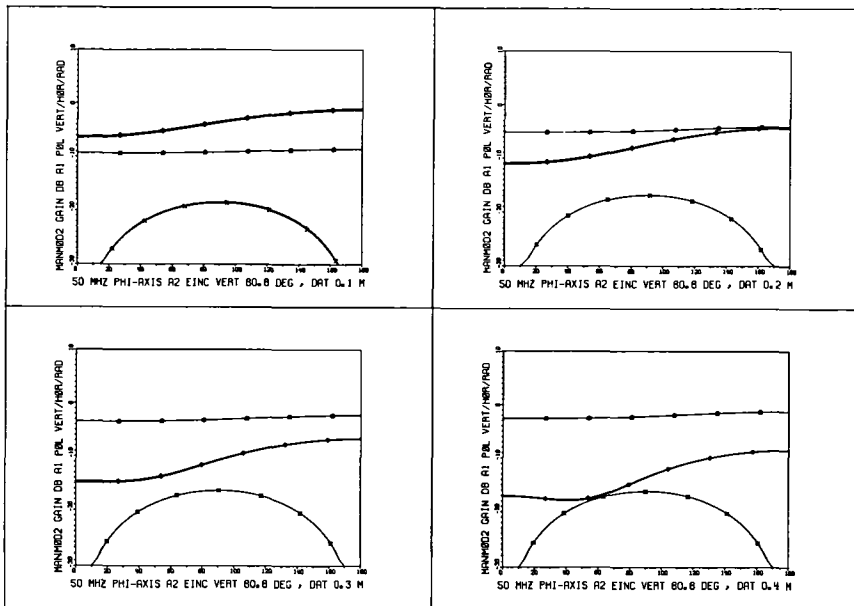


FIGURE 101c Azimuthal radiation patterns MANMOD2 at 50 MHz.

### AZIMUTHAL RADIATION PATTERNS IN THE 75 MHz RANGE

- FZYL : 75 MHz
- MANMOD 1 : 75 MHz
- MANMOD 2 : 80 MHz

The three figures show the azimuthal radiation patterns of the field components  $E_v$ ,  $E_r$  and  $E_h$  at  $dat = 0.1, 0.2, 0.3$  and  $0.4$  m.

Effect of the body shape:

- $E_v$  varies extremely between FZYL 75 MHz and MANMOD1 75 MHz, but  $E_v$  varies less (about 10 dB) between FZYL 75 MHz and MANMOD2 80 MHz.
- $E_r$  is almost constant versus  $\phi$  and the amplitude varies within 5 dB between the three bodies at constant  $dat$ .
- $E_h$  varies only within 1 dB

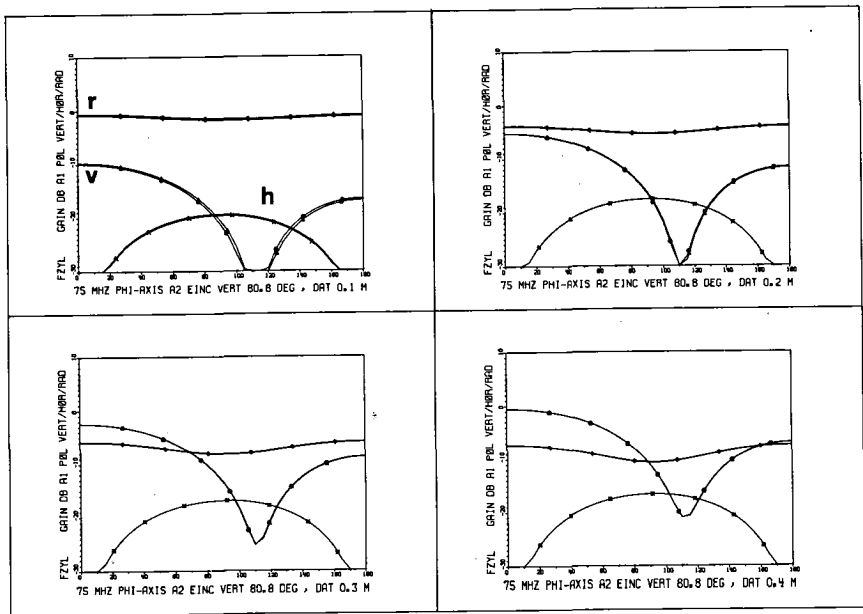


FIGURE 102a Azimuthal radiation patterns FZYL at 75 MHz.

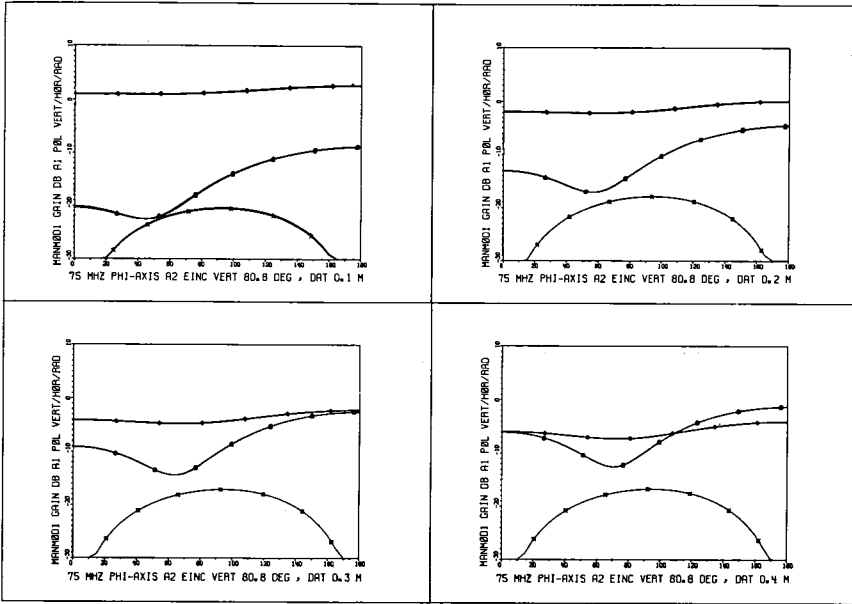


FIGURE 102b Azimuthal radiation patterns MANMOD1 at 75 MHz.

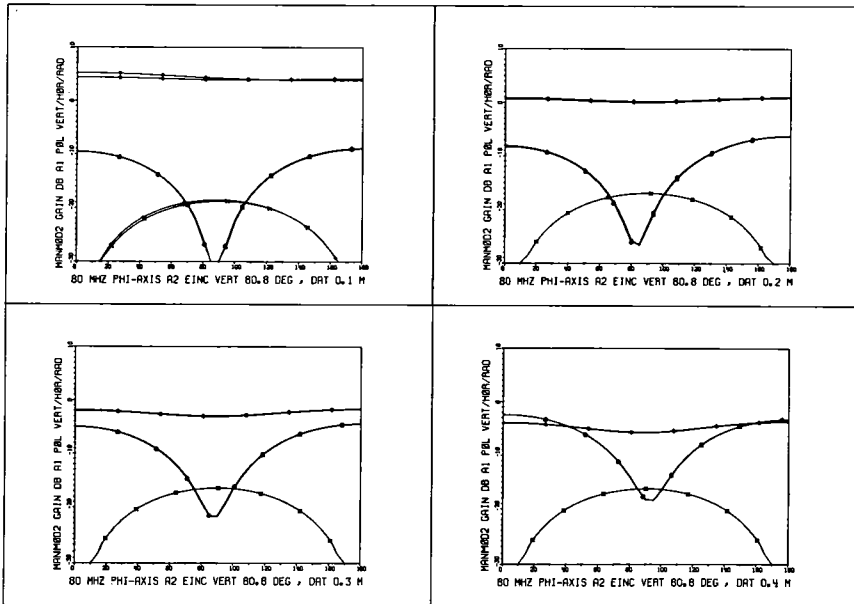


FIGURE 102c Azimuthal radiation patterns MANMOD2 at 80 MHz.



# AZIMUTHAL RADIATION PATTERNS IN THE 85 MHZ RANGE

- FZYL : 85 MHz
- MANMOD 1 : 90 MHz
- MANMOD 2 : 90 MHz

The three figures show the azimuthal radiation patterns of the field components  $E_v$ ,  $E_r$  and  $E_h$  at  $d_{at} = 0.1, 0.2, 0.3$  and  $0.4$  m.

Effect of the body shape:

- $E_v$  varies very much between FZYL 85 MHz and MANMOD1 90 MHz (12 dB), but  $E_v$  varies less between FZYL 85 MHz and MANMOD2 90 MHz (3 dB)
- $E_r$  is almost independent on  $\phi$  and differs in amplitude within 5 dB between the three bodies
- $E_h$  varies only within 2 dB

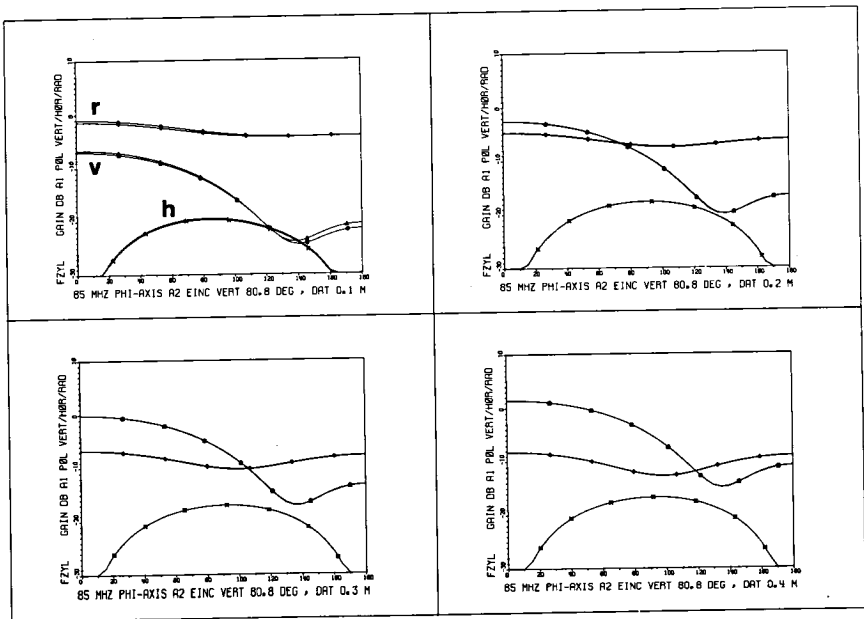


FIGURE 103a Azimuthal radiation patterns FZYL at 85 MHz.

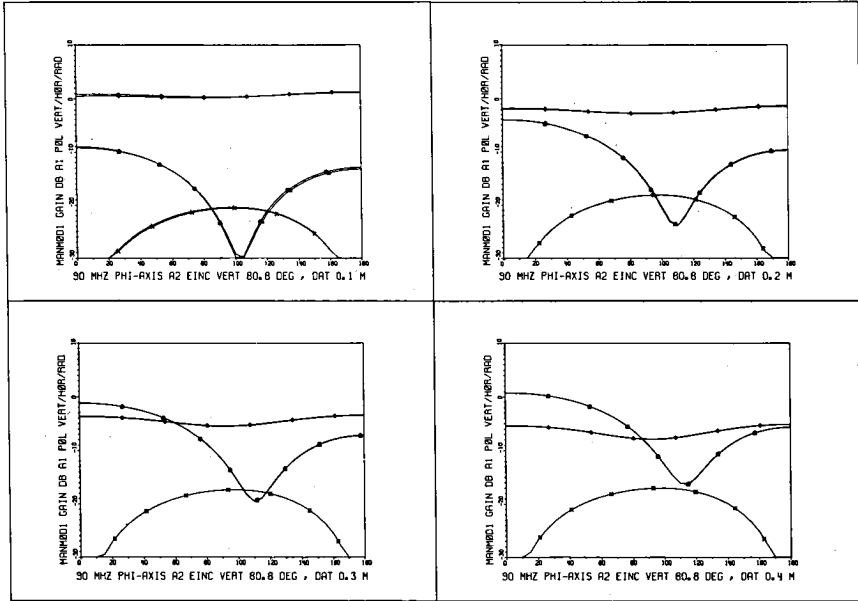


FIGURE 103b Azimuthal radiation patterns MANMOD1 at 90 MHz.

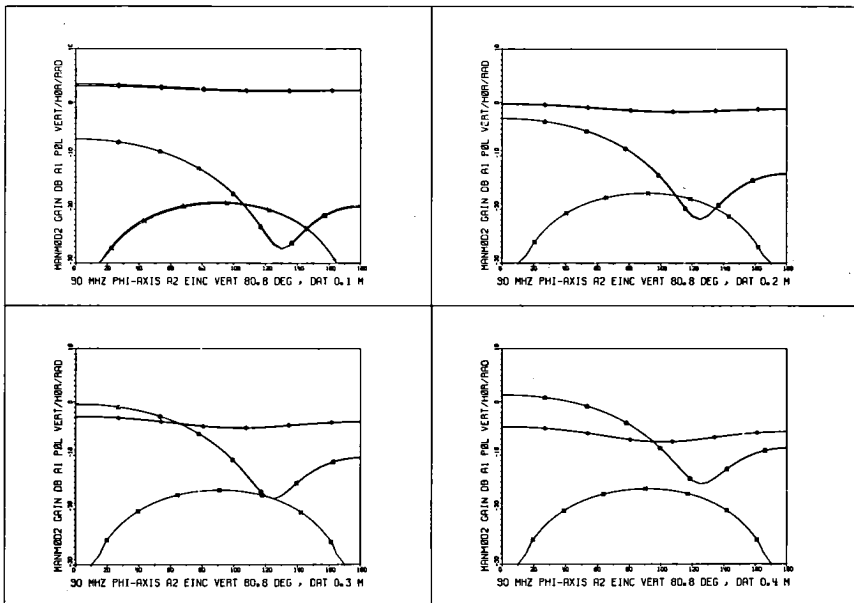


FIGURE 103c Azimuthal radiation patterns MANMOD2 at 90 MHz.

# AZIMUTHAL RADIATION PATTERNS IN THE 200 MHZ RANGE

- FZYL : 200 MHz
- MANMOD 1 : 200 MHz
- MANMOD 2 : 200 MHz

The three figures show the azimuthal radiation patterns of the field components  $E_v$ ,  $E_r$  and  $E_h$  at  $d_{at} = 0.1, 0.2, 0.3$  and  $0.4$  m.

Effect of the body shape:

- $E_v$  varies within 5 dB
- $E_r$  is almost independent on  $\phi$  up to  $d_{at} = 0.3$  m and varies only 3 dB between the three bodies. At  $d_{at} = 0.4$   $E_r$  becomes dependent on  $\phi$  and varies within 5 dB between the three bodies.
- $E_h$  varies within 10 dB and develops two peaks, especially with MANMOD 1

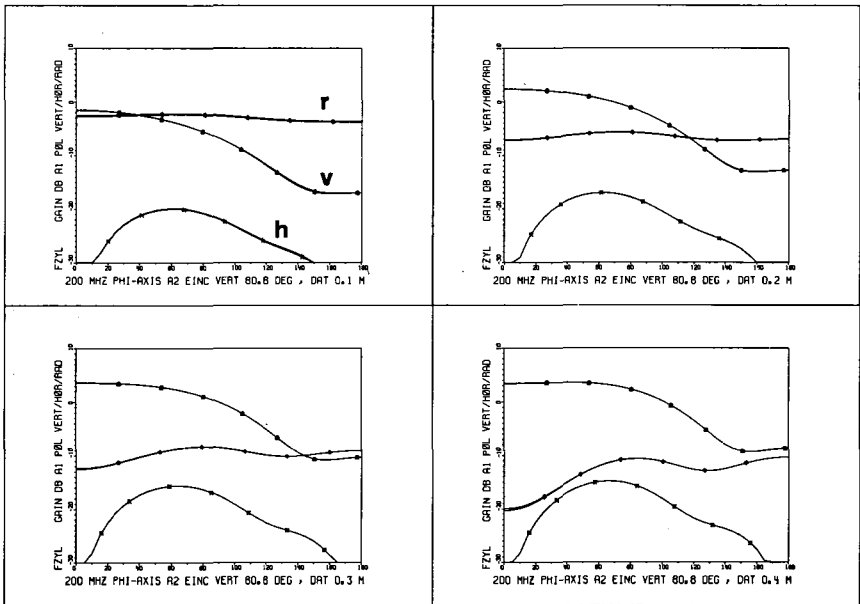


FIGURE 104a Azimuthal radiation patterns FZYL at 200 MHz.

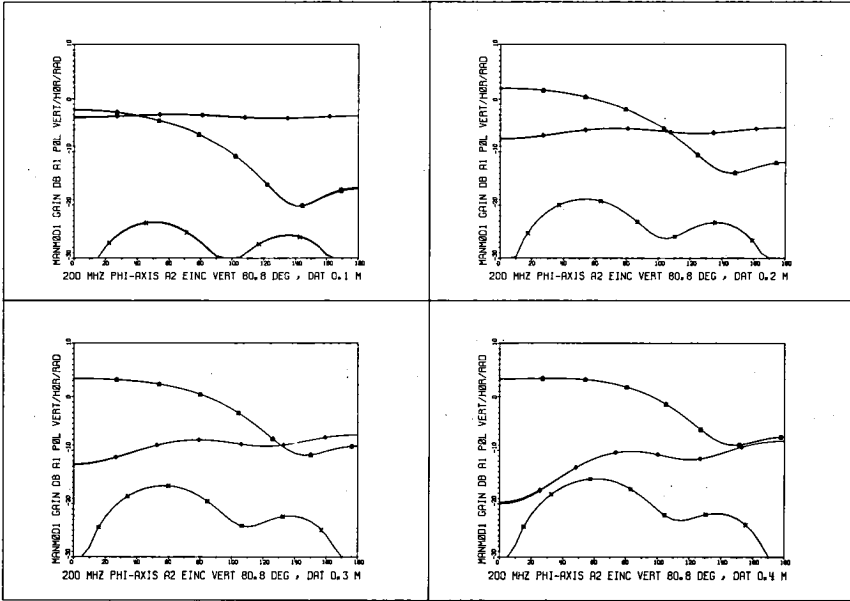


FIGURE 104b Azimuthal radiation patterns MANMOD1 at 200 MHz.

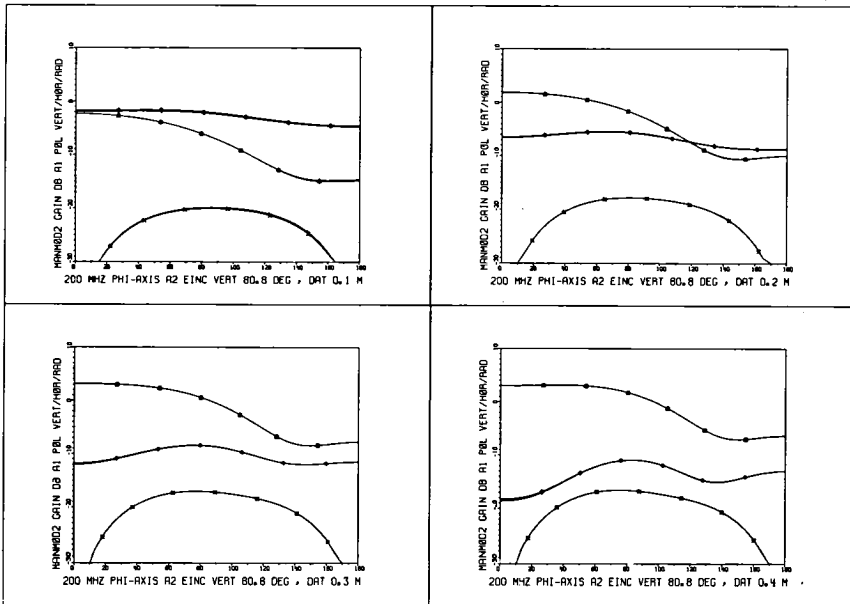


FIGURE 104c Azimuthal radiation patterns MANMOD2 at 200 MHz.

### AZIMUTHAL RADIATION PATTERNS IN THE 800 MHz RANGE

- FZYL : 800 MHz
- MANMOD1 : 800 MHz
- MANMOD2 : 800 MHz

The three figures show the azimuthal radiation patterns of the field components  $E_v$ ,  $E_r$  and  $E_h$  at  $d_{at} = 0.1, 0.2, 0.3$  and  $0.4$  m.

The accuracy of the results are very doubtful, because the computer program limitations have been exceeded at this high frequency (see section 10.3.4.).

Effect of the body shape:

- $E_v$  varies within 6 dB
- $E_r$  varies within 16 dB
- $E_h$  changes very much in wave form and amplitude

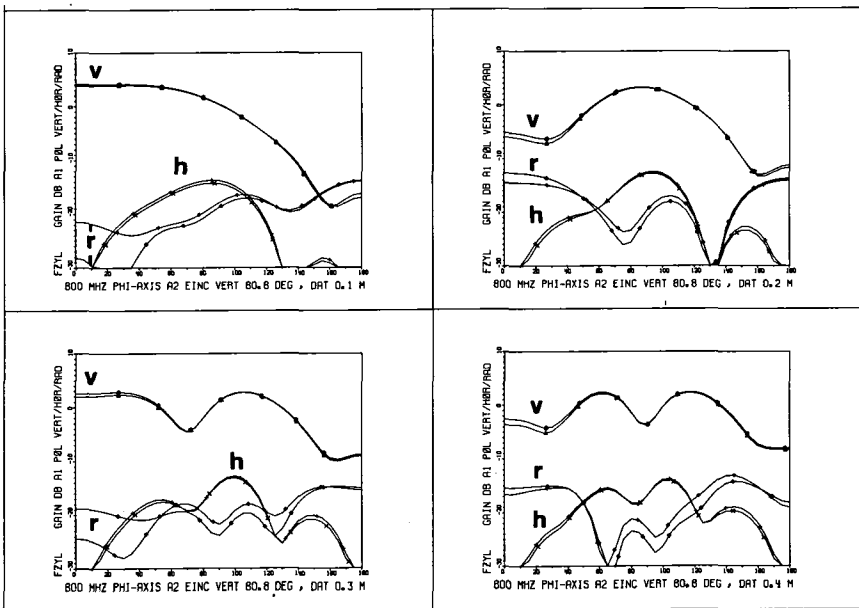


FIGURE 105a Azimuthal radiation patterns FZYL at 800 MHz.

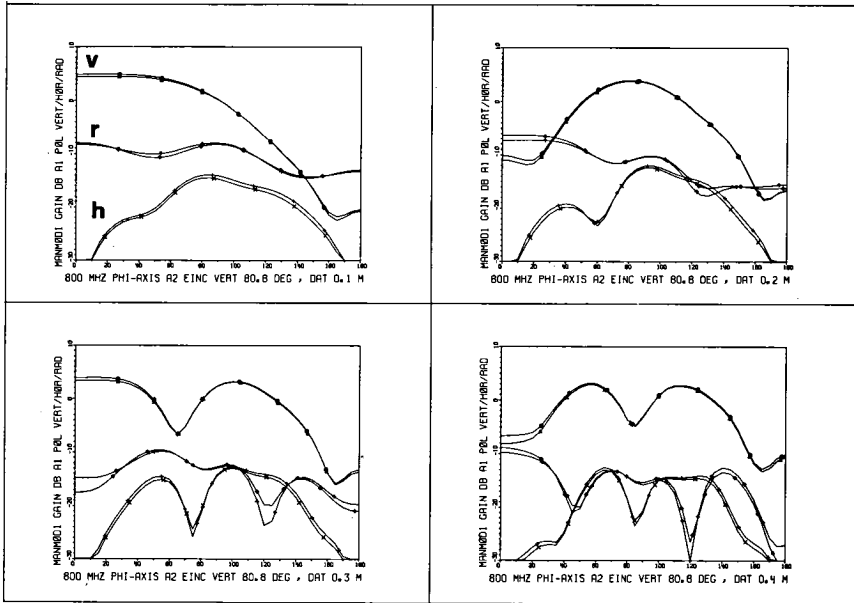


FIGURE 105b Azimuthal radiation patterns MANMOD1 at 800 MHz.

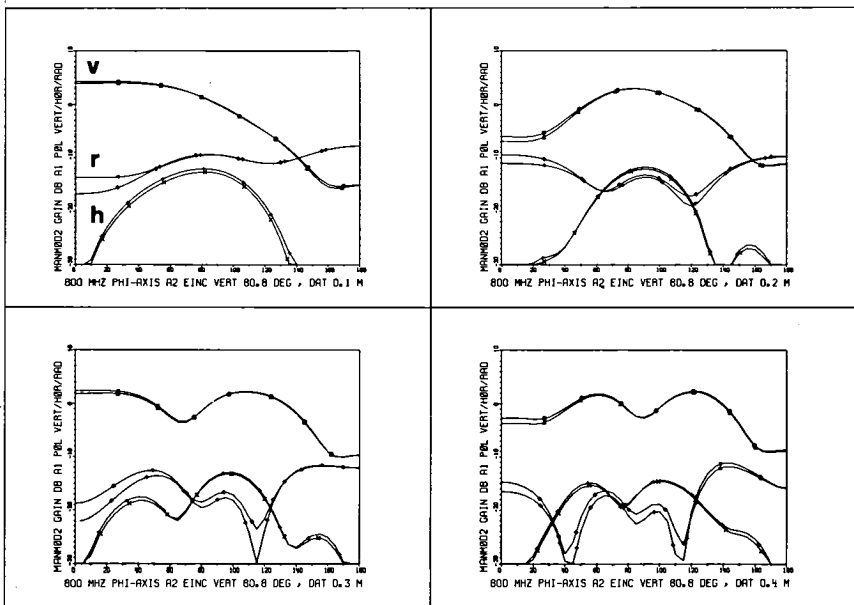


FIGURE 105c Azimuthal radiation patterns MANMOD2 at 800 MHz.

## L E B E N S L A U F

28. 7. 1943      Geboren in Baden (AG)
- 1950 - 1955      Primarschule in Wettingen (AG)
- 1955 - 1958      Bezirksschule in Baden und Wettingen
- 1958 - 1959      Oberrealsschule der Kantonsschule Zürich Stadt
- 1959 - 1963      Lehre als Maschinen-Schlosser bei Brown, Boverie & Cie
- 1963 - 1966      Teilzeit-Arbeit als FEAM bei Brown, Boverie & Cie und  
zweiter Bildungsweg bei der Akademikergemeinschaft in  
Zürich,  
Eidgenössische Matura, Typus C
- 1966 - 1970      Studium der Elektrotechnik an der Abt. III B der ETH  
Zürich. Hilfs-Assistent am Lehrstuhl für Apparatebau  
der Elektrotechnik der ETH Zürich, Industrietätigkeit.  
Abschluss als Dipl. El. Ing. ETH
- seit 1971      Leiter der Gruppe Messtechnik am Laboratorium für Bio-  
mechanik der ETH Zürich
- 1974      Organisator und Chairman des Second International  
Symposium on Biotelemetry, Davos, May 20-24, 1974
- 1974 - 1976      Vice-president der International Society on Biotelemetry  
und seither member of the scientific council
- seit 1978      Beirat der Schweizerischen Gesellschaft für Biomed-  
izinische Technik, Mitglied des Schweizerischen Fach-  
kommission FK-62 der IEC-SEV, Experte des Internatio-  
nalen TC-62 der IEC (Probleme der Biotelemetrie)